PhD Thesis

Multifunctionalization of Nanoscale Particles for Cancer Theranostics

By

Uday Narayan Pan

Department of Chemistry
Indian Institute of Technology Guwahati

Multifunctionalization of Nanoscale Particles for Cancer Theranostics

A thesis submitted by

Uday Narayan Pan

Roll No. 126122042

to

Indian Institute of Technology Guwahati

for the award of the degree of

Doctor of Philosophy

Department of Chemistry
Indian Institute of Technology Guwahati
Guwahati – 781039
India

December 2018

Statement

This thesis entitled **"*Multifunctionalization of Nanoscale Particles for Cancer Theranostics*"** is a work of research and investigation carried out by me under the supervision of Dr. Anumita Paul, Professor, Department of Chemistry, Indian Institute of Technology Guwahati. This thesis has been submitted by me to the Department of Chemistry, Indian Institute of Technology Guwahati for the award of the degree of Doctor of Philosophy. I further declare that this work has not been submitted anywhere else for any degree, diploma, associateship or membership etc. of any Institute or University to the best of my knowledge.

_____

Uday Narayan Pan
Department of Chemistry
IIT Guwahati,
Guwahati-781039, Assam
India
Date:
Place: Guwahati, Assam

Certificate

It is certified that the thesis entitled **"*Multifunctionalization of Nanoscale Particles for Cancer Theranostics*"** being submitted to the Indian Institute of Technology Guwahati by *Uday Narayan Pan (Roll. No. 126122042)* for the award of the degree of Doctor of Philosophy in Chemistry, is a bonafide record of research work carried out by him. The information and data reported by him are solely the results of his original findings. He has meticulously carried out the investigations and followed the guidelines of the laboratory. This work has not been submitted elsewhere for any degree or diploma.

_____

Anumita Paul
Thesis Supervisor
Professor,
Department of Chemistry,
IIT Guwahati,
Guwahati-781039, Assam,
India.
Date:
Place: Guwahati, Assam

Dedicated to my beloved parents

Mr.Banshi Badan Pan

and

Mrs. Manjusri Pan

Acknowledgements

I would like to express my foremost acknowledgement to my thesis supervisor Prof. Anumita Paul for her continuous support, encouragement, and help throughout my research work. Her profound scientific knowledge, critical analysis of experimental results and innovative ideas regarding the designing of experiments has helped me to solve difficult problems and improved my research work significantly. She has been a wonderful mentor to me.

I would like to express my sincere gratitude to Prof. Arun Chattopadhyay, who is a great inspiration for me. He has truly introduced me in the field of research and has done hand holding during the entire course of my PhD. I express my profound gratitude and deep regards, for his exemplary guidance, monitoring and constant encouragement throughout the progress of this thesis. He has also helped me to see life and science in their full depth, and taught me how to deal with the challenges. His advice has always helped me to reinvent myself time to time. I always consider myself fortunate for having been associated with such an inspiring and encouraging personality.

I would also like to thank sir and madam for providing me such a wonderful lab facilities, giving me enormous amount of freedom and teaching me the most important ethical aspect of research. I fell truly honoured as a part of this research group.

I would like to thank my doctoral committee members for periodically evaluating my research works. Their valuable suggestions have helped me to improve my work significantly.

I am extremely thankful to all my collaborators for their support and advices. A special thanks to Dr. Pallab Sanpui, he has helped me in many ways during my course of PhD. I would also like to thank Dr. Satyapriya Bhandari for his kind help.

I would like to express my gratitude to all the faculty and staff members of Department of Chemistry and Centre for Nanotechnology for their support. I am also thankful to the Central Instrument Facility and Department of Physics for permitting me to use their high-end instruments facilities.

I would also like to acknowledge all my past and present lab members for providing me such a wonderful atmosphere in the lab. Which has helped me to carry out my research smoothly.

I would like to acknowledge all of my friends for their constant support and encouragement.

Finally, I would like to thank my parents for their unconditional love, limitless support and sacrifices.

Thank you for your support

Uday

Contents

Abstract

Cancer is a highly heterogeneous disease with inter-patient variations, which prevent conventional chemotherapy from being fully effective. Herein, we explore the possibility of using multifunctional theranostic nanoparticles (MFTNPs) for simultaneous imaging, targeting and therapy of cancer cells *in vitro.* This could be useful for addressing challenges arising out of inter-patient variations and to further develop personalized therapeutic strategies thus reducing the vulnerability and increasing the chance of patient survival. The main focus of the current thesis is the development of MFTNPs by unifying discrete "functional components" into a single nanosystem with the potential of simultaneously performing multiple task including multimodal imaging of the disease site, successful delivery and controlled release of the drug, providing with additional therapeutic module in the form of hyperthermia and magnetically targeted therapy *in vitro*.

The thesis addresses two different approaches for the fabrication of the MFTNPs. The first strategy employs biocompatible and biodegradable protein (like bovine serum albumin and lysozyme) matrices for the unification of different functional nanomaterials for fabricating the MFTNPs. In this approach, we have developed an ideal plasmonic and magneto luminescent MFTNPs by integrating the three main functionalities of inorganic nanomaterials namely magnetic, plasmonic and luminescence and demonstrated successful application of these MFTNPs in bioimaging, magnetic targeting, plasmonic photothermal therapy and drug delivery. On the other hand, in the second strategy, we explore the newly developed method of "surface complexation" on nanomaterials for the fabrication of a single nanocrystal based MFTNPs capable of possibly single particle-level bioimaging and cancer therapy.

The present thesis is comprised of six chapters as described below.

Chapter 1 provides an introduction of the thesis and literature review regarding the applications nanomaterials in cancer theranostics. This chapter presents a brief idea about different theranostics applications of plasmonic, magnetic and

luminescent nanomaterials. It also discusses the processes for developing multifunction nanocarriers, multifunctional theranostics nanomaterials and their advantages in cancer theranostics.

Chapter 2 describes the fabrication of plasmonic and magneto-luminescent multifunctional nanocarriers (MFNCs) by assembling gold nanorods, iron oxide nanoparticles, and gold nanoclusters within BSA nanoparticles. The MFNCs showed self-tracking capability through single and two-photon imaging, and the potential for magnetic targeting *in vitro*. Appreciable T_2-relaxivity exhibited by the MFNCs indicated favorable conditions for magnetic resonance imaging. In addition to successful plasmonic-photothermal therapy of cancer cells (HeLa) *in vitro*, the MFNCs demonstrated efficient loading and delivery of doxorubicin to HeLa cells leading to significant cell death. These MFNCs with their multimodal imaging and therapeutic capabilities could be promising candidates for cancer theranostics.

Chapter 3 discusses the fabrication of a plasmonic-magneto-luminescent multifunctional nanocarrier (PML-MF nanocarrier) by lysozyme-mediated agglomeration of gold-coated iron-oxide nanoparticles (IO@AuNPs) and subsequent coating of these agglomerates with BSA-stabilized gold nanoclusters (BSA-AuNCs). Agglomeration-mediated red-shifting of the plasmonic absorbance peak of IO@AuNPs within PML-MFNCs towards NIR-biological window helped in plasmonic photothermal therapy (PPTT) by PML-MFNCs. PML-MFNCs demonstrated excellent *in vitro* bioimaging and magnetic targeting capabilities due to strong photoluminance and superparamagnetism of the constituent AuNCs and IO@AuNPs, respectively. PML-MF nanocarriers showed successful loading and delivery of doxorubicin to cancer cells with significant killing efficiency that could be synergistically improved by combining with PPTT.

Chapter 4 demonstrates the fabrication of a novel class of magnetofluorescent theranostic nanoparticles (MFTNPs) based on 'surface-complexation' of zinc ferrite ($ZnFe_2O_4$) NPs with 8-hydroxyquinoline (HQ). The potential of HQ surface complexed $ZnFe_2O_4$ NPs (HQ-ZFNP) in fluorescence-based bioimaging of different cancer cells was successfully demonstrated. The superparamagnetic behavior of the HQ-ZFNP was exploited effectively in magnetic targeting *in vitro*. Finally, a

well-known hydrophobic anti-malarial and prospective anti-cancer drug artemisinin was efficiently loaded into the MFTNPs. Artemisinin loaded MFTNPs were observed to induce superior anti-proliferative response, as compared to free drug, in cancer cells in a synergistic mechanism with combination index of 0.1 or less.

Chapter 5 discusses fabrication of novel magnetofluorescent nanoparticles by complexation of zinc ions present on the surface of zinc ferrite nanoparticle with 8-hydroxy-2-quinolinecarboxaldehyde (HQCald). The as prepared HQCald-complexed $ZnFe_2O_4$ NPs showed good quantum yield (3.62%), high photostability, considerable excited state lifetime (5.31 ns) and high saturation magnetization (12.7 emu g^{-1}). These magnetofluorescent nanoparticles demonstrated bioimaging capability both at the ensemble and single particle levels, and *in vitro* magnetic targeting. Moreover, the pronounced anti-proliferative efficacy of these nanoparticles against cancer cells, with appropriate targeting strategies, can lead to potential cancer theranostics.

Chapter 6 contains conclusion and future prospects.

भारतीय प्रौद्योगिकी संस्थान गुवाहाटी
Indian Institute of Technology Guwahati

CHAPTER 1

Introduction

According to the US National Cancer Institute (Office of Technology and Industrial Research 2006) "*Nanotechnology will change the very foundations of cancer diagnosis, treatment, and prevention*".[1-2] More specifically, the unique optoelectronic and physico-chemical properties of nanoscale materials, compared to their bulk counterpart, make them apt choice for biodiagnostics and cancer treatment.[3-10] Notably, cancer is one of the leading causes of death worldwide. According to the World Health Organization (WHO), approximately one out of six deaths is caused by cancer globally[11-12] Various cancer treatment options such as chemotherapy, surgery and radiotherapy have been aggressively pursued to counter the disease. Nonetheless, their applications are limited due to damage of healthy cells and incomplete abolition of malignant tumors.[12-16] Thus at this juncture material scientist face a challenging task of developing newer nanoscale based materials, which will not only address the issues faced by the present day anticancer treatment options but also have diagnostic capabilities in addition to therapeutic abilities.[3-10] In this regard, nanoscale materials offer unique platform to load therapeutic molecules for selective targeting of cancer cells concomitant with reduced side effect profile and also provide new diagnostic and therapeutic tools like plasmonic photothermal therapy, magnetic hyperthermia, magnetic resonance imaging and photo luminescence emission based optical imaging.[3-10] Importantly, nanoscale materials empower combination therapy with different drug molecules, multimodal therapy with different therapeutic modalities and also permit simultaneous diagnosis and therapy known as theranostic action.[3-10] Hence, this is directed towards the development of new cancer treatment strategies to reduce the vulnerability and increase the chance of survival to the patient.[3-10,17]

1.1. Nanomaterials in cancer theranostics

As of now, three different categories of inorganic nanomaterials i.e., plasmonic, magnetic and luminescent materials, have been widely demonstrated for their use in biomedical applications including cancer theranostics.[3-10, 17-18] These broad categories are described briefly.

1.1.1. Plasmonic nanomaterials and their applications in cancer theranostics

Nanomaterials composed of noble metals like gold, silver and palladium interact with external electromagnetic radiations.[6-7] Under the exposure of a particular wavelength of light surface electrons of these nanomaterials (depending upon their size, shape and constituent metals) form plasmons (coherent oscillation of surface electrons), that cause strong extinction of light (absorption and scattering). This phenomenon is known as surface plasmon resonance (SPR, Figure 1.1).[6-7, 19] Metallic nanomaterials exhibiting SPR are known as plasmonic nanomaterials.

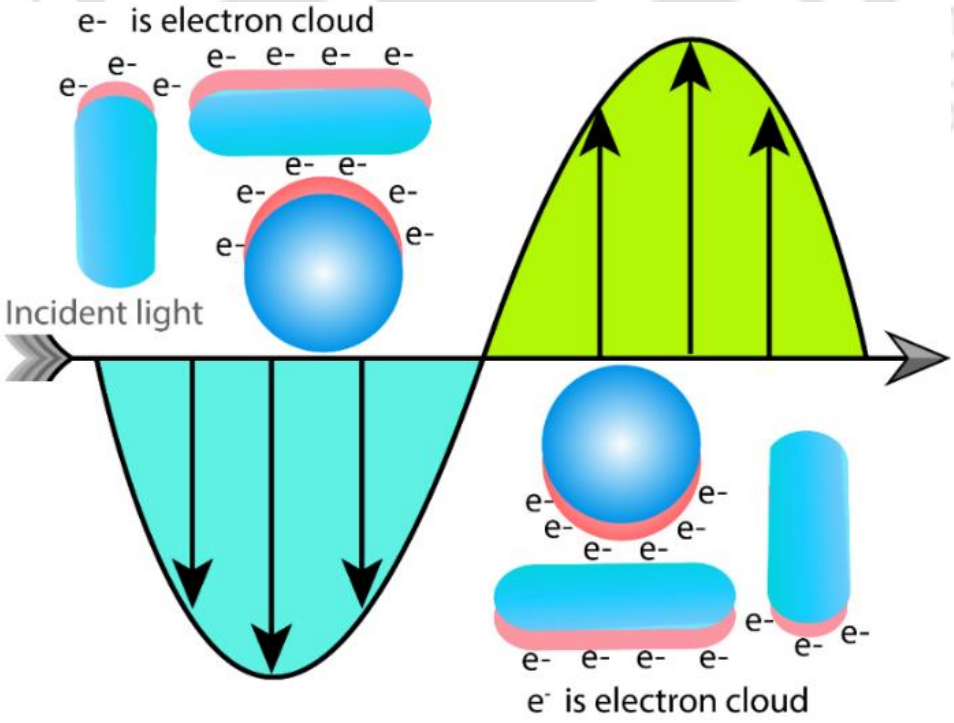

Figure 1.1. Representation of localized surface plasmon resonance of noble metal nanomaterials in presence of external electromagnetic radiation.

1.1.1.1 *Plasmonic Photothermal Therapy (PPTT)*

Plasmonic nanomaterials, strongly absorb photon energy from light and can convert them to heat energy, following nonradiative energy dissipation.[20-22] If the heat energy generated under laser irradiation, is sufficiently high to raise the local temperature of the disease site to destroy the tumor then the therapeutic process is termed as plasmonic photothermal therapy (PPTT). Basically, PPTT is a minimally-invasive therapeutic technique where plasmonic nanomaterials are heated using near infrared laser to destroy malignant tumors (Figure 1.2).[6-7, 20-24]Among many plasmonic nanomaterials, gold nanostructures are superior therapeutic agent, for PPTT, due to their efficiency and rapid conversion of photon energy to heat energy, ease of surface functionalization, biocompatibility and higher extinction cross-sections (compared to organic chromophores).[6-7, 20-24]

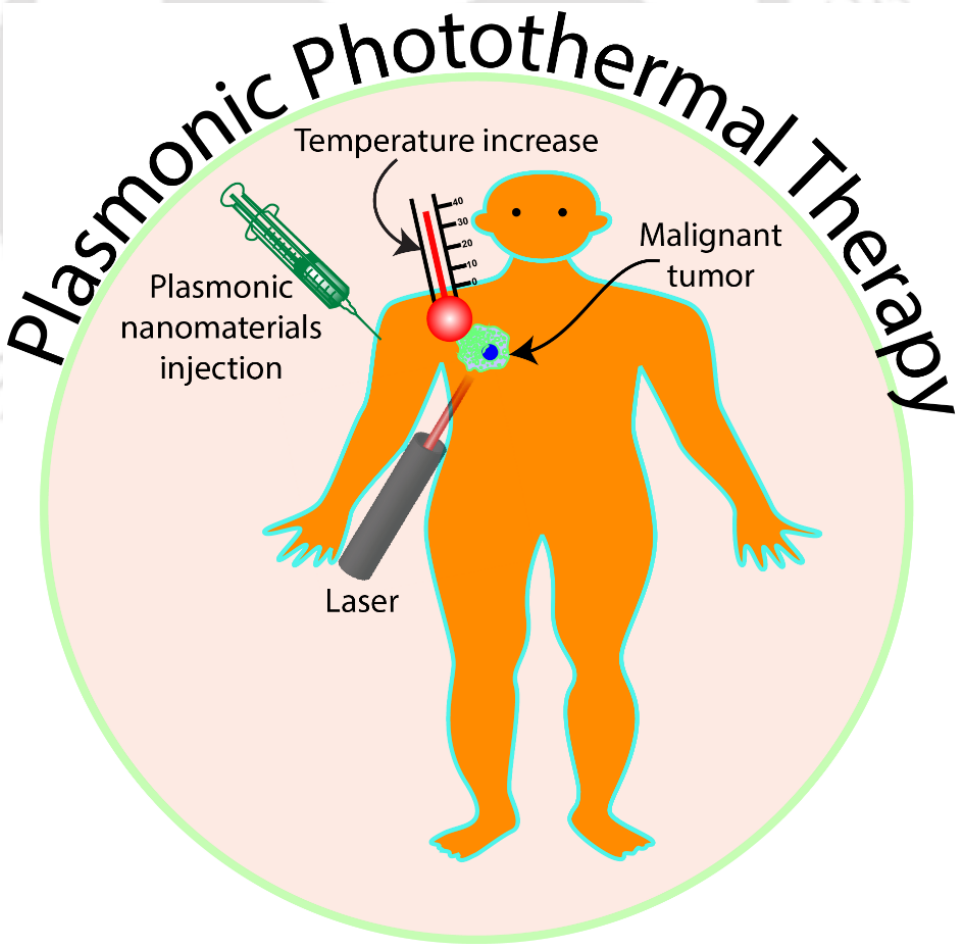

Figure 1.2. Schematic representation of plasmonic photothermal therapy.

Gold based nanostructures such as gold nanorods, gold nanocages or gold nanoshell on silica or iron oxide nanoparticles have widely been studied for PPTT.[6-7, 20-24] In PPTT, cells surrounding the gold nanostructures are directly heated up and as a result, the local temperature increases from ten to hundred degrees Celsius over the physiological temperature (within a short span of time) and leads to the efficient eradication of the malignant tumors with minimum collateral damage.[6-7, 20-24]

1.1.1.2 Other Applications

In addition to PPTT, plasmonic nanomaterials have also been used for photothermal imaging, two-photon luminescence imaging, enhancing drug release from nanocarriers and improving efficiency of photodynamic therapy.[20-31]

1.1.2. Magnetic nanomaterials and their applications in cancer theranostics

Magnetic nanoparticles, mainly iron oxide and ferrites (Zn, Co, Mn, Cu, Mg, and Ca), have attracted tremendous attention due to their multiple biomedical utilities derived from superparamagnetic nature with exceptionally high saturation magnetization.[10, 32-35] Superparamagnetism enables magnetic nanoparticles for various biomedical applications such as magnetic targeting, magnetic resonance imaging (MRI) and magnetic hyperthermia. Properties like small and uniform size, high biocompatibility and easy surface functionalization also enhanced their demand for clinical cancer theranostics.[10, 32-35]

1.1.2.1 Magnetic Resonance Imaging (MRI)

Superparamagnetic nanoparticles has been clinically used as negative MRI contrasting agent (T_2).[10, 32-35] 120-180 nm IONPs coated with dextran (commonly known as Feridex) and 60 nm IONPs coated with carboxydextran (commonly known as Resovist) are clinically approved T_2 MRI contrasting agents.[36] In recent years, small sized and highly monodispersed superparamagnetic nanoparticles has been developed as MRI contrasting agents to significantly enhance the contrasting capacity.[10, 32-35] Different shaped nanomaterials (Figure 1.3),[32-37] multiple surface coating agents has also been introduced to improve their relaxivity.[32-37] Monodispersed and small sized superparamagnetic nanomaterials hold immense potential towards MRI-based diagnosis of cancer.

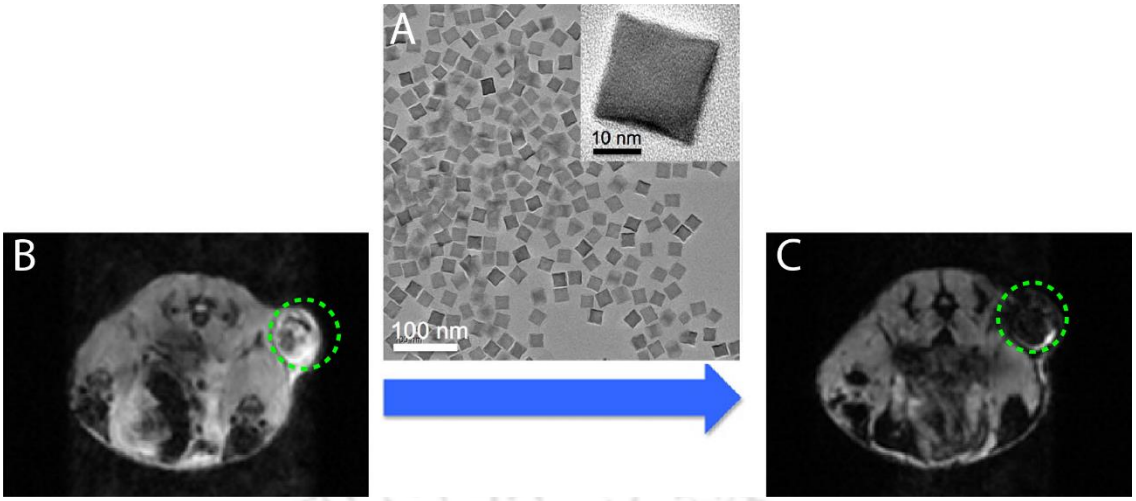

Figure1.3. (A) TEM images of iron oxide nanocubes (ION Cubes). *In vivo* magnetic resonance images of the tumor site (B) before and (C) 1 h after intravenous injection of ION Cubes. Green doted circle represent the tumor sites. (The above figure is reproduced from reference 37 with prior permission)

1.1.2.2 Magnetic Hyperthermia

Recently, magnetic hyperthermia has been emerged as a minimally invasive potential therapeutic alternative for cancer treatment because of less side effect, localized nature and combination therapeutic possibilities with conventional therapeutic techniques.[32-40] Due to "magnetic losses" superparamagnetic nanoparticles generate heat when they are placed in an alternating magnetic field.[40-41] If the frequency of the alternating magnetic field is sufficiently high, a very small quantity of superparamagnetic nanoparticles may increase the local temperature of the disease sites and resulting in killing of the cancerous cells and thus making them desirable for reducing of collateral damage.[32-41] In this regard, various magnetic nanomaterials such as iron oxide, ferrite nanoparticles and nanocubes have already been studied. Multiple coating agents (such as biocompatible polymers, proteins and liposomes) for the magnetic nanomaterials have also been investigated to improve the efficiency of the hyperthermia and biocompatibility of the nanomaterials.[32-41]

1.1.2.3 Magnetic Targeting

Delivery of the therapeutic load efficiently and specifically to the disease site to reduce side effects, is an important target in cancer theranostics.[17, 42-44] Different targeting techniques such as passive targeting following enhanced permeability and retention (EPR) effect, active targeting using specific organic molecules to target overexpressed receptors have been studied widely. The clinical applicability of both the mentioned techniques suffer from the drawbacks related to either heterogeneity of tumors or inter-patient differences in receptor over expression.[17, 42-44] Under this circumstances, the development of less inter-patient dependent targeting technique, with high targeting efficiency, is critically important. Owing to less dependency on tumor behaviors, receptors over expression and biological pathway, targeting of drug loaded magnetic nanoparticles (using external magnetic field at the disease site) make them potential alternative compared to the traditional targeting techniques.[32-41,45-46] Due to the more controllable and predictable nature of magnetic targeting, a variety of magnetic vehicles has been developed for the delivery of therapeutic agents to the specific sites in the body.[32-41, 45-46] Moreover, magnetic targeting increase the local concentration of the magnetic nanoparticles in disease sites and thus also improve the potentiality of magnetic hyperthermia (Figure 1.4).[32-41, 45-46]

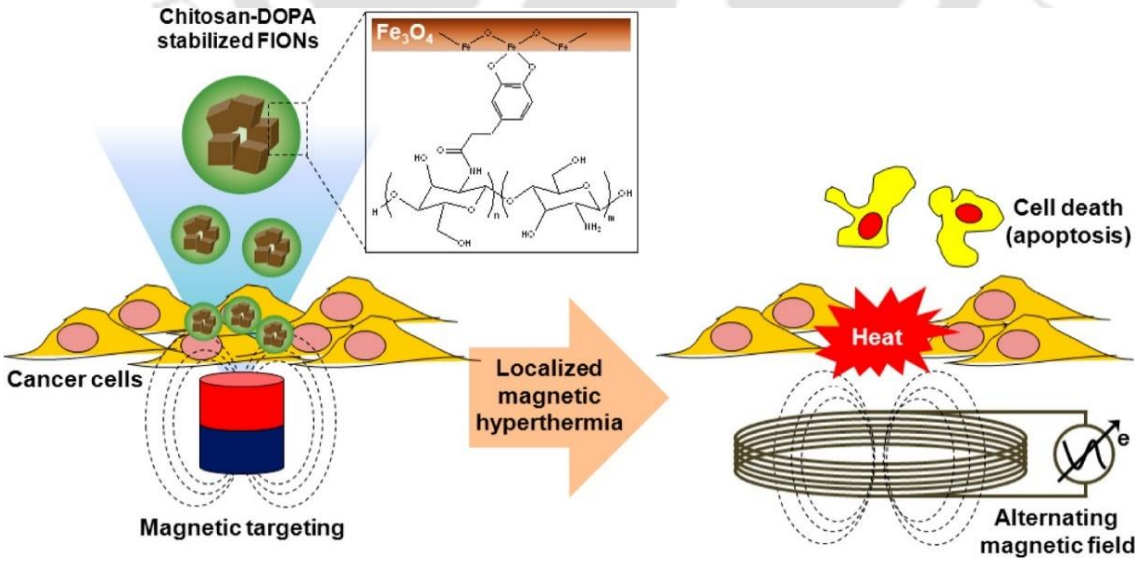

Figure1.4. Schematic illustration of chitosan oligosaccharide-stabilized ferrimagnetic iron oxide nanocubes (Chito-FIONs) and their applications for the magnetic targeting induced localized magnetic hyperthermia of cancer cells. (The above figure is reproduced from reference 32 with prior permission)

1.1.3. Luminescent nanomaterials and their applications in cancer theranostics

Luminescence bioimaging offers versatile low-cost, high contrast, highly sensitive and selective, non-invasive optical imaging technique for identifying morphological specifications of cells/tissues and investigating behavior of microspecies of living cells/animals.[8-9, 47-50] In last two decades, enormous improvements in resolution of luminescence bioimaging, including single molecular/particle level imaging of the fluorophores, helped to understand various complex biological phenomena.[8-9, 47-50]

1.1.3.1 Luminescent probe

Luminescent probes have been used as imaging agents for the purpose of bioimaging. There are basically two kinds of luminescent imaging probes, (a) intrinsic luminescent species like nicotinamide adenine dinucleotide (NADH) or chlorophyll and (b) external luminescent probe like fluorescent organic dyes or nanomaterials.[8-9, 47-50] So far, organic dye molecules and quantum dots has been extensively used for bioimaging.[8-9, 47-50] However, the application potential of organic dyes is limited due to their fast photobleaching, small Stokes-shifted emission, aggregation-induced fluorescence quenching and small excitation cross-section for two-photon imaging. Whereas the toxicity due to leaching of constituent heavy metal ions in the intercellular environment hamper the bioimaging applications of quantum dots.[8-9, 47-50] In this regard, ultra-small gold nanoclusters (AuNCs, with size less than 2 nm) have drawn much attention due to their high photostability, high biocompatibility, large Stokes - shifted emission, longer emissive lifetime and broad two-photon excitation cross-section. AuNCs have been widely studied both *in vitro* and *in vivo* bioimaging due to the above mentioned advantages (Figure 1.5).[8-9, 47-50]

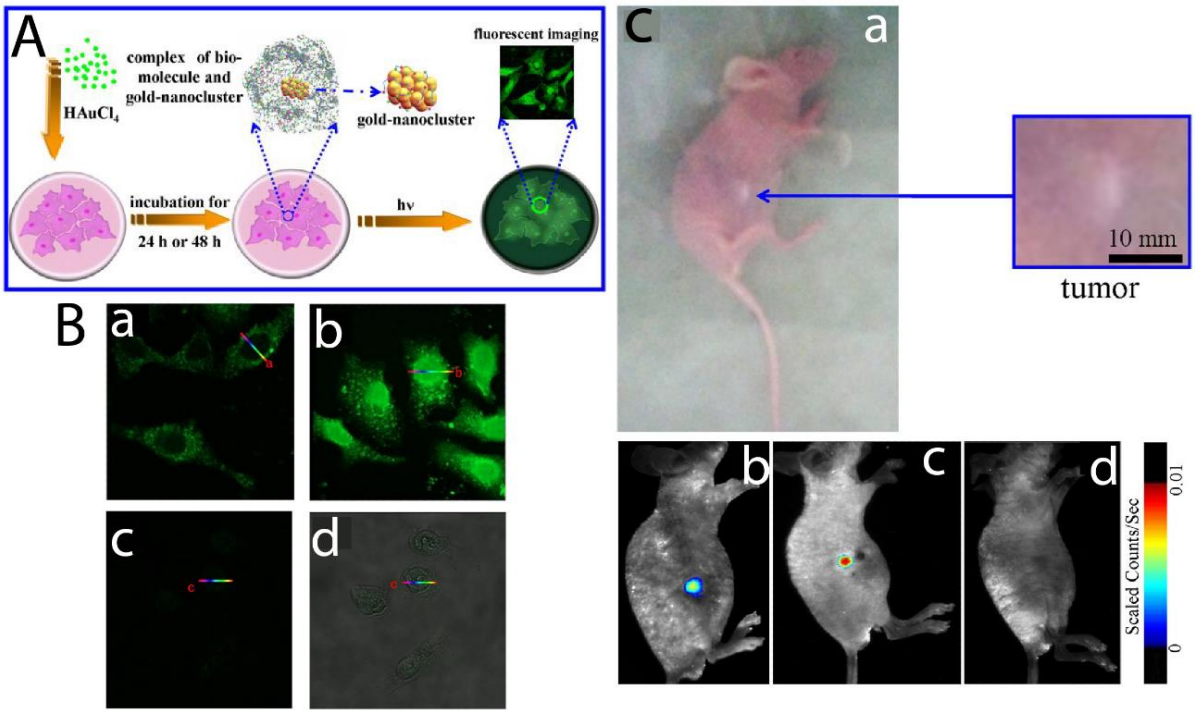

Figure1.5. (A) Schematic depiction of biosynthesis of gold nanoclusters in cells for imaging. (B) Confocal laser scanning images of HepG2 (a&b) and L02 control cells (c and d) incubated with identical 10 mmol/L $HAuCl_4$ solutions. (C) Representative xenograft tumor mouse models of hepatocellular carcinoma observed in normal light (a) or by *in vivo* fluorescence imaging (b) 24 h after a subcutaneous injection of 10 mmol/L $HAuCl_4$ solution near the tumor. In (a), the inset shows an enlarged view of the xenograft tumor. Xenograft tumor mouse models of chronic myeloid leukemia observed by *in vivo* fluorescence imaging (c) 24 h after a subcutaneous injection of 10 mmol/L $HAuCl_4$ solution near the tumor. (d) Control mouse observed by *in vivo* fluorescence imaging 48 h after a subcutaneous injection of 10 mmol/L $HAuCl_4$ solution in the right side of their abdomen. (The above figure and the caption is reproduced from reference 49 with prior permission)

1.2 Nanocarriers

Nanocarriers for chemotherapeutic drugs have been developed to overcome multiple problems associated with the traditional chemotherapy like nonspecific action of the drug, premature degradation and insolubility of some of the drugs in aqueous medium. In this regard, a variety of nanocarriers have been developed for different chemotherapeutic drugs. Some of the nanocarriers that have been approved by Food and Drug Administration (FDA) for clinical use, are listed in next page.[3-5, 51-52]

Market name	Type of the nanocarrier	Drug loaded in the nanocarrier
Abraxane[3]	Albumin Nanoparticles	Paclitaxel
Doxil/Caelyx[3]	PEGylated liposomes	Doxorubicin
Oncaspar[3]	Polymer–protein conjugate	Peg-L-asparaginase
Nanoxel[3]	Polymeric micelle	Paclitaxel

1.2.1 Benefits of nanocarriers

Nanocarriers possess multiple advantages, which are as follows:

1. Nanocarriers, with appropriate targeting strategy, could lead to significant reduction in collateral damage caused by the nonspecific nature of the chemotherapeutic drugs.[3-5]
2. Improve the aqueous solubility of the hydrophobic drugs and thus make administration easier with increased bioavailability.[3-5]
3. Protect the drugs from premature degradation by keeping them away from external environment during circulation in blood.[3-5]
4. Facilitate slow or controlled release of the drug and thus improve the efficiency of the drug in eradication of the tumor.[3-5]

1.2.2 Category of Nanocarriers

Different types of nanocarriers, based on the constituent materials like protein, polymer, dendrimer, metal nanoparticles, liposomes, micelles, carbon nanotubes and quantum dots, have been developed (Figure 1.6).[3-5, 51-52]

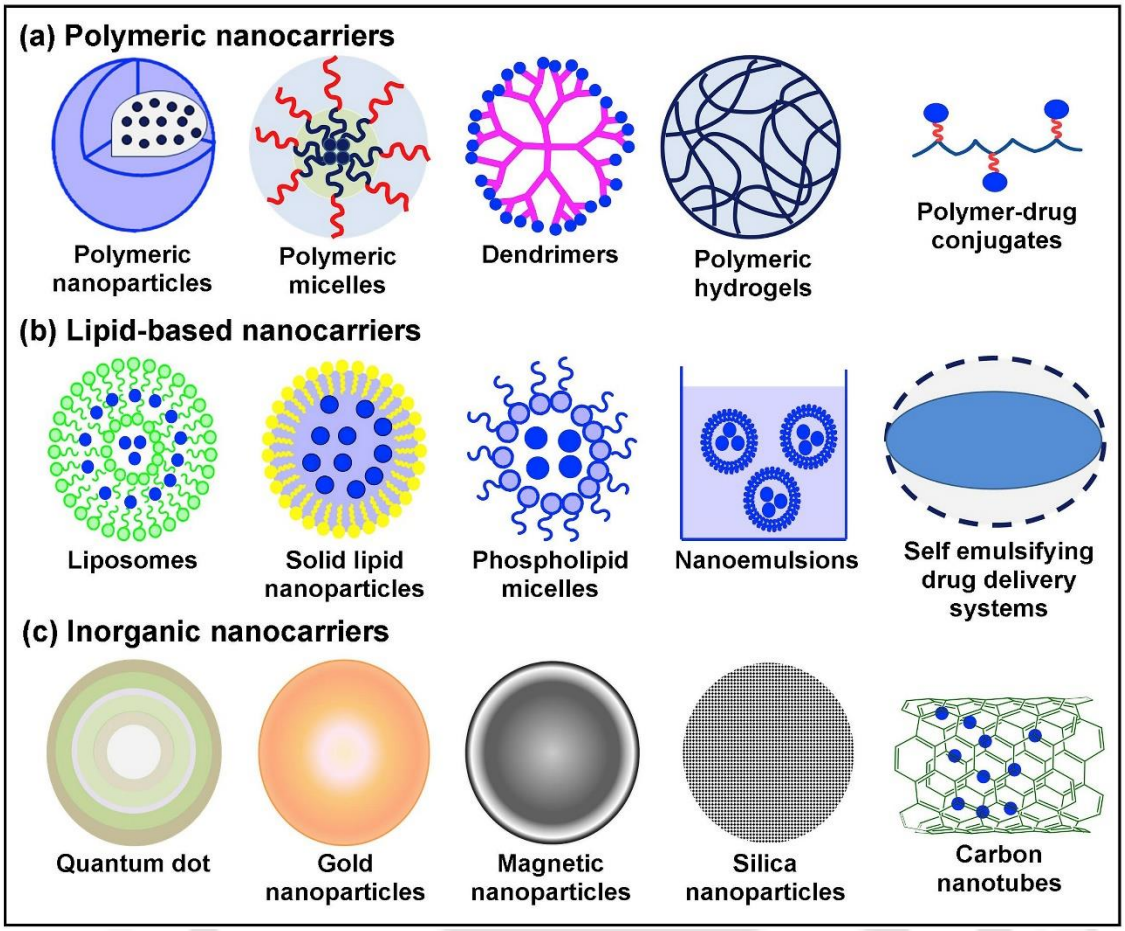

Figure 1.6. Examples of different types of nanocarriers used for drug delivery. (The above figure is reproduced from reference 51 with prior permission)

1.2.3 Multifunctional nanocarriers

With the advancement in the fabrication of nanocarriers for chemotherapeutic drugs, the development of multifunctional nanocarriers has become a current and important trend in last few of years.[3-5, 17-18] Nanocarriers that perform multiple task like multimodal imaging, therapy, drug delivery by integrating multiple 'functional units' in a single platform, are known as multifunctional nanocarriers (Figure 1.7).[17-18] Improvement in the synthesis techniques of basic nanoparticles and growing medical needs have encouraged scientists to focus on the development of extremely complex nanocarriers for cancer theranostics.[17-18] As discussed before, cancer is a highly heterogeneous disease, with varying nature from patient to patient, and thus makes the job of the conventional chemotherapy

very difficult. Hence, more image-guided treatments are needed to tackle the inter patient variances and to develop further personalized actions based on the responses and condition of the patient.[17-18, 52-56] Multifunctional nanocarriers offer multimodal imaging in various stages of the treatment and thus improve the efficiency of the therapy and diagnosis. In addition, multifunctional nanocarriers offer the unique opportunity of combination therapy, based on the therapeutic capability of different inorganic nanoparticles and chemotherapeutic drugs, that may even cause complete eradication of the tumor and reduce the chances of drug resistance. [17-18, 52-56]Multifunctional nanocarriers could also ensemble all the targeting strategies (like passive targeting, molecular targeting and magnetic targeting) to significantly reduce collateral damage. Thus, by acting in highly interactive path multifunctional nanocarriers hold the potential of revolutionizing orthodox cancer therapy and may bring paradigm shift in survival of patients.[17-18, 52-56]

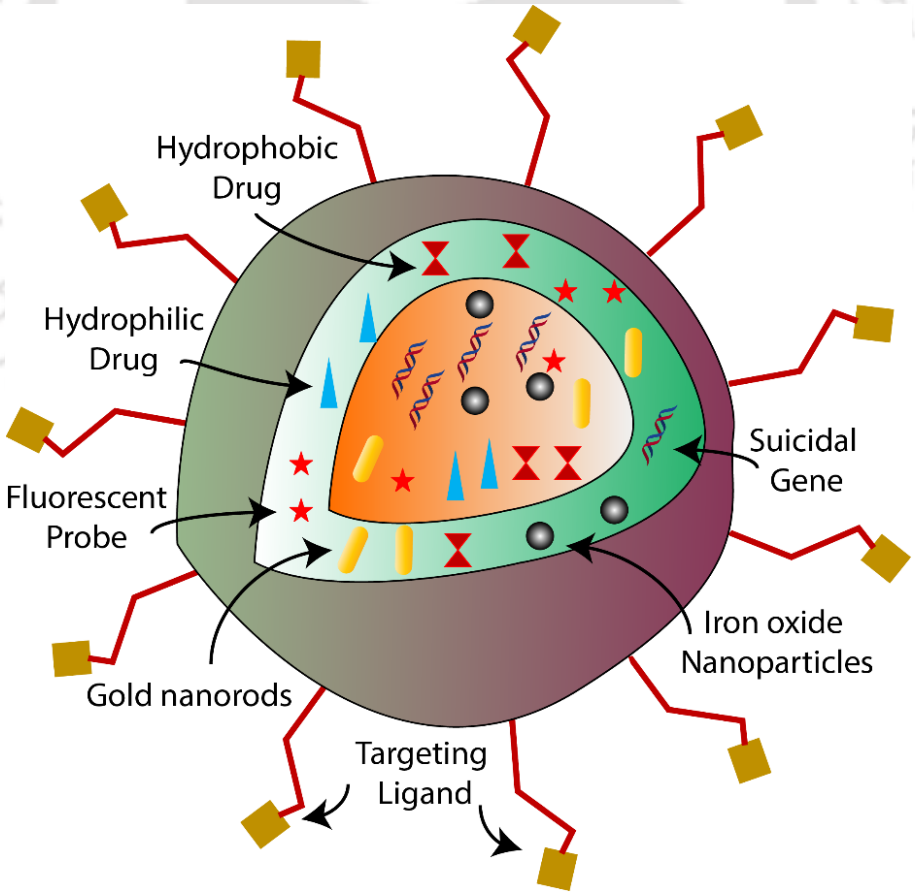

Figure 1.7. Graphical representation of multifunctional nanocarrier.

1.2.3.1 Role of Proteins in Development of Multifunctional Nanocarriers

As discussed earlier, multifunctional nanocarriers are developed by integrating individual "functional units" in a single platform. Hence, a unifying matrix is required to develop multifunctional nanocarriers.[52-60] Among the different unifying matrixes, biofriendly and biodegradable polymers, proteins and silica matrixes, are well-known. Proteins remain as the preferred choice among all because of their high biocompatibility, high stability in physiological conditions, biodegradability, capacity to interact with broad spectrum of hydrophobic and hydrophilic molecules and being non-cytotoxic in nature.[52-67] Moreover, proteins not only help to integrate different functional nanomaterials in a single dais but also tune the nanomaterials properties in such a way that can enhance the therapeutic application potential of the nanomaterials.[68-70] Albumin and lysozyme (Lyz) are two important proteins, which have been extensively used to develop different types of nanocarriers, including multifunctional ones. Albumins are present in blood plasma and commonly act as carriers for vitamins, hormones, fatty acids, drugs and metal ions.[52-70] Importantly, some types of tumors like prostate, lung and breast tumors possess over-expressed albumin receptors, hence, facilitate preferential accumulation of albumin based nanocarriers.[61-67, 70] Above all, albumins efficiently interact with a broad spectrum of inorganic nanoparticles and their stabilizers - which make them ideal unifying matrices for the development multifunctional nanocarriers (Figure 1.8).[52-70] On the other hand, Lyz, an antimicrobial enzyme, has also been used for drug targeting to kidney. For the capability of interacting with different inorganic nanomaterials, Lyz could also be used for developing multifunctional nanocarriers.[68-70]

1.2.4 Nanoparticle-Protein Agglomerates as Nanocarriers

Different nanoparticles, especially small sized gold nanoparticles (AuNPs), have been reported to form stable nanoscale agglomerates when interacted with some specific proteins.[67-73] At physiological pH, positively charged protein like lysozyme (Lyz), has the propensity to attach on the surface of negatively charged AuNPs.

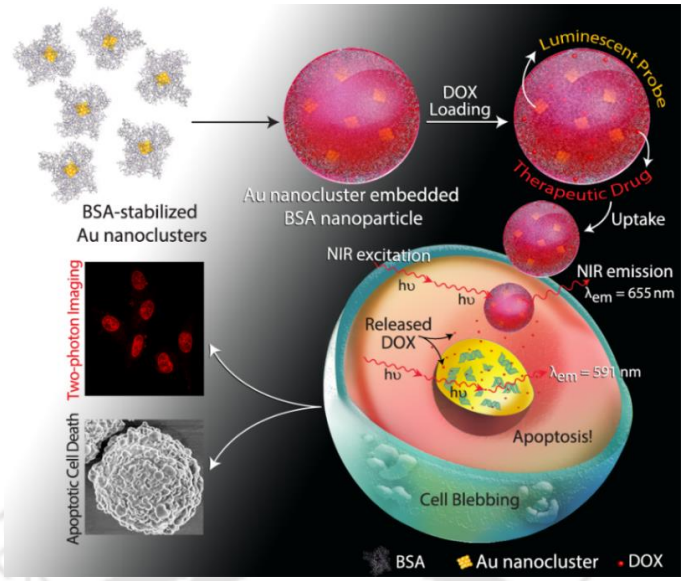

Figure 1.8. Schematic depiction of the preparation of gold nanocluster embedded BSA nanoparticles for bioimaging and delivery of chemotherapeutic drug doxorubicin to cancer cells. (The above figure is reproduced from reference 70 with prior permission)

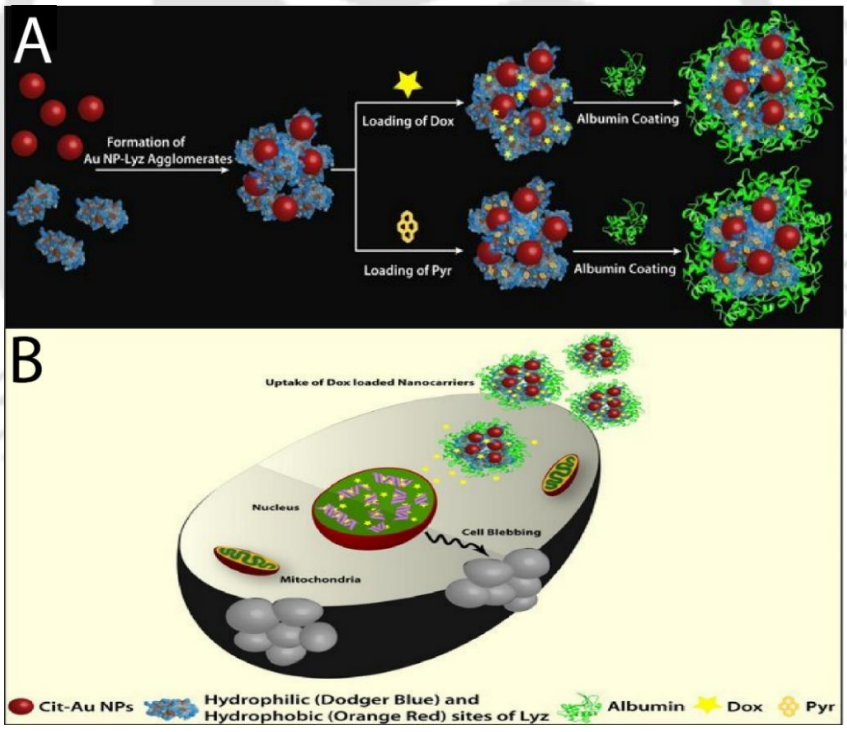

Figure 1.9. Schematic depiction of AuNPs-Lyz agglomeration based fabrication of nanocarriers, subsequent loading of doxorubicin (Dox) and pyrene (Pyr), their uptake succeeding release of the cargo molecules inside the tumor cell leading to cell death. (A) Nanocarriers were fabricated in three steps, first preparation of the Lyz mediated agglomerates of AuNPs, second loading of Dox (hydrophilic drug) or Pyr (hydrophobic molecule) and third coating of the loaded nanocarriers with bovine serum albumin (BSA) for better stability. (B) Uptake of the drug loaded nanocarriers by the cancerous cell, release of Dox subsequently causing cell death by activating apoptosis. The above figure is reproduced with permission from references 67.

Nanoparticle surfaces facilitate partial unfolding of the Lyz - which enmesh more protein molecules and nanoparticles resulting to the agglomeration of the AuNPs. [67-73] As protein possess both hydrophilic and hydrophobic sites, these nanoparticle-protein agglomerates, are capable of both loading and delivery of the hydrophilic as well as hydrophobic drug molecules to the cancer cells (Figure 1.9). [67-73] In addition to that, agglomeration of AuNPs by protein cause broadening and red shifting of the SPR peak of AuNPs towards biological spectral window region - which could enhance the efficiency of the plasmonic photothermal therapy (PPTT). [67-73]

1.3 Multifunctional Theranostics Nanoparticles

The term theranostics is the combination of two fields; diagnosis and therapy. Multifunctional theranostics nanoparticles (MFTNPs), are basically those nanoparticles, which simultaneously perform therapy and diagnosis of the diseases. MFTNPs also provide monitoring of the responses of the patients following various noninvasive imaging techniques along with precise therapy. [3-5, 17-18, 52-56] Multifunctional nanocarriers, as discussed above, also fall in the category of MFTNPs.

1.3.1 Role of Surface complexation in development of Multifunctional Theranostics Nanoparticles

The surface of quantum dots (Qdots) and metal oxide nanoparticles are comprised of metal ions, which allow them to react to form inorganic complexes with external complexing agents, particularly with organic ligands.[74-81] This also show that the choice of organic ligands is important in order to form inorganic complexes on the surface of Qdot and/or metal oxides nanoparticles. Recently many studies have demonstrated the use of different organic ligands for the formation of inorganic complexes on the surface of a presynthesized Qdot and subsequently conferring new and advantageous emission properties to such

complexed Qdot (otherwise termed as quantum dot complex (QDC)) in comparison to their parents components and thus demonstrated their various applications ranging from white light generation to sensing purposes.[74-81] One of the prime aims of this thesis is to form inorganic complexes on the surface of magnetic nanoparticles, which will endow the multifunctional nanoparticle with anticancer activity. Thus, the strategy of the formation of inorganic complexes, with anticancer activities, on the surface of magnetic metal oxide nanoparticles, could be used as an alternative method for the development of multifunctional theranostic nanomaterials.[74-81]

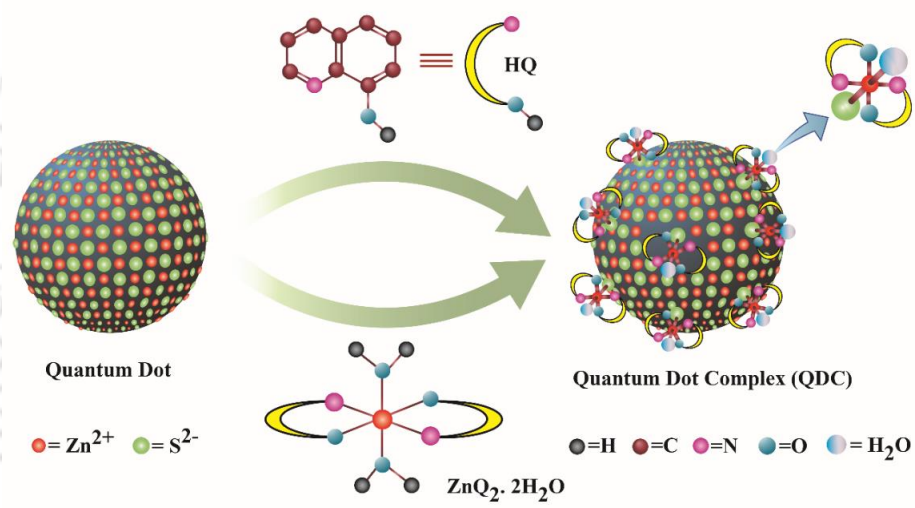

Figure 1.10. Graphical depiction of reaction between zinc sulfide Qdots and 8-Hydroxyquinoline (HQ) to form quantum dot complex (QDC).The above figure is reproduced with permission from references number 74.

1.4 Overview of the Thesis

The primary aim of the thesis is the fabrication of multifunctional nanocarriers/nanoparticles following Integration of independent functional components, which are basically plasmonic, magnetic, and fluorescent in nature, and thereby their use in cancer theranostics. The thesis is comprised of four separate research works - in addition to introduction (**Chapter 1**), which is

comprised of literature survey. The salient features of each work are separately highlighted as follows:

Chapter 2 describes the fabrication of plasmonic and magneto-luminescent multifunctional nanocarriers (MFNCs) by assembling gold nanorods, iron oxide nanoparticles, and gold nanoclusters within BSA nanoparticles and finally, their (MFNCs) use for single and two-photon imaging, *in vitro* magnetic targeting, magnetic resonance imaging, plasmonic photo thermal therapy and delivery of doxorubicin to HeLa cells.

Chapter 3 discusses protein-nanoparticle agglomeration-based fabrication of an advance plasmonic-magneto luminescent multifunctional nanocarrier (PML-MF nanocarrier) and their use in plasmonic photo thermal therapy, bioimaging, magnetic targeting, drug delivery and combination therapy.

Chapter 4 demonstrates the fabrication of a novel class of magneto-fluorescent theranostic nanoparticles (MFTNPs), based on the 'surface-complexation' of zinc ferrite ($ZnFe_2O_4$) NPs with 8-hydroxyquinoline (HQ) and the applications of these MFTNPs, following loading with well-known hydrophobic anti-malarial and prospective anti-cancer drug artemisinin, in fluorescence-based bioimaging in different cancer cells, *in vitro* magnetic targeting and synergistic anticancer activity.

Chapter 5 discusses the fabrication of novel magneto-fluorescent nanoparticles by complexation of zinc ions, present on the surface of zinc ferrite nanoparticle, with 8-hydroxy-2-quinolinecarboxaldehyde (which acts as an anticancer agent) and the use of these magneto fluorescent nanoparticles in bioimaging (both at the ensemble and single particle levels), magnetic targeting and antiproliferative efficacy in cancer cells.

References

1. Mansoori, G.A.; Mohazzabi, P.; McCormack, P.; Jabbari' S. Nanotechnology in cancer prevention, detection and treatment: bright future lies ahead *World Rev. Sci. Technol. Sustain. Dev.,* **2007,** *4,* 226-257.
2. Bhati, W.; Vishwa, A. Nanotechnology method comparison for early detection of cancer *Int. J. Intell. Syst. Appl.,* **2013** *03*, 58-65.
3. Peer, D.; Karp, J. M.; Hong, S.; Farokhzad, O.; Margalit, R.; Langer, R. Nanocarriers as an emerging platform for cancer therapy *Nat. Nanotechnol.* **2007**, 2, 751– 760.
4. Lammers, T.; Aime, S.; Hennink, W. E.; Storm, G.; Kiessling, F. Theranostic Nanomedicine *Acc. Chem. Res.* **2011**, *44*, 1029-1038.
5. Lim, E.-K.; Kim, T.; Paik, S.; Haam, S.; Huh, Y.-M.; Lee, K. Nanomaterials for Theranostics: Recent Advances and Future Challenges *Chem. Rev.* **2015**, *115*, 327– 394.
6. Huang, X.; Jain, P. K.; El-Sayed, I. H.; El-Sayed, M. A. Gold Nanoparticles: Interesting Optical Properties and Recent Applications in Cancer Diagnostics and Therapy *Nanomedicine* **2007**, *2,* 681-693.
7. Jain, P. K.; Huang, X.; El-Sayed, I. H.; El-Sayed, M. A Noble metals on the nanoscale: Optical and photothermal properties and some applications in imaging, sensing, biology, and medicine *Acc. Chem. Res*. **2008** *41*, 1578– 1586.
8. Yao, J.; Yang, M.; Duan, Y. Chemistry, Biology, and Medicine of Fluorescent Nanomaterials and Related Systems: New Insights into Biosensing, Bioimaging, Genomics, Diagnostics, and Therapy *Chem. Rev.* **2014**, *114*, 6130– 6178.
9. Chen, L.-Y.; Wang, C.-W.; Yuan, Z.; Chang, H.-T. Fluorescent Gold Nanoclusters: Recent Advances in Sensing and Imaging *Anal. Chem.* **2015**, 87, 216– 229.
10. Pankhurst, Q. A.; Connolly, J.; Jones, S. K.; Dobson, J. Applications of Magnetic Nanoparticles in Biomedicine *J. Phys. D: Appl. Phys.* **2003**, *36*, 167– 181.
11. World Health Organization (WHO), News, Fact sheets. https://www.who.int/news-room/fact-sheets/detail/cancer
12. Bray, F.; Ferlay, J.; Soerjomataram, I.; Siegel, R. L.; Torre, L. A.; Jemal, A. Global Cancer Statistics 2018: GLOBOCAN Estimates of Incidence and Mortality Worldwide for 36 Cancers in 185 Countries. *Ca-Cancer J. Clin.* **2018**, *68*, 394-424.
13. Safarinejad, M. R.; Shafiei, N.; and Safarinejad, S. Quality of life and sexual functioning in young women with early-stage breast cancer 1 year after lumpectomy, *Psycho-Oncology*, **2012**, *22, 6*, 1242-1248.
14. Chou, A. J.; Gorlick, R. Chemotherapy resistance in osteosarcoma: current challenges and future directions *Expert Rev. Anticancer Ther.* **2006**, 6, 1075–1085.
15. American Cancer Society; Chemotherapy Side Effects. https://www.cancer.org/treatment/treatments-and-side-effects/treatment-types/chemotherapy/chemotherapy-side-effects.html

16. Advantages and disadvantages of radiotherapy; Pancreatic Cancer UK. https://www.pancreaticcancer.org.uk/information-and-support/treatments-for-pancreatic-cancer/radiotherapy-for-pancreatic-cancer/
17. Bao, G.; Mitragotri, S.; Tong, S. Multifunctional nanoparticles for drug delivery and molecular imaging *Annu. Rev. Biomed. Eng.* **2013**, *15*, 253– 282.
18. Bigall, N. C.; Parak, W. J.; Dorfs, D. Fluorescent, Magnetic and Plasmonic—Hybrid Multifunctional Colloidal Nano Objects. *Nano Today* **2012**, *7*, 282-296.
19. Ghosh, S. K.; Pal, T. Interparticle Coupling Effect on the Surface Plasmon Resonance of Gold Nanoparticles: From Theory to Applications *Chem. Rev.* **2007**, *107*, 4797– 4862.
20. Huang, X. H.; El-Sayed, M. A. Plasmonic Photo-Thermal Therapy (PPTT) *Alex. J. Med.* **2011**, 47, 1– 9.
21. Abadeer, N. S.; Murphy, C. J. Recent Progress In Cancer Thermal Therapy Using Gold Nanoparticles *J. Phys. Chem. C* **2016**, *120*, 4691– 4716.
22. Dickerson, E. B.; Dreaden, E. C.; Huang, X. H.; El-Sayed, I. H.; Chu, H. H.; Pushpanketh, S.; McDonald, J. F.; El-Sayed, M. A. Gold Nanorod Assisted Near-Infrared Plasmonic Photothermal Therapy (PPTT) of Squamous *Cell Carcinoma in Mice Cancer Lett.* **2008**, *269*, 57– 66.
23. Huang, X. H., Jain, P. K., El-Sayed, I. H., and El-Sayed, M. A. Plasmonic photothermal therapy (PPTT) using gold nanoparticles *Lasers Med. Sci.* **2008** *23,* 217– 228.
24. Mackey, M. A.; Ali, M. R. K.; Austin, L. A.; Near, R. D.; El-Sayed, M. A. The Most Effective Gold Nanorod Size for Plasmonic Photothermal Therapy: Theory and *In Vitro* Experiments *J. Phys. Chem. B* **2014**, *118*, 1319– 1326.
25. Anker, J. N.; Hall, W. P.; Lyandres, O.; Shah, N. C; Zhao, J.; Van Duyne, R. P. Biosensing with Plasmonic Nanosensors *Nat. Mater.* **2008**, *7*, 442– 453.
26. Lasne, D.; Blab, G. A.; Berciaud, S.; Heine, M.; Groc, L.; Choquet, D.; Cognet, L.; Lounis, B. Single Nanoparticle Photothermal Tracking (SNaPT) of 5-nm Gold Beads in Live Cells *Biophys. J.* **2006**, *91*, 4598-4604.
27. Durr, N. J.; Larson, T.; Smith, D. K.; Korgel, B. A.; Ben-Yakar, A. Two-Photon Luminescence Imaging of Cancer Cells Using Molecularly Targeted Gold Nanorods *Nano Lett.* **2009**, 7, 941– 945.
28. Wang, H.; Huff, T. B.; Zweifel, D. A.; He, W.; Low, P. S.; Wei, A.; Cheng, J.-X. In vitro and in vivo two-photon luminescence imaging of single gold nanorods *Proc. Natl. Acad. Sci. U.S.A*. **2005,** *102*, 15752– 15756.
29. Kah, J. C.; Chen, J.; Zubieta, A.; Hamad-Schifferli, K. Exploiting the Protein Corona around Gold Nanorods for Loading and Triggered Release *ACS Nano* **2012**, *6*, 6730– 6740.
30. Jang, B.; Park, J.-Y.; Tung, C.-H.; Kim, I.-H.; Choi, Y. Gold Nanorod-Photosensitizer Complex for Near-Infrared Fluorescence Imaging and Photodynamic/Photothermal Therapy *In Vivo ACS Nano* **2011**, *5,* 1086– 1094.

31. Lucky, S. S.; Soo, K. C.; Zhang, Y. Nanoparticles in Photodynamic Therapy *Chem. Rev.* **2015**, *115*, 1990– 2042.
32. Bae, K. H.; Park, M.; Do, M. J.; Lee, N.; Ryu, J. H.; Kim, G. W.; Kim, C.; Park, T. G.; Hyeon, T. Chitosan Oligosaccharide-Stabilized Ferrimagnetic Iron Oxide Nanocubes for Magnetically Modulated Cancer Hyperthermia *ACS Nano* **2012**, *6*, 5266– 5273.
33. Hajba, L.; Guttman, A. The Use of Magnetic Nanoparticles in Cancer Theranostics: Toward Handheld Diagnostic Devices *Biotechnol. Adv.* **2016**, *34*, 354– 361.
34. Reddy, L. H.; Arias, J. L.; Nicolas, J.; Couvreur, P. Magnetic Nanoparticles: Design and Characterization, Toxicity and Biocompatibility, Pharmaceutical and Biomedical Applications *Chem. Rev*. **2012**, *112,* 5818-5878.
35. Barcena, C.; Sra, A. K.; Chaubey, G. S.; Khemtong, C.; Liu, J. P.; Gao, J. Zinc Ferrite Nanoparticles as MRI Contrast Agents *Chem. Commun.* (Cambridge, U.K.) **2008**, 2224– 2226.
36. Wang, Y. J. Superparamagnetic Iron Oxide Based MRI Contrast Agents: Current Status of Clinical Application *Quant. Imaging Med. Surg.* **2011**, *1*, 35– 40.
37. Lee, N.; Choi, Y.; Lee, Y.; Park, M.; Moon, W. K.; Choi, S. H.; Hyeon, T. Water-Dispersible Ferrimagnetic Iron Oxide Nanocubes with Extremely High R2 Relaxivity for Highly Sensitive *in Vivo* MRI of Tumors *Nano Lett.* **2012**, *12*, 3127– 3131.
38. Thiesen, B.; Jordan, A. Clinical Applications of Magnetic Nanoparticles for Hyperthermia *Int. J. Hyperthermia* **2008**, *24*, 467– 474.
39. Guardia, P.; Di Corato, R.; Lartigue, L.; Wilhelm, C.; Espinosa, A.; Garcia-Hernandez, M.; Gazeau, F.; Manna, L.; Pellegrino, T. Water-Soluble Iron Oxide Nanocubes with High Values of Specific Absorption Rate for Cancer Cell Hyperthermia Treatment *ACS Nano* **2012**, *6*, 3080– 3091.
40. Perigo, E. A.; Hemery, G.; Sandre, O.; Ortega, D.; Garaio, E.; Plazaola, F.; Teran, F. J. Fundamentals and Advances in Magnetic Hyperthermia *Appl. Phys. Rev.* **2015**, *2*, 041302-041306.
41. Hergt, R.; Dutz, S.; Roder, M. Effects of Size Distribution on Hysteresis Losses of Magnetic Nanoparticles for Hyperthermia *J. Phys.: Condens. Matter* **2008**, 20, 385214-385226.
42. Gao, X.; Cui, Y.; Levenson, R. M.; Chung, L. W. K.; Nie, S. In vivo cancer targeting and imaging with semiconductor quantum dots *Nat. Biotechnol*. **2004**, *22,* 969– 976.
43. Steichen, S. D.; Caldorera-Moore, M.; Peppas, N. A. A review of current nanoparticle and targeting moieties for the delivery of cancer therapeutics *Eur. J. Pharm. Sci.* **2013**, *48*, 416– 427.
44. Bazak, R.; Houri, M.; El Achy, S.; Kamel, S.; Refaat, T. Cancer Active Targeting by Nanoparticles: A Comprehensive Review of Literature *J. Cancer Res. Clin. Oncol.* **2015**, *141*, 769– 784.

45. Li, Z. W.; Yin, S. N.; Cheng, L.; Yang, K.; Li, Y. G.; Liu, Z. Magnetic Targeting Enhanced Theranostic Strategy Based on Multimodal Imaging for Selective Ablation of Cancer Adv. Funct. Mater. **2014**, *24*, 2312– 2321.
46. Veiseh, O.; Gunn, J. W.; Zhang, M. Design and Fabrication of Magnetic Nanoparticles for Targeted Drug Delivery and Imaging *Adv. Drug Delivery Rev.* **2010**, *62*, 284– 304.
47. Yang, L.; Zhao, Q.; Feng, W.; Li, F. Luminescent chemodosimeters for bioimaging *Chem. Rev.* **2013**, *113*, 192-270.
48. Wolfbeis, O. S. An Overview of Nanoparticles Commonly Used in Fluorescent Bioimaging *Chem. Soc. Rev*. **2015**, *44*, 4743-4768.
49. Wang, J.; Zhang, G.; Li, Q.; Jiang, H.; Liu, C.; Amatore, C.; Wang, X. In Vivo Self-Bio-Imaging of Tumors Through in Situ Biosynthesized Fluorescent Gold Nanoclusters *Sci. Rep.* **2013**, *3*, 1157-1163.
50. Chan, W. C. W.; Maxwell, D. J.; Gao, X. H.; Bailey, R. E.; Han, M. Y.; Nie, S. M. Luminescent Quantum Dots for Multiplexed Biological Detection and Imaging *Curr. Opin. Biotechnol.* **2002**, *13*, 40– 46.
51. Arora, D.; Jaglan, S. Nanocarriers based delivery of nutraceuticals for cancer prevention and treatment: A review of recent research developments. *Trends Food Sci. Technol.* **2016**, *54*, 114– 126.
52. Sun, T.; Zhang, Y. S.; Pang, B.; Hyun, D. C.; Yang, M.; Xia, Y. Engineered Nanoparticles for Drug Delivery in Cancer Therapy *Angew. Chem., Int. Ed.* **2014**, *53*, 12320– 12364.
53. Torchilin, V. P. Multifunctional nanocarriers *Adv. Drug Delivery Rev.* **2012**, *64,* 302– 315.
54. Lee, D.-E.; Koo, H.; Sun, I.-C.; Ryu, J. H.; Kim, K.; Kwon, I. C. Multifunctional Nanoparticles for Multimodal Imaging and Theragnosis *Chem. Soc. Rev.* **2012**, *41*, 2656– 267.
55. de Dios, S. A.; Díaz-Garcia, M. E. Multifunctional nanoparticles: Analytical prospects *Anal. Chim. Acta* **2010**, *666*, 1– 22.
56. Selvan, S. T., Tan, T. T., Yi, D. K., and Jana, N. R. Functional and multifunctional nanoparticles for bioimaging and biosensing *Langmuir,* **2010**, *26*, 11631–11641.
57. Hawkins, M. J.; Soon-Shiong, P.; Desai, N. Protein nanoparticles as drug carriers in clinical medicine *Adv. Drug Delivery Rev*. **2008**, *60*, 876– 885.
58. Anhorn, M. G.; Wagner, S.; Kreuter, J.; Langer, K.; von Briesen, H. Specific Targeting of HER2 Overexpressing Breast Cancer Cells with Doxorubicin-Loaded Trastuzumab-Modified Human Serum Albumin Nanoparticles *Bioconjugate Chem.* **2008**, *19*, 2321– 2331.
59. Krishna, A. D.; Mandraju, R. K.; Kishore, G.; Kondapi, A. K. An Efficient Targeted Drug Delivery through Apotransferrin Loaded Nanoparticles *PLoS One* **2009**, *4*, e7240-7253.
60. Liechty, W. B.; Kryscio, D. R.; Slaughter, B. V.; Peppas, N. A. Polymers for drug delivery systems Annu. Rev. Chem. Biomol. Eng. **2010**, *1*, 149– 173.

61. Lohcharoenkal, W.; Wang, L.; Chen, Y. C.; Rojanasakul, Y. Protein nanoparticles as drug delivery carriers for cancer therapy *BioMed Res. Int.* **2014**, *2014, 12-24.*
62. Kratz, F.; Elsadek, B. Clinical impact of serum proteins on drug delivery *J. Controlled Release* **2012**, *161,* 429– 445.
63. Mohanta, V.; Madras, G.; Patil, S. Layer-by-Layer Assembled Thin Film of Albumin Nanoparticles for Delivery of Doxorubicin *J. Phys. Chem. C* **2012**, *116*, 5333– 5341.
64. Kratz, F. Albumin as a drug carrier: design of prodrugs, drug conjugates and nanoparticles *J. Controlled Release* **2008**, 132, 171– 183.
65. Miele, E.; Spinelli, G. P.; Miele, E.; Tomao, F.; Tomao, S. Albumin-Bound Formulation of Paclitaxel (Abraxane® ABI-007) in the Treatment of Breast Cancer *Int. J. Nanomed*. **2009**, *4*, 99-105.
66. Haas, M., Kluppel, A. C., Wartna, E. S., Moolenaar, F., Meijer, D. K., de Jong, P. E., and de Zeeuw, D. Drug-targeting to the kidney: renal delivery and degradation of a naproxen-lysozyme conjugate *in vivo Kidney Int.* **1997**, *52*, 1693– 1699.
67. Khandelia, R.; Jaiswal, A.; Ghosh, S. S.; Chattopadhyay, A. Gold Nanoparticle–Protein Agglomerates as Versatile Nanocarriers for Drug Delivery *Small* **2013**, *9*, 3494– 3505.
68. Khandelia, R.; Jaiswal, A.; Ghosh, S. S.; Chattopadhyay, A. Polymer Coated Gold Nanoparticle–Protein Agglomerates as Nanocarriers for Hydrophobic Drug Delivery *J. Mater. Chem. B* **2014**, *2*, 6472– 6477.
69. Sanpui, P.; Paul, A.; Chattopadhyay, A., Theranostic Potential of Gold Nanoparticle-Protein Agglomerates. *Nanoscale* **2015**, *7*, 18411-18423.
70. Khandelia, R.; Bhandari, S.; Pan, U. N.; Ghosh, S. S.; Chattopadhyay, A., Gold Nanocluster Embedded Albumin Nanoparticles for Two-Photon Imaging of Cancer Cells Accompanying Drug Delivery. *Small* **2015**, *11*, 4075-4081.
71. Hang, D.; Neumann, O.; Wang, H.; Yuwono, V. M.; Barhoumi, A.; Perham, M.; Hartgerink, J. D.; Wittung-Stafshede, P.; Halas, N. J. Gold Nanoparticles Can Induce the Formation of Protein-Based Aggregates at Physiological pH *Nano Lett.* **2009**, *9*, 666– 671.
72. Nath, N.; Chilkoti, A. Interfacial Phase Transition of an Environmentally Responsive Elastin Biopolymer Adsorbed on Functionalized Gold Nanoparticles Studied by Colloidal Surface Plasmon Resonance. *J. Am. Chem. Soc.* **2001**, *123,* 8197–8202.
73. Deka, J.; Paul, A.; Chattopadhyay, A. Sensitive Protein Assay with Distinction of Conformations Based on Visible Absorption Changes of Citrate-Stabilized Gold Nanoparticles *J. Phys. Chem. C* **2009**, *113*, 6936– 6947.
74. Bhandari, S.; Roy, S.; Chattopadhyay, A. Enhanced Photoluminescence and Thermal Stability of Zinc Quinolate Following Complexation on the Surface of Quantum Dot *RSC Adv.* **2014**, *4*, 24217–24221.

75. Bhandari, S.; Khandelia, R.; Pan, U. N.; Chattopadhyay, A. Surface Complexation-Based Biocompatible Magnetofluorescent Nanoprobe for Targeted Cellular Imaging *ACS Appl. Mater. Interfaces* **2015**, *7*, 17552–17557.

76. Bhandari, S.; Roy, S.; Pramanik, S.; Chattopadhyay, A. Surface Complexation Reaction for Phase Transfer of Hydrophobic Quantum Dot from Nonpolar to Polar Medium *Langmuir* **2014**, *30*, 10760– 10765.

77. Bhandari, S.; Pramanik, S.; Khandelia, R.; Chattopadhyay, A. Gold Nanocluster and Quantum Dot Complex in Protein for Biofriendly White-Light-Emitting Material *ACS Appl. Mater. Interfaces* **2016**, *8*, 1600– 1605.
78. Roy, S.; Bhandari, S.; Chattopadhyay, A. Quantum Dot Surface Mediated Unprecedented Reaction of Zn^{2+} and Copper Quinolate Complex. *J. Phys. Chem. C* **2015**, *119*, 21191– 21197.
79. Roy, S.; Pramanik, S.; Bhandari, S.; Chattopadhyay, A. Surface Complexed ZnO Quantum Dot for White Light Emission with Controllable Chromaticity and Color Temperature. *Langmuir* **2017**, *33*, 14627– 14633.
80. Pramanik, S.; Bhandari, S.; Roy, S.; Chattopadhyay, A. Synchronous Tricolor Emission-Based White Light from Quantum Dot Complex *J. Phys. Chem. Lett.* **2015**, *6*, 1270– 1274.
81. Bhandari, S.; Roy, S.; Pramanik, S.; Chattopadhyay, A. Double Channel Emission from a Redox Active Single Component Quantum Dot Complex *Langmuir* **2015**, *31*, 551– 561.

CHAPTER 2

Protein-Based Multifunctional Nanocarriers for Imaging, Photothermal Therapy and Anti-Cancer Drug Delivery

In this chapter, a simple approach for the fabrication of a plasmonic and magneto-luminescent multifunctional nanocarriers (MFNCs) by assembling gold nanorods, iron oxide nanoparticles and gold nanoclusters within BSA nanoparticles is reported. The MFNCs showed self-tracking capability through single and two photon imaging, and the potential for *in vitro* magnetic targeting. Appreciable T_2-relaxivity exhibited by the MFNCs indicated favorable conditions for magnetic resonance imaging. In addition to successful plasmonic-photothermal therapy of cancer cells (HeLa) *in vitro*, the MFNCs demonstrated efficient loading and delivery of doxorubicin to HeLa cells leading to significant cell death. The present MFNCs with their multimodal imaging and therapeutic capabilities could be eminent candidates for cancer theranostics.

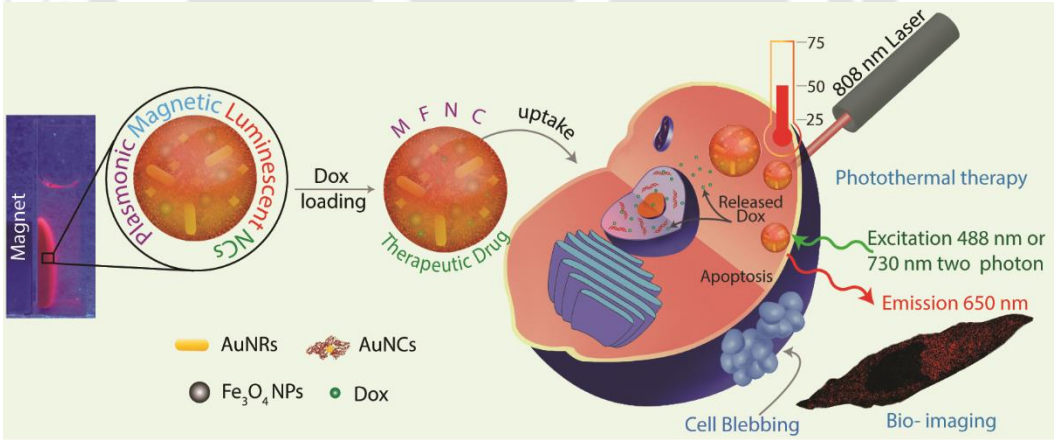

[ACS Appl. Mater. Interfaces 2017, 9, 19495−19501] - Reproduced with permission from the American Chemical Society.

2.1 Experimental section

***2.1.1 Materials*:** Iron(III) chloride hexahydrate ($FeCl_3.6H_2O$), gold (III) chloride solution ($HAuCl_4$), tetramethylammonium hydroxide (TMAOH), oleylamine, fluorescein isothiocyanate isomer I (FITC) and cetyltrimethylammonium bromide (CTAB) were purchased from Sigma Aldrich Co., USA. Sodium oleate, oleic acid, sodium hydroxide (NaOH), silver nitrate ($AgNO_3$), sodium borohydride and acetone were procured from Merck, India. Ascorbic acid and bovine serum albumin (BSA) were obtained from Sisco Research Laboratories Pvt. Ltd., India. Doxorubicin hydrochloride (Dox) and 3-(4,5-dimethylthiazol-2-yl)-2,5-diphenyltetrazolium bromide (MTT) were from Parenteral Drugs India Ltd. and Himedia, India, respectively. All chemicals were used without further purification. Milli-Q grade water (>18 MΩ cm, Millipore) was used in all the experiments.

***2.1.2 Preparation of gold nanorods (Au NRs)*:** Au NRs were prepared by following the method developed by Sau *et al.*[1] To prepare gold seed particles, 7.5 mL of CTAB (0.1 M) solution and 0.25 mL of aqueous $HAuCl_4$ (0.01 M) solution were mixed by gentle inversion in a 15 mL centrifuge tube. The solution appeared bright brown-yellow in color. Then 0.6 mL of freshly prepared ice cold $NaBH_4$ (0.01 M) solution was added to it all at once, followed by rapid mixing by inversion for 2 min. At this point, color of the solution changed to pale brown-yellow. The centrifuge tube was finally kept in a water bath maintained at 25 °C for 2 h and the sample was used immediately after that.

For the growth of Au NRs, 151.04 mL of CTAB (0.1 M) solution, 6.4 mL of $HAuCl_4$ (0.01 M) solution, and 1.28 mL of $AgNO_3$ (0.01 M) solution were added sequentially into a conical flask, followed by gentle mixing. The mixture appeared bright brown-yellow in color, but became colorless upon addition of 0.96 mL ascorbic acid (0.10 M). For growth of Au NRs, 0.64 mL of seed solution was added to this growth solution, gently mixed for 10 s and was kept in a water bath at 25 °C for 14 h. Au NRs were precipitated by centrifugation at 20000 rcf (20 min at 25 °C), washed thrice to remove excess CTAB and finally were redispersed in 1 mL of water.

***2.1.3 Preparation of iron oxide nanoparticles (Fe_3O_4 NPs)*:** Fe_3O_4 NPs were prepared, by using previously reported protocol,[2] in two steps: i) formation of iron (III) oleate complex and ii) thermal decomposition of iron (III) oleate complex to produce Fe_3O_4 NPs. To prepare iron (III) oleate complex, 3.24 g of $FeCl_3.6H_2O$ and 18.25 g of sodium oleate were added to the solvent mixture (18 mL hexane, 8 mL ethanol and 15 mL water) and refluxed at 70 °C under stirring for 4 h. After completion of reaction, brown crystals of iron (III) oleate complex were vigorously washed with ethanol-water mixture for 5 times to remove excess sodium oleate and were then dried for further use. To prepare Fe_3O_4 NPs, 300 mg of iron (III) oleate complex was added to a mixture of oleylamine and oleic acid (3:1) and heated at 120 ^oC under reflux condition for 1 h. At this point, the solution color changed to black. The temperature was then increased to 200 ^oC with simultaneous purging with nitrogen gas. Finally, the temperature of the reaction mixture was raised to 300 ^oC and kept for another 2 h under reflux and stirring to complete the formation of Fe_3O_4 NPs. The Fe_3O_4 NPs were precipitated by adding ethanol to the reaction mixture and washed with ethanol-hexane mixture to remove excess oleic acid and olelylamine.

For phase transfer of Fe_3O_4 NPs, excess ethanol was added to precipitate NPs followed by magnetic separation. Fe_3O_4 NPs were transferred to water using 25% aqueous solution of TMAOH as phase transferring agent under strong sonication. Finally, the phase transferred product was separated from excess TMAOH by magnetic separation (using rare-earth magnet) and subsequently washed four times with water, in the presence of the magnet. The washed Fe_3O_4 NPs were dispersed in 500 mL Milli-Q water for further use.

***2.1.4 Preparation of BSA-stabilized luminescent gold (Au) nanoclusters*:** BSA-stabilized luminescent Au nanoclusters were prepared by following previously reported method.[3] In brief, 5 mL aqueous solution of gold (III) chloride (10 mM) was mixed with 5 mL of aqueous BSA (50 mg mL^{-1}) solution by vigorous stirring for 2 min at 37 °C. Then pH of the reaction mixture was adjusted to 12.0 (by adding 1 M NaOH) and kept at 37 °C under vigorous stirring for 12 h. At the completion of the reaction, a deep brown solution with bright red luminescence

(under UV light, λ_{ex} = 365 nm) was obtained, indicating the formation of BSA-stabilized Au nanoclusters.

***2.1.5 Preparation of plasmonic magneto- luminescent multifunctional nanocarriers (MFNCs)*:** BSA nanocarriers incorporating magnetic, luminescent and plasmonic functionalities were prepared by conventional desolvation technique.[4-5] Briefly, 3.3 mL dispersion of as-synthesized Au nanoclusters was taken in a 100 mL round bottom flask. To this, 5 mL of Fe_3O_4 NPs suspension and 1.3 mL of Milli-Q water were added under vigorous stirring at 30 °C. Then, 0.4 mL of Au NR dispersion was added to the mixture dropwise and they were allowed to mix for 2 h. For desolvation, acetone was added drop by drop through a peristaltic pump at a flow rate of 1 mL min^{-1} until the mixture became turbid. Then the temperature of the mixture was raised to 50 °C and the same was stirred (750 rpm) at this temperature for 12 h to complete the formation of MFNCs. Acetone was removed using rotary evaporator to avoid aggregation of particles during centrifugation. To remove unreacted materials, MFNCs were washed three times following centrifugation at 20,000 rcf and 4 °C for 20 min. Finally, the pellet was redispersed in 4.2 mL of Milli-Q water and kept for further use.

***2.1.6 Photostability studies*:** Photostabilities of Au nanoclusters and MFNCs were studied in a Perkin Elmer LS55 fluorimeter at λ_{ex} of 365 nm and 505 nm. For this, aqueous dispersions of as-prepared Au nanoclusters, MFNCs and ethanolic solution of FITC were taken in cuvettes. Subsequently, fluorescence intensities of the samples were recorded at an interval of 0.1 sec under constant irradiation of light for a total time period of 1800 sec.

***2.1.7 Cell culture and cell viability assay*:** Human cervical cancer cell line, HeLa was procured from National Center for Cell Sciences (NCCS), Pune, India. The cells were cultured in Dulbecco's modified Eagle's medium (DMEM) supplemented with L-glutamine (4 mM), penicillin (50 U mL^{-1}), streptomycin (50 mg mL^{-1}) and 10% (v/v) fetal bovine serum and maintained at 37 °C in an incubator with 5% CO_2 and humidified environment. Following the desired treatment (as specifically

mentioned in appropriate section), the viability of HeLa cells was measured by (3-(4,5-dimethylthiazol-2-yl)-2,5-diphenyltetrazolium bromide) (MTT)-based cell viability assay.[5] The absorbance of the formazan product at 550 nm was measured in a Bio-Rad 680 microplate reader. The assay for each sample was carried out in triplicate. Cell viability was calculated by the formula:

% cell viability = (Absorbance of treated sample / Absorbance of control sample) × 100

***2.1.8 Confocal laser scanning microscopy (CLSM) and magnetic targeting*:** For CLSM, HeLa cells were grown onto coverslips by placing the coverslips inside a 6-well plate and seeding 2 ×10^5 cells per well. After growth for overnight, the HeLa cells were treated with 161.7 μg mL^{-1} MFNCs for 4 h. Then, the cells were washed with PBS, fixed in formaldehyde (4%) solution for 15 min, washed thoroughly with PBS and finally mounted on glass slides following standard protocols.[5] The slides were observed under Zeiss LSM 780 confocal microscope with conventional argon ion laser (excitation at 488 nm) as well as multi-photon Ti-sapphire laser (excitation at 730 nm).

To demonstrate the magnetic targeting of MFNCs *in vitro*, HeLa cells were grown onto two coverslips kept inside a culture dish (35 mm) as described above. Then, the cells were treated with MFNCs (161.7 μg mL^{-1}) for 2 h, with a rare-earth magnet placed under the culture dish just beneath one coverslip, while being away from the other one. Following the treatment, the cells were prepared as described above for visualization under Zeiss LSM 780 confocal microscope with argon laser (excitation at 488 nm).

***2.1.9 Plasmonic photothermal heating and plasmonic photothermal therapy (PPTT) in vitro*:** To check the heat generation by MFNCs under NIR irradiation, aqueous dispersions of varying concentrations of MFNCs (with extinction 0.35, 0.695 and 0.966), Au NRs (with extinction 0.665) and MFNCS without Au NRs, respectively, were taken in vials with small magnetic bars placed inside them for stirring. The vials were subjected to laser irradiation (High Power Focusable 2W 808 nm IR laser; MOD808-2W, Brand Name: dep, Laser type: Diode)

for 20 min with constant stirring for homogenous heat distribution. The temperatures of the dispersions were recorded using digital thermometer. For control experiment, only water (without any nanomaterials) was also subjected to irradiation. For *in vitro* PPTT, HeLa cells were seeded (1 ×10^4 cells/well) in a 96-well microtiter plate and grown overnight. Next day, the cells were treated with 161.7 μg mL^{-1} MFNCs or MFNCs without Au NRs for 6 h and then subjected to laser irradiation for 10 min (each well) with 2W 808 nm IR laser. A parallel set of experiment was also carried out under similar condition without laser irradiation. Then the cells were allowed to proliferate for another 24 h and the viability of HeLa cells was calculated by MTT assay as described earlier.

***2.1.10 Magnetic Resonance Imaging (MRI)*:** A 1.5 T MRI instrument (GE 1.5 T Signa Advantage, GE Healthcare) was used to record the R_2 map images of aqueous dispersions of MFNCs with varying iron concentrations (0 μM, 14.29 μM, 28.58 μM, 57.16 μM, 114.32 μM, 228.63 μM, and 457.27 μM). The measurement parameters were as follows: external MR field (H) = 1.5 T, number of acquisition (NEX) = 1, field of view (FOV) = 18 cm, phase FOV = 1 cm, matrix size = 256 × 192, slice thickness = 2 mm, spacing gap = 0 mm, pixel bandwidth = 88.33, flip angle = 90 °, time of repetition (TR) = 2000 ms, and the time of echo (TE) = 7.8 ms, 27.9 ms, 46.5 ms, 74.4 ms, 139.4 ms, 281.2 ms and 472.6 ms.

***2.1.11 Preparation of Dox-loaded multifunctional nanocarriers (Dox-MFNCs)*:** Dox was loaded into the MFNCs by adding 2 mL of Dox solution (exact concentration of Dox in the as-prepared solution being 16.39 μg mL^{-1}) to 1 mL dispersion of as-prepared MFNCs (1475 μg) and subsequently the final volume of the mixture was adjusted to 10 mL by adding water. Then, the mixture was stirred at 750 rpm for 2 h at 30 ˚C under dark condition. The Dox-MFNCs were separated by centrifugation (20,000 rcf, 4 ˚C, 20 min) and finally redispersed in water. The Dox-MFNCs were characterized by Hitachi U-2900 UV-vis spectrophotometer, FluoroMax-4 spectrofluorimeter, VSM, DLS and TEM in the same way as discussed above for MFNCs. The fluorescence intensity of Dox (λ_{ex} = 480 nm and λ_{em} = 590 nm) in the supernatant was measured and the corresponding Dox concentration

was estimated from the calibration curve. The calibration curve was prepared by making various dilutions of the drug in the supernatant obtained following the centrifugation of unloaded MFNCs (thus normalizing the interference from the media constituents and pH) and plotting the emission intensities as a function of drug concentrations.[5] The encapsulation efficiency for Dox was determined by using the formula:

$$Encapsulation\ efficiency\ (\%) = \{([Dox]_{ini} - [Dox]_{sup})/\ [Dox]_{ini}\} \times 100$$

where, $[Dox]_{ini}$ and $[Dox]_{sup}$ are the concentrations of Dox in the solution initially taken for the loading and in the supernatant after pelleting down the drug-loaded MFNCs, respectively.

***2.1.12 Stability of luminescence of Dox-loaded MFNCs in water and human blood serum*:** The freshly prepared Dox-loaded MFNCs were re-dispersed either in water or in human blood serum (obtained from a healthy donor following the standard guidelines of IIT Guwahati) and the emission spectra (λ_{ex} = 365 nm and 505 nm) of the dispersions were recorded immediately. The MFNCs dispersion in water and human blood serum were incubated at 4 ˚C and 37 ˚C, respectively, with the emission spectra being recorded at regular intervals.

***2.1.13 Dox-MFNCs treatment on HeLa cells*:** HeLa cells (1 ×10^4 cells/well) were seeded in a 96-well microtiter plate followed by overnight incubation. Subsequently, the media were replaced with fresh one and the cells were treated with varying concentrations of Dox-MFNCs (13.5 –161.7 μg mL^{-1}) or Dox (0.12 – 0.82 μg mL^{-1}) for 36 h. The viability (%) of HeLa cells, post Dox-MFNCs or Dox treatment, was calculated by MTT assay. For CLSM, HeLa cells were grown on cover slips as mentioned earlier and treated with 161.7 μg mL^{-1} of Dox-loaded MFNCs or 3.1 μg mL^{-1} of Dox for 4 h. Post treatment, the cells were prepared for confocal microscopy as described earlier for MFNCs-treated cells. Finally, the cells were observed under the confocal microscope (Zeiss LSM 780) with argon ion laser (excitation at 488 nm) as well as multi-photon laser (excitation at 730 nm).

***2.1.14 FESEM analyses of Dox-loaded MFNCs treated HeLa cells*:** HeLa cells, seeded (2×10^5) in 35 mm cell culture plate, were grown overnight. Next day, the medium was replaced with fresh medium supplemented with 161.7 μg mL^{-1} of Dox-loaded MFNCs (equivalent to 3.1 μg mL^{-1} of Dox). Following 4 h treatment with the Dox-loaded MFNCs, the cells were thoroughly washed with PBS, trypsinized, pelleted down by centrifugation and fixed in 2% glutaraldehyde solution. The fixed cells were washed in graded ethanol solutions followed by resuspension in absolute ethanol. The suspension of HeLa cells without treatment was also prepared. The cell suspensions, obtained from treated as well as non-treated HeLa cells, were deposited on aluminium foil-wrapped glass slides for observation under FESEM.

2.2 Results and Discussion

As synthesize gold nanorods (AuNRs) showed an average length of 34.7 ± 5.1 nm and aspect ratio of 3.3 ± 0.6 nm, iron oxide nanoparticles (IONPs) and BSA stabilized gold nanoclusters (AuNCs) showed an average size of 8.2 ± 2.2 nm and 1.6 ± 0.2 nm respectively calculated from their respective TEM images (Figure 2.1).

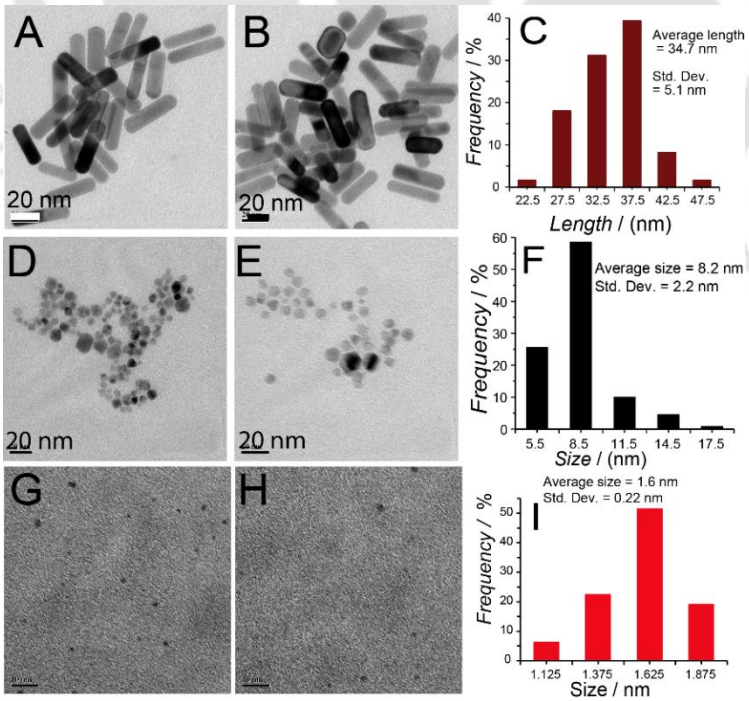

Figure 2.1. (A-B) Representative TEM images of as-prepared AuNRs (scale bar: 20

nm). (C) Length distribution of AuNRs (calculated based on 61 AuNRs using Image J software) showing an average length of 34.7 ±5.1 nm. (D-E) Representative TEM images of as-prepared IONPs (scale bar: 20 nm). (F) Size-distribution of IONPs (calculated based on 109 NPs using Image J software) showing an average size of 8.2 ± 2.2 nm. (G-H) Representative TEM images of as-prepared BSA-stabilized Au nanoclusters (scale bar: 10 nm). (I) Size-distribution of Au nanoclusters (calculated based on 31 Au nanoclusters using Image J software) showing an average cluster size of 1.6 ± 0.2 nm.

The formation of AuNRs and IONPs was further confirmed from their respective high resolution TEM (HRTEM) images, corresponding inverse fast Fourier transform (IFFT) patterns, Selected area electron diffraction pattern (SAED) and powder X-ray powder diffraction (XRD) (Figure 2.2)

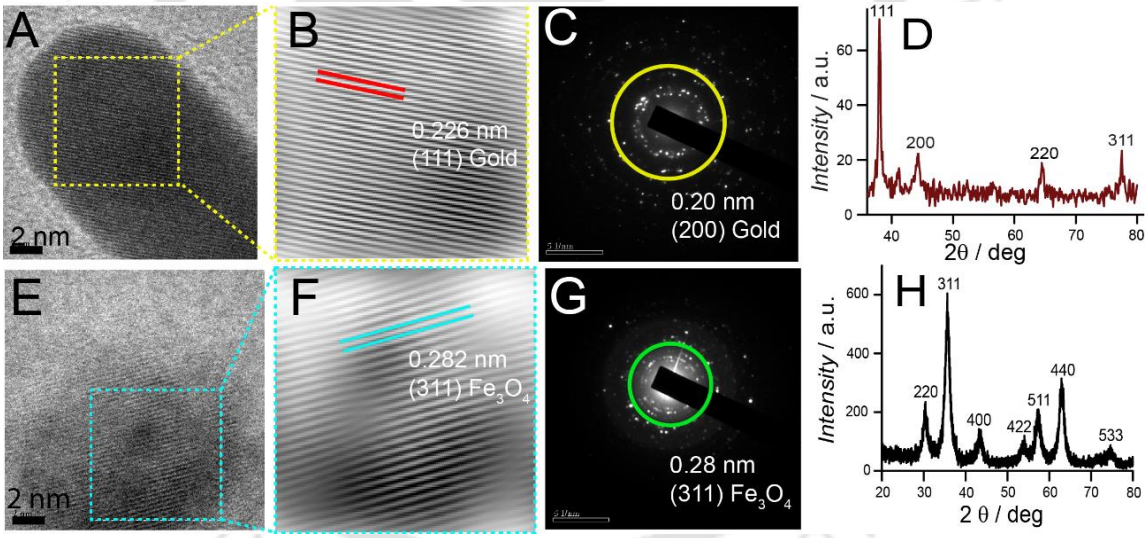

Figure 2.2. (A) HRTEM image of a AuNR (scale bar: 2 nm) showing lattice fringes with corresponding IFFT pattern (B) revealing d = 0.226 nm of the (111) planes. (C) Selected area electron diffraction pattern (SAED) of AuNRs. (D) Powder XRD pattern of AuNRs showing peaks at 2θ = 38^0, 44.4^0, 64.5^0, and 77.5^0 corresponding to (111), (200), (220) and (311) planes, respectively, of face-centered cubic close packing arrangement of the gold. (E) HRTEM image of a IONP that (scale bar: 2 nm) demonstrated lattice fringes with corresponding IFFT pattern (F) showing inter-planar distance of d =0.282 nm due to (311) planes of inverse spinel Fe_3O_4 NPs. (G) SAED pattern of IONPs. (H) Powder XRD pattern of IONPs showing characteristic peaks at 2θ = 30^0, 35.6^0, 43.8^0, 53.1^0, 57.4^0, 63^0 and 74.5^0 corresponding to (220), (311), (400), (422), (511), (440), (533) planes of inverse spinel Fe_3O_4 NPs.

As described in the experimental section multifunctional nanocarriers (MFNCs) were fabricated by adopting desolvation-based approach. Field emission scanning electron microscopic (FESEM) and transmission electron microscopic (TEM) images (Figure 2.3 A, B) demonstrated that the MFNCs were nearly spherical in shape with an average size of 120.5 ± 27.6 nm (from FESEM, Figure 2.3C). The average hydrodynamic diameter (d_H) of water-dispersed MFNCs was estimated to be 203.1 nm through DLS measurements (Figure 2.3 D). The apparent increase in d_H, as compared to the size observed in FESEM and TEM, could be due to the hydration layer formed at the nanocarrier surface in water.[6] Since the optimal size-range for effective tumor-accumulation through 'enhanced permeation and retention' (EPR) effect is reported to be 10-200 nm,[7] the present MFNCs (~120 nm in size and d_H ~203 nm) show the potential for 'passive targeting' *in vivo*.

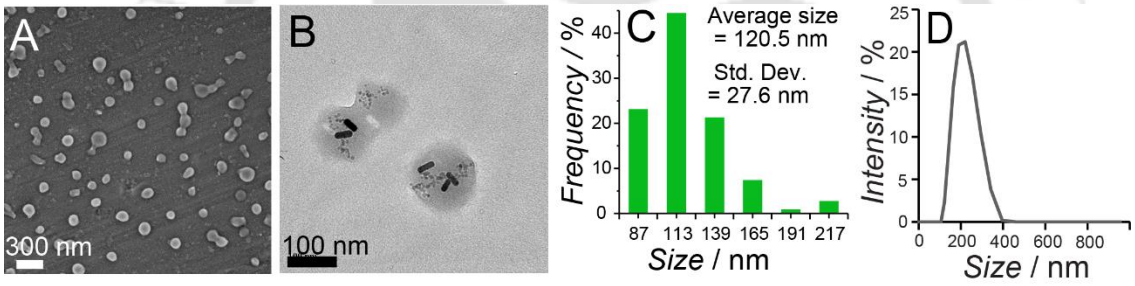

Figure 2.3. Representative (A) FESEM and (B) TEM images of MFNCs (scale bar: A - 300 nm, B - 100 nm). (C) Size-distribution of MFNCs, calculated based on 108 particles from FESEM image using Image J software, showing an average size of 120.5 ±27.6 nm. (D) Size-distribution of the MFNCs dispersed in water as measured by DLS.

As is evident in TEM images at higher magnifications (Figure 2.4 A-C), individual MFNCs comprised of – in addition to the easily identifiable Au NRs – IONPs and Au nanoclusters, which could be distinguished based on the significant difference in their respective sizes. Furthermore, high resolution TEM (HRTEM) images of MFNCs and corresponding inverse fast Fourier transform (IFFT) patterns (Figure 2.4 D-G) confirmed the presence of Au NRs and IONPs by revealing the characteristic lattice fringes due to (111) plane of face-centred cubic

(fcc) Au NRs and (311) plane of inverse spinel Fe_3O_4 NPs (IONPs), respectively.[8-10] It may be mentioned here that the distribution of AuNRs and IONPs among the MFNCs (Figure 2.4 B and A.2.1, Appendix) was not uniform. This could be due to the possible heterogenity of interaction of AuNRs and IONPs with BSA during the prepararion of MFNCs.

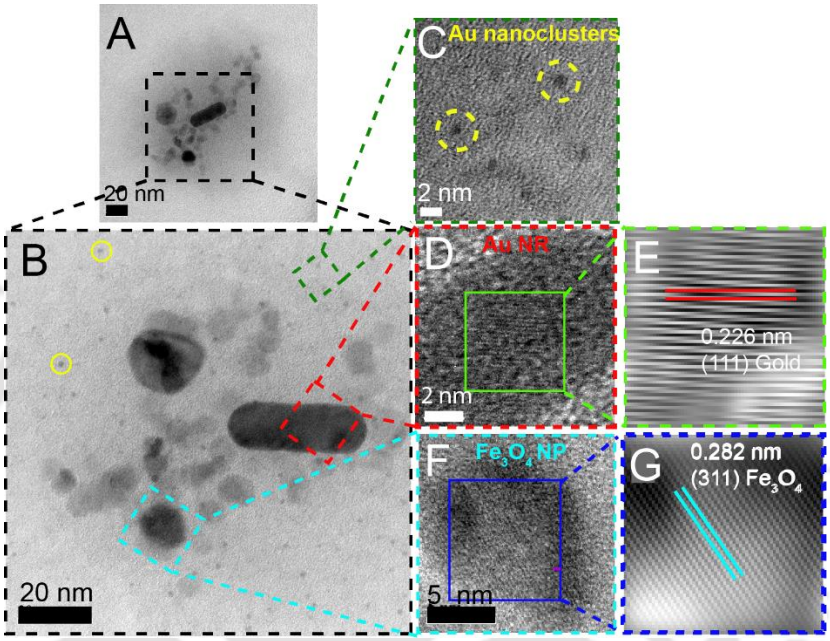

Figure 2.4. TEM image of a typical MFNC (A) and at higher magnification (B) showing component Au NR, IONPs and ultra-small Au nanoclusters (some of them marked with yellow circles for guidance) (scale bar: 20 nm). HRTEM images, focused at different regions of the same MFNC, demonstrating the presence of (C) individual Au nanoclusters (scale bar: 2 nm), (D) lattice fringes of Au NR (scale bar: 2 nm) with corresponding IFFT pattern (E) and (F) lattice fringes of IONPs (scale bar: 5 nm) with corresponding IFFT pattern (G).

The brown-colored colloidal dispersion of MFNCs exhibited bright red PL (Figure 2.5 A, Figure A.2.2, Appendix) when irradiated with UV light (λ_{ex} = 365 nm). Moreover, due to the presence of the IONPs, the MFNCs could easily be separated from the colloidal dispersion by an external magnet as shown in (Figure 2.5 A). The vibrating sample magnetometric (VSM) measurement revealed super-paramagnetism in the MFNCs with a saturation magnetization of 4.66 emu g^{-1} (at room temperature) (Figure 2.5 B). However, this value was lower than that

observed with free IONPs (27.88 emu g^{-1}, Figure 2.5 C). This could be a result of incorporating non-magnetic components namely Au nanoclusters, Au NRs and BSA within the MFNCs.

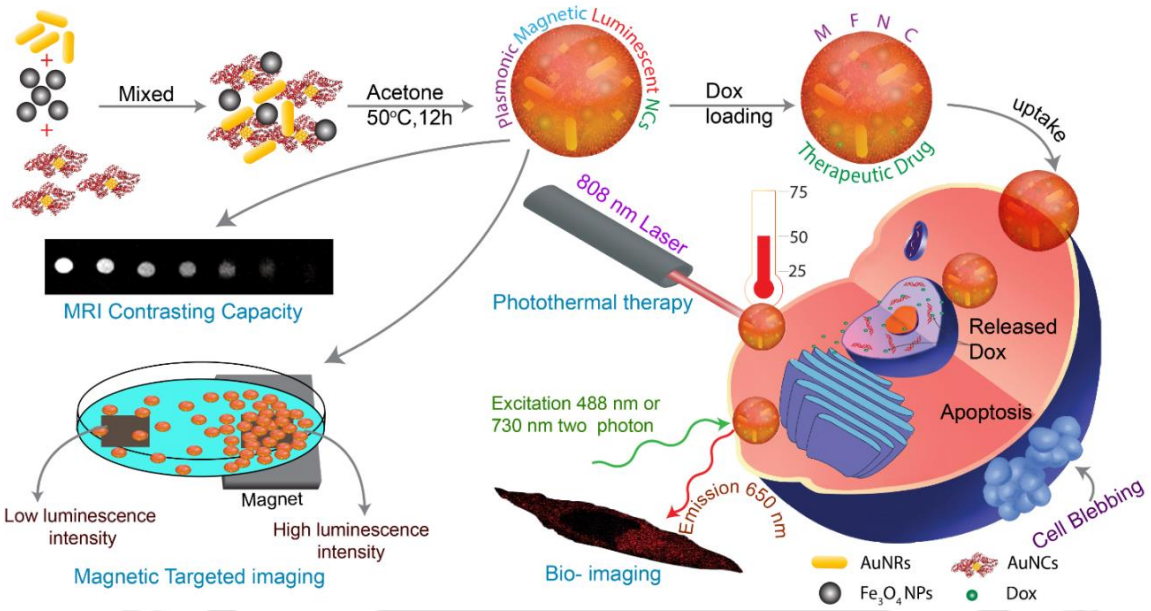

Scheme 2.1. Schematic depiction of preparing MFNCs, their capacity for *in Vitro* MRI contrasting and magnetic targeting, Two-Photon imaging, plasmonic photothermal therapy, and inducing cell death in cancer cells (HeLa), following successful loading and delivery of anticancer drug Dox.

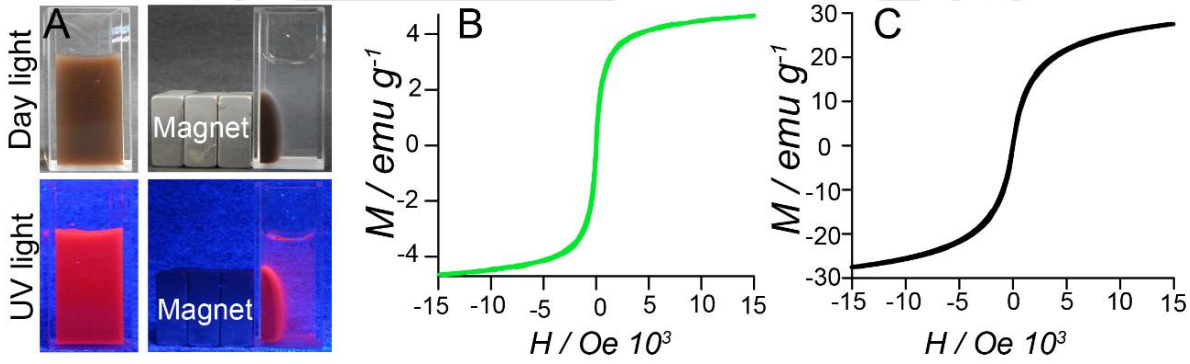

Figure 2.5. (A) Digital photographs of aqueous dispersion of MFNCs in daylight (upper panel) and UV light (lower panel) in absence (left panel) or presence (right panel) of external magnet. (B) Hysteresis loop (magnetic moment, M versus applied magnetic field, H) of MFNCs measured in VSM. (C) Hysteresis loop (magnetic moment, M versus applied magnetic field, H) of as-prepared Fe_3O_4 NPs measured in vibrating sample magnetometer.

The extinction spectrum of MFNCs (Figure 2.6 A) showed distinct band around 800 nm due to the characteristic longitudinal LSPR of the component Au NRs.[1] However, the extinction maximum of the Au NRs was observed to be red-shifted by 50 nm in MFNCs as compared to that of CTAB-stabilized free Au NRs (750 nm). The frequency-dependent extinction coefficients of metallic nanomaterials including Au NRs are highly sensitive to dielectric functions of the medium and the surface coating material(s) as well as the volume-fraction of the latter.[11, 12] Thus, the shift in extinction maximum of Au NRs could be due to change in local environment surrounding the Au NRs within MFNCs. Nonetheless, this was all the more advantageous as the red-shift of the Au NR-associated LSPR band allowed the MFNCs to better match the wavelength of the NIR laser (808 nm) employed for PPTT of cancer cells in the present study. The PL excitation spectrum of BSA-stabilized Au nanoclusters showed a weak shoulder around 365 nm and a broad band with maximum at 505 nm, which did not change significantly following the formation of MFNCs (Figure 2.6 B). However, when excited at 505 nm, the PL emission maximum of MFNCs (λ_{em} = 650 nm) was observed to be blue-shifted by ~13 nm from that of as-synthesized Au nanoclusters (λ_{em} = 663 nm) (Figure 2.6 C). Similar blue-shift was also noticed upon excitation at 365 nm (Figure A.2.3, Appendix). The shift in the emission maximum, as demonstrated in our previous study,[5] was due to the change in pH of the aqueous dispersion of MFNCs (pH 8.8) as compared to that of the Au nanoclusters (pH 12.0). Interestingly, the MFNCs were found to be much superior to FITC (commonly used organic dye for bioimaging) in terms of photostability and did not exhibit significant photobleaching or blinking (Figure 2.6 D, Figure A.2.4, Appendix) indicating their potential in bioimaging applications, especially as self-tracking delivery vehicles.

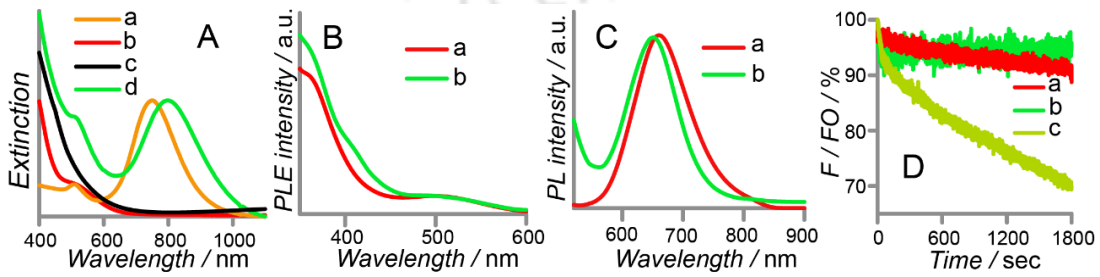

Figure 2.6. (A) Normalized extinction spectra of (a) Au NRs, (b) Au nanoclusters, (c) IONPs and (d) MFNCs. (B) Normalized excitation spectra of (a) BSA-stabilized Au

nanoclusters (λ_{em} = 663 nm) and (b) MFNCs (λ_{em} = 650 nm). (C) Normalized emission spectra of (a) BSA-stabilized Au nanoclusters and (b) MFNCs. (D) Photostability of (a) BSA-stabilized Au nanoclusters, (b) MFNCs and (c) FITC at excitation 505 nm.

To investigate the self-tracking capability of the MFNCs following their internalization by cancer cells *in-vitro*, MFNCs treated HeLa cells were prepared according to the method mentioned in experimental section and subsequently observed under confocal laser scanning microscope (CLSM) with both one-photon (argon ion laser, excitation at 488 nm) and two-photon (Ti-sapphire laser, excitation at 730 nm) excitation sources. The red PL of MFNCs was successfully observed inside HeLa cells, following their uptake, under one-photon (Figure 2.7 A, Figure A.2.5, Appendix) as well as two-photon excitation (Figure 2.7 B). The control (non-treated) HeLa cells did not exhibit any fluorescence under similar experimental conditions (Figure A.2.6, Appendix). The results demonstrated that our MFNCs could be probed intracellularly with either conventional one-photon or two-photon imaging. Most importantly, successful two-photon imaging of MFNCs within cancer cells – with excitation and emission falling within the biological window (650-900 nm) – is expected to expand their applicability for effective *in vivo* imaging. Moreover, the presence of IONPs within the MFNCs supports the possibility of their application as contrasting agent in MRI. The T_2-relaxivity of the MFNCs was calculated to be 448.04 mM^{-1} s^{-1} (Figure 2.8). The exceptional PL properties coupled with appreciable T_2-relaxivity of the MFNCs, indeed, demonstrated their potential in multimodal *in vivo* imaging.

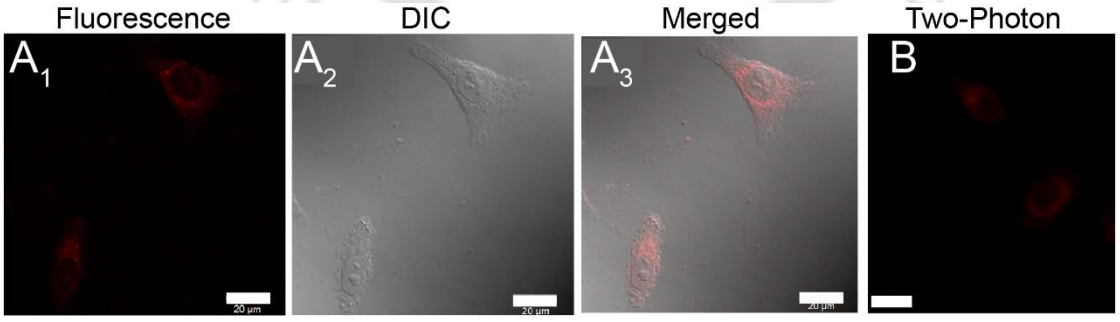

Figure 2.7. CLSM images of HeLa cells, following incubation with MFNCs for 4 h,under (A) one photon (488 nm laser; 1, 2 and 3 denote fluorescence, DIC and merged image, respectively) and (B) two photon (730 nm multi-photon laser) excitation (scale bar: 20 μm).

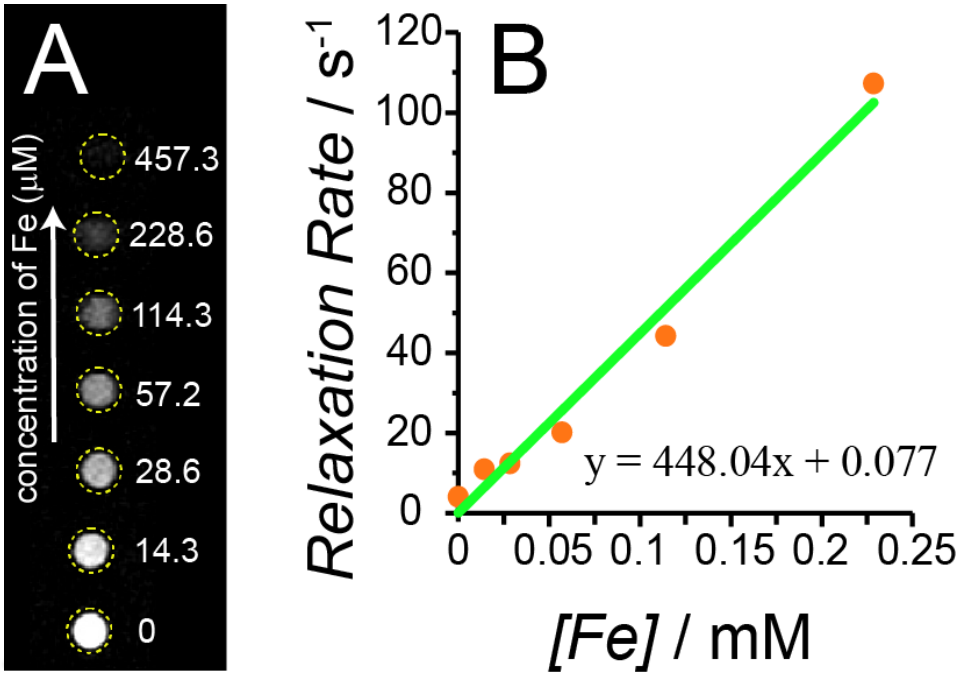

Figure 2.8. (A) T_2-weighted MR images of MFNCs at various dilutions with corresponding concentrations of Fe mentioned adjacent to them (TR = 2000 ms and TE = 7.8 ms). (B) T_2 relaxivity of MFNCs calculated from the plot of relaxation rate versus Fe concentration.

Magnetic targeting has drawn much attention in therapeutic applications as drug-loaded magnetic nanocarriers could be directed to the diseased area using external magnetic field with reduced side effects caused by non-specific drug release.[14-15] Possible magnetic targeting of the present MFNCs was explored *in vitro* by growing HeLa cells on two separate coverslips inside a cell culture dish and subsequently incubating them with MFNCs while keeping an external magnet just beneath one of the cover slips as shown in **Figure 2.9** After 2 h of incubation, when the coverslips were observed under CLSM, the cells on the cover slip just above the magnet were found to show more red PL due to the MFNCs as compared to the ones on the other cover slip (kept away from the magnet) (Figure 2.9). This revealed that the MFNCs were effectively attracted toward the external magnet resulting in higher uptake by HeLa cells near to the magnet.

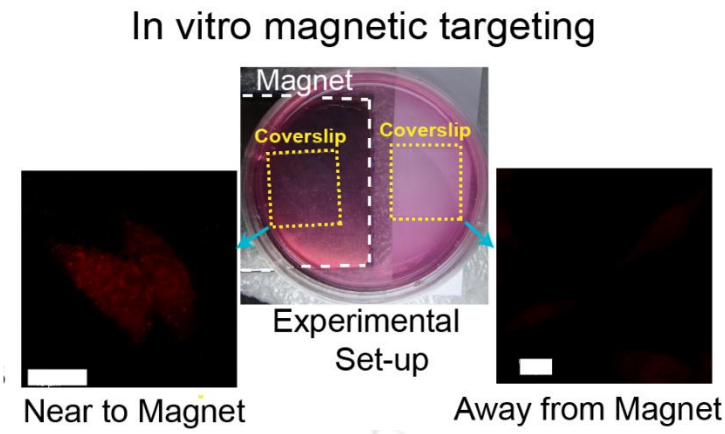

Figure 2.9. *In vitro* magnetic targeting of MFNCs: Experimental set-up (middle) and CLSM images of HeLa cells on cover slips kept near (left) and away (right) from the magnet, respectively.

As mentioned earlier, the MFNCs with extinction maxima at 800 nm are expected to exhibit PPTT of cancer cells. To pursue this, the MFNCs were first dispersed in water at room temperature and the dispersions having different concentrations (with extinction of 0.35, 0.695 and 0.966 at 808 nm) were irradiated with 808 nm NIR laser (Figure 2.10 A). The temperatures of all the three dispersions containing MFNCs were increased by ~20 ˚C within 10 min of irradiation, with only marginal increase in temperature later on. However, control experiment with MFNCs devoid of Au NRs (TEM image in Figure A.2.7, Appendix) resulted in an increment of ~3 ˚C only under similar conditions, indicating the importance of incorporated Au NRs (within MFNCs) in generating heat under NIR irradiation. Interestingly, when comparable amount of Au NRs was considered, the MFNCs (extinction 0.695) were found to be as efficient as free Au NRs (extinction 0.665) in generation of heat (with temperature increase of 19.7 ˚C and 20.8 ˚C; respectively, by 10 min). The PPTT-efficiency of the MFNCs *in vitro* was assessed by irradiating MFNCs-treated HeLa cells for 10 min and determining the cell viability at 24 h post-irradiation. As is evident in Figure 2.10 B, 55% or more HeLa cells were killed as a result of NIR irradiation in presence of MFNCs. Control experiments with HeLa cells in absence of MFNCs eliminated the possibility of cell death due to laser irradiation only. Moreover, similar experiment with MFNCs without Au NRs did not show any change in cell viability following NIR irradiation

signifying the importance of plasmonic nature of the MFNCs for PPTT as an additional therapeutic modality. The results of *in vitro* PPTT by the MFNCs are of particular interest from *in vivo* view-point as the 808 nm NIR-laser has been shown to provide deep-tissue penetration with minimum attenuation of light during PPTT in animal models thus improving the overall therapeutic efficacy.[16]

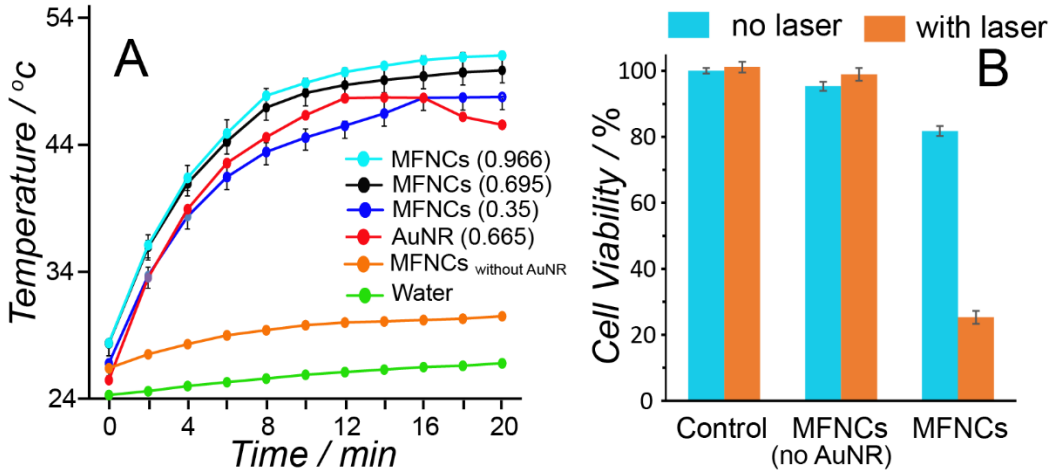

Figure 2.10. (A) Changes in temperatures of aqueous dispersions of MFNCs (with extinction of 0.966, 0.695 and 0.35 at 808 nm), free Au NRs (with extinction of 0.665 at 808 nm), MFNCs without Au NRs and water under NIR laser (808 nm) irradiation. (B) Viability of HeLa cells after treatment with MFNCs or MFNCs without Au NRs and subsequent NIR laser (808 nm) irradiation for 10 min. HeLa cells without any nanomaterial treatment were used as control. The MTT assay was performed at 24 h post-irradiation.

Finally, the ability of the MFNCs to deliver chemotherapeutic drugs and eventually kill cancer cells was demonstrated *in vitro* using Dox as the model anticancer drug. Dox was loaded into the MFNCs by incubating 147.5 μg mL^{-1} MFNCs with 3.28 μg mL^{-1} Dox under gentle stirring for 2 h (as described in the experimental section). The successful loading of Dox into the MFNCs was confirmed by fluorescence spectroscopy which revealed an additional peak at ~590 nm, characteristic of Dox fluorescence, in the emission spectrum of Dox-loaded MFNCs (Dox-MFNCs) (Figure 2.11 A). The drug-loading efficiency of the

MFNCs for Dox was estimated to be ~92%. The efficient loading of Dox by MFNCs, as reported previously,[5,17] could be due to the interaction of Dox with BSA through electrostatic interaction as well as hydrogen bonding. Zeta potential (ζ) of Dox-MFNCs (ζ = −20.8 ± 0.8 mV) at physiological pH was found to be increased when compared to unloaded MFNCs (ζ= −36.8 ± 0.7mV), possibly due to the incorporation of positively charged Dox molecules (pk_a 8.4). However, loading Dox into the MFNCs did not result in significant alteration of the morphological, magnetic, extinction and PL properties of the MFNCs (Figure 2.11, B-E). The d_H of the Dox-MFNCs, 206 nm as measured by DLS (Figure 2.11, F), was well suited for possible passive targeting as mentioned earlier. Release kinetics of Dox from the Dox-MFNCs *in vitro* was studied in PBS (pH 7.4) at 37 °C. The results (Figure 2.12 A) essentially showed linear increase in cumulative Dox release in first 5 h accompanied by slow release in later time points. Approximately 21% Dox was found to be released from the Dox-MFNCs within 24 h. The stability of the theranostic nanocarriers in the biological media is critical for their intended biomedical applications. The stability of the Dox-MFNCs was checked by following their emission spectra and it was observed that they were stable over a period of 24 h in human blood serum and 7 days in water (Figure 2.12 B-C). Moreover, TEM analysis (Figure 2.12 D) revealed that the overall morphology of the Dox-MFNCs did not change significantly after incubation in PBS (pH 7.4) for 7 days. The sizes of the constituent Au NRs and IONPs were found to be intact too.

Following their incubation for 4 h, the uptake of Dox-MFNCs by HeLa cells was followed under CLSM with single photon and two-photon (Figure 2.13 B) excitation. The MFNCs, as already demonstrated in Figure 2.7 tended to remain in the cytoplasm of HeLa cells following their internalization while free Dox was observed to accumulate in the nucleus of the HeLa cells (bright red PL in Figure 2.13 A). Careful observation of the two-photon CLSM images of HeLa cells treated with Dox-MFNCs (Figure 2.13 B and A.2.8, Appendix) and in comparison to those with MFNCs (Figure 2.7, A.2.5, Appendix) and free Dox (Figure 2.13 A) indicated successful internalization of Dox-MFNCs and subsequent release of Dox (exhibiting strong PL in the nucleus) inside HeLa cells.

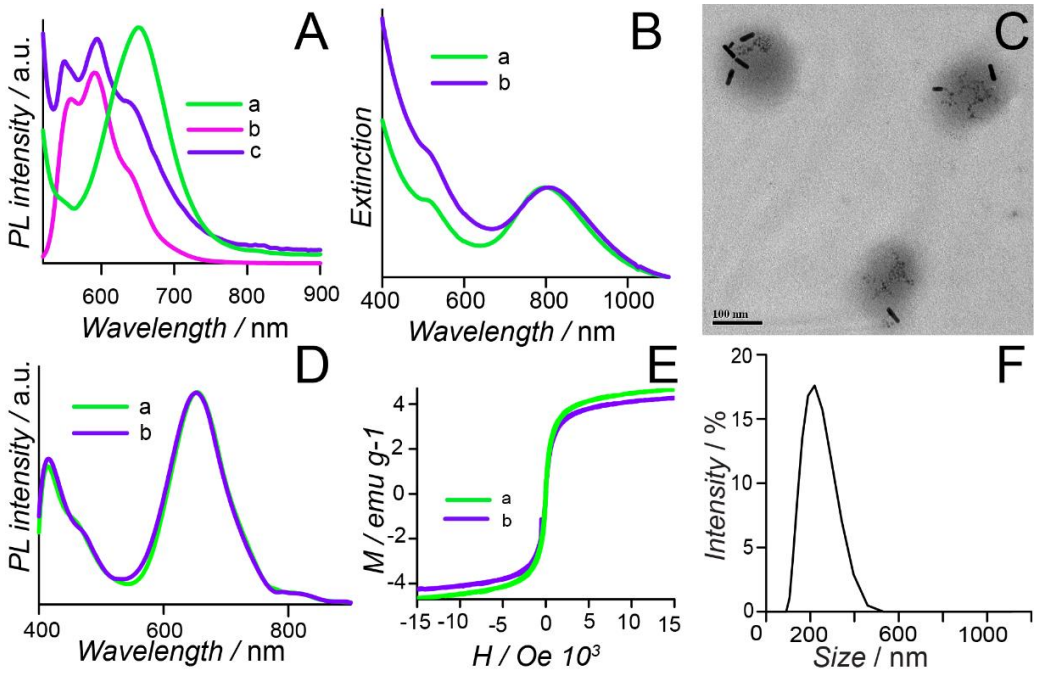

Figure 2.11. (A) Normalized emission spectra of (a) MFNCs, (b) Dox and (c) Dox-MFNCs at λ_{ex} of 505 nm. (B) Normalized extinction spectra of (a) MFNCs and (b) Dox-MFNCs. (C) TEM image of Dox-MFNCs (scale bar: 100 nm). (D) Normalized emission spectra (a) MFNCs and (b) Dox-MFNCs at λ_{ex} of 365 nm. (E) Hysteresis loops of (a) MFNCs and (b) Dox-MFNCs. (F) Size-distribution curve of Dox-MFNCs as measured in DLS.

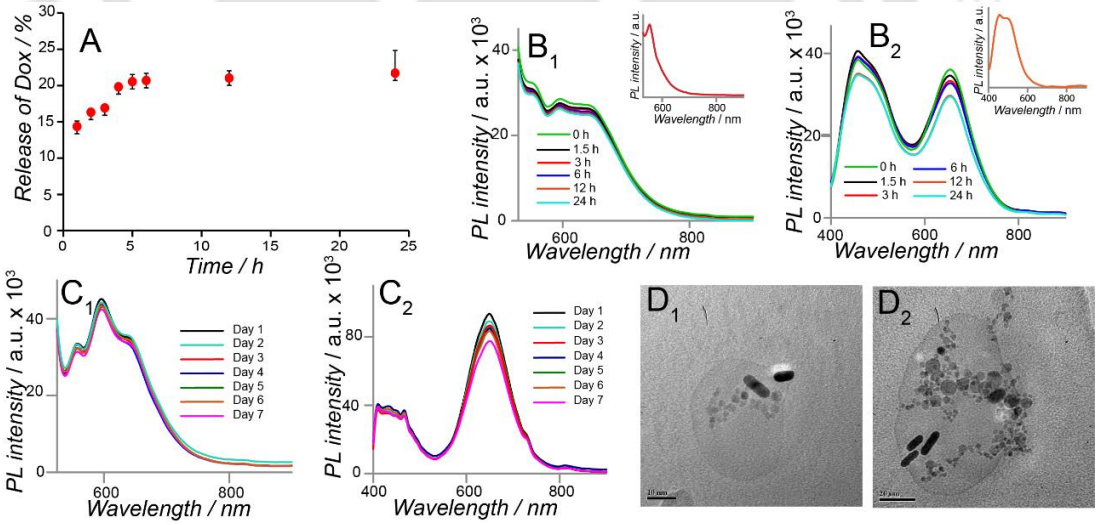

Figure 2.12. (A) Release kinetics of Dox from Dox-loaded MFNCs in PBS (pH 7.4). Stability of Dox-MFNCs in (B) human blood serum (HBS) and (C) water was studied by measuring their PL intensities in corresponding medium with time. Emission spectra of Dox-MFNCs in HBS at (B_1) λ_{ex} = 505 nm and (B_2) λ_{ex} = 365 nm at different time intervals; insets: emission spectra of only HBS at corresponding excitations. Emission spectra of Dox-MFNCs in water at (C_1) λ_{ex} = 505 nm and (C_2) λ_{ex} =365 nm at different time intervals. (D_1, D_2) TEM images of Dox-MFNCs after 7 days of incubation in PBS (pH 7.4) at 37 °C.

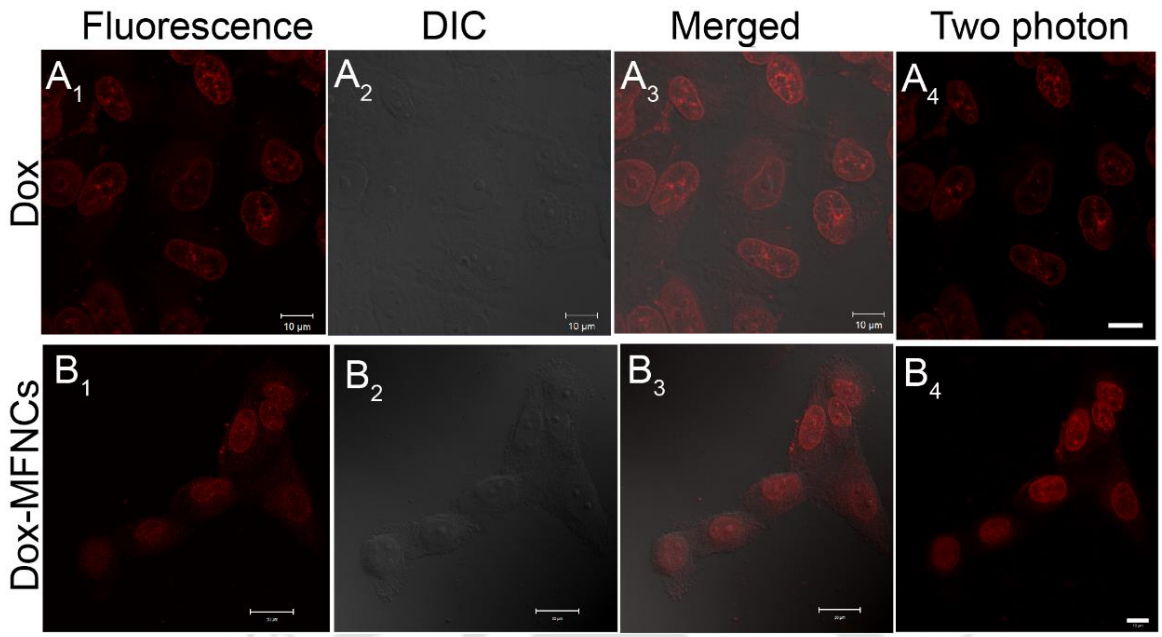

Figure 2.13. Confocal microscopic images of HeLa cells treated with (A) Dox and (B) Dox-MFNCs; Subscript 1, 2, 3 and 4 refer to fluorescence, DIC, merged and two photon images, respectively. Scale bars: 10 μm (A) and 20 μm (B).

As a result of successful delivery of Dox by MFNCs to HeLa cells, Dox-MFNCs were also found to efficiently kill the cancer cells in a dose-dependent manner (Figure 2.14 A). The IC_{50} value of the Dox-MFNCs for HeLa cells, as determined by the cell viability assay (Figure 2.14 A), was found to be 119 μg mL^{-1}, which corresponded to 2.3 μg mL^{-1} Dox. However, slow/incomplete release of Dox from MFNCs could lead to the apparent increase in IC_{50} values as compared to free Dox (IC_{50} = 0.5 μg mL^{-1}, Figure 2.14 B).[5, 13] Induction of 'apoptosis' or programmed cell death in HeLa cells, following the treatment with Dox-MFNCs, was monitored from the characteristic apoptotic bodies observed under FESEM as shown in Figure 2.15. Interestingly, the MFNCs themselves did not exhibit significant cytotoxicity against HeLa cells (less than 14% cell death even at as high concentration as 161.7 μg mL^{-1}, Figure 2.14 A) indicating their suitability in theranostic applications.

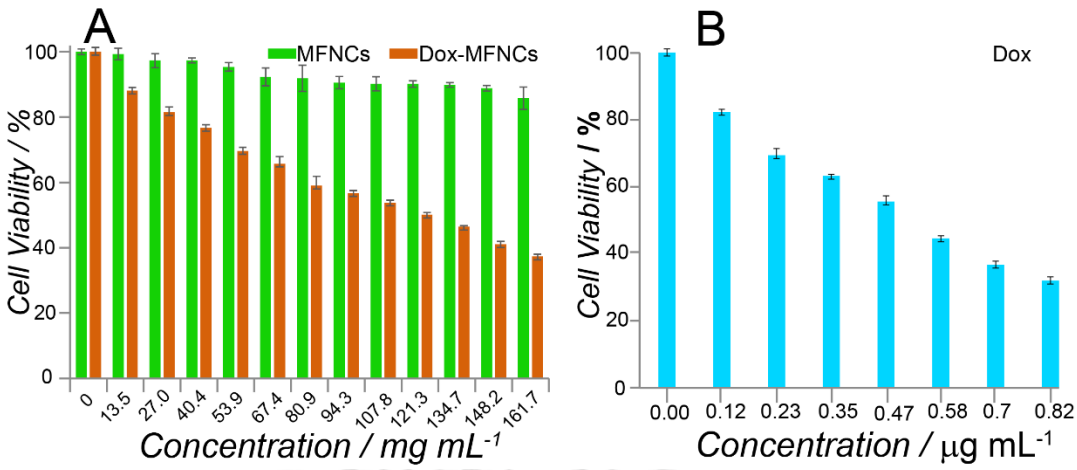

Figure 2.14. Viability of HeLa cells treated with varying concentrations of (A) MFNCs and Dox-MFNCs (B) Dox for 36 h.

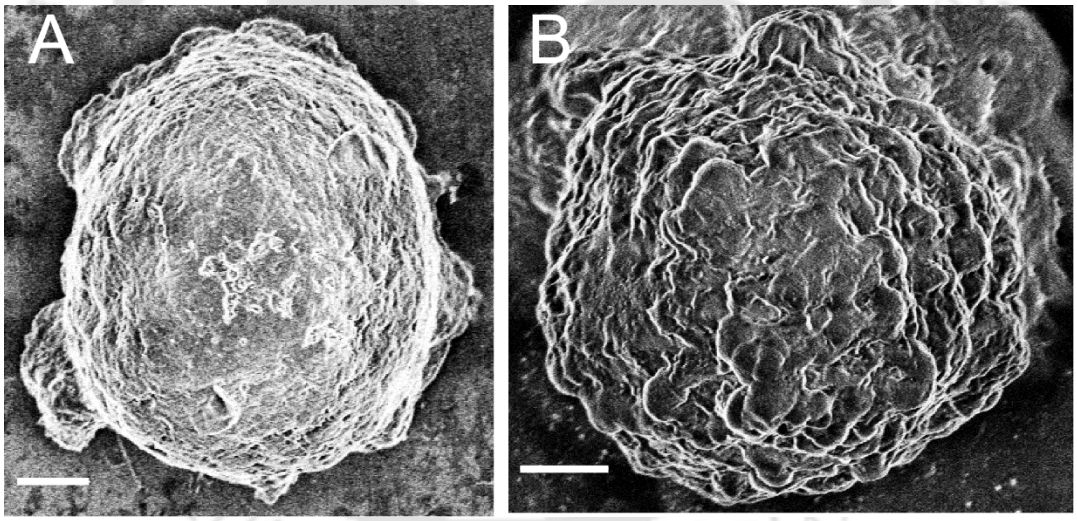

Figure 2.15. FESEM images of (A) non-treated and (B) Dox-MFNCs-treated HeLa cells (scale bar: 2 μm).

2.3. Conclusion

In summary, we have successfully developed BSA-based plasmonic magneto-luminescent nanocarriers (herein referred as MFNCs) by assembling Au NRs, IONPs and Au nanoclusters in protein, without affecting their individual

properties. The potential of the MFNCs as self-tracking luminescent probes in theranostic applications was validated *in vitro* by single as well as two photon fluorescence imaging. Moreover, the MFNCs showed considerable T_2-relaxivity and capability of being magnetically guided, appropriate for MRI application and targeted drug delivery, respectively. Significant extinction of the MFNCs in the NIR window, owing to the characteristic plasmonic nature of the nanocarriers, led to successful PPTT of HeLa cells *in vitro*. Following efficient loading of Dox, the MFNCs were observed to deliver the anticancer drugs to HeLa cells successfully leading to significant cell death while the PL of the nanocarriers helped in visualizing the delivery through fluorescence microscopy. With the proven serum stability, the present MFNCs could be ideal candidates for cancer theranostics wherein they are expected to, following their accumulation in tumor through size-dependent passive targeting and/or magnetic guidance, provide multimodal therapy and imaging of cancer cells simultaneously.

References:

1. Sau, T. K.; Murphy, C. J., Seeded high yield synthesis of short Au nanorods in aqueous solution. *Langmuir* **2004**, *20* (15), 6414-6420.
2. Bhandari, S.; Khandelia, R.; Pan, U. N.; Chattopadhyay, A., Surface Complexation-Based Biocompatible Magnetofluorescent Nanoprobe for Targeted Cellular Imaging. *ACS Appl. Mater. Interfaces* **2015**, *7* (32), 17552-17557.
3. Xie, J.; Zheng, Y.; Ying, J. Y., Protein-directed synthesis of highly fluorescent gold nanoclusters. *J. Am. Chem. Soc.* **2009**, *131* (3), 888-889.
4. Jun, J. Y.; Nguyen, H. H.; Chun, H. S.; Kang, B.-C.; Ko, S., Preparation of size-controlled bovine serum albumin (BSA) nanoparticles by a modified desolvation method. *Food Chemistry* **2011**, *127* (4), 1892-1898.
5. Khandelia, R.; Bhandari, S.; Pan, U. N.; Ghosh, S. S.; Chattopadhyay, A., Gold Nanocluster Embedded Albumin Nanoparticles for Two-Photon Imaging of Cancer Cells Accompanying Drug Delivery. *Small* **2015**, *11* (33), 4075-4081.
6. Chen, O.; Riedemann, L.; Etoc, F.; Herrmann, H.; Coppey, M.; Barch, M.; Farrar, C. T.; Zhao, J.; Bruns, O. T.; Wei, H.; Guo, P.; Cui, J.; Jensen, R.; Chen, Y.;

Harris, D. K.; Cordero, J. M.; Wang, Z.; Jasanoff, A.; Fukumura, D.; Reimer, R.; Dahan, M.; Jain, R. K.; Bawendi, M. G., Magneto-Fluorescent Core-Shell Supernanoparticles. *Nat. Commun.* **2014**, *5*, 5093.

7. Yokoyama, M., Drug Targeting with Nano-Sized Carrier Systems. *J. Artif. Organs* **2005**, *8* , 77-84.

8. Bhandari, S.; Khandelia, R.; Pan, U. N.; Chattopadhyay, A., Surface Complexation-Based Biocompatible Magnetofluorescent Nanoprobe for Targeted Cellular Imaging. *ACS Appl. Mater. Interfaces* **2015**, *7*, 17552-17557.

9. Xie, J.; Zheng, Y.; Ying, J. Y., Protein-Directed Synthesis of Highly Fluorescent Gold Nanoclusters. *J. Am. Chem. Soc.* **2009**, *131* , 888-889.

10. Johnson, C. J.; Dujardin, E.; Davis, S. A.; Murphy, C. J.; Mann, S., Growth and Form of Gold Nanorods Prepared by Seed-Mediated, Surfactant-Directed Synthesis. *J. Mater. Chem.* **2002**, *12* , 1765-1770.

11. Sanpui, P.; Paul, A.; Chattopadhyay, A., Theranostic Potential of Gold Nanoparticle-Protein Agglomerates. *Nanoscale* **2015**, *7* , 18411-18423.

12. Underwood, S.; Mulvaney, P., Effect of the Solution Refractive Index on the Color of Gold Colloids. *Langmuir* **1994**, *10* , 3427-3430.

13. Khandelia, R.; Jaiswal, A.; Ghosh, S. S.; Chattopadhyay, A., Polymer Coated Gold Nanoparticle–Protein Agglomerates as Nanocarriers for Hydrophobic Drug Delivery. *J. Mater. Chem. B* **2014**, *2* , 6472-6477.

14. Huang, J.; Li, Y.; Orza, A.; Lu, Q.; Guo, P.; Wang, L.; Yang, L.; Mao, H., Magnetic Nanoparticle Facilitated Drug Delivery for Cancer Therapy with Targeted and Image-Guided Approaches. *Adv. Funct. Mater.* **2016**, *26*, 3818–3836.

15. Rao, Y. f.; Chen, W.; Liang, X. g.; Huang, Y. z.; Miao, J.; Liu, L.; Lou, Y.; Zhang, X. g.; Wang, B.; Tang, R. k., Epirubicin-Loaded Superparamagnetic Iron-Oxide Nanoparticles for Transdermal Delivery: Cancer Therapy by Circumventing the Skin Barrier. *Small* **2015**, *11* , 239-247.

16. Choi, W. I.; Kim, J.-Y.; Kang, C.; Byeon, C. C.; Kim, Y. H.; Tae, G., Tumor Regression In Vivo by Photothermal Therapy Based on Gold-Nanorod-Loaded, Functional Nanocarriers. *ACS nano* **2011**, *5* , 1995-2003.

17. Agudelo, D.; Bourassa, P.; Bruneau, J.; Bérubé, G.; Asselin, É.; Tajmir-Riahi, H.-A., Probing the Binding Sites of Antibiotic Drugs Doxorubicin and N-(Trifluoroacetyl) Doxorubicin with Human and Bovine Serum Albumins. *PLoS One* **2012**, *7* , e43814.

CHAPTER 3

Protein-Nanoparticle Agglomerates as Plasmonic-Magneto-Luminescent Multifunctional Nanocarrier for Imaging and Combination Therapy

Fabrication of a plasmonic-magneto-luminescent multifunctional nanocarrier (PML-MF nanocarrier) by lysozyme-mediated agglomeration of gold-coated iron-oxide nanoparticles (IO@AuNPs) and subsequent coating of these agglomerates with BSA-stabilized gold nanoclusters (BSA-AuNCs) is reported in this chapter. Agglomeration-mediated red-shifting of the plasmonic absorbance peak of IO@AuNPs within PML-MFNCs towards NIR-biological window helped in plasmonic photothermal therapy (PPTT) by PML-MFNCs. PML-MFNCs demonstrated excellent *in vitro* bioimaging and magnetic targeting capabilities due to strong photoluminance and superparamagnetism of the constituent AuNCs and IO@AuNPs, respectively. PML-MF nanocarriers showed successful loading and delivery of doxorubicin to cancer cells with significant killing efficiency that could be synergistically improved by combining with PPTT.

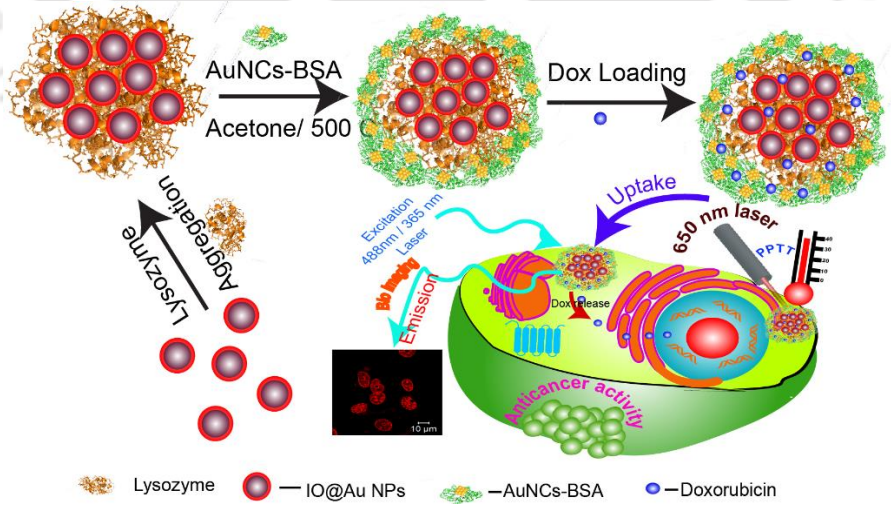

This research work is under revision for publication in the journal *ACS Appl. Bio Mater.

3.1 Experimental section

3.1.1 Materials: Gold (III) chloride solution, iron (III) chloride hexahydrate ($FeCl_3.6H_2O$), sodium oleate, oleylamine, tetramethylammonium hydroxide (TMAOH), hexane, dimethyl sulfoxide (DMSO), fluorescein isothiocyanate isomer I (FITC) were purchased from Sigma Aldrich Co., USA. Oleic acid, Lysozyme, sodium hydroxide (NaOH), acetone and bovine serum albumin were procured from Merck, India. Doxorubicin hydrochloride (Dox) was purchased from Parenteral Drugs India Ltd. and 3-(4,5-dimethylthiazol-2-yl)-2,5-diphenyltetrazolium bromide was obtained from Himedia, India.Ethanol was purchased from Tedia (USA). Chemicals were used with no additional purification. Milli-Q grade water (>18 MΩ cm, Millipore) was used as solvent for some of the experiments.

3.1.2 Synthesis of iron oxide nanoparticles (IONPs): IONPs were synthesized following thermal decomposition of iron oleate complexes. Iron oleate complex was synthesized by mixing 3.24 g of $FeCl_3.6H_2O$ and 18.25 g of sodium oleate in a solvent mixture of 30 mL hexane, 40 mL ethanol and 70 mL water and thereafter refluxing at 70 °C under stirring for 4 h. After 4 h of the reflux brown colored iron oleate complex was collected from upper hexane layer and washed with ethanol and water for many times and finally dried and stored at room temperature for further use.

To prepare IONPs, 300 mg of the iron oleate complex was added to 1:3 mixture of oleic acid oleylamine. The mixture was first stirred at room temperature for 30 min; then the temperature was increased to 120 °C and kept under stirring for 1 h at this temperature. The color of the solution was found to change to black at this point and the temperature was further increased to 200 °C and nitrogen gas was purged. Finally, the temperature was raised to 310 °C and kept under reflux at this temperature for 2 h more. After the completion of the reaction, the mixture was allowed to cool down and ethanol was added for precipitation of IONPs. Finally, IONPs were washed with ethanol and hexane mixture for several times to remove unreacted stabilizers and salt and then dissolved in 50 mL of hexane and store at room temperature for further use.[1]

3.1.3 Phase transfer of IONPs: Excess ethanol was added to hexane dispersion of IONPs for precipitation of the NPs and then NPs were separated using external magnet. 25% aqueous solution of tetramethylammonium hydroxide (TMAOH) was added and sonicated for 5h. Finally, IONPs were separated using external magnet and washed with water and redispersed in 500 mL of Milli-Q water and stored for further use.[1]

3.1.4 Synthesis of IO@Au NPs: IO@Au NPs were prepared following citrate mediated reduction of Au^{3+} in presence of IONP seeds.[2-6] Briefly, 10 mL of the water dispersion of IONPs was mixed with 90 mL of water; then 100 mg trisodium citrate dihydrate was added to it and sonicated for several hours. The mixture was then heated to boil. Once boiling started, 1 mL of 17.3 mM $HAuCl_4$ was added to it and the reflux was continued for another 1 h. After completion of the reaction, deep red colored IO@Au formed, which was characterized using TEM, XRD, UV-visible spectroscopy and VSM and was used for the preparation of PML-MF nanocarriers.

3.1.5 Preparation of lysozyme (Lyz) solution: 0.1 mg/mL solution of Lyz was prepared by dissolving solid Lyz in PBS buffer (pH 7.4).

3.1.6 Formation of Lyz mediated nanoscale agglomerates of IO@Au NPs (Lyz-IO@Au agglomerates): 600 µL of 0.1 mg/mL Lyz solution was added to 35 mL of the as synthesized aqueous dispersion of IO@Au NPs and then it was shaken gently for 30 s. The deep red colored IO@Au turned purple-blue, confirming agglomeration of IO@Au NPs. Lyz-IO@Au agglomerates were characterized using TEM and UV-visible spectroscopy.

3.1.7 Synthesis of luminescent AuNCs-BSA: BSA-stabilized luminescent Au NCs were synthesized following reported protocol.[7] Briefly, 5 mL of 10 mM aqueous solution of $HAuCl_4$ and 5 mL of 50 mg/mL aqueous solution of BSA were

first mixed well under vigorous stirring for 2 min at 37 °C. Then 1 M NaOH solution was added to adjust the pH of the reaction mixture at 12. Then the reaction mixture was stirred vigorously at 37 °C for 12 h. After 12 h, the reaction mixture turned deep brown and showed red luminescent emission under UV light of transilluminator, indicating the formation of AuNCs-BSA.

3.1.8 Preparation of PML-MF nanocarriers: PML-MF nanocarriers were prepared by coating Lyz-IO@Au agglomerates with AuNCs-BSA following acetone based desolvation technique.[7] Briefly, 30 mL of as prepared Lyz-IO@Au agglomerates was mixed with 5 mL of as synthesized AuNCs-BSA and pH of the resulting mixture was adjusted to 7.4. Then acetone was added dropwise to it until the mixture turned turbid and then the temperature was raised to 50 °C and kept under gentle stirring for 12 h. PML-MF nanocarriers were separated from the undesired organic solvent, chemicals and unreacted materials by first removing the acetone using rotary evaporator followed by centrifugation. Finally, the pellet was redispersed in water and stored at 4 °C.

3.1.9 Photostability study: Photostability of PML-MF nanocarriers and FITC was tested using aqueous dispersion of PML-MF nanocarriers and ethanolic solution of FITC. Sample was irradiated with light and emission intensity was recorded with time. For each sample, experiment was performed for up to 1800 s and PL emission intensity was recorded with an interval of 0.1 s.

3.1.10 Preparation of Dox loaded PML-MF nanocarriers (DPML-MF nanocarriers): In a 10 mL of total mixture (referred here as loading mixture), aqueous dispersion of PML-MF nanocarriers (containing 1.623 mg of PML-MF nanocarriers), and aqueous solution of Dox (containing 32.8 μg of Dox) were mixed. The mixture was then stirred for 2 h at room temperature. Finally, the mixture was centrifuged and the pellet washed several times followed by redispersion in water.

BSA and Lyz protein molecules possess both hydrophobic and hydrophilic amino acids and interact strongly with Dox. Presence of these proteins helped in Dox loading in PML-MFNCs. The encapsulation efficiency of Dox was calculated using PL emission of Dox (emission maximum at 591 nm) as probing tool. The emission intensity of Dox present in the supernatant after pelleting down the DPML-MF nanocarriers from the loading mixture was measured. To convert the emission intensity to concentration of Dox, a standard curve was constructed by dissolving different amount of Dox, taking the supernatant of PML-MF nanocarriers as solvent. The supernatant of PML-MF nanocarriers was taken as the solvent to remove the influence of different materials present in the supernatant on the PL emission of Dox. Finally, encapsulation efficiency of Dox was calculated by using the following formula,

$$\textit{Encapsulation efficiency (\%)} = \{(CDL - CDS) \,/\, CDL\} \times 100$$

Where CDL is concentration of Dox present in the loading mixture and CDS is concentration of Dox present in the supernatant after pelleting down the DPML-MF nanocarriers.

3.1.11 Cell viability assay: MTT (3-(4,5-dimethylthiazol-2-yl)-2,5-diphenyltetrazolium bromide based cell viability assay was performed to find out the cytotoxic effect of PML-MF nanocarriers and DPML-MF nanocarriers. HeLa, HepG2 and A375 cells were purchased from National Center for Cell Sciences, India. All the cells were grown in an incubator (5% CO2 and 37 °C) and in DMEM (Dulbecco's modified Eagle's medium) with 10% FBS (fetal bovine serum) and Penicillin- Streptomycin (100 U mL^{-1}). All the experiments were performed in 96-well cell culture plates taking 10,000 cells in each well. Cells were either treated with PML-MF nanocarriers or DPML-MF nanocarriers and/or irradiated with laser and MTT based variability assay was performed 30 h post treatment or 24 h post irradiation. Fromazane was dissolved in DMSO and absorbance at 570 nm was

recorded using Bio-Rad 680 microplate reader. Finally, absorbance was converted to cell viability using the following formula,

Cell Viability (%) = (Absorbance of formazane in the treated sample / Absorbance of formazane in control sample) × 100

3.1.12 Cell imaging: HeLa, HepG2 and A375 - all the cells were grown on coverslips placed in Petri dish. 3×10^5 numbers of cells were added on each Petri dish and grown overnight. Cells were then treated with PML-MF nanocarriers or DPML-MF nanocarriers for 2 h and then washed with PBS and fixed using formaldehyde and ethanol. Finally, cells were observed under Carl Zeiss laser scanning confocal microscope LSM 880 with 355 and 488 nm laser excitations.

3.1.13 Magnetic targeting: For this experiment we had taken a 60 mm petri dish and placed two coverslips at a distance. 3×10^5 HeLa cells were added to the petri dish and grown overnight. A powerful neodymium magnet was placed below one of the two coverslip. 150 µg/mL of PML-MF nanocarriers was added to it and incubated for 2 h and then cells present on both the coverslips were fixed with formaldehyde and ethanol and observed under observed under Carl Zeiss laser scanning confocal microscope LSM 880 with 355 and 488 nm laser excitations.

3.1.14 Plasmonic photothermal heating and therapy: Aqueous dispersion PML-MF nanocarriers and IO@Au NPs were taken in vials and kept under stirring and then irradiated with 0.5 W 650 nm laser and temperature of the dispersion was measured with a time interval. For in vitro plasmonic photothermal therapy, 10,000 HeLa cells were grown on each well of a 96-well plate. Different concentration of PML-MF nanocarriers, DPML-MF nanocarriers and IO@Au NPs were added to each well; treated the cells for 6 h and then irradiated with 0.5 W 650 nm laser for 10 min. MTT based cell viability assay was carried out 24 h post irradiation. A control experiment was carried out where cells were irradiated with laser only to check the effect of laser irradiation on cells. All the experiments were repeated in triplicate.

3.2 Results and Discussion

As described in the experimental section, in order to construct PML-MF nanocarrier, first oleic acid stabilized iron oxide nanoparticles (IONPs) were prepared by thermal decomposition of iron-oleate complexes and then phase-transferred to water using tetramethylammonium hydroxide (TMAOH).[1] The average size of the IONPs produced were calculated to be 6.7 ± 1.2 nm from TEM images (Figure 3.1 A-C). Selected area diffraction pattern (SAED) and inverse fast Fourier transform (IFFT) of high resolution TEM (HRTEM) image of IONPs showed the presence of characteristic 311 plane of iron oxides. (Figure 3.1 D-F).[1-4] Moreover, powder XRD pattern of IONPs showed characteristic peaks (2θ) at 30.4°, 35.6°, 43.4°, 53.8°, 57.3°, 63.1°, 74.5° from (220), (311), (400), (422), (511), (440) and (533) planes (Figure 3.1 G) of cubic inverse spinal iron oxides.[1-4] As-prepared IONPs were found to be superparamagnetic (with saturation magnetization 27.6 emu g^{-1}, Figure 3.1 H). Digital images (Figure 3.1 I) showed IONPs could easily be separate from their dispersion using external magnet.

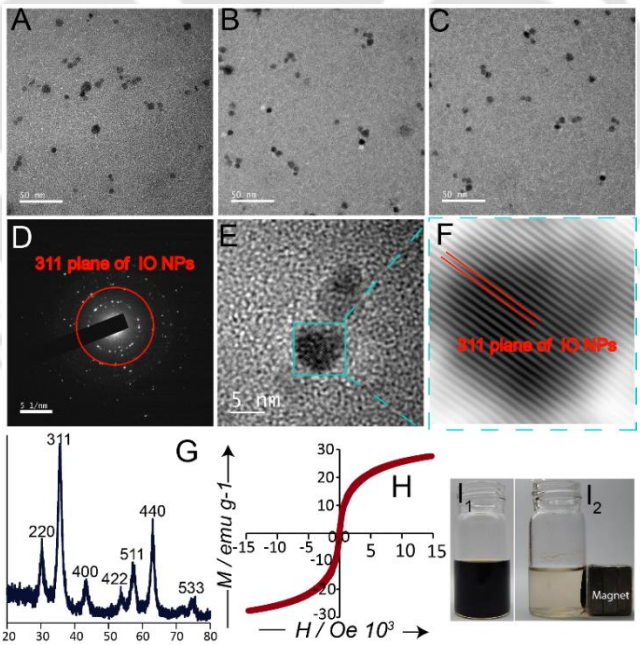

Figure 3.1. (A-C) TEM images of IONPs. (D) SAED of IONPs. (E) HRTEM and (F) corresponding IFFT pattern of IONPs. (G) Powder XRD of IONPs. (H) Hysteresis loop of IONPs studied under VSM. (I) Digital images of IONPs where suffixes 1 and 2 represent photograph taken in absence and presence of magnet.

As escribed in the experimental section IO@Au NPs (comprising of Au shell around IONP core) were prepared in aqueous medium by reducing Au^{3+} onto IONPs using boiling citrate e method.[2-6] Following the reduction of Au^{3+}, the color of the black IONP dispersion turned red, indicating the formation of gold shell (Figure A.3.1, Appendix). The formation of Au shell around IONPs resulted in a distinct surface plasmon resonance (SPR) peak at 521 nm as observed in the extinction spectrum of IO@Au NPs, which was otherwise absent in IONPs (Figure 3.2 A).[2-6] The average size of IO@Au NP was estimated, (form TEM images) to be 9.3 ± 2.6 nm, which was larger than that of IONPs, thus, indicating 2.6 nm thick Au shell formed around the IO core (Figure 3.2 B). Analyses of SAED and IFFT (from HRTEM image) patterns revealed the presence of both Au (111) and IO (311) planes in a single IO@Au NP (Figure 3.2 C-E). Elemental mapping also showed presence of both Fe and Au in the same particle (Figure 3.2 F).

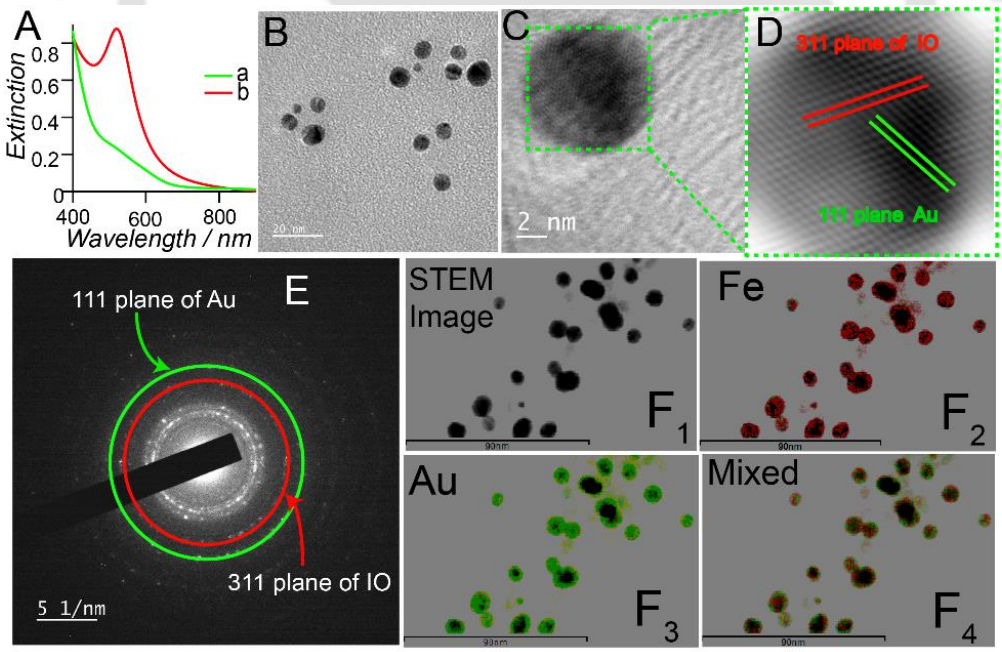

Figure 3.2. (A) Extinction spectra of (a) IONPs, (b) IO@Au NPs (B) TEM images of IO@AuNPs. (C) HRTEM and (D) corresponding IFFT pattern of IO@AuNPs showing both Au and IO planes. (E) SAED pattern of IO@AuNPs showing presence of both the planes of Au and IO. (F) Elemental mapping of IO@Au NPs showing the presence of both Au (green) and Fe (red), (F_1) scanning transmission electron microscopic image (STEM) of IO@Au NPs, (F_2) showing the mapping of Fe, (F_3) showing the mapping of Au, (F_4) merged image of F_1, F_2 and F_3.

The powder XRD pattern of IO@Au demonstrated the peaks (2θ) at 30.4°, 35.5°, 44.4°, 53.8°, 56.6°, and 75.4°, characteristic of (220), (311), (400), (422), (511), (533) planes of iron oxide and (2θ) at 38.42°, 45.5°, 64.8, 77.7 corresponding to (111), (200), (220) and (311) planes of Au[2-6] (Figure 3.3 A). Vibrating sample magneto-metric (VSM) analyses showed that IO@Au were superparamagnetic with a saturation magnetization of 12.5 emu g^{-1} (Figure 3.3 B). Digital image (Figure 3.3 C) also showed the magnetic nature and easy separation of IO@Au NPs from aqueous dispersion. Taken together, the experimental data mentioned above confirmed the formation of IO@Au NPs.

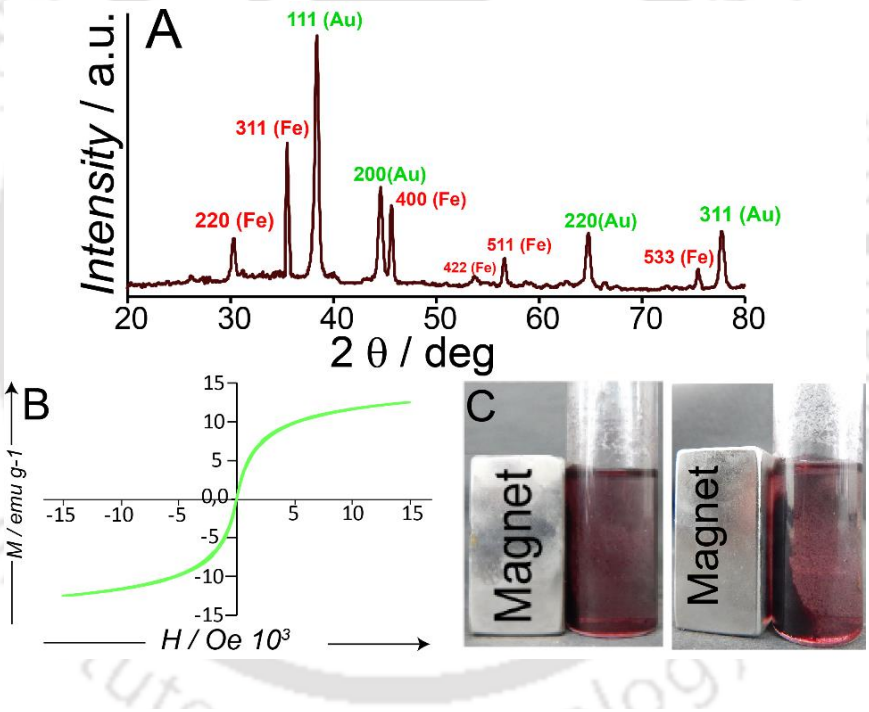

Figure 3.3. (A) Powder XRD pattern of IO@AuNPs showing presence of both the peaks of Au and IO. (B) Hysteresis loop measured in VSM showing superparamagnetic nature of IO @Au NPs. (C) Magnetic separation of IO@AuNPs under external magnetic field (both the photographs are of same sample placed in different position).

As described in the experimental section Lysozyme (Lyz) mediated formation of stable nanoscale agglomerates was carried out by adding Lyz solution to the aqueous dispersion of IO@Au NPs followed by gentle mixing.[8-10]

Color of the dispersion immediately turned purple-blue, indicating the completion of the agglomeration (Figure A.3.1, Appendix).[8-10] Absorption spectroscopy showed that addition of Lyz to the aqueous dispersion of IO@Au NPs caused the broadening and red-shifting of the SPR peak (λ_{am} at 600 nm) of IO@Au NPs due to Lyz-mediated agglomeration (Figure 3.4 A and G).[8-10] TEM images, HRTEM and corresponding IFFT pattern, SAED and elemental mapping confirmed the formation of agglomerates of the IO@Au NPs (Lyz-IO@Au agglomerates) (Figure 3.4).[2-4, 8-10]

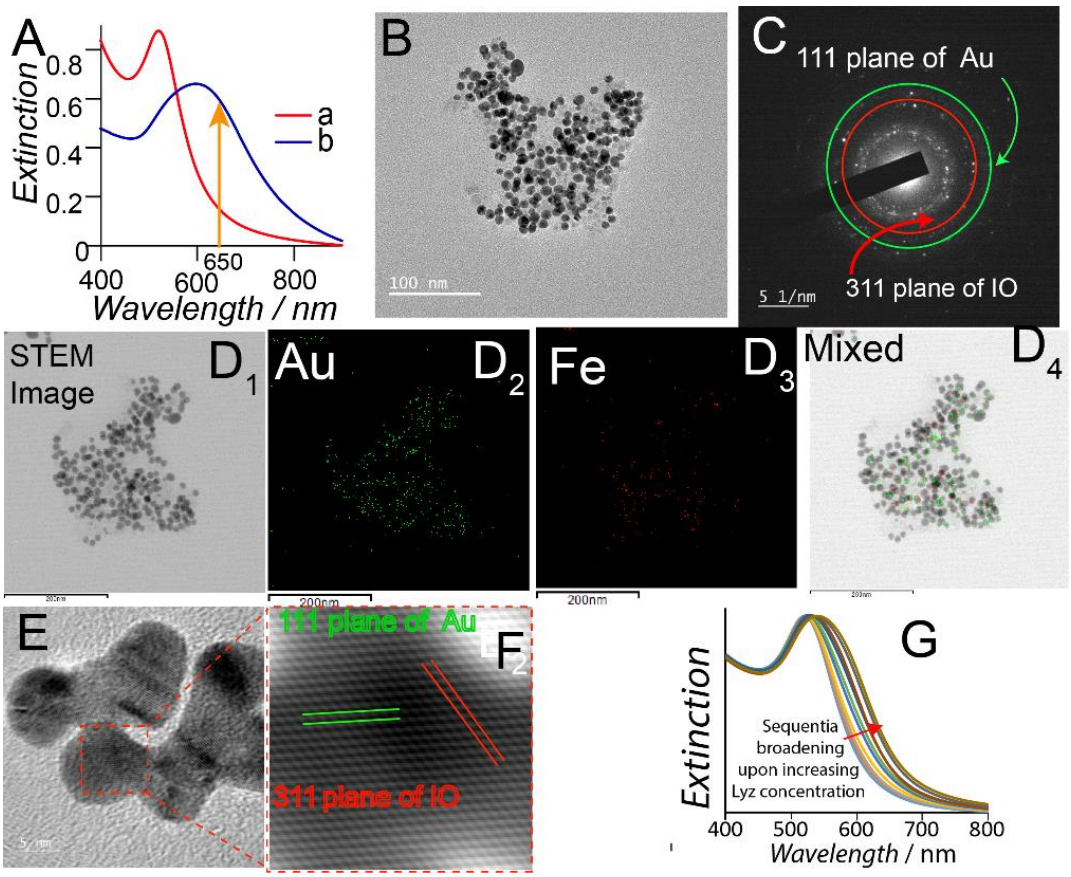

Figure 3.4. (A) Extinction spectra of (a) IO@Au NPs (b) Lyz-IO@Au agglomerates. (B) TEM images Lyz-IO@Au agglomerates. (C) SAED pattern of Lyz-IO@Au agglomerates showing presence of both the planes of Au and IO. (D) Elemental mapping of Lyz-IO@Au agglomerates showing the presence of both Au (green) and Fe (red); (D_1) scanning transmission electron microscopic image (STEM) of Lyz-IO@Au agglomerates, (D_2) showing the mapping of Au, (D_3) showing the mapping of Fe, (D_4) merged image of D_1, D_2 and D_3. (E) HRTEM of Lyz-IO@Au agglomerates and (F) corresponding IFFT pattern, also showing the presence of both the planes of Au and IO. (G) Normalized UV-vis spectra of IO@Au NPs with increasing concentration of lysozyme showing sequential broadening and red shifting of SPR absorbance spectrum of IO@Au.

TEM images, digital images , emission and excitation spectra (Figure 3.5) confirmed the formation of AuNCs-BSA. The emission spectra of AuNCs-BSA (at 505 nm as well as 365 nm excitation) showed strong emission peak at 666 nm due to the core nanoclusters (Figure 3.5 D-E). In the emission spectrum of AuNCs-BSA (at 365 nm excitation) an additional emission peak appeared at ~ 450 nm (Figure 3.5 E), due to BSA as reported earlier.[7] However, control experiment with aqueous BSA solution demonstrated strong emission maximum at 345 nm (Figure A.3.2) confirming that the emission around 666 nm in AuNCs-BSA originated from core AuNCs but not from BSA.

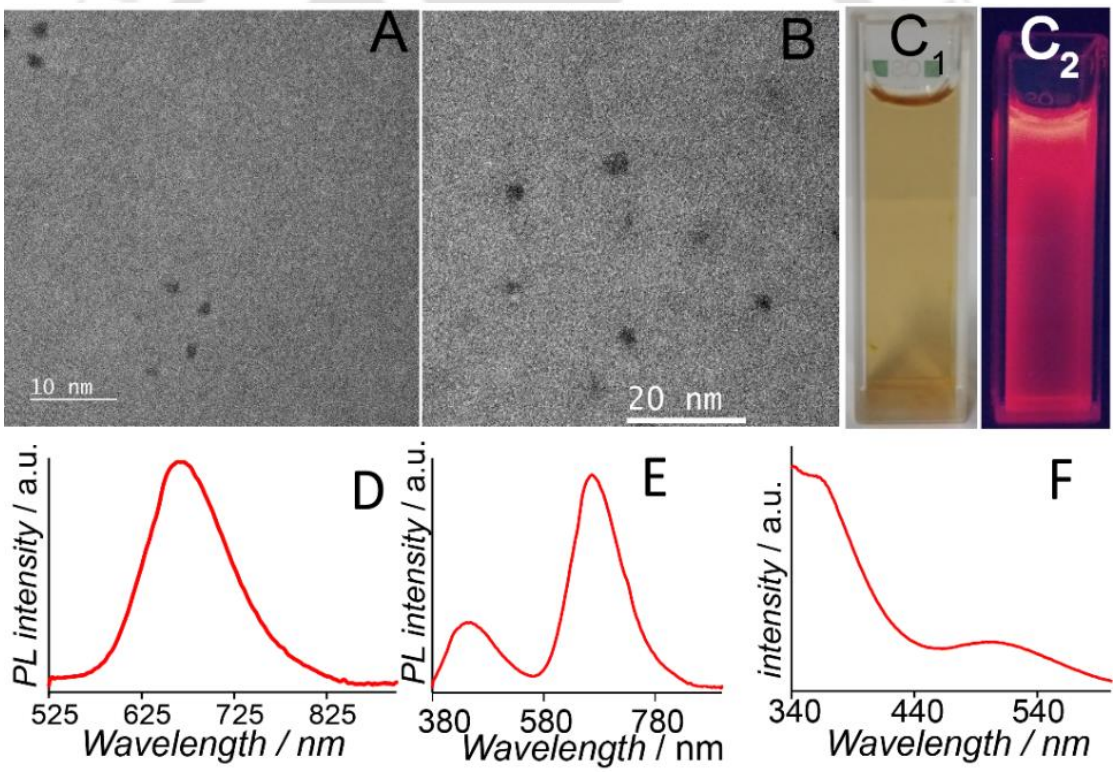

Figure 3.5. (A-B) TEM images of AuNCs-BSA. (C) Digital images of Au@BSA NCs. Suffixes 1 and 2 represent photographs recorded in day light and in UV light, respectively. (D) Emission spectra of AuNCs-BSA at an excitation of 488 nm. (E) Emission spectra of AuNCs-BSA at an excitation of 365 nm. (F) Excitation spectra of AuNCs-BSA with emission maxima fixed at 666 nm.

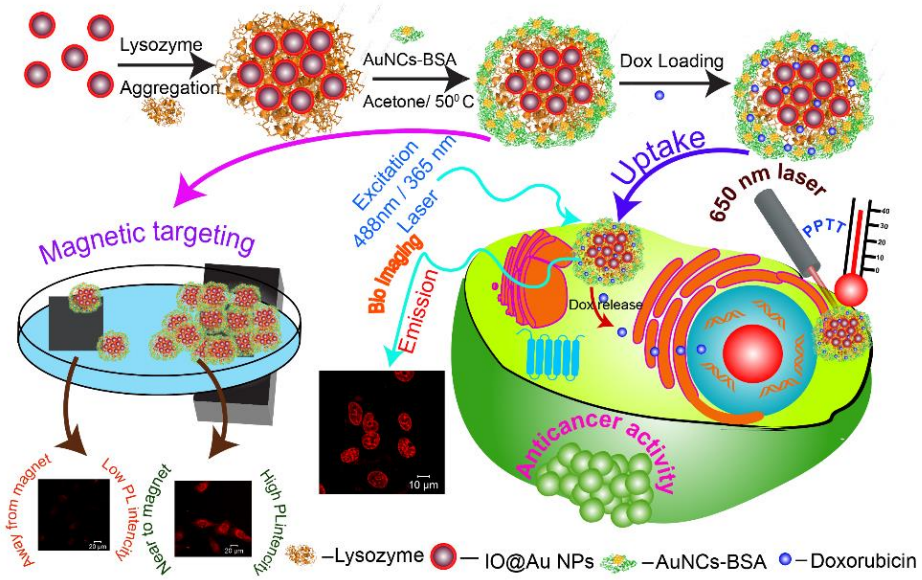

Scheme 3.1. A schematic representation of the fabrication of PML-MF nanocarrier and its capacity for plasmonic photothermal therapy, drug delivery, bioimaging and *in vitro* magnetic targeting.

Finally, the PML nanocarriers were fabricated by coating of Lyz-IO@Au agglomerates with AuNCs-BSA matrix in an acetone-mediated desolvation method followed by heat stabilization as described in the experimental section(Scheme 3.1).[7] The BSA coating around Lyz-IO@Au agglomerates was observed in the TEM images of PML-MF nanocarrier (Figure 3.6 A-B, D). Further investigation of TEM images, HRTEM, corresponding IFFT pattern, SAED and elemental mapping (Figure 3.6 C-J) confirmed the presence of both IO@Au NPs and AuNCs-BSA in the final PML-MF nanocarrier construct. The average hydrodynamic diameter of the PML-MF nanocarriers was found to be 711 nm in DLS measurements (Figure A.3.3, Appendix). The digital images in (Figure 3.7 A) showed that PML-MF nanocarrier could be easily separated by an external magnet, clearly demonstrating their plasmonic-magnetofluorescent nature. Analysis of extinction spectra showed slight broadening following coating of AuNCs-BSA, this is due further agglomeration of IO@Au NPs in presence of acetone and AuNCs-BSA (Figure 3.7 B). VSM analysis showed PML-MF nanocarrier are superparamagnetic in nature with saturation magnetization 2.3 emu g^{-1} (Figure 3.7 C).

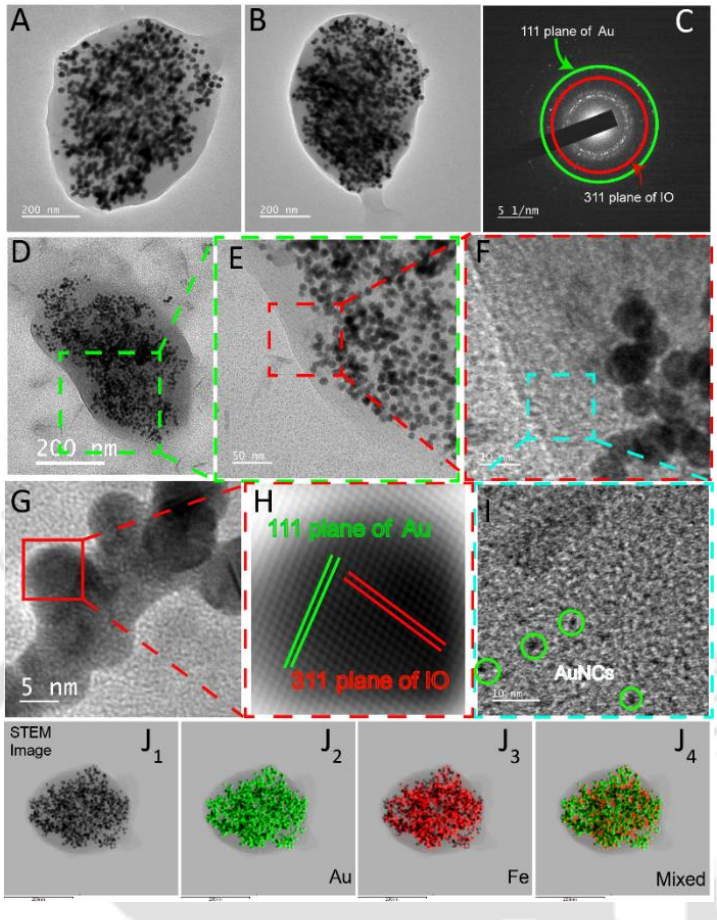

Figure 3.6. (A-B, D) TEM images of PML-MF nanocarrier. (C) SAED pattern of PML-MF nanocarrier showing diffraction patterns of both Au and IO. (E-F, I) Magnified TEM images of "D" showing presence of IO@Au NPs and AuNCs-BSA. (G) HRTEM of one IO@Au NP present inside PML-MF nanocarrier and (H) corresponding IFFT pattern showing lattice fringes of both Au and IO. (J) Elemental mapping of PML-MF nanocarrier showing the presence of both Au (green) and Fe (red), (J_1) Scanning transmission electron microscopic image (STEM) of PML-MF nanocarrier, (J_2) showing the mapping of Au, (J_3) showing the mapping of Fe, (J_4) merged image of J_1, J_2 and J_3.

The excitation spectrum of AuNCs-BSA showed a broad band around 505 nm and a hump at 365 nm (Figure 3.7 D).[7] As is evident from Figure 3.7 D, the excitation spectrum did not change significantly following the formation of PML-MF nanocarrier. However, the emission spectra of PML-MF nanocarrier – at both the excitation wavelength of 505 nm and 365 nm – showed a blue shift of 8 nm in emission maxima (λ_{em}=658 nm) compared to those of as-synthesized AuNCs-BSA (λ_{em}=666 nm) (Figure 3.7 E-F). This shift in λ_{em} was due to the change in pH of the medium.[7] Moreover, PML-MF nanocarrier showed higher photostability (Figure

3.7 G) than FITC indicating its superiority over the organic dyes in bioimaging applications.[7]

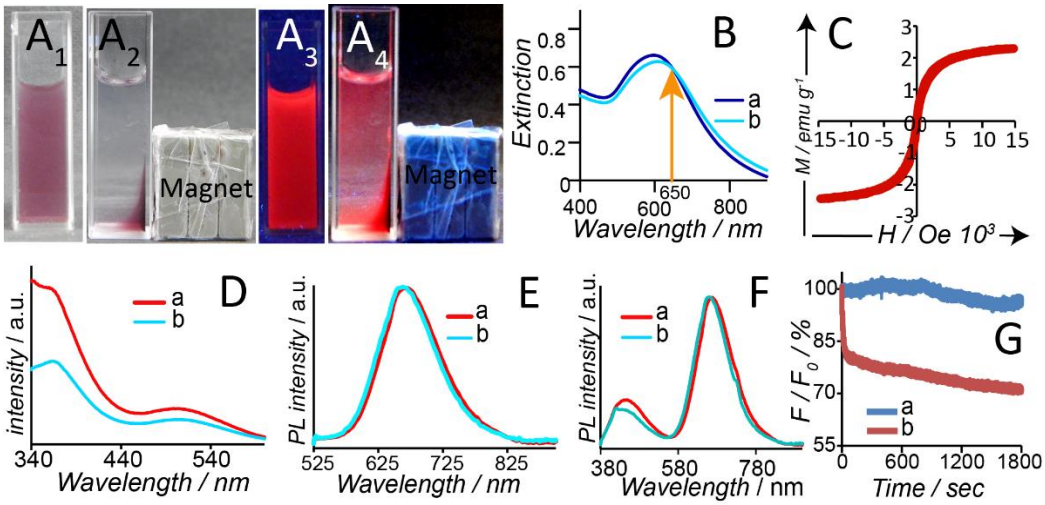

Figure 3.7. (A) Digital images of aqueous dispersion of PML-MF nanocarrier, (A_1, A_2) in day light and (A_3, A_4) under UV light, showing its easy magnetic separation and magnetofluorescent nature. (B) Extinction spectra of (a) Lyz-IO@Au agglomerates and (b) PML-MF nanocarrier. (C) VSM hysteresis loop of PML-MF nanocarrier showing superparamagnetic nature of it. (D) Excitation spectra of (a) AuNCs-BSA and (b) PML-MF nanocarrier with emission maxima fixed at 666 nm and 658 nm, respectively. (E) Emission spectra of (a) AuNCs-BSA and (b) PML-MF nanocarrier at an excitation of 505 nm. (F) Emission spectra of (a) AuNCs-BSA and (b) PML-MF nanocarrier at an excitation of 365 nm. (G) Photostability of (a) PML-MF nanocarriers (λ_{em} = 658 nm) and (b) FITC (λ_{em} = 525 nm) studied at λ_{ex} of 505 nm.

As mentioned earlier, the Lyz-mediated agglomeration of IO@Au NPs caused broadening and red shifting of SPR peak. Consequently, PML-MF nanocarrier showed 3.3 fold increase, compared to IO@Au, in the absorbance at 650 nm (Figure 3.4 A, 3.7 B), making the former a potential candidate for PPTT of cancer cells. Indeed, the aqueous dispersion of PML-MF nanocarrier, when irradiated with 650 nm laser, showed a rapid increase of temperature of 5.3 °C within 10 min followed by further increase of 0.83 °C over the next 10 min of time (Figure 3.8 A). However, control experiment with as-synthesize IO@Au showed only slight increase in temperature (1.5°C over 20 min) under similar set of

conditions (Figure 3.8 A), indicating the importance of Lyz-mediated agglomeration to enhance the PPTT ability of IO@Au NPs in PML-MF nanocarrier. Furthermore, PPTT efficacy of the PML-MF nanocarrier *in vitro* was tested by first incubating the HeLa cells with PML-MF nanocarrier for 6 h followed by laser irradiation (with 0.5 W 650 nm laser) for 10 min. Finally, MTT-based viability assay was carried out after 24 h of irradiation to estimate the cell death (Figure 3.8 B). Results showed that 24 % of the HeLa cells were killed when laser irradiation was applied after PML-MF nanocarrier treatment at 200 μg/mL (Figure 3.8 B). PML-MF nanocarrier treated cells (without laser irradiation) did not showed any killing after 30 h of incubation (Figure 3.8 B). Control experiment with non-treated HeLa cells, on the other hand, recorded no cell death as a result of laser irradiation only (Figure 3.8 C). Moreover, IO@Au NPs treated HeLa cells when irradiated with laser also did not show significant killing; only 5% cells were killed when laser irradiation was applied after treatment of 200 μg/mL IO@Au NPs (Figure 3.8 D). Thus, the above results established PML-MF nanocarrier as an efficient PPTT agent.

The bioimaging capability of PML-MF nanocarrier *in vitro* was investigated on three different types of cancer cells HeLa, HepG2 and A375 and one normal cell HEK. Cells were first grown on a coverslip, subsequently treated with PML-MF nanocarrier (150 μg/mL) for 2 h and then fixed as described in the experimental section. Fixed cells were then imaged under confocal laser scanning microscope (CLSM) with 488 nm and 365 nm laser excitations. Bright red PL of PML-MF nanocarriers were observed inside all the four kinds of cells at both the excitations (Figure 3.9, 3.10). Moreover, the *Z*-staking images in both depth and orthogonal projection for all the three different kinds of cancer cell lines confirmed the internalization of PML-MF nanocarrier by the cells (Figure 3.11). The non-treated (control) cells of all cell lines did not show any such PL under similar sets of experimental conditions (Figure A.3.4, A.3.5, Appendix), thus, establishing the PML-MF nanocarrier as bioimaging probe.

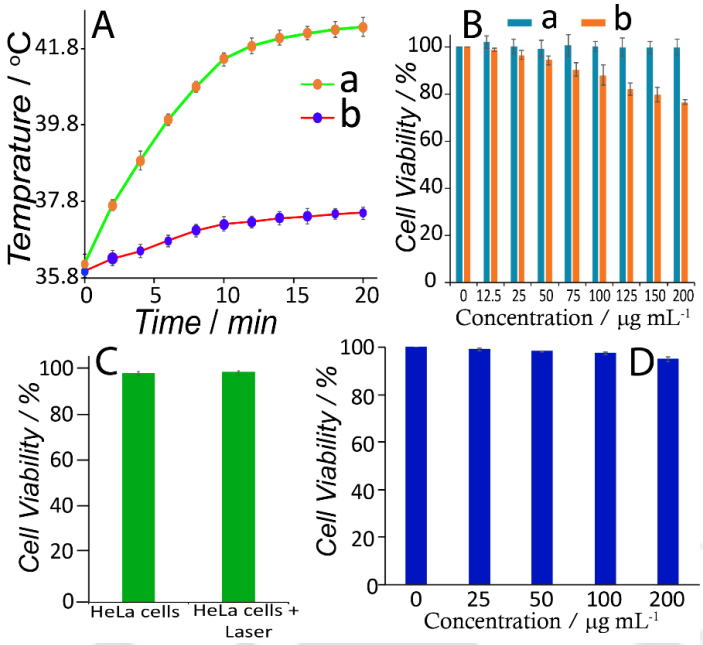

Figure 3.8. (A) Temperature changes occurring under 650 nm laser irradiation of (a) PML-MF nanocarriers and (b) IO@Au NPs dispersed in water. (B) MTT based viability assay of HeLa cells treated with (a) PML-MF nanocarriers and (b) IO@Au NPs followed by 650 nm laser irradiation for 10 min. (C) Viability of HeLa cells to estimate the effect of laser irradiation (D) Viability of HeLa cells, treated with IO@Au NPs for 6 h and then irradiated with 650 nm laser for 10 min and then again incubated for 24 h.

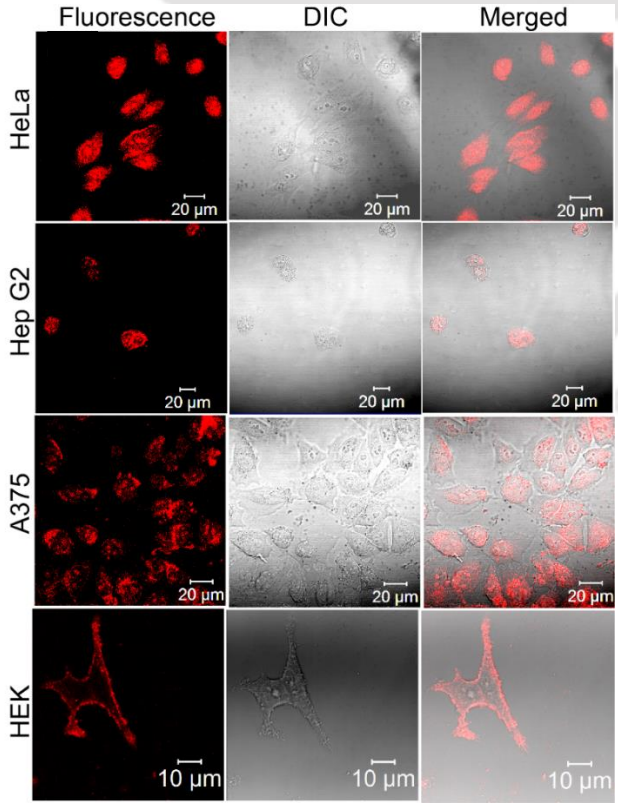

Figure 3.9. CLSM images of HeLa, HepG2, A375 and HEK cells treated with PML-MF nanocarrier for 2 h; images were recorded with 488 nm excitation laser.

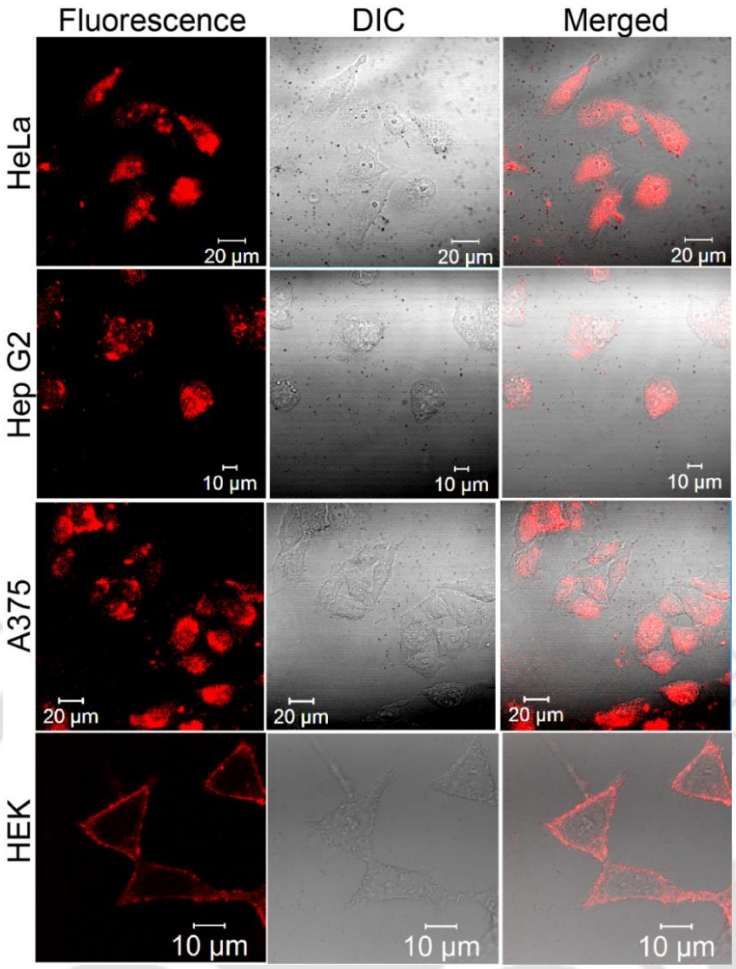

Figure 3.10. CLSM images of HeLa, HepG2, A375 and HEK cells treated with PML-MF nanocarriers for 2 h and recorded at 355 nm excitation.

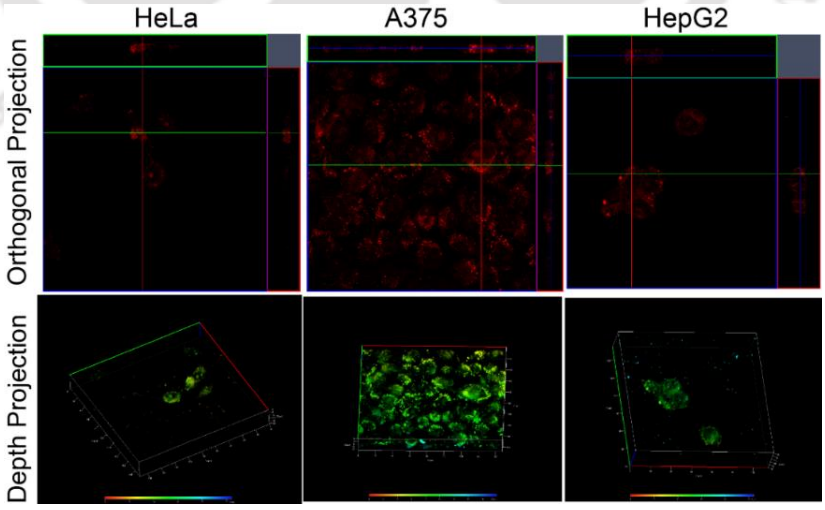

Figure 3.11. Z-staking CLSM image of PML-MF nanocarrier treated HeLa, HePG2 and A375 cells with corresponding orthogonal and depth projections showing the internalization PML-MF nanocarriers by the cells.

In order to get insight into uptake of PML-MF nanocarriers, internalization studies were performed in presence of sodium azide (NaN_3), a well-kwon inhibitor of endytosis pathway.[11] When HeLa cells were incubated with PML-MF nanocarrier in the presence of NaN_3, 82% decrease in the uptake of PML-MF nanocarriers was estimated from the CLSM images (Figure 3.12). This indicated the endocytosis being the preferred pathway for uptake of PML-MF nanocarriers.

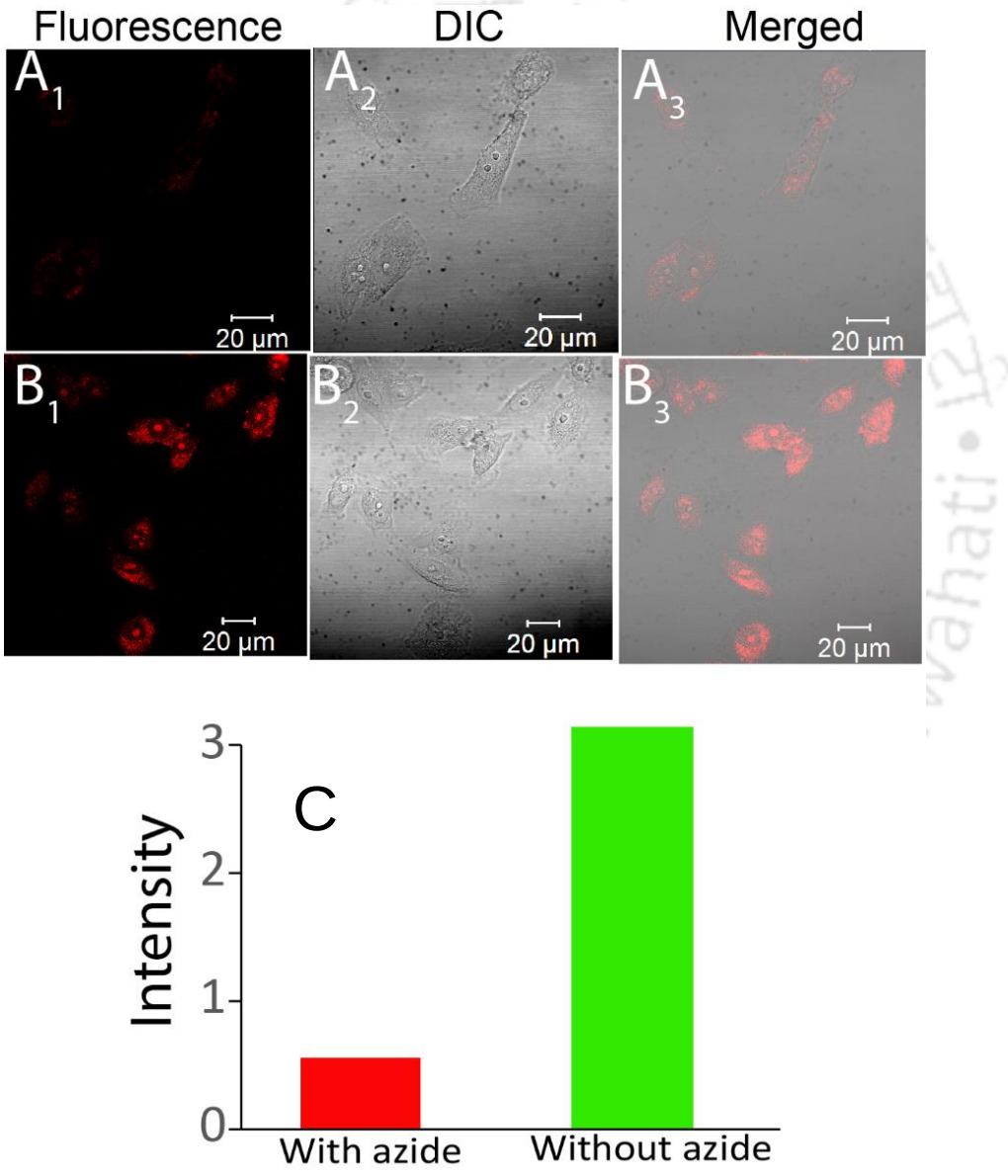

Figure 3.12. CLSM images of HeLa cells treated with PML-MF nanocarrier (A) in presence and (B) in absence of sodium azide (0.1%). (C) PL emission intensity plot calculated from image "**A**" and "**B**", showing 82% decrease in PL emission intensity in **"A"** compared to **"B"** due to presence of known endocytosis inhibitor sodium azide, indicating endocytosis as the preferred way of uptake.

Targeting of diseases site is another important aspect of modern day cancer theranostic.[12] Magnetic nanocarriers (MNs) could be guided by peripheral magnetic field towards disease site to avoid collateral damages. As discussed above vibrating sample magnetometric (VSM) analysis showed that PML-MF nanocarrier are superparamagnetic in nature with saturation magnetization 2.3 emu g^{-1}. Although the value is lower compare to IO NPs (27.6 emu g^{-1}) and IO@Au NPs (12.5 emu g-1) due to contribution of diamagnetic gold shell and AuNCs-BSA, still it is high enough for magnetic targeting.[1] In this regard, a model experiment was performed *in vitro* where HeLa cells were grown on two coverslips placed opposite to each other in a 60 mm petri dish.[1] A powerful rare earth magnet was then placed at the bottom of one of the coverslips and the cells were incubated with PML-MF nanocarrier for 2 h (Figure 3.13). Finally, following fixation, the cells were visualized under CLSM (488 nm laser excitation). It was observed that cells present on the coverslip placed just above the magnet showed much higher PL emission intensity compared to those present on the coverslip away from magnet (Figure 3.13), indicating the potential of PML-MF nanocarrier for magnetic targeting.

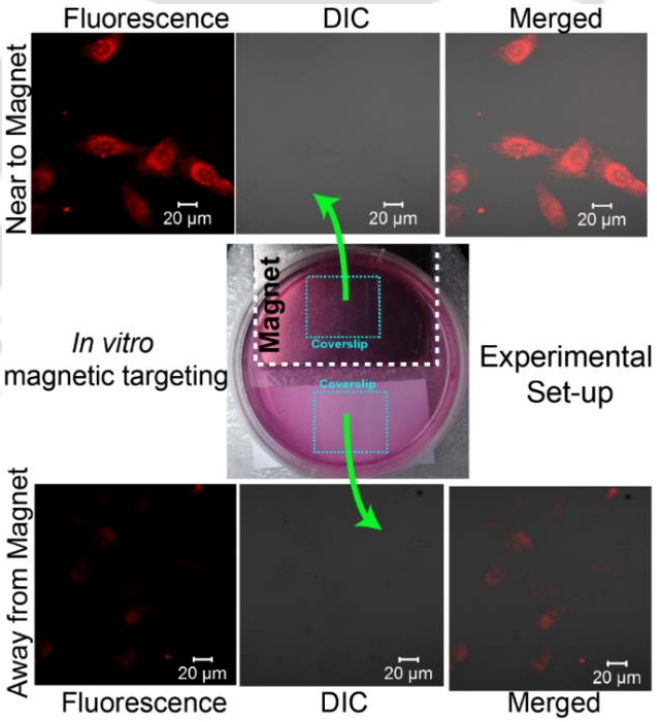

Figure 3.13. *In vitro* magnetic targeting: CLSM images of HeLa cells treated with PML-MF nanocarrier. Top panel represents cells close to the magnet and bottom panel represents cells away from magnet.

As is evident from previous discussions, Lyz (helped in the agglomeration of IO@Au) and BSA of Au NCs-BSA composite (helped in coating the Lyz-IO@Au agglomerates) together provided significant amount of protein matrices within PML-MF nanocarrier. Considering the ability of proteins to efficiently carry hydrophilic and hydrophobic drug molecules, the potential of the present PML-MF nanocarrier a drug-carrier was evaluated by loading chemotherapeutic drug Dox. Loading of the drug was carried out by incubating 3.28 μg mL^{-1} of Dox with 162.3 μg mL^{-1} of PML-MF nanocarrier under stirring for 2 h as described in the experimental section. PL emission spectrum of Dox-loaded PML-MF nanocarrier (DPML-MF nanocarrier) exhibited an additional peak at 591 nm (characteristic of Dox), confirming the loading of the drug into PML-MF nanocarrier (Figure 3.14 A). Encapsulation efficiency for Dox was calculated to be 82 %. The kinetics of Dox release from DPML-MF nanocarrier was also studied in two different pH buffers i.e., PBS buffer (pH 7.4) and acetate buffer (pH 4.4). Results showed that 30% of the Dox was being released in PBS buffer (pH=7.4) and 37% in acetate buffer (pH=4.4) upon 24 h of incubation at 37 °C (Figure 3.14 B, C). A comparatively fast release of Dox was noticed up to 6 h and thereafter a slow release up to 24 h was observed in both the buffers. DPML-MF nanocarrier was also found to be stable in human blood serum (HBS) up to 24 h as tested by monitoring the PL emission of DPML-MF nanocarrier with time. (Figure 3.14 D).

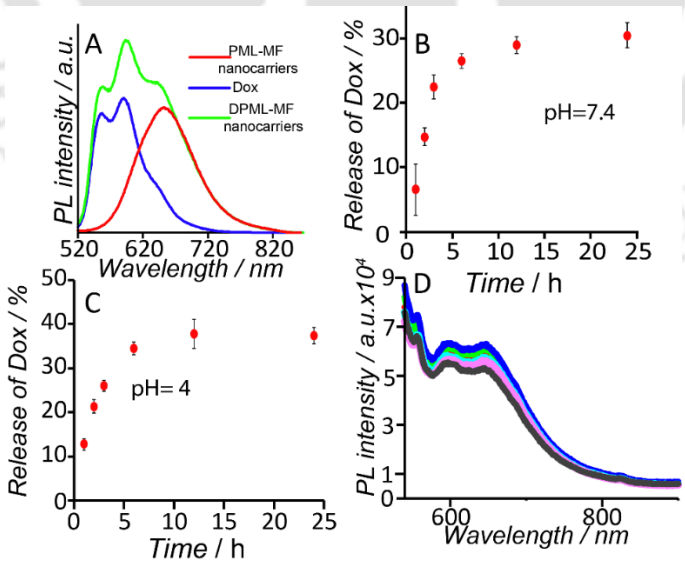

Figure 3.14. (A) Emission spectra of PML-MF nanocarriers, Dox and DPML-MF nanocarriers at an excitation of 505 nm. Release of Dox from DPML-MF nanocarriers with time, being incubated at 37 °C in (B) pH 7.4 PBS and (C) pH 4 acetate buffers, respectively. (D) Stability of DPML-MF nanocarriers in human blood serum. The PL emission intensities of DPML-MF nanocarrier dispersed in HBS was measured with time at excitation 505 nm.

The internalization of DPML-MF nanocarrier by cancer cells was confirmed from the CLSM images (Figure 3.15) of cells treated with DPML-MF nanocarrier for 2 h as described in the experimental section. In order to observe the Dox emission from the DPML-MF nanocarrier-treated cells, they were examined under CLSM by irradiation with 488 nm laser of 0.2 mW power, since preliminary experiments (data not shown) established that laser power of less than 10 mW did not result in detectable emission from the PML-MF treated cells. When irradiated with 488 nm laser bright red emission of Dox was observed predominantly from the nuclei of the DPML-MF nanocarrier-treated cells from the cells which was absent in PML-MF nanocarrier treated cells. As Dox is known to bind to the DNA of the cells, thus, CLSM images in Figure 3.15 essentially confirmed the release of Dox within cells.[8]. Z staking images of DPML-MF nanocarrier treated cells also confirmed the internalization of the DPML-MF nanocarrier by the cells (Figure 3.16).[8]

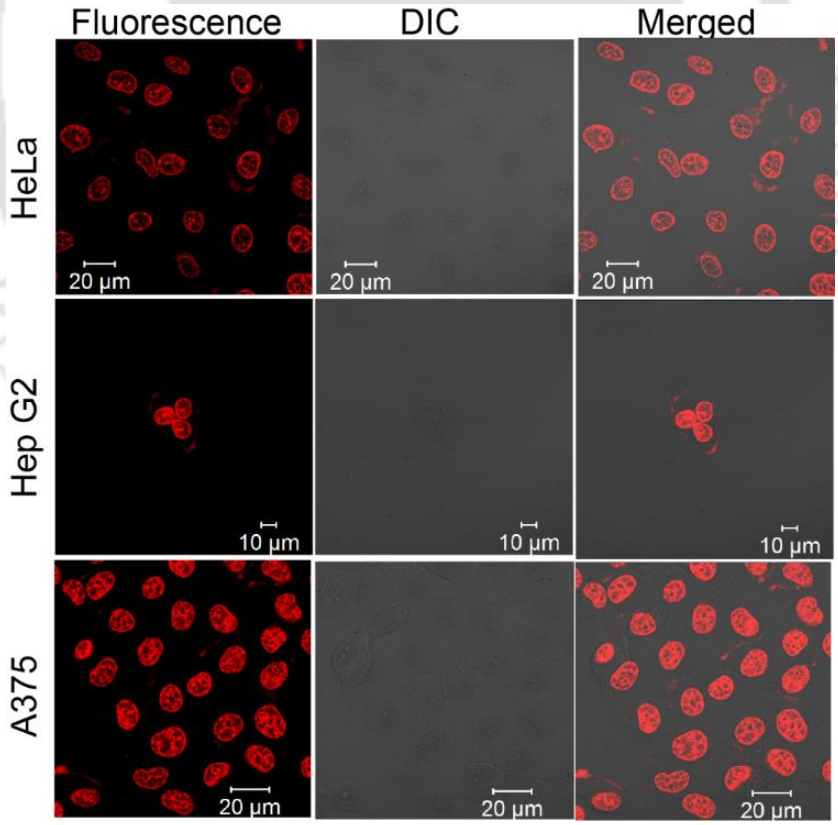

Figure 3.15. CLSM images of HeLa, HepG2 and A375 cells treated with DPML-MF nanocarriers for 2 h and excited at 488 nm excitation.

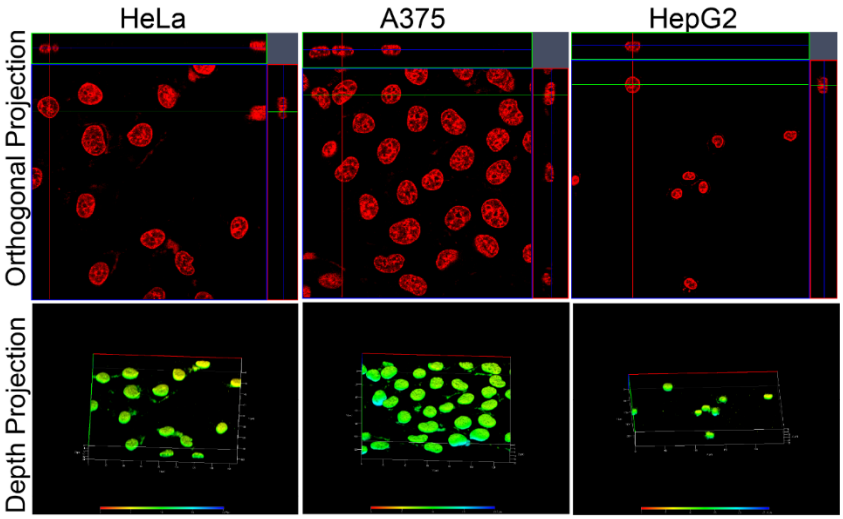

Figure 3.16. Z-staking CLSM image of DPML-MF nanocarrier treated cells with corresponding orthogonal and depth projections showing the internalization DPML-MF nanocarriers by the cells

Successful uptake of DPML-MF nanocarrier by cancer cells was expected to result in considerable antiproliferative efficacy, which was pursued by MTT-based cell viability assay (Figure 3.17 A-C). Results of MTT assay showed that PML-MF nanocarrier did not possess considerable killing effect as it was only able to kill 1.2 % of HeLa, 2.6 % of Hep G2 and 3.1 % of A375 cells even at as high concentration as 200 µg/mL (for HeLa) and 150 µg/mL (HepG2 and A375). However, DPML-MF nanocarrier showed considerable killing effect in dose-dependent manner with IC_{50} values 154.4 µg/mL, 121.6 µg/mL and 93.4 µg/mL for HeLa, HePG2 and A375 cells, respectively, which corresponded to 3.1 µg/mL, 2.4 µg/mL and 1.9 µg/mL of Dox as calculated from the encapsulation efficiency. In a parallel set of experiments, IC_{50} values of free Dox was found to be 0.65 µg/mL, 0.57 µg/mL and 0.47 µg/mL for HeLa, HePG2 and A375 cells, respectively (Figure 3.18). This increase in IC_{50} values in terms of Dox amount for DPML-MF nanocarrier as compared to free Dox could be due to incomplete or slow release of Dox from DPML-MF nanocarrier as mentioned in previous studies.[8] MTT assay was also performed in normal cells (HEK) as a control experiment and the results (Figure 3.19) showed that PML-MF nanocarriers did not kill HEK cells significantly. Nonetheless, DPML-MF nanocarriers showed significant antiproliferative effect in HEK cells with IC_{50} value of 211 µg/mL, similar to the cancerous cells. Although selective anti-cancer response of the DPML-MF nanocarriers was not observed in the present study, suitable active targeting strategies coupled with magnetic

targeting can be employed to enable these nanocarriers for preferential eradication of cancer *in vivo*.

Considering the therapeutic potential of DPML-MF nanocarrier both as antiproliferative and PPTT agent, the combination therapeutic efficacy of these nanocarriers was evaluated by irradiating DPML-MF nanocarrier treated HeLa cells with 650 nm laser. The result of MTT-based cell viability assay, presented in Figure 3.17 C, clearly demonstrated that combined therapeutic module comprised of 650 nm laser mediated PPTT of DPML-MF nanocarrier-treated HeLa cells was superior in killing the cancer cells when compared to those of either DPML-MF-treated or PPTT of PML-MF nanocarrier-treated HeLa cells. Moreover, the isobologram plot (Figure 3.17D) further revealed the synergistic therapeutic potential of DPML-MF nanocarrier along with PPTT and established DPML-MF nanocarrier as a multimodal therapeutic material. The reason for synergistic action, although not completely elucidated in the present study, could be the release of additional Dox due to laser irradiation.[13]

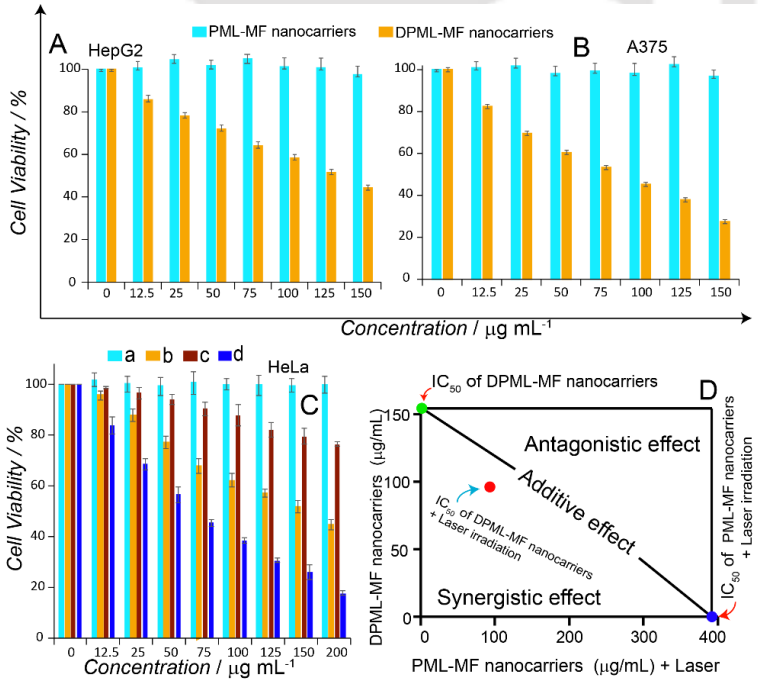

Figure 3.17. (A-B) MTT based cell viability of HePG2, A375 cells treated with varying concentrations of PML-MF nanocarrier and DPML-MF nanocarrier. (C) MTT based cell viability of HeLa cells treated with (a) PML-MF nanocarrier, (b) DPML-MF nanocarrier, (c) PML-MF nanocarrier then irradiated with 650 nm laser and (d) DPML-MF nanocarrier then irradiated with 650 nm laser. (D) Isobologram plots showing synergistic effect.

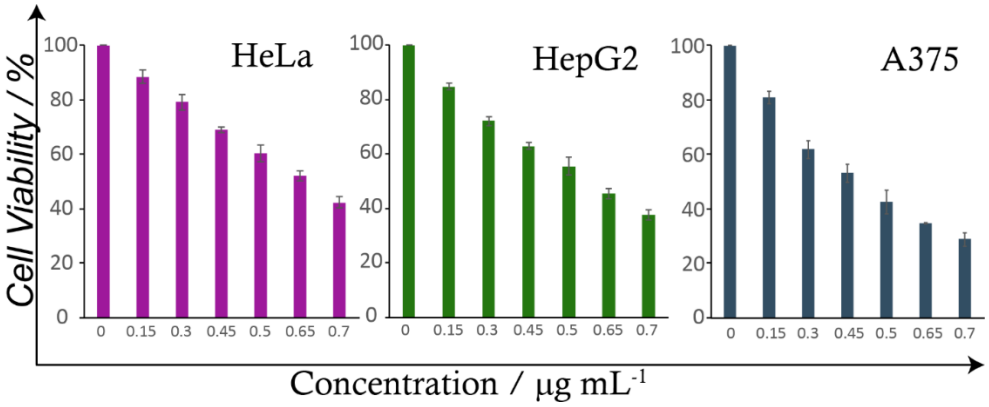

Figure 3.18. MTT based cell viability of HePG2 and A375 cells treated with varying concentrations of Dox.

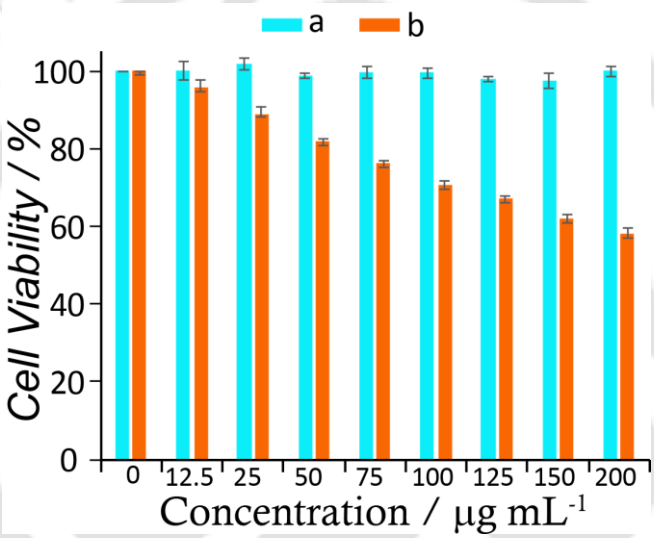

Figure 3.19. MTT based cell viability of HEK cells treated with (a) PML-MF nanocarriers and (b) Dox loaded PML-MF nanocarriers, respectively.

3.3. Conclusion

In conclusion, we have developed an advanced plasmonic magneto luminescent multifunctional nanocarrier (PML-MF nanocarrier) using the Lyz-mediated agglomeration of IO@Au NPs followed by successful coating of the agglomerates with luminescent AuNCs-BSA. Agglomeration significantly enhanced the plasmonic absorbance of the IO@Au NPs in NIR biological window, and thus facilitated *in vitro* plasmonic photothermal therapy. Luminescent nature of AuNCs-BSA remained unaffected in PML-MF nanocarrier, and thus, acted as a probe for bioimaging for different kinds of cancer cells including HeLa, HepG2 and

A375. Superparamagnetic nature of PML-MF nanocarrier was utilized for *in vitro* magnetic targeting, indicating the possibility of targeted drug delivery. Presence of proteins in PML-MF nanocarrier helped to efficiently load and deliver chemotherapeutic drug Dox to cancer cells with significant killing effect. Finally, DPML-MF nanocarrier showed synergistic therapeutic ability *in vitro*, when combined with laser irradiation of nanocarrier treated HeLa cells. Combining therapeutic modalities like PPTT and anticancer drug delivery with magnetic targeting, luminescence-based imaging capability and appreciable blood serum stability, PML-MF nanocarrier, developed in the present form could be a potential candidate for cancer theranostics.

References:

1. Bhandari, S.; Khandelia, R.; Pan, U. N.; Chattopadhyay, A., Surface Complexation-Based Biocompatible Magnetofluorescent Nanoprobe for Targeted Cellular Imaging. *ACS Appl. Mater. Interfaces* **2015**, *7* (32), 17552-17557.
2. Lo, C.-K., Xiao, D., and Choi, M. M. F. Homocysteine-protected Gold-coated Magnetic Nanoparticles: Synthesis and Charaterization *J. Mater. Chem.* **2007** 17, 2418– 2427.
3. Li, Y.; Bin, Q.; Lin, Z.; Chen, Y.; Yang, H.; Cai, Z.; Chen, G. Synthesis and Characterization of Vinyl-Functionalized Magnetic Nanofibers for Protein Imprinting *Chem. Commun.* **2015**, 51, 202– 205
4. Zhou, T.; Wu, B.; Xing, D. Bio-modified Fe_3O_4 Core/Au Shell Nanoparticles for Targeting and Multimodal Imaging of Cancer Cell *J. Mater. Chem.* **2012**, 22, 470– 477.
5. Pham, T. T. H.; Cao, C.; Sim, S. J. Application of Citrate-stabilized Gold-coated Ferric Oxide Composite Nanoparticles for Biological Separations *J. Magn. Magn. Mater.* **2008**, 320, 2049– 2055.
6. Lu, Q. H., Yao, K. L., Xi, D., Liu, Z. L., Luo, X. P. and Ning, Q. Synthesis and Characterization of Composite Nanoparticles Comprised of Gold Shell and Magnetic Core/Cores *J. Magn. Magn. Mater.* **2006**, 301, 44-49.

7. Khandelia, R.; Bhandari, S.; Pan, U. N.; Ghosh, S. S.; Chattopadhyay, A., Gold Nanocluster Embedded Albumin Nanoparticles for Two-Photon Imaging of Cancer Cells Accompanying Drug Delivery. *Small* **2015,** *11* (33), 4075-4081.
8. Khandelia, R.; Jaiswal, A.; Ghosh, S. S.; Chattopadhyay, A. Gold Nanoparticle–Protein Agglomerates as Versatile Nanocarriers for Drug Delivery *Small* **2013***, 9*, 3494– 3505.
9. Khandelia, R.; Jaiswal, A.; Ghosh, S. S.; Chattopadhyay, A. Polymer Coated Gold Nanoparticle–Protein Agglomerates as Nanocarriers for Hydrophobic Drug Delivery *J. Mater. Chem. B* **2014**, *2,* 6472– 6477.
10. Sanpui, P.; Paul, A.; Chattopadhyay, A., Theranostic Potential of Gold Nanoparticle-Protein Agglomerates. *Nanoscale* **2015***, 7* (44), 18411-18423.
11. Dutta, A.; Dutta, D.; Sanpui, P. Chattopadhyay, A. Biomimetically crystallized protease resistant zinc phosphate decorated with gold atomic clusters for bioimaging *Chem. Commun*. **2017**, *53*, 1277-1280.
12. Li, Z.; Yin, S.; Cheng, L.; Yang, K.; Li, Y.; Liu, Z. Magnetic Targeting Enhanced Theranostic Strategy Based on Multimodal Imaging for Selective Ablation of Cancer *Adv. Funct. Mater.* **2014,** *24*, 2312– 2321.
13. Kah, J. C.; Chen, J.; Zubieta, A.; Hamad-Schifferli, K. Exploiting the Protein Corona around Gold Nanorods for Loading and Triggered Release *ACS Nano* **2012***, 6,* 6730– 6740.

CHAPTER 4

Synergistic Anticancer Potential of Artemisinin When Loaded with 8-Hydroxyquinoline-Surface Complexed-Zinc Ferrite Magnetofluorescent Nanoparticles and Albumin Composite

In this chapter fabrication of a novel class of magnetofluorescent theranostic nanoparticles (MFTNPs) following 'surface-complexation' of zinc ferrite ($ZnFe_2O_4$) NPs with 8-hydroxyquinoline is reported. The potential of these MFTNPs in fluorescence-based bioimaging of different cancer cells was successfully demonstrated. The superparamagnetic behavior of the MFTNPs was exploited effectively in magnetic targeting *in vitro*. Finally, a well-known hydrophobic anti-malarial and prospective anti-cancer drug artemisinin was efficiently loaded into MFTNPs. Artemisinin loaded MFTNPs were observed to induce superior anti-proliferative response, as compared to free drug, in cancer cells in a synergistic mechanism with combination index of 0.1 or less.

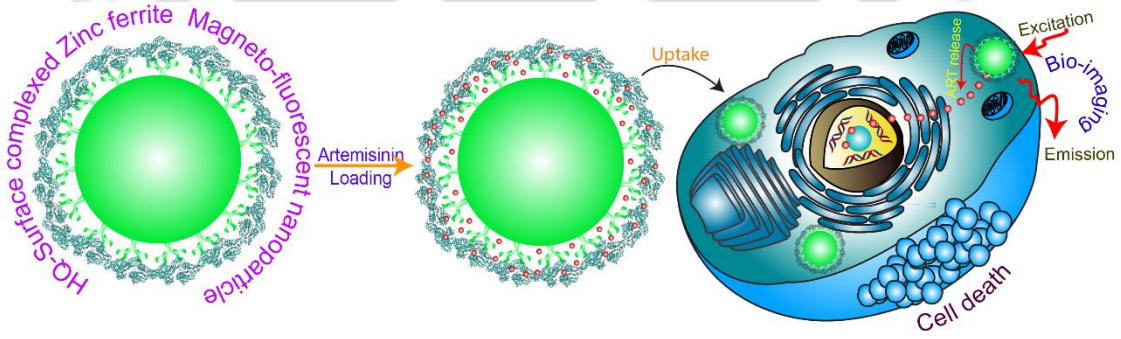

***[ACS Appl. Bio Mater. 2018, *1*, 1229−1235] - Reproduced with permission from the American Chemical Society.**

4.1 Experimental section

4.1.1 Materials: Artemisinin, iron chloride hexahydrate ($FeCl_3.6H_2O$), trioctylphosphine oxide (TOPO), 1-octadecene, sodium oleate and fluorescein isothiocyanate isomer I were purchased from Sigma Aldrich. 8-Hydroxyquinoline, zinc chloride ($ZnCl_2$), bovine serum albumin (BSA), oleic acid, and hexane were procured from Merck, India. 3-(4,5-dimethylthiazol-2-yl)-2,5-diphenyltetrazolium bromide (MTT) and ethanol were obtained from Himedia, India and Tedia USA, respectively. All chemicals were used without further purification. Milli-Q grade water was used in all the experiments.

4.1.2 Preparation of Zinc ferrite nanoparticles ($ZnFe_2O_4$ NPs): $ZnFe_2O_4$ NPs (*ZFNPs*) were synthesized in two steps. In the first step, a mixture of zinc oleate and iron oleate at 1:2 ratio was prepared. For that, 26.8 mmol of $FeCl_3.6H_2O$, 13.4 mmol of $ZnCl_2$ and 36.5 g of sodium oleate were dissolved in 3:4:7 water, ethanol and hexane mixture and refluxed for 4 h at 70 ^oC. A brown color mixture of 1:2 Zn-oleate and Fe-oleate complexes was separated from upper hexane layer, then washed with water:ethanol mixture for five times, dried and kept for further use.

In the second step 300 mg of 1:2 Zn-oleate and Fe-oleate complex mixture, 50 µL of oleic acid and 25 mg of TOPO were added in 10 mL of 1-octadecene and heated at 120 °C under reflux for 1 h. Then temperature was raised to 200 °C and N_2 gas were purged through it. Once N_2 purging was completed temperature was again raised to 310 °C and kept at this temperature for 2 h in order to complete the synthesis of $ZnFe_2O_4$ NPs. On completion of reaction, $ZnFe_2O_4$ NPs were washed with ethanol:hexane mixture and magnetically separated with the cycle being completed for five times to remove excess reactants and then redispersed in 50 mL of hexane and stored for further use.[1]

4.1.3 Preparation of HQ-ZFNPs@BSA: First 2 mL of the stock $ZnFe_2O_4$ NPs dispersion was diluted to 10 mL using hexane. For surface complexation, 50 µL of the 10 mM ethanolic solution of HQ was added to it under sonication. Complexation reaction happened immediately after addition of HQ. Surface

complexed $ZnFe_2O_4$ NPs (HQ-ZFNPs) were separated using magnet and then washed with ethanol:hexane mixture and redispersed in 1% aqueous BSA solution under strong sonication. Aqueous dispersion of HQ-ZFNPs@BSA was further separated with magnet and washed with 1% BSA solution for two times and finally dispersed in 1% aqueous BSA solution and kept at 4 °C.

4.1.4 Loading of Artemisinin (ART): To load ART into HQ-ZFNPs@BSA, first 2 ml of the stock $ZnFe_2O_4$ NPs dispersion was diluted to 10 mL using hexane and then 50 µL of 10 mM ethanolic solution of HQ was added to it under sonication for complexation. Once the complexation was over HQ-ZFNPs were separated using powerful neodymium magnet and a mixture of 2 mL of 1% BSA solution and 50 µL of 5 mg/mL ART was added and sonicated for 2 h. ART loaded HQ-ZFNPs@BSA was separated and washed following centrifugation. Encapsulation efficiency of artemisinin was calculated by determining the amount of ART present on the supernatant and comparing it with the amount of ART was initially added. To calculate the amount of ART present on supernatant a NaOH based spectrophotometric estimation method of ART was used.[2] A standard curve was also produced by mixing different amount of ART in the supernatant of HQ-ZFNPs@BSA followed by measuring the absorbance following the same NaOH based estimation method.[2] Supernatant of HQ-ZFNPs@BSA was taken as solvent to dilute ART-solutions to avoid influence of pH and other materials present in the supernatant, on the absorbance during estimation process.[3] The following formula was used to calculate the encapsulation efficiency,

$$\textit{Encapsulation efficiency (\%)} = \{(C_{add} - C_{sup}) / C_{add} \} \times 100$$

Where C_{add} is concentration of ART originally added and C_{sup} is concentration of ART present in the supernatant after pelleting down the ART loaded HQ-ZFNPs@BSA.

***4.1.5 Photostability*:** Photostabilities of aqueous dispersions of HQ-ZFNs@BSA and ethanolic solution of FITC were measured in HORIBA JobinYvon FluoroMax-4

spectrofluorimeter. Data were recorded under constant irradiation of 365 nm up to 1800 s at an interval of 0.1 s.

4.1.6 Cell viability assay: HeLa, HepG2, A375, HEK, L132 and 3T3 cells were acquired from NCCS, Pune, India. Cell culture medium was prepared by mixing 10% (v/v) fetal bovine serum (FBS) and Penicillin- Streptomycin (100 U mL−1) with Dulbecco's modified Eagle's medium (DMEM) under incubation at 37 °C and 5% CO_2. MTT-based cell viability assay was performed in 96-wells plate with 10,000 cells. Cells were treated with different concentrations of different (as appropriate) materials for 24 h. For MTT assay, absorbance of the Fromazane was measured using Bio-Rad 680 microplate reader and cell viability calculated using the following formula:

$$Cell\ Viability\ (\%) = \{\frac{A\ (T)}{A\ (C)}\} \times 100$$

Here *A(T)* absorbance of Fromazane in the treated sample, *A(C)* absorbance of Fromazane in non-treated control sample. Combination indices were calculated using CompuSyn software.

4.1.7 Sample preparation for CLSM imaging: Cells were grown on a cover slip and treated with 100 µg/mL of HQ-ZFNs@BSA for 2 h. After treatment, cells were fixed with formaldehyde and chilled ethanol and mounted on a glass slide using glycerol. Images were taken in Carl Zeiss LSM 880 microscope with 355 laser excitation.

To show the presence of HQ-ZFNPs@BSA inside lysosome, HeLa cells were treated with a mixture of HQ-ZFNPs@BSA and Red DND-99 LysoTracker for 2h and then images were taken under 365 and 561 laser excitations.

***4.1.8 Magnetically targeted imaging*:** In a 60 mm petri dish two coverslips were positioned at maximum distance to each other and HeLa cells were grown on them for overnight. Next, a powerful neodymium magnet was placed at the bottom of only one coverslip. Then, 100 µm/mL HQ-ZFNs@BSA was added to the petri-dish and kept for 2 h. Cells were then fixed using formaldehyde and ethanol and images were taken in Carl Zeiss LSM 880 microscope.

4.2 Results and Discussion

The average size of the zinc ferrite nanoparticles (ZFNPs) was estimated to be 6 ± 1.3 nm from transmission electron microscopic (TEM) images (Figure 4.1 A, B). High resolution TEM (HR-TEM) images (Figure 4.1 C) with corresponding inverse fast Fourier transform (IFFT) (Figure 4.1 D) and selected area electron diffraction (SAED) patterns (Figure 4.1 E) indicated the production of $ZnFe_2O_4$ NPs with typical lattice fringes for 311 planes [4] The XRD pattern (Figure 4.1 F) further confirmed the formation of FCC $ZnFe_2O_4$ NPs.[5]

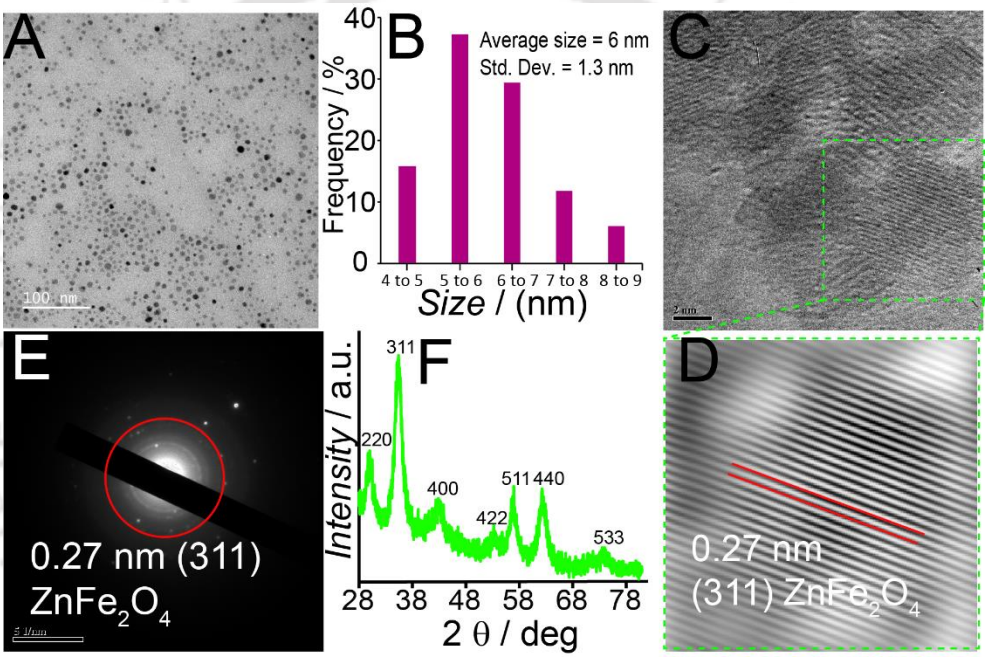

Figure 4.1. (A) TEM image of ZFNPs; (B) size distribution (calculated from 50 NPs) of ZFNPs (C) HRTEM of ZFNPs with corresponding (D) IFFT pattern and (E) SAED pattern. (F) Powder X-ray Diffraction (XRD) pattern of ZFNPs showing characteristic peaks at 2θ of 29.7°, 35.4°, 43.0°, 53.5°, 56.8°, 62.4° and 74.0°, corresponding to (220), (311), (400), (422), (511), (440) and (533) planes.

As mentioned in the experimental section ZFNPs were subjected to surface complexation with HQ by adding 10 mM of HQ solution to $ZnFe_2O_4$ NPs dispersion with mild sonication. Surface complexation of HQ with ZFNPs was evaluated by examining the Fourier transform infrared (FTIR) spectra of individual

components (namely HQ and ZFNPs) and HQ-surface complexed-ZFNPs (HQ-ZFNPs) (Figure 4.2). FTIR spectrum of HQ-ZFNPs, as is evident from Figure 4.2, showed characteristic peaks of HQ at 1500 cm^{-1}, 1468 cm^{-1}, 822 cm^{-1} and 745 cm^{-1}, thus indicating successful surface complexation. Notably, shifting of C-O-H stretching band from 1070 cm^{-1} to 1110 cm^{-1} due to the formation of C-O-Zn bonds confirmed HQ-complexation onto ZFNPs surfaces in ZnQ_2 type complexes.[6-7]

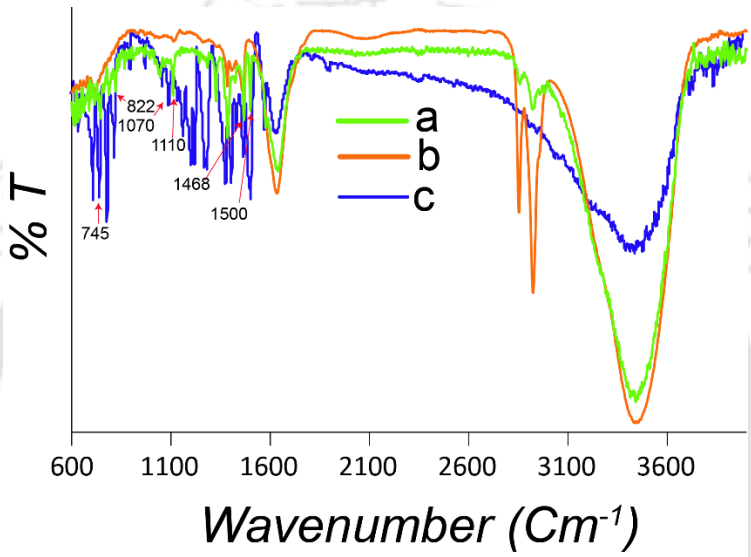

Figure 4.2. FTIR spectra of (a) HQ-ZFNPs, (b) ZFNPs and (c) HQ.

It may be mentioned here that as-prepared HQ-ZFNPs were observed to be poorly water-dispersible. To circumvent this issue, HQ-ZFNPs were redispersed in 1% (w/v) aqueous solution of BSA under gentle sonication as described in the experimental section. This resulted in the BSA-coating around the HQ-ZFNPs,[8] which not only rendered the later water dispersible but also offered the opportunity to load anti-cancer drug molecules by providing hydrophobic and hydrophilic regions.[6-8] TEM images (Figure 4.3 A) of BSA-stabilized HQ-ZFNPs (hereafter referred as HQ-ZFNPs@BSA) revealed average particle size of 6 ± 1.2 nm(Figure 4.3 B). Moreover, HR-TEM images (Figure 4.3 C) with corresponding IFFT (Figure 4.3 D) and SAED (Figure 4.3 E) pattern demonstrated characteristic lattice fringes for 311 planes.[1,4] The presence of iron and zinc were confirmed in

Energy-dispersive X-ray spectroscopy (EDX) of HQ-ZFNPs@BSA (Figure 4.3 F). XRD pattern of HQ-ZFNPs@BSA (Figure 4.3 G) displayed characteristic peaks (2θ) at 30.0°, 35.4°, 43.0°, 53.3°, 56.8°, 62.5° and 74.3°, similar to $ZnFe_2O_4$ NPs. Thus, TEM and XRD analyses confirmed that the size and crystallinity of the core $ZnFe_2O_4$ NPs were not affected as a result of surface complexation with HQ and subsequent coating with BSA. The average hydrodynamic diameter (δ_H) and zeta potential (ζ) of HQ-ZFNPs@BSA dispersed in water at physiological pH were measured to be 22 nm and -20.8 ± 3.2 eV, respectively (Figure 4.4).

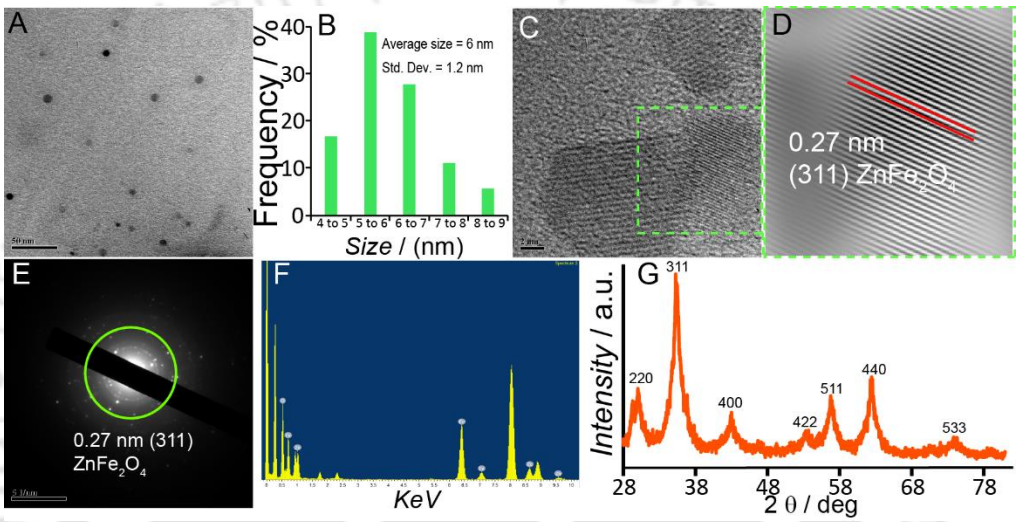

Figure 4.3. (A) TEM image of HQ-ZFNPs@BSA. (B) size distribution of HQ-ZFNPs@BSA. (C) HR-TEM image and (D) corresponding IFFT pattern of of HQ-ZFNPs@BSA (E) SAED pattern of HQ-ZFNPs@BSA (F) EDX spectrum of HQ-ZFNPs@BSA displaying the presence of iron and zinc. (G) Powder X-ray Diffraction (XRD) pattern of HQ-ZFNPs@BSA showing characteristic peaks at 2θ of 29.7°, 35.4°, 43.0°, 53.5°, 56.8°, 62.4° and 74.0°, corresponding to (220), (311), (400), (422), (511), (440) and (533) planes.

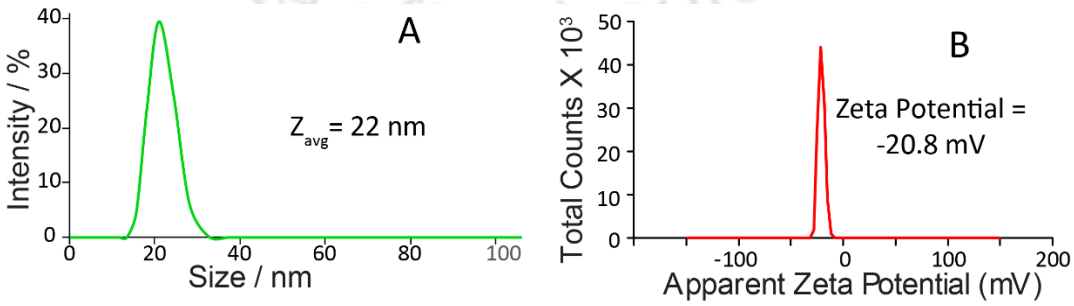

Figure 4.4. (A) Size-distribution of HQ-ZFNPs@BSA dispersed in water as measured by DLS. (B) Zeta potential distribution of aqueous dispersion of HQ-ZFNPs@BSA at physiological pH.

Aqueous dispersion of HQ-ZFNPs@BSA was observed to exhibit strong green fluorescence under ultraviolet (365 nm) irradiation (Figure 4.5 A), whereas individual constituents namely HQ (ethanolic solution) or ZFNPs (hexane dispersion) did not show any noticeable emission under similar conditions (Figure A.4.1, Appendix). Moreover, due to the superparamagnetic nature of core $ZnFe_2O_4$ NPs, HQ-ZFNPs@BSA could be pulled out from aqueous dispersion by the use of a rare earth magnet as shown in Figure 4.5 $A_{3,4}$. It may be mentioned here that the value of saturation magnetization of HQ-ZFNPs@BSA, as determined by vibrating sample magnetometry (VSM) (Figure 4.5 B), was found to be 14.1 emu g^{-1} (at room temperature), which was lower than that recorded with as prepared ZFNPs (23.9 emu g^{-1}), possibly due to the presence of non-magnetic BSA in the former.[6]

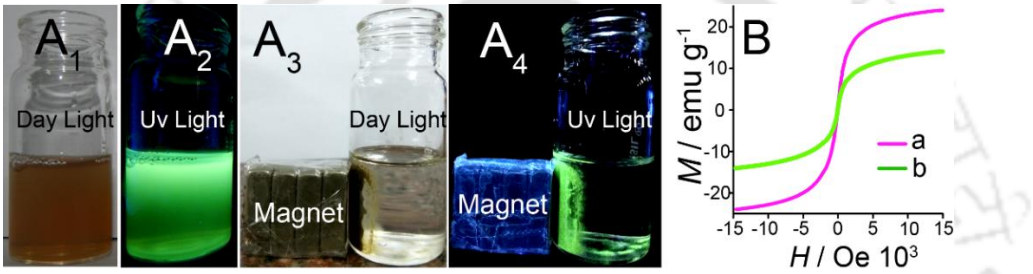

Figure 4.5. (A) Digital photographs of HQ-ZFNPs@BSA dispersed in water in ($A_{1,2}$) absence and ($A_{3,4}$) presence of external magnetic field. (B) VSM based hysteresis study of (a) ZFNPs and (b) HQ-ZFNs@BSA.

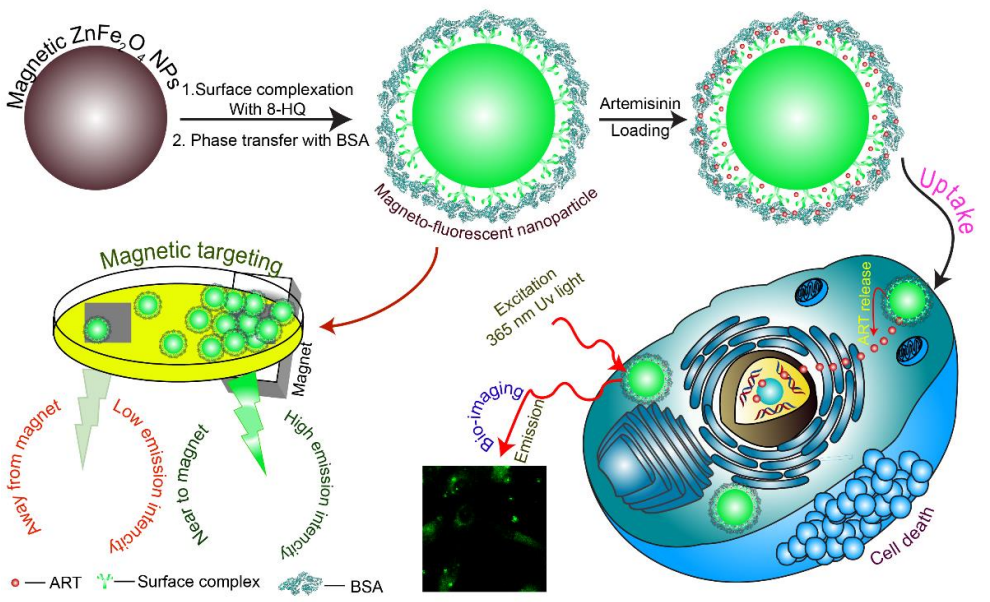

Scheme 4.1. Schematic representation of fabricating HQ-ZFNP-based magneto-fluorescent theranostic nanoparticles, and their use in bioimaging and magnetic targeting *in vitro*. Also depicted is the loading of artemisinin (ART) into BSA-coated HQ-ZFNPs with subsequent delivery of the drug resulting in killing of cancer cells.

HQ has been reported to demonstrate an absorbance peak at 316 nm and a weak emission peak at 520 nm with a quantum yield (QY) of 0.2%.[7] ZFNPs dispersed in hexane, in the present study, were observed not to exhibit any noticeable absorbance peak (Figure 4.6 A). Powder of HQ-ZFNPs showed a weak band around 365 nm in the UV-visible absorption spectrum because of Zn-HQ complex formation onto ZFNPs surfaces, while aqueous solution of BSA showed a strong absorbance peak at 285 nm (Figure 4.6 B, C).[24] Aqueous dispersion of HQ-ZFNPs@BSA also displayed an absorbance band around 365 nm due to the presence of Zn-HQ complexes on the surface of ZFNPs (Figure 4.6A).[6] Fluorescence spectroscopy (Figure 4.6D) revealed negligible emission of ZFNPs (dispersed in hexane) with emission maximum around 423 nm at an excitation wavelength of 365 nm.[4] However, aqueous dispersion of HQ-ZFNPs@BSA showed intense emission with maximum at 503 nm when excited at 365 nm (Figure 4.6D). The emission maxima of HQ-ZNFPs@BSA was observed to be blue-shifted by 15 nm as compared to that of HQ-ZFNPs (emission maxima =518 nm), possibly because of the BSA-coating and solvent (Figure 4.6E).[7] Emission spectrum of aqueous BSA solution showed strong PL emission maximum at 345 nm when excited at 278 nm (Figure 4.6F).[9] The QY of HQ-ZFNPs@BSA was estimated to be 6.3% with respect to quinine sulphate; whereas the value was only 0.53 % for ZFNPs under similar conditions.[4] The excitation spectrum of HQ-ZFNPs@BSA showed a distinct peak at 365 nm (Figure 4.6G).[6-7] HQ-ZFNPs@BSA showed an excited state lifetime of 22.7 ns (Figure 4.6 I) and significantly higher photostability than routinely employed fluorescent dye FITC under continuous irradiation of 365 nm (Figure 4.6H). Additionally, HQ-ZFNPs@BSA was observed to be stable in human blood serum till 24 h (Figure 4.6J), indicating their potential in bio-imaging applications.

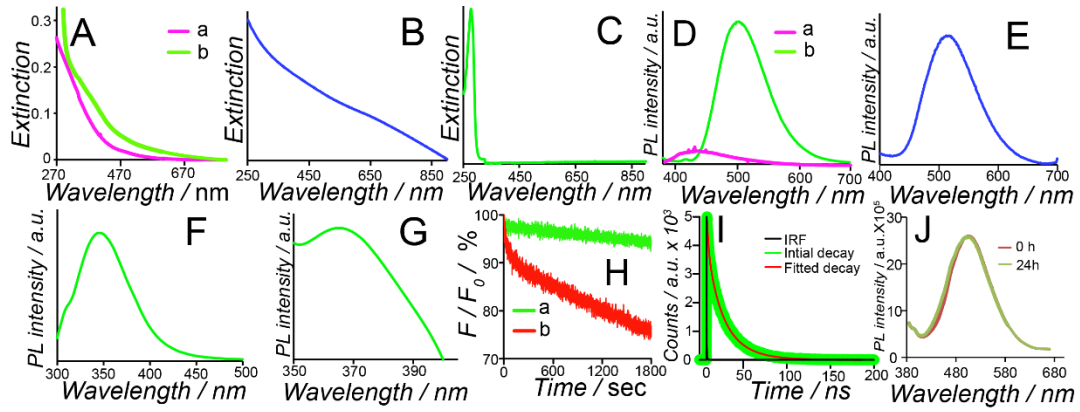

Figure 4.6. (A) UV-vis absorption spectra of (a) ZFNPs and (b) HQ-ZFNPs@BSA. UV-vis spectra of (B) powdered HQ-ZFNPs (C) aqueous solution of BSA. (D) Fluorescence spectra of (a) ZFNPs and (b) HQ-ZFNPs@BSA at excitation of 365 nm. Emission spectra of (E) powdered HQ-ZFNPs with excitation at 365 nm (λem=518 nm) and (F) aqueous solution of BSA with excitation at 278 nm (λem=345 nm) (G) Excitation spectrum of HQ-ZFNPs@BSA. The emission maximum was set at 503 nm. (H) Photostability of (a) HQ-ZFNPs@BSA and (b) FITC. (I) Time-resolved photoluminescence spectrum of HQ-ZFNPs@BSA. (J) Stability of HQ-ZFNPs@BSA in human blood serum measured in terms of fluorescence emission intensity.

The bio-imaging capacity of magneto-fluorescent HQ-ZFNPs@BSA was further explored *in vitro* on HeLa, HepG2 and A375 cells. Briefly, the cells were treated with HQ-ZFNPs@BSA for 2 h, fixed with formaldehyde and imaged under a confocal laser scanning microscope (CLSM) as described in experimental section. As evident from Figure 4.7 bright green fluorescence of HQ-ZFNPs@BSA was observed in all three types of cells following their incubation with the former. The *Z*-stacked images (Figure 4.8) of treated cells in both orthogonal and depth projection lines confirmed the internalization of HQ-ZFNPs@BSA by the cells. Non-treated cells, however, exhibited no such fluorescence under with identical experimental conditions (Figure A.4.2, Appendix) proving the potential of HQ-ZFNPs@BSA as fluorescent bio-imaging agent.[6]

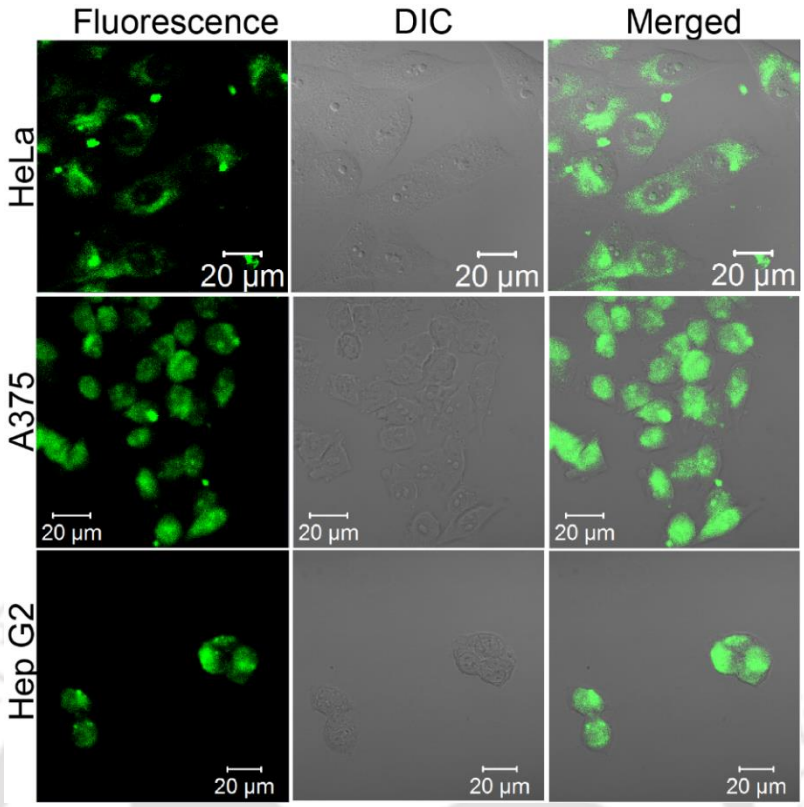

Figure 4.7. CLSM images of HQ-ZFNPs@BSA-treated HeLa, A375 and HepG2 cells irradiated with 355 nm laser.

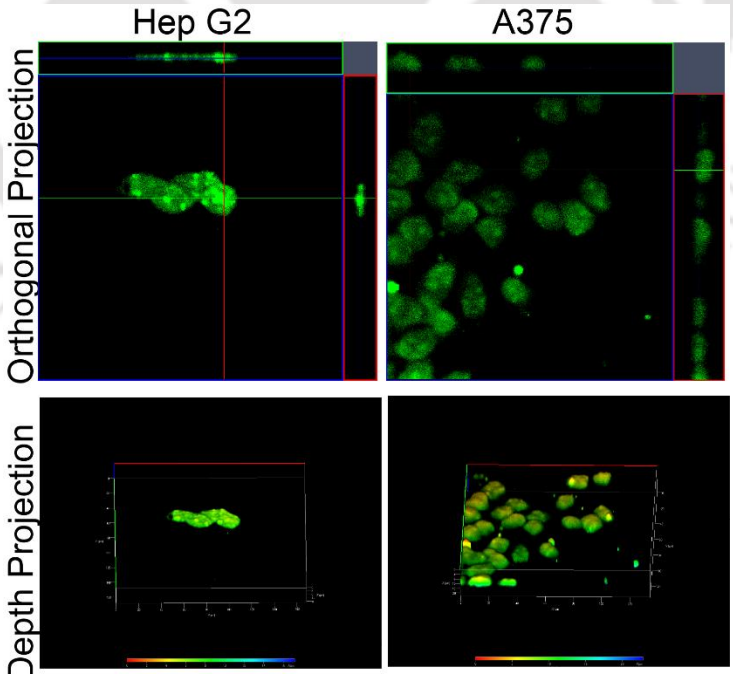

Figure 4.8. CLSM Z-staking images of different cell lines showing internalization of HQ-ZFNPs@BSA.

Superparamagnetic nature of HQ-ZFNPs@BSA was exploited in a prototype experiment in order to demonstrate the prospect of these magneto-fluorescent nanoparticles in possible magnetic-targeting. For this, HeLa cells were grown on two coverslips and then treated with HQ-ZFNPs@BSA, placing a powerful rare-earth magnet under only one of these two coverslips. Following 2 h treatment, cells on both the coverslips were fixed and visualized under CLSM (Figure 4.9) using imaging parameters mentioned above in the experimental section. HeLa cells on the coverslip placed over the magnet demonstrated significantly higher degree of intracellular fluorescence emission as compared to those on coverslip away from the magnet, demonstrating the prospect of HQ-ZFNPs@BSA for magnetic targeting.[6] It may be mentioned here that presence of magnetic field has been reported to slow the growth of cancer cells both *in vitro* and *in vivo* models.[10] Moreover, the anti-cancer efficacy of external magnetic field could dramatically be enhanced with the help of paramagnetic nanoparticles due to the possibility of magnetic hyperthermia of cancer cells.[11] Similarly, magnetic targeting of HQ-ZFNPs@BSA to cancer affected areas followed by magnetic hyperthermia using alternating magnetic field could also lead to efficient eradication of the tumors without affecting the nearby healthy tissues.[11]

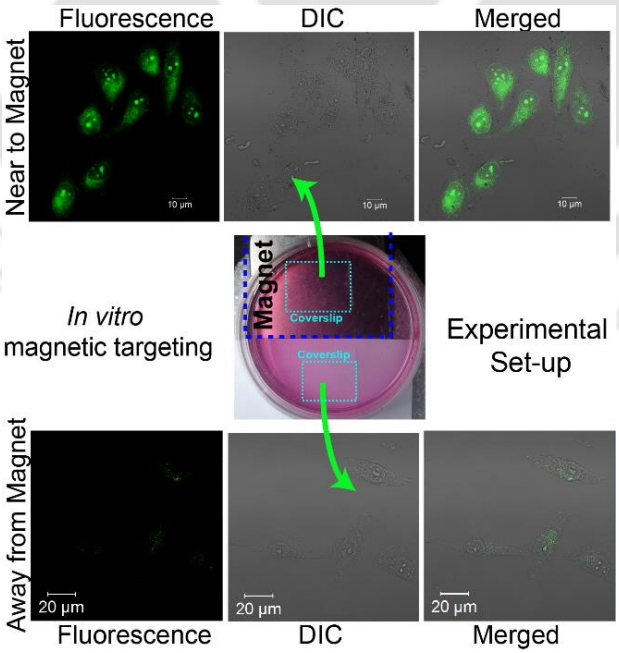

Figure 4.9. Demonstration of *in vitro* magnetic targeting with HQ-ZFNPs@BSA in HeLa cells by CLSM. Experimental setup employed is shown in middle panel. The images of cells on cover slips placed near and far from external magnet are shown in top and bottom panel, respectively.

The encapsulation efficiency of ART was estimated to be 79%. The amount of ART present in 1 mg of drug loaded HQ-ZFNPs@BSA was calculated to be 0.23 μg. The BSA coating around HQ-ZFNPs could play an important role in efficient encapsulation of the hydrophobic drug, ART.[8] The cytotoxicity of ART-loaded HQ-ZFNPs@BSA against cancer cells was assessed by treating various cancer cells with free ART, HQ-ZFNPs@BSA or ART-loaded HQ-ZFNPs@BSA for 24 h and subsequently calculating the cell viability by MTT assay (Figure 4.10). MTT assay revealed that HQ-ZFNPs@BSA, when compared to non-treated control, was able to inhibit the proliferation of cancer cells. In fact, HQ-ZFNPs@BSA demonstrated cytostatic responses in cancer cells with marginal decrease (6.3% in HeLa, 17.2% in A375 and 16.1% in HepG2) in cell viabilities with increasing dosage. Previous studies also reported anti-proliferative and cytostatic nature Fe-HQ complexes.[13-14] Free ART, on the other hand, could not induce significant anti-proliferative response in the cancer cells with mere 14.3% (HeLa), 20.7% (A375) or 12.1% (HepG2) decrease in cell viability even at test concentration as high as 100 μg/mL of the drug.[15-16] Surprisingly, ART, when loaded into HQ-ZFNPs@BSA showed pronounced anti-proliferative response against cancer cells with drastic reduction of % cell viability in a concentration-dependent manner (Figure 4.10). For example, ART-loaded HQ-ZFNPs@BSA decreased the cell viability by 88.7%, 96.8% and 84.5% in HeLa, A375 and HepG2 cells, respectively, at the maximum test concentration of 100 μg/mL. The IC_{50} values of ART-loaded HQ-ZFNPs@BSA were calculated to be 63.0 μg/mL, 70.2 μg/mL and 53.3 μg/mL, respectively, for HeLa, Hep G2 and A375 cell lines. Further analyses based on combination indices (CI) (Table 4.1) and isobologram plot (Figure 4.11) revealed that the anti-proliferative effect of free ART was improved, following its loading into HQ-ZFNPs@BSA, by synergistic mechanism. The CI were as low as 0.01, 0.04 and 0.1 in HeLa, HepG2 and A375 cells, respectively, indicating pronounced synergism of ART and its carrier, HQ-ZFNPs@BSA. On the other hand, although non-cancerous cells namely HEK (human embryonic kidney), L132 (human embryonic lung), and 3T3 (mouse embryonic fibroblast) were observed to respond to HQ-ZFNPs@BSA and ART-loaded HQ-ZFNPs@BSA in a similar fashion as that of cancer cells (Figure 4.10), the corresponding CI values (L132 = 0.82, 3T3= 0.43 and HEK= 0.22) were

much higher than those of tested cancer cells indicating the synergistic killing by ART-loaded HQ-ZFNPs@BSA more efficient in the latter. Nonetheless, further studies with large number of cancer as well as normal cell lines are required in order to comment conclusively on the cancer cell-specific killing of ART-loaded HQ-ZFNPs@BSA.

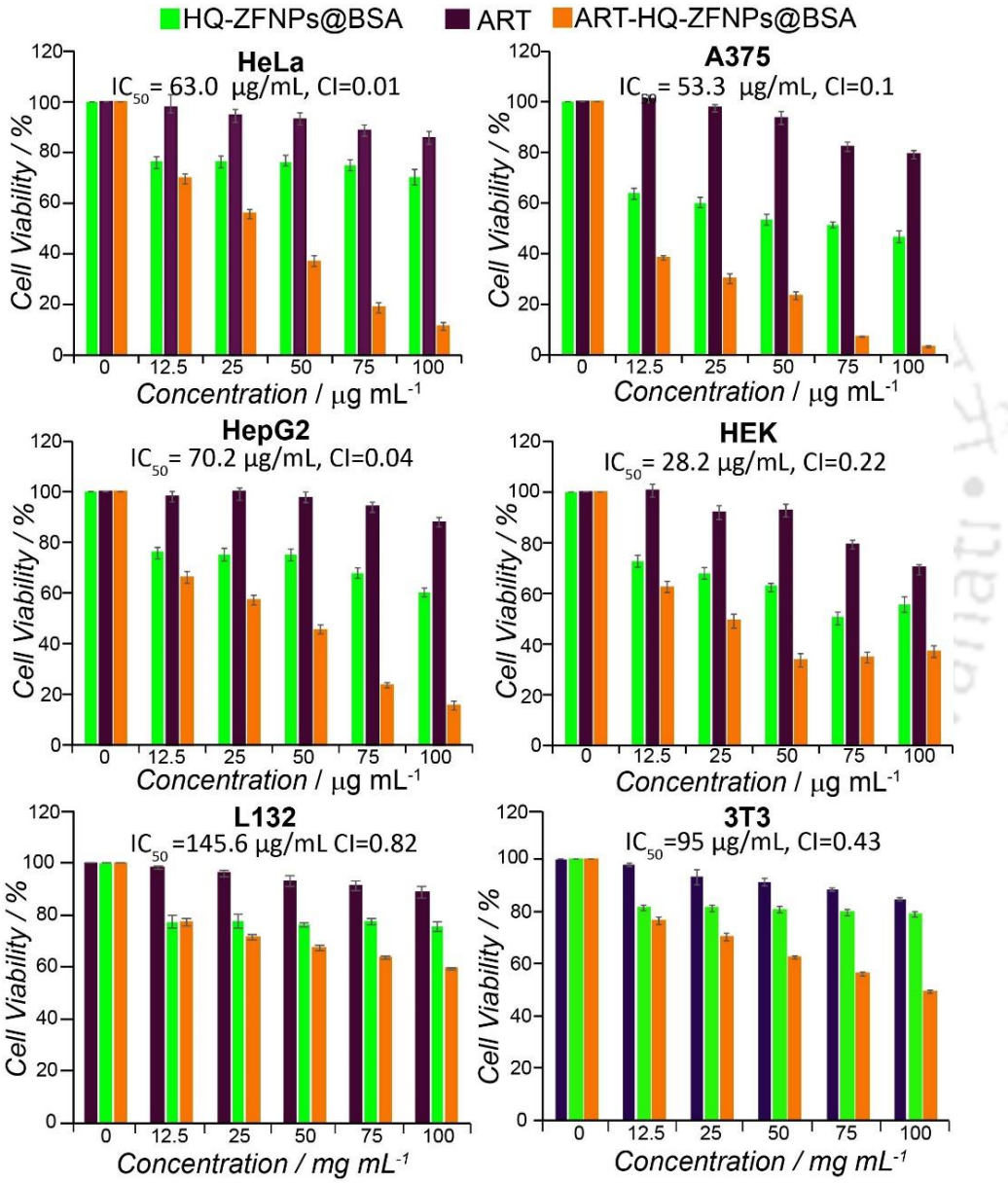

Figure 4.10. MTT-based cell viability of HeLa, HepG2, A375, HEK, L132 and 3T3 cells treated with free ART, HQ-ZFNPs@BSA or ART-loaded HQ-ZFNPs@BSA for 24 h. The IC50 values and combination indices (CI) of ART-loaded HQ-ZFNPs@BSA for each cell line are also mentioned.

Table 4.1. Combination indices of ART-loaded HQ-ZFNPs@BSA in different cell line.

Cell line	Combination Index (CI)
HeLa	0.012
Hep G2	0.036
A375	0.096
HEK	0.22
L132	0.82
3T3	0.43

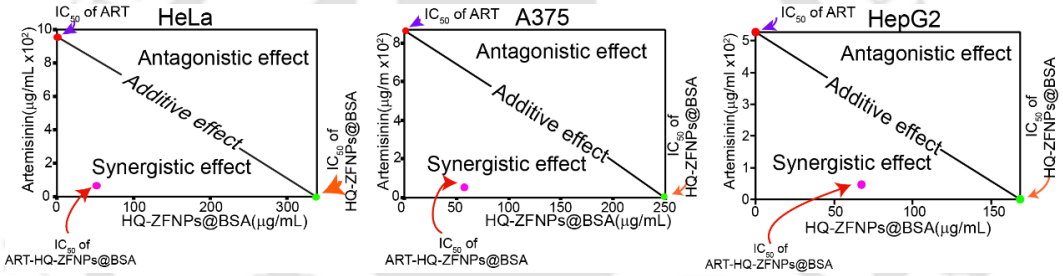

Figure 4.11. Isobologram plots showing synergistic effect of ART loaded HQ-ZFNPs@BSA in HeLa, A375 and HePG2 cells.

This striking enhancement of the anti-proliferative effect of ART could be partially due to the increased bio-availability of the hydrophobic drug due to loading into HQ-ZFNPs@BSA.[17] Besides, as a result of cellular internalization of ART-loaded HQ-ZFNPs@BSA, the Fe^{3+} ions present in ZFNPs would be converted to Fe^{2+} in intra-cellular condition,[16,18] which could activate ART to generate carbon centered radicals and consequent ROS killing cancer cells. To find out the uptake pathway of HQ-ZFNPs@BSA in the present study, HeLa cells were simultaneously treated with HQ-ZFNPs@BSA and 0.1% sodium azide (NaN_3, a known inhibitor of endocytosis).[19] CLSM images, when compared with appropriate control, revealed 89% reduction in PL in HeLa cells co-treated with HQ-ZFNPs@BSA and NaN_3 confirming endocytosis being the preferred uptake route for HQ-ZFNPs@BSA

(Figure 4.12).[19] Moreover, co-localization experiments involving the labeling of lysosomes with LysoTracker (Figure 4.13) successfully demonstrated the presence of HQ-ZFNPs@BSA inside the lysosomes of treated HeLa cells confirming the fusion of HQ-ZFNPs@BSA-containing endosomes with lysosomes.[20] The fact that lysosome has an internal pH of 4.5-5 and oxide type nanoparticles (iron oxide/ zinc ferrite) are known to leach constituent ions at acidic medium could be the main reason behind the Fe^{3+} release from HQ-ZFNPs@BSA inside the treated cells.[17]

Moreover, cancer cells are known to uptake large amount of iron to support their rapid proliferation and thus have higher intracellular iron content as compared to normal cells.[21] The higher basal iron content inside cancer cells could also lead to efficient killing of cancer cells by the present ART-loaded HQ-ZFNPs@BSA. To this end, profiling of various cancer cells in terms of iron content – either through direct quantification of intracellular iron by inductively coupled plasma mass spectrometry (ICP-MS) or via indirect estimation of iron-transporting transferrin receptors[22] – might open up newer strategies for nanoparticle-based formulations of ART including the present one.

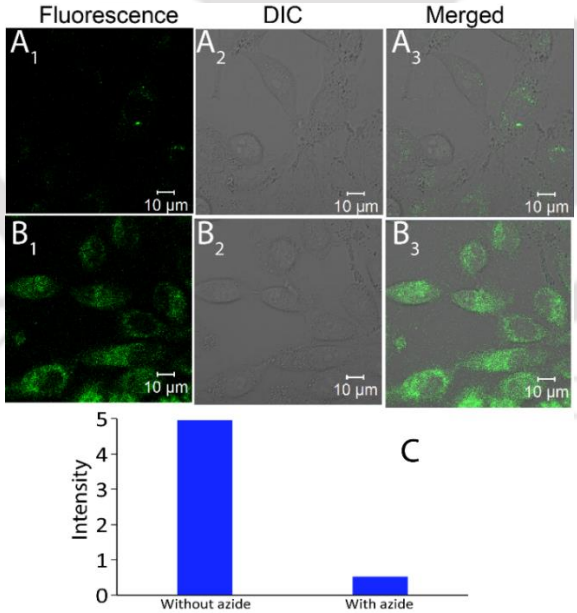

Figure 4.12. CLSM images of HeLa cells treated with HQ-ZFNPs@BSA (A) in presence and (B) in absence of sodium azide (0.1%). (C) PL emission intensity plot calculated from image "A" and "B", showing 89% decrease in PL emission intensity in "A" compared to "B" due to presence of known endocytosis inhibitor sodium azide. Indicating endocytosis as the preferred way of uptake of HQ-ZFNPs@BSA by HeLa cells.

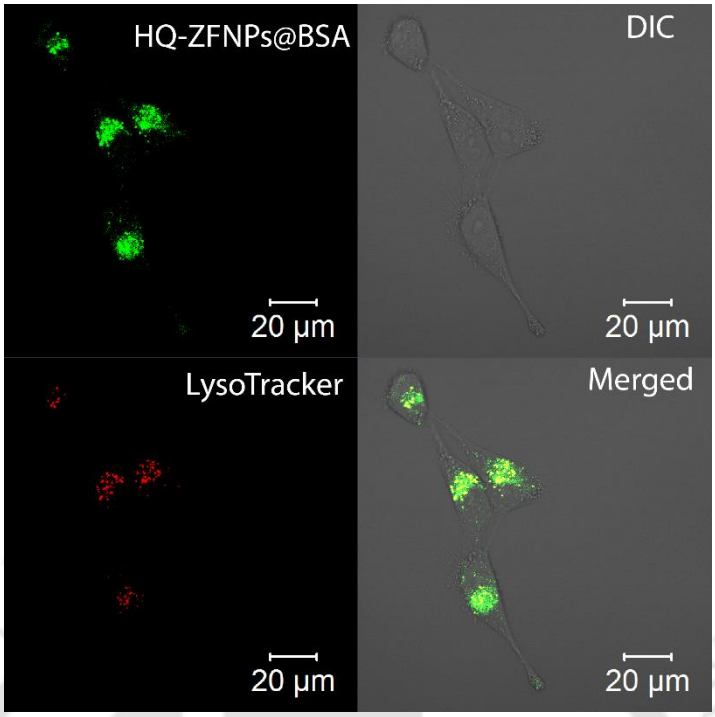

Figure 4.13. CLSM Images of HeLa cells showing co-localization of HQ-ZFNPs@BSA with LysoTracker-labeled lysosomes.

4.3. Conclusion

In conclusion, we have developed a magnetofluorescent nanoparticle (HQ-ZFNPs@BSA) based on the surface complexation of $ZnFe_2O_4$ NP with HQ as complexing ligand. HQ-ZFNPs@BSA demonstrated their capability in bioimaging as well as magnetic targeting *in vitro*. Additionally, HQ-ZFNPs@BSA were able to efficiently encapsulate potential hydrophobic anti-cancer drug ART and dramatically enhance the anti-proliferative efficacy against tested cancer cell lines in a synergistic fashion with CI of 0.1 or less. With appropriate cancer targeting strategy, the potential of multi-modal imaging, magnetic targeting and therapeutic efficacy of ART-loaded HQ-ZFNPs@BSA could certainly be exploited in future cancer theranostics.

References:

1. Xu, Y.; Sherwood, J.; Qin, Y.; Holler, R. A.; Bao, Y. A General Approach to the Synthesis and Detailed Characterization of Magnetic Ferrite Nanocubes *Nanoscale* **2015**, *7*, 12641– 12649.
2. A. Bharati, S.C. Sabat A Spectrophotometric Assay for Quantification of Artemisinin *Talanta,* **82**, 2010, 1033-1037.
3. Khandelia, R.; Bhandari, S.; Pan, U. N.; Ghosh, S. S.; Chattopadhyay, A. Gold Nanocluster Embedded Albumin Nanoparticles for Two-Photon Imaging of Cancer Cells Accompanying Drug Delivery *Small* **2015**,*11*, 4075– 4081.
4. Song, H.; Zhu, L.; Li, Y.; Lou, Z.; Xiao, M.; Ye, Z. Preparation of ZnFe2O4 Nanostructures and Highly Efficient Visible-Light-Driven Hydrogen Generation with the Assistance of Nanoheterostructures *J. Mater. Chem. A* **2015**, *3*, 8353– 8360.
5. Manikandan, A.; Vijaya, J. J.; Sundararajan, M.; Meganathan, C.; Kennedy, L. J.; Bououdina, M. Optical and Magnetic Properties of Mg-Doped ZnFe2O4 Nanoparticles Prepared By Rapid Microwave Combustion Method Superlattices *Microstruct*. **2013**, *64*, 118– 131.
6. Bhandari, S.; Khandelia, R.; Pan, U. N.; Chattopadhyay, A. Surface Complexation-Based Biocompatible Magnetofluorescent Nanoprobe for Targeted Cellular Imaging *ACS Appl. Mater. Interfaces* **2015**, *7*, 17552– 17557.
7. Bhandari, S.; Roy, S.; Chattopadhyay, A. Enhanced Photoluminescence and Thermal Stability of Zinc Quinolate Following Complexation on the Surface of Quantum Dot *RSC Adv.* **2014**, *4*, 24217–24221.
8. Pan, H. C; Liang, F.; Mao, C.; Zhu, J.; Chen, H. Highly Luminescent Zinc(II)-Bis(8-hydroxyquinoline) Complex Nanorods: Sonochemical Synthesis, Characterizations, and Protein Sensing *J. Phys. Chem. B* **2007**, 111,5767– 5772.
9. Wani, T. A.; Bakheit, A. H.; Zargar, S.; Hamidaddin, M. A.; Darwish, I. A. Spectrophotometric and Molecular Modelling Studies on *in vitro* Interaction of Tyrosine Kinase Inhibitor Linifanib with Bovine Serum Albumin. *PLoS ONE* , **2107,** *12*, 176015-176027.
10. Sengupta, S.; Balla, V. K. A Review on the Use of Magnetic Fields and Ultrasound for Non-invasive Cancer Treatment *J. Adv. Res.* **2018,** *14,* 97-111.
11. Hajipour, M.J.; Akhavan, O.; Meidanchi, A.; Laurent, S.; Mahmoudi, M. Hyper thermia-Induced Protein Corona Improves the Therapeutic Effects of Zinc Ferrite Spinel-Graphene Sheets against Cancer *RSC Adv.***2014**, 4, 62557– 62565.

12. Liu, R.; Cheng, Z.; Jiang, X. Comparative Studies on the Interactions of Dihydroartemisinin and Artemisinin with Bovine Serum Albumin Using Spectroscopic Methods. *Luminescence* **2014**, *29*, 1033–1046.
13. Oliveri, V.; Vecchio, G. 8-Hydroxyquinolines in Medicinal Chemistry: a Structural Perspective *Eur. J. Med. Chem.,* **2016**, *120*, 252-274.
14. Prachayasittikul, V.; Prachayasittikul, S.; Ruchirawat, S.; Prachayasittikul, V . 8-Hydroxyquinolines: A Review of Their Metal Chelating Properties and Medicinal Applications *Drug Des., Dev. Ther.* **2013**, 7, 1157– 1178.
15. Wong, Y. K.; Xu, C.; Kalesh, K. A.; He, Y.; Lin, Q.; Wong, W. S. F.; Shen, H.-M.; Wang, J. Artemisinin As an Anticancer Drug: Recent Advances in Target Profiling and Mechanisms of Action. *Med Res Rev* 2017; **37**: 1492–1517.
16. Wang, D. D.; Zhou, J. J.; Chen, R. H.; Shi, R. H.; Wang, C. L.; Lu, J.; Zhao, G. Z.; Xia, G. L.; Zhou, S.;Liu, Z. B.; Wang, H. B.; Guo, Z.; Chen, Q. W. Core-shell Metal-Organic Frameworks as Fe^{2+} Suppliers for Fe^{2+}-Mediated Cancer Therapy Under Multimodality Imaging *Chem. Mater.* **2017**, *29,* 3477–3489.
17. Chen, J.; Guo, Z.; Wang, H.; Zhou, J.; Zhang, W.; Chen, Q. Multifunctional Mesoporous Nanoparticles as pH-Responsive Fe^{2+} Reservoirs and Artemisinin Vehicles for Synergistic Inhibition of Tumor Growth *Biomaterials* **2014**, *35*, 6498– 6507.
18. Knutson, M. D. Iron Transport Proteins: Gateways of Cellular and Systemic Iron Homeostasis. *J Biol Chem.* **2017**, *4*, 292(31), 12735-12743.
19. Dutta, A.; Dutta, D.; Sanpui, P. Chattopadhyay, A. Biomimetically crystallized protease resistant zinc phosphate decorated with gold atomic clusters for bioimaging *Chem. Commun*. **2017**, *53*, 1277-1280.
20. Oh, N.; Park, J. H. Endocytosis and Exocytosis of Nanoparticles in ammalian Cells *Int. J. Nanomed.* **2014**, *9* 51– 63.
21. Wong, Y. K.; Xu, C.; Kalesh, K. A.; He, Y.; Lin, Q.; Wong, W. S. F.; Shen, H.-M.; Wang, J. Artemisinin As an Anticancer Drug: Recent Advances in Target Profiling and Mechanisms of Action. *Med Res Rev* 2017; **37**: 1492–1517.
22. Garcı ´a, J. A.; Ferna´ndez, D. T.; A´lvarez, E. A.; Gonza´lez, E. B.; Montes-Bayo´n, M.; Sanz-Medela, A. Iron Speciation, Ferritin Concentrations and Fe : Ferritin Ratios in Different Malignant Breast Cancer Cell Lines: on the Search for Cancer Biomarkers *Metallomics,* **2016,** *8,* 1090-1096.

CHAPTER 5

Surface Complexed-Zinc Ferrite Magnetofluorescent Nanoparticles for Killing Cancer Cells and Single Particle Level Cellular Imaging

In this chapter fabrication of novel magnetofluorescent nanoparticles by complexation of zinc ions present on the surface of zinc ferrite nanoparticle ($ZnFe_2O_4$ NP) with 8-hydroxy-2-quinolinecarboxaldehyde (HQCald) is reported. The as prepared HQCald-complexed $ZnFe_2O_4$ NPs showed good quantum yield (3.62%), high photostability, considerable excited state lifetime (5.31 ns) and high saturation magnetization (12.7 emu g^{-1}). These magnetofluorescent nanoparticles demonstrated bioimaging capability both at the ensemble and single particle levels, and *in vitro* magnetic targeting. Moreover, the pronounced anti-proliferative efficacy of these nanoparticles against cancer cells, with appropriate targeting strategies, can lead to potential cancer theranostics.

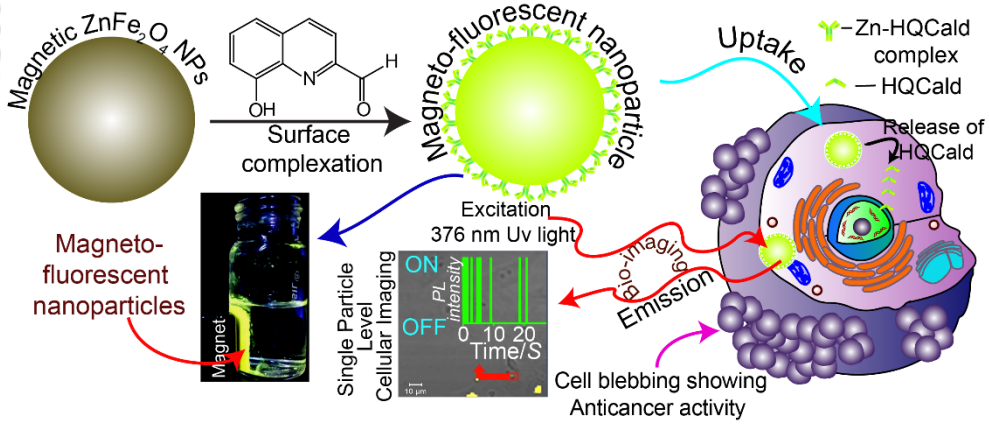

***[ACS Appl. Nano Mater. 2018, 1, 2496−2502.] - Reproduced with permission from the American Chemical Society.**

5.1 Experimental Section

5.1.1 Materials: Iron (III) chloride hexahydrate ($FeCl_3.6H_2O$), 1-octadecene, trioctylphosphine oxide (TOPO), sodium oleate, 8-hydroxy-2-quinolinecarboxaldehyde (HQCald), quinine sulphate and fluorescein isothiocyanate isomer I (FITC) were acquired from sigma aldrich USA. Zinc chloride dry ($ZnCl_2$), oleic acid, hexane, dimethyl sulfoxide (DMSO), bovine serum albumin (BSA) were bought from Merck, India. 3-(4,5-dimethylthiazol-2-yl)-2,5-diphenyltetrazolium bromide (MTT) were acquired from Himedia, India. Green fluorescencent lysosomal staining kit (LysoTracker) were purchased from abcam. Ethanol were acquired from Tedia USA. All chemicals were used without further purification. Milli-Q grade water was used in all the experiments.

5.1.2 Preparation of Zinc Ferrite Nanoparticles (ZFNs):

5.1.2.1 Preparation of mixed Zinc (II) and Iron (III) oleate complexes (Zn:Fe=1:2): To synthesize zinc ferrite nanoparticles ($ZnFe_2O_4$ NPs), precursor zinc (II) and iron (III) oleate complex mixture of molar ratio 1:2 were prepared. Briefly, 26.8 mmol of $FeCl_3.6H_2O$, 13.4 mmol of $ZnCl_2$ and 36.5 g sodium oleate were added in a solvent mixture containing 30 mL water, 40 mL ethanol and 70 mL hexane. The resulting mixture was stir-mixed thoroughly and refluxed under stirring for 4 h at 70°C. At the end of the reaction brown colored mixture of two oleate complexes were separated from upper hexane layer and washed vigorously with ethanol and water mixture to remove *free oleate.*[1]

5.1.2.2 Thermal decomposition of mixed Zn (II) and Fe (III) oleate complexes to prepare $ZnFe_2O_4$ NPs (ZFNs): $ZnFe_2O_4$ NPs (ZFNs) were synthesized by thermal decomposition of mixed Zinc (II) and Iron (III) oleate complexes (1:2). Briefly, 300 mg of as prepared mixed Zinc (II) and Iron (III) oleate complexes, 50 µL of oleic acid and 25 mg of TOPO were mixed in 10 mL of 1-octadecene and refluxed at 120 °C for 1 h. This resulted in change of color of the solution to black. Then temperature was first increased to 200°C, nitrogen gas purged through it and further heated at 310°C for 2 h. After completion of reaction $ZnFe_2O_4$ NPs

were washed with ethanol and hexane solvent mixture for 5 times and finally redispersed in 500 mL hexane.[1]

5.1.3 Preparation of 8-Hydroxy-2-quinolinecarboxaldehyde (HQCald) solution: 20 mM solution of HQCald were prepared by dissolving HQCald powder in ethanol under 2 min sonication.

5.1.4 Preparation of HQCald-ZFNs: 2 mL dispersion of as prepared $ZnFe_2O_4$ NPs (in hexane) was first diluted with additional 8 mL of hexane. Then 50 µL of 20 mM ethanolic solution of HQCald was added to it and sonicated for 1 minute. After completion of complexation, $ZnFe_2O_4$ NPs with surface complexed HQCald (HQCald-ZFNs) were separated with magnet and the washed three times with hexane-ethanol mixture following magnetic separation. Finally HQCald-ZFNs were dispersed in 1% BSA solution under sonication for 3 h then again washed twice with water following magnetic separation and finally dispersed in 1% aqueous BSA solution and stored at 4°C for further use.

5.1.5 Quantification of HQCald present in HQCald-ZFNs: A calibration curve was obtained by mixing different amount of ethanolic solution of HQCald in hexane followed by measuring their absorbance at 374 nm. In all the solutions of different concentrations of HQCald the ratio of hexane and ethanol were kept fixed according with the supernatant remained after the magnetic separation of HQCald-ZFNs from a mixture of ZFNs and HQCald. Following complexation of HQCald with ZFNs and subsequent magnetic separation of HQCald-ZFNs, the absorbance of the supernatant was compared with the calibration curve to determine the amount of HQCald complexed onto ZFNs. It was determined that 121 µg of HQCald was complexed to 1 mg of HQCald-ZFNs.

5.1.6 Photostability study: Photostabilities of HQCald-ZFNs and fluorescein isothiocyanate isomer I (FITC) were studied in HORIBA JobinYvon FluoroMax-4 spectrofluorimeter. Aqueous dispersion of HQCald-ZFNs and ethanolic solution of FITC were irradiated continuously with 376 nm light and fluorescence emission intensity were recorded upto1800 s with an interval of 0.1 s.

5.1.7 Quantum Yield calculation (QY): Quantum yield was calculated with respect to the reference dye quinine sulphate. Quinine sulphate solution was prepared in 0.1 M H_2SO_4. The following formula is used to calculate the quantum yield of HQCald-ZFNs.

$$Q_s = Q_R \times \frac{I_s}{I_R} \times \frac{A_R}{A_S} \times \frac{\eta_S^2}{\eta_R^2}$$

Where, Q_S is the QY of sample, Q_R is the QY of quinine sulphate, I_S is the area under emission spectrum of sample, I_R is the area under emission spectrum of quinine sulphate, A_R is the absorbance of the quinine sulphate, A_S is the absorbance of the sample, η represents refractive index of the solvent suffix S and R represent sample and reference. Refractive Index of water is 1.33. Q.Y. of quinine sulphate is 0.54 (54 %).

5.1.8 Cell viability assay: Human hepatocyte carcinoma (HepG2), cervical cancer (HeLa) and malignant melanoma (A375) cell lines were purchased from National Center for Cell Sciences (NCCS), Pune, India. All the cells were grown under in humidified 5% CO_2 incubator at 37 °C. Dulbecco's modified Eagle's medium (DMEM) with 10% (v/v) fetal bovine serum (FBS) and Penicillin-Streptomycin (100 U mL^{-1}) were used as culture medium. MTT (3-(4,5-dimethylthiazol-2-yl)-2,5-diphenyltetrazolium bromide) based cell viability assay were performed using 5000 cells in quadrate for each test concentration in 96-well cell culture plates. Subsequently, cells were treated with different concentration of HQCald-ZFNs, $ZnFe_2O_4$ NPs (transferred to water using BSA) and HQCald for 48 h. Then media were removed, the purple colored Fromazane product of MTT dissolved in DMSO and absorbance at 570 nm were measured in a Bio-Rad 680 microplate reader with reference absorbance at 655 nm. Cell viability were calculated flowing the formula,

$$\mathrm{Cv}(\%) = \{\frac{\mathrm{Abs\ (T)}}{\mathrm{Abs\ (C)}}\} \times 100$$

Where Cv is the cell viability, Abs (T) absorbance of treated sample, Abs (C) absorbance of non-treated control sample.

***5.1.9 Sample preparation for bioimaging*:** Coverslips were first placed at the bottom of the petri plate and 3×10^5 numbers of cells of HeLa, HepG2 or A375 cells were grown on the coverslips for 24 h. Then the cells were treated with 150 µg/mL of HQCald-ZFNs for 2 h. After treatment, cells were washed vigorously with PBS, fixed with 1% formaldehyde for 10 min and then kept in chilled ethanol for additional 10 min. After washing with PBS coverslips were mounted on a glass slide using glycerin as mounting agent. Finally the cells were imaged in Carl Zeiss laser scanning electron microscope LSM 880. For fluorescence images 355 nm laser was used while 488 nm Ar ion laser used as transmitted light source.

To show the presence HQCald-ZFNs within the lysosomes, HeLa cells were grown on coverslip (as described above) and then the cells were treated with a mixture of HQCald-ZFNs (150µg/mL) and green fluorescent LysoTracker (2µL/mL) for 2h. After the completion of treatment cells were washed 3 times with PBS and fixed following the same protocol described above. CLSM images were then taken using 355nm and 488nm laser. For better visibility (especially in the merged image) pseudo *blue* color is used to label LysoTracker's emission.

5.1.10 Single Particle imaging: HQCald-ZFNs and Zn-HQCald samples were prepared by drop casting on a 0.17 mm coverslip. HeLa cells sample were prepared by treating HeLa cells with 1.5 µg/mL HQCald-ZFNs and then cells were fixed with formaldehyde (following the above protocol). Samples were visualized under Carl Zeiss LSM-880 super resolution confocal laser scanning microscope with 355nm excitation having maximum power 63 mW. Plan-Apochromat, 63x /1.40, oil- immersion objective, GaAsP detector and Airyscan detector were used to visualize single particle and to collect the emission spectrum of the single particles. The blinking profiles were recorded with frame size 64 × 64 μm^2.

5.1.11 Magnetic targeting: Two coverslips were placed opposite to each other in a 60 mm petri plate. 3×10^5 HeLa cells were then grown on the coverslips for 24 h. A strong rare-earth magnet were placed at the bottom of one of the coverslips such that the other coverslip stay away from the magnet. Then the cells were treated with 150 µm/mL HQCald-ZFNs for 2 h. Subsequently, cells were washed, fixed and mounted as described before. Cells were visualized and images were captured in Carl Zeiss laser scanning electron microscope LSM 880 with an excitation of 355 nm laser source. DIC images were taken under 488 nm argon ion laser as transmitted light source.

5.2 Results and Discussion

Superparamagnetic $ZnFe_2O_4$ NPs (ZFNs) having an average size of 6 ±1.3 nm (Figure. 5.1A-B) were prepared by thermal decomposition of mixed oleate complexes of Fe and Zn as described in the experimental section.[1-2] High resolution TEM (HR-TEM) images with corresponding inverse fast Fourier transform (IFFT) and selected area diffraction (SAED) patterns (Figure. 5.1C-E) confirmed the formation of ZFNs by revealing characteristic lattice fringes due to (311) and (440) planes of face-centered cubic (FCC) $ZnFe_2O_4$ NPs.[1] Moreover, powder XRD pattern of $ZnFe_2O_4$ NPs (Figure. 5.1F) also demonstrated characteristic peak at 2θ of 30.0°, 35.4°, 43.1°, 53.6°, 56.8°, 62.4° and 74.0°, originating from (220), (311), (400), (422), (511), (440) and (533) planes.[3]

In normal spinal structure of $ZnFe_2O_4$ NPs, Zn^{2+} ions occupy tetrahedral sites while alternate octahedral sites are taken up by Fe^{3+} ions.[3-4] The Zn^{2+} ions present on the surface of $ZnFe_2O_4$ NPs have the capacity to form complex with HQ and its derivatives.[5-6] Surface complexation of these Zn^{2+} ions in the present work was performed by adding ethanolic solution of HQCald to $ZnFe_2O_4$ NPs (dispersed in hexane) under gentle sonication as described in the experimental section.

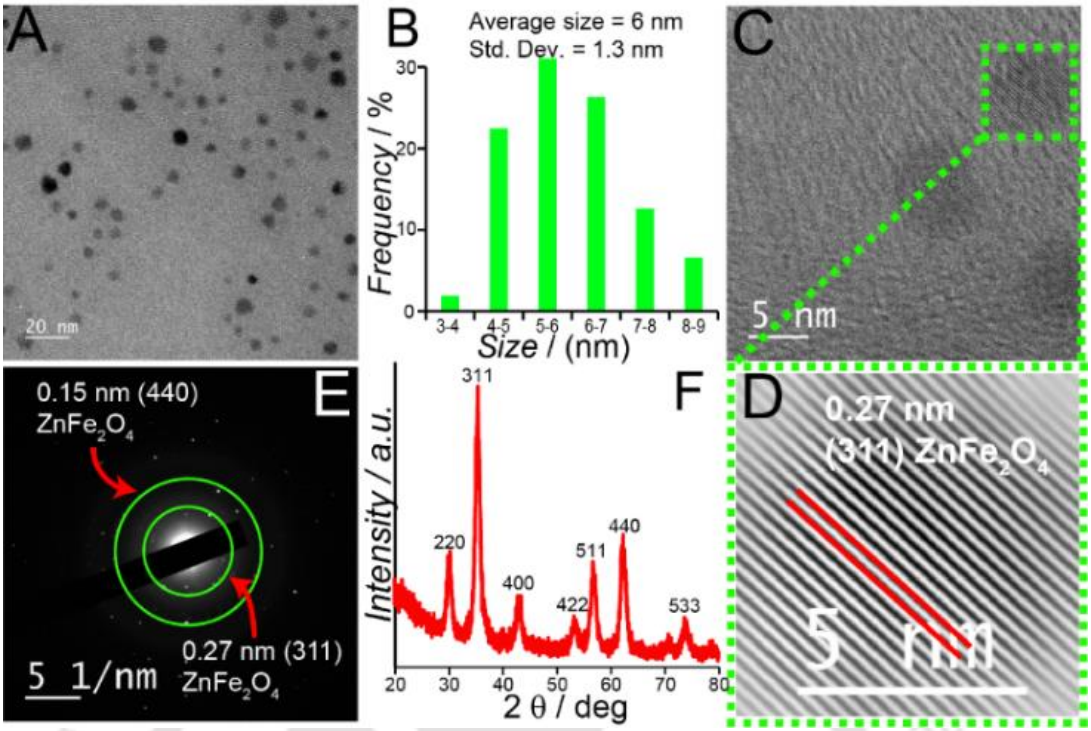

Figure 5.1. (A) TEM images of $ZnFe_2O_4$ NPs. (B) Size distribution of $ZnFe_2O_4$ NPs calculated based on 233 nanoparticles. (C) HRTEM of $ZnFe_2O_4$ NPs and (D) IFFT pattern of corresponding NP. (E) SAED pattern of $ZnFe_2O_4$ NPs. (F) Powder XRD pattern of $ZnFe_2O_4$ NPs and showing characteristic peaks for (220), (311), (400), (422), (511), (440), (533) planes.

Following complexation reaction, $ZnFe_2O_4$ NPs with surface-complexed HQCald (referred as HQCald-ZFNs) were thoroughly washed with hexane-ethanol mixture to remove unreacted ligands and detached stabilizers. Successful surface-complexation was confirmed by FTIR analysis of HQCald-ZFNs, which revealed characteristic peaks at 1702 cm^{-1}, 1605 cm^{-1}, 1577 cm^{-1}, 1502 cm^{-1}, 1470 cm^{-1}, 1330 cm^{-1}, 830 cm^{-1}, 745 cm^{-1}, 605 cm^{-1} due to HQCald (Figure. 5.2, Table 5.1). The generation of a new peak at 1110 cm^{-1} also indicated formation of Zn-$(HQCald)_2$ type complexes on the surface of ZFNs (Figure. 5.2).[5-8] As prepared HQCald-ZFNs were found to be poorly dispersible in water, possibly due to insolubility of Zn-HQCald complexes in water[7,9] However, water-dispersability of as prepared HQCald-ZFNs was achieved by coating them with BSA taking advantage of the strong interaction between HQ-Zn complexes and BSA.[8]

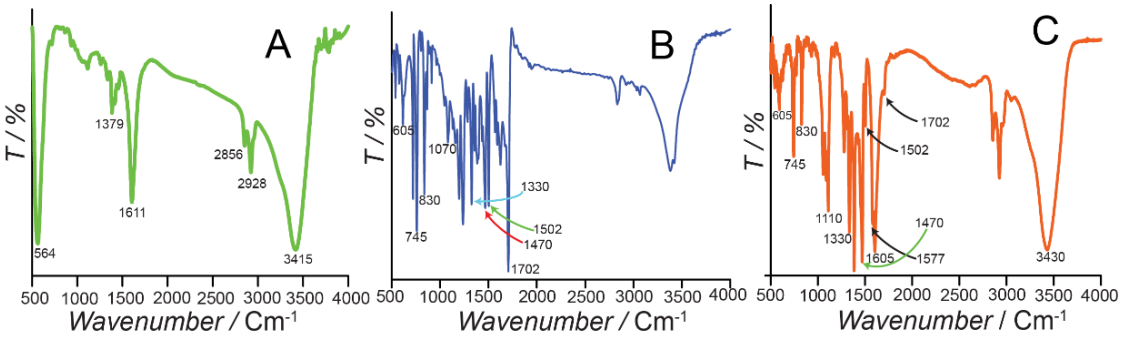

Figure 5.2. FTIR spectra of (A) $ZnFe_2O_4$ NPs and (B) HQCald (C) HQCald-ZFNs showing characteristic peaks.

Table 5.1. Representing FTIR peak values with corresponding functional groups.

Wave number (Cm^{-1})	Functional group
1702	C=O stretching of -CHO
1605	C-C or C-N bond stretching
1577	C-C or C-N bond stretching
1502	Pyridyl group of HQcald
1470	Phenyl group of HQCald
1330	C-H bending
1110	-C-O-Zn bond Stretching
830	C-H bond out of plane wagging
745	C-H out plane wagging in plane ring deformation
605	in-plane ring deformation

TEM images of HQCald-ZFNs showed particles with an average size of 6 ±1.1 nm indicating no changes in the sizes of core $ZnFe_2O_4$ NPs following surface complexation (Figure 5.3 A, B). HR-TEM images of HQCald-ZFNs, and corresponding IFFT and SAED patterns (Figure. 5.3 C, D, E) revealed characteristic lattice fringes due to (311) and (440) planes of fcc $ZnFe_2O_4$.[1] Energy-dispersive X-ray spectroscopy (EDX) from TEM also confirmed the presence of both Zn and Fe in HQCald-ZFNs (Figure A.5.1, Appendix). Moreover, powder XRD pattern of HQCald-ZFN demonstrated characteristic peaks of (220), (311), (400), (422), (511), (440), (533) planes of crystalline $ZnFe_2O_4$ NPs.[3] (Figure. 5.3, F) Taken

together, XRD and HRTEM analyses demonstrated that the overall size as well as crystallinity of the core $ZnFe_2O_4$ NPs remained unaffected following surface complexation with HQCald.[5-7]

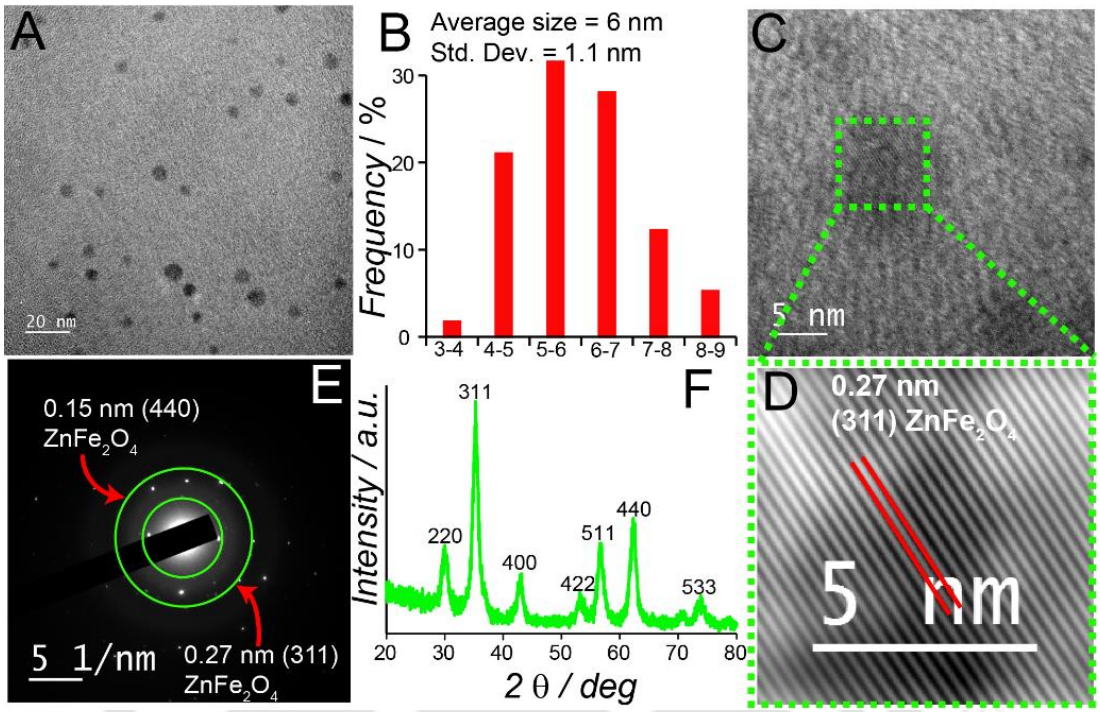

Figure 5.3. (A) TEM images of HQCald-ZFNs (B) Size distribution of HQCald-ZFNs calculated based on 144 nanoparticles. (C) HRTEM of HQCald-ZFNs and (D) IFFT pattern of corresponding NP. (E) SAED pattern of HQCald-ZFNs. (F) Powder XRD pattern of HQCald-ZFNs and showing characteristic peaks for (220), (311), (400), (422), (511), (440), (533) planes.

HQCald in the present study was found to exhibit strong absorption at 374 nm. Although ZFNs dispersed in hexane did not show any noticeable absorption maxima, aqueous dispersion of HQCald-ZFNs was observed to demonstrate absorption band around 402 nm (Figure. 5.4 A) possibly due to the formation of Zn-HQCald complex on the surface of ZFNs. The water dispersed HQCald-ZFNs, when irradiated with UV light, showed strong yellow PL (Figure. 5.4 B). It may be noted here that neither $ZnFe_2O_4$ NPs nor HQCald individually exhibited any noticeable PL (Figure A.5.2, Appendix).[10-11] Moreover, HQCald-ZFNs could easily be separated from aqueous dispersion by simply using an external magnet

(Figure. 5.4 C). Further spectroscopic analyses revealed intense PL emission of HQCald-ZFNs with λ_{max} around 524 nm when excited at 376 nm (Figure. 5.4 D). PL excitation spectrum of HQCald-ZFN showed a clear peak at 376 nm (Figure. 5.4 E). The PL quantum yield (QY) of HQCald-ZFNs with respect to quinine sulphate was estimated to be 3.62%. On the other hand, $ZnFe_2O_4$ NPs was found to be weakly luminescent with emission maxima around 423 nm and QY of 0.5% (Figure. 5.4 D).[10-11] HQCald demonstrated negligible luminescence (QY = 0.2%) with λ_{max} emission at 536 nm under similar conditions. In addition to strong PL, HQCald-ZFNs were observed to be highly photostable when compared to commonly use organic dye fluorescein isothiocyanate isomer I (FITC) (Figure. 5.4 F). It also exhibited an excited state lifetime of 5.31 ns (Figure. 5.4 G). HQCald-ZFNs were also stable in human serum upto 24 h as indicated by the unchanged PL intensity over the test period (Figure 5.4 H). Overall, the PL characteristics of HQCald-ZFNs demonstrated appropriate intensity as well as stability often desirable of a potential bioimaging probe.

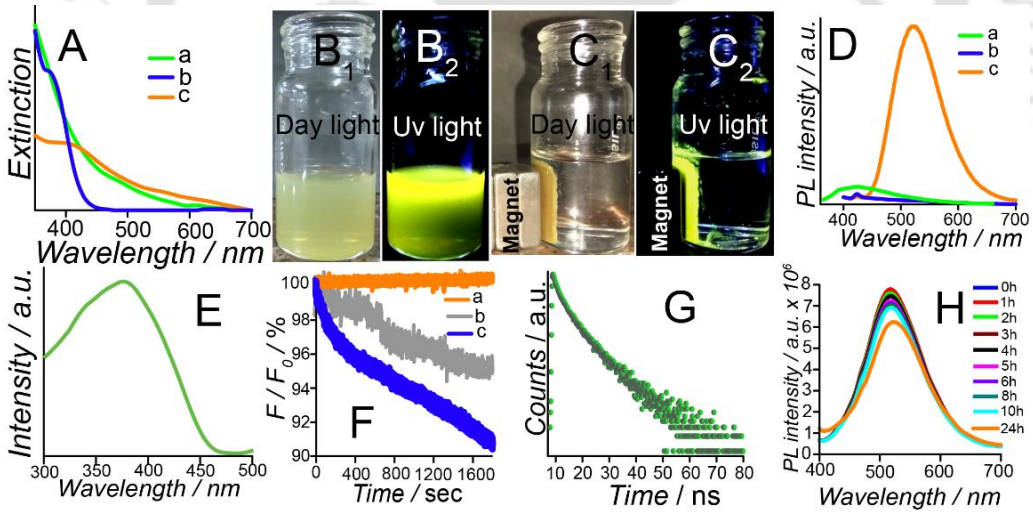

Figure 5.4. (A) UV-vis absorption spectra of (a) $ZnFe_2O_4$ NPs, (b) HQCald and (c) HQCald-ZFNs. (B) Digital photographs of HQCald-ZFNs dispersed in water. (C) Digital photographs of HQCald-ZFNs in presence of external magnetic field. (D) Emission spectra of (a) $ZnFe_2O_4$ NPs, (b) HQCald and (c) HQCald-ZFN at excitation of 376 nm. (E) Excitation spectrum of HQCald-ZFNs (λ_{max}~ 376 nm) (F) Photostability of (a) HQCald-ZFN (b) Zn-HQCald and (c) FITC under irradiation of 376 nm light. (G) Time-Resolved Photoluminescence spectrum of HQCald-ZFNs. (H) Stability of HQCald-ZFNs in human blood serum measured in terms of PL emission intensity with time.

Single particle level measurement of HQCald-ZFNs acquired in super resolution CLSM at 355 nm excitation showed emission spectrum similar to that of the aqueous dispersion of HQCald-ZFNs (Figure 5.5 A). Blinking property and Airy disk based point-spread-function distribution confirmed the possible single particle nature of the HQCal-ZFNs (Figure. 5.5 B, C, D).[12] Careful study of the blinking profile of a HQCald-ZFN single particles showed a significant increase in ON state (93%), compared to a Zn-HQcald complex (5%) at single particle level and thus validating the potential of HQCald-ZFNs for use in single particle level bioimaging (Figure. 5.5 B,E).[13]

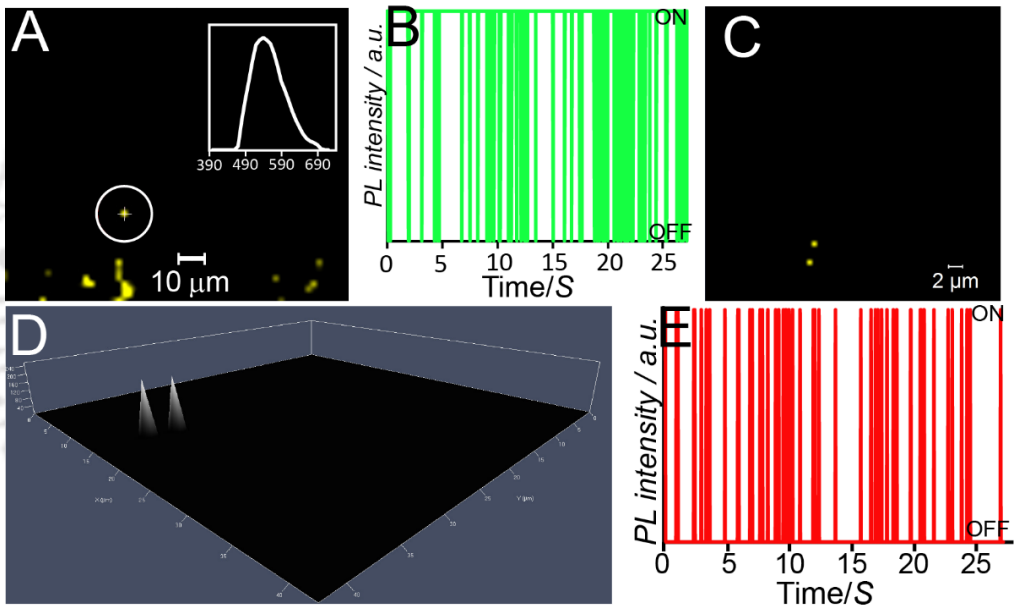

Figure 5.5. (A) Super resolution CLSM images of single HQCald-ZFN nanoparticles, corresponding emission spectrum (inset) of the encircled single particle at 355 nm excitation. (B) Blinking profile of single HQCald-ZFN nanoparticle. (C) Single particle images of HQCald-ZFNs and (D) corresponding point-spread-function profile. (E) Blinking profile of single Zn-HQCald complex.

The robust PL of HQCald-ZFN was further explored in bioimaging of cancer cells in ensemble and single particle level. In this regard, three types of cancer cell lines namely HeLa (cervical), HepG2 (liver), and A375 (skin) and one normal cell line HEK 293 (embryonic kidney) were incubated with HQCald-ZFN for 2 h and

subsequently observed under confocal laser scanning microscope (CLSM) with 355 nm laser as the excitation source (as described in the experimental section). As is evident from CLSM images (Figure 5.6, 5.7 A.5.3-5, Appendix), all three types of cancer cells and the one normal cell demonstrated bright yellow color following treatment with HQCald-ZFNs indicating bio-labeling capability of the later. Further Z-stacking analyses with corresponding orthogonal and depth projection of CLSM images (Figure 5.8) confirmed the internalization of HQCald-ZFNs by the cancer and normal cells. Additionally, non-treated control cells did not show such emission under CLSM (Figure A.5.6-7, Appendix) establishing the potential of HQCald-ZFNs as a probe for imaging cancer cells. Possible single particle level imaging of HQCald-ZFN present inside HeLa cells was recorded by incubating the cells with HQCald-ZFN for 2 h as described in the experimental section. Cells were then visualized under CLSM (λ_{ex}=355nm). Distinct single particle level blinking behavior of HQCald-ZFN was observed when present inside the cells. (Figure.5.9). Blinking profile of the HQCald-ZFN present inside the HeLa cell (cervical cancer cells) showed a reduction of *ON* state (to 4%) compared to free HQCald-ZFN possibly due to interaction with cellular components.[14] Whereas single HQCald-ZFN present inside human embryonic kidney cells (HEK 293), a normal cell line showed *ON* state of ~ 10% (Figure.5.9) This single particle level imaging study may open up possibility for intracellular level sensing as a diagnostic tool.[14-16]

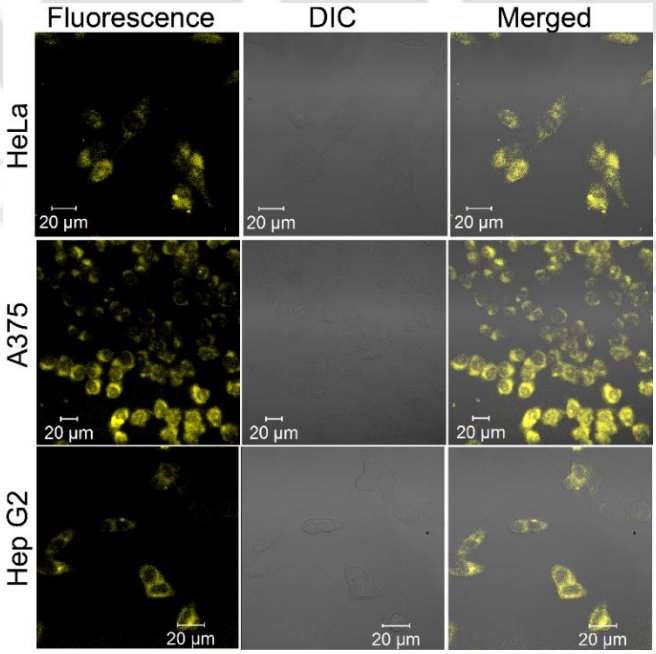

Figure 5.6. Confocal laser scanning microscopy images of HeLa, A375, and HepG2 cells treated with HQCald-ZFNs for 2 h and then irradiated with 355 nm laser source.

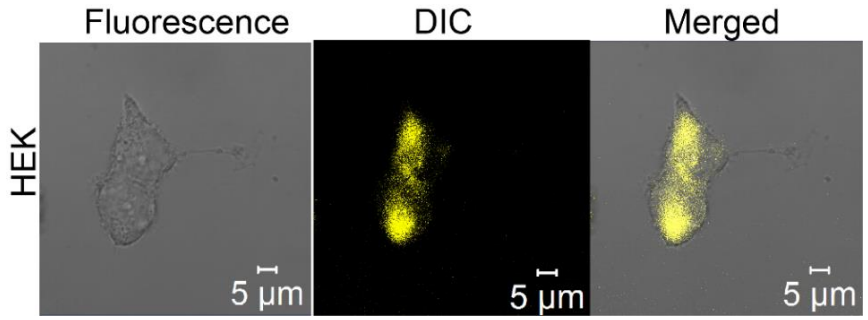

Figure 5.7. CLSM images of HEK cells treated with HQCald-ZFNs for 2 h.

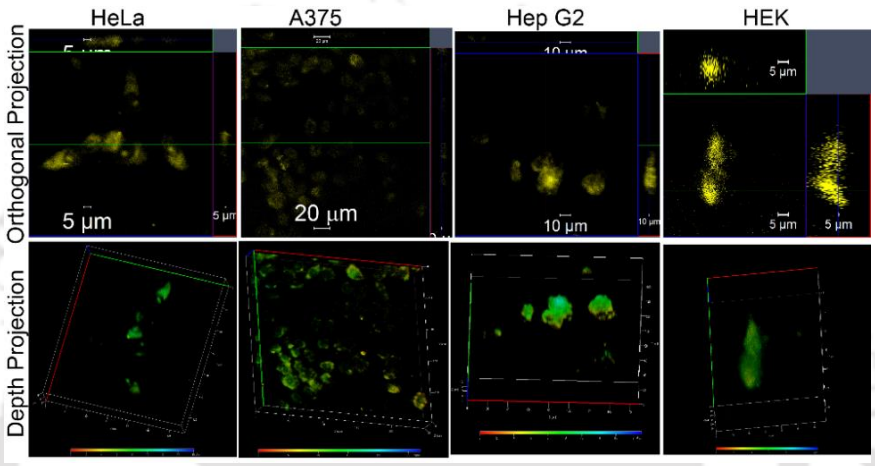

Figure 5.8. CLSM Z-staking images of HeLa, Hep G2, A375and HEK cells treated with HQCald-ZFNs for 2 h and subsequently irradiated with 355 nm laser in both orthogonal and depth projection confirmed internalization of HQCald-ZFNs.

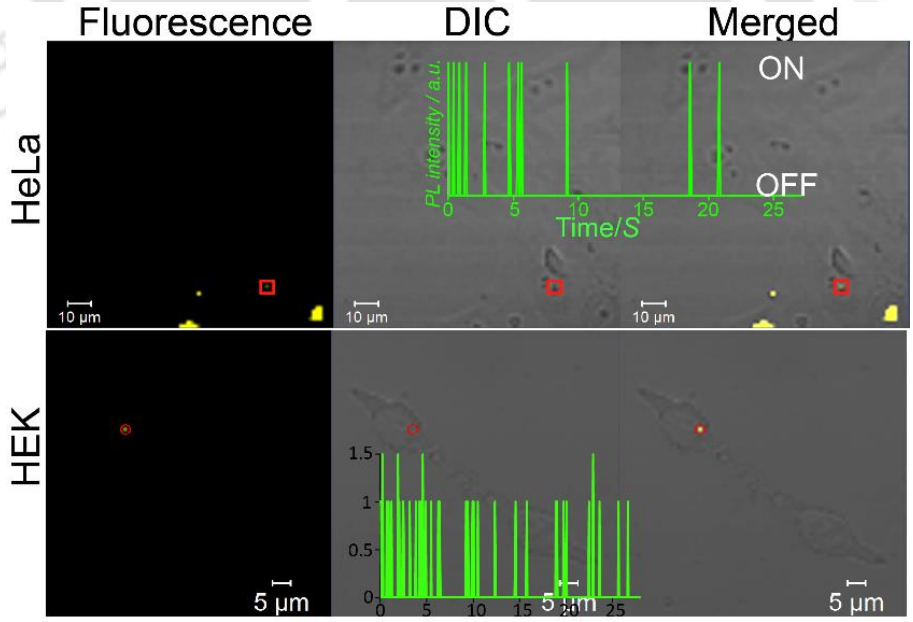

Figure 5.9. CLSM image of single HQCald-ZFN particles present inside HEK cells and corresponding blinking profile (inset) of the encircled single HQCald-ZFN particle.

HQCald-ZFNs also demonstrated superparamagnetism with a saturation magnetization value of 12.7 emu g^{-1} as recorded in vibrating sample magnetometry (VSM). The apparent reduction of saturation magnetization in HQCald-ZFN, when compared to that of parent $ZnFe_2O_4$ NPs (20.9 emu g^{-1}), could be due to contribution of diamagnetic BSA and HQCald to the overall mass only (Figure 5.10). The superparamagnetic nature of HQCald-ZFN could be exploited in magnetically targeted labeling of cancer cells. To this end, as a proof-of-concept experiment, HeLa cells were grown on two coverslips and subsequently incubated with HQCald-ZFNs in presence of an external magnet kept only under one coverslip as descried in the experimental section (Figure 5.11). The coverslips, when visualized under CLSM, revealed that cells on the coverslip near to the magnet showed considerably higher PL compared to those away from magnet and thus indicating the potential for magnetically targeted cellular imaging (Figure 5.11).[17] It may be mentioned here that the superparamagnetic HQCald-ZFNs could also be used as MRI contrasting agent extending the imaging modalities possible with these MTNPs.[18]

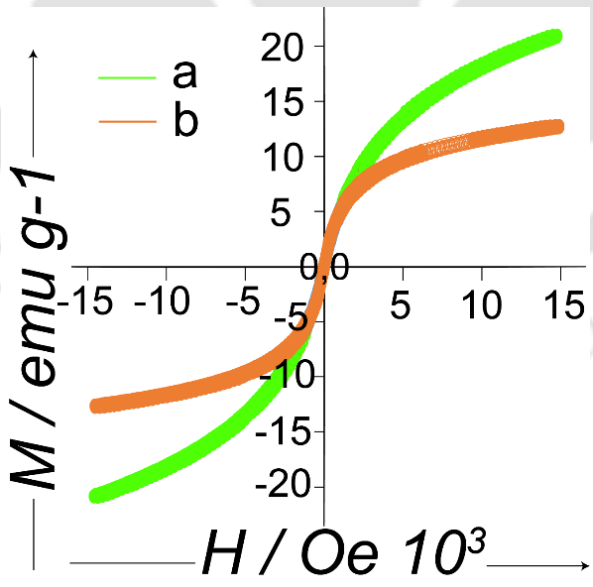

Figure 5.10. Vibrating sample magnetometric measurement (M vs H) of (a) $ZnFe_2O_4$ NPs and (b) HQCald-ZFNs.

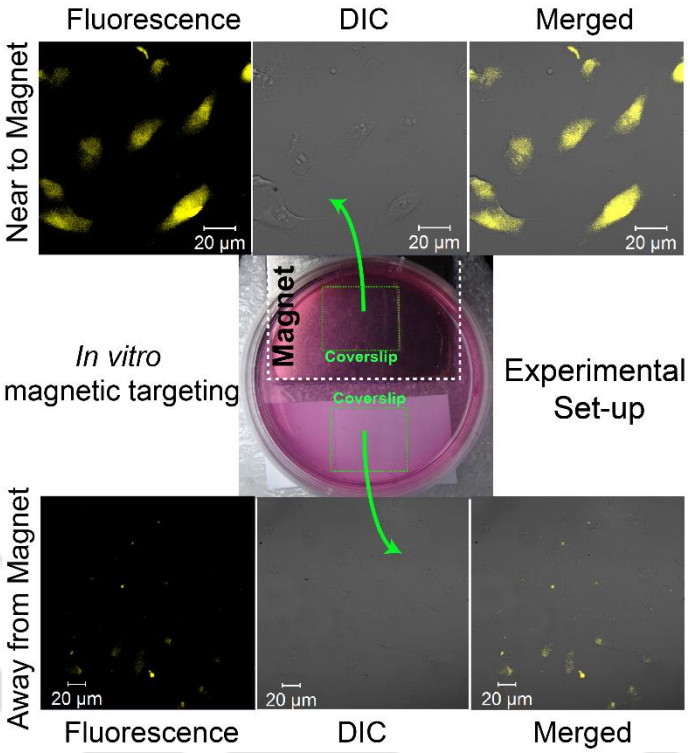

Figure 5.11. CLSM images of HeLa cells treated with HQCald-ZFNs for 2 h, images in upper panel correspond to the cells placed near to external magnet while those in lower panel correspond to the cells placed away from the magnet.

Anti-proliferative efficacy of HQCald-ZFNs against cancer cells was evaluated by MTT-based cell viability assay as described in experimental section. As is evident from MTT assay (Figure 5.12), ZFNs did not exhibit significant cytotoxicity against cancer cells and was only able to reduce the cell proliferation by 14% (at 150 µg/mL), 15% (at 150 µg/mL) and 7% (at 100 µg/mL) in HeLa, HepG2 and A375 cells, respectively, after 48 h of treatment with maximum concentrations tested. However, HQCald-ZFNs demonstrated strong anti-proliferative activity in a dose-dependent manner with IC_{50} values of 81.1 µg/mL, 32.6 µg/mL and 12.9 µg/mL against HeLa, HepG2 and A375 cells, respectively (Figure 5.12, Table 5.2). The amount of HQCald complexed with 1 µg of HQCald-ZFNs was estimated to be 0.12 µg in the present study (as described in the experimental section). Hence, in other words, the IC_{50} values in terms of HQCald complexed with ZFNs were 9.7 µg/mL (HeLa), 3.9 µg/mL (HepG2) and 1.5 µg/mL

(A375), respectively (Table 5.2). Free HQCald, reported to exhibit significant anticancer activity,[9,19] was found to possess IC_{50} values of 54.2 µg/mL (HeLa), 35.0 µg/mL (HepG2) and 8.7 µg/mL (A375) in the present study. Clearly, considering the amount of HQCald, HQCald-ZFN was superior to free HQCald in killing cancer cells. It may be noted here that treatments with normal cells (human embryonic kidney, HEK 293) revealed an IC_{50} value of 19.3 µg/mL for HQCald-ZFNs and 19.0 µg/mL for HQCald (Table 5.2 and Figure A.5.8, Appendix) indicating non-specific anti-proliferative characteristic of HQCald-ZFN. Well established targeting strategies, however, could be availed to develop HQCald-ZFN-based anti-cancer strategy.

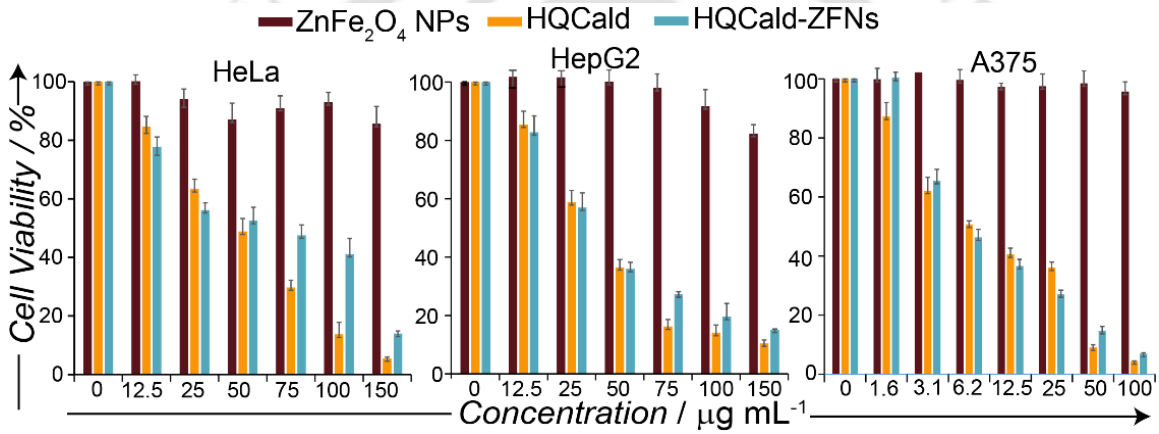

Figure 5.12. Cell viability of HeLa, HepG2 and A375 cells treated with different concentrations of $ZnFe_2O_4$ NPs, HQCald and HQCald-ZFNs for 48 h.

Table 5.2. IC_{20}, IC_{50} and IC_{80} values for different cell lines treated with different materials.

Cell line	Material	IC_{20}(µg/ml)	IC_{50}(µg/ml)	IC_{80}(µg/ml)
HeLa	HQCald	40.2	54.2	73.1
	HQCald-ZFNs	60.1	81.1	109.4
Hep G2	HQCald	26.0	35.0	47.3
	HQCald-ZFNs	24.2	32.6	43.9
A375	HQCald	5.3	8.7	14.4
	HQCald-ZFNs	8.5	12.9	19.6
HEK	HQCald	14.1	19.0	25.6
	HQCald-ZFNs	14.3	19.3	26.1

In order to gain better understanding of the mechanism of action behind the appreciable anti-proliferative efficacy of HQCald-ZFNs, the pathway of uptake was further explored since it was already evident from imaging experiments (Figure 5.6) that HQCald-ZFNs were efficiently internalized by the cancer cells. To this end, cancer cells were incubated with HQCald-ZFNs either in presence of sodium azide or at 4 °C. Both of these incubation parameters are well established factors to inhibit cellular endocytosis of external materials including various nanomaterials as described in the experimental section.[20] Results (Figure 5.13) showed that inhibitors of endocytosis drastically lowered the internalization of HQCald-ZFNs by cancer cells establishing endocytosis being the predominant uptake pathway.

As a consequence of endocytosis, the endosomes carrying HQCald-ZFNs were likely to fuse with lysosome, a cellular organelle with internal pH of 4.5-5.[21] Labeling with LysoTracker revealed co-localization of HQCald-ZFNs with lysosomes in treated HeLa cells confirming the presence of HQCald-ZFNs within the lysosomes (Figure 5.14). Since Zn-HQ type complexes become less stable in acidic environment, HQCald-ZFN is expected to liberate free HQCald within the lysosome.[22] Preliminary studies indeed demonstrated the release of HQCald ligand from HQCald-ZFN in acidic medium (acetate buffer pH 4.8), as probed by the characteristic absorbance at 374 nm (Figure 5.15). Interestingly, incubation of HQCald-ZFN in pH 7.4 (PBS) did not reveal significant release of ligand (Figure 5.15). Taken together, the experimental evidences suggested that HQCald-ZFN were internalized by the cancer cells through endocytosis and subsequently exposed to the acidic environment of the lysosome resulting in the release of HQCald ligand that efficiently killed the cancer cells.

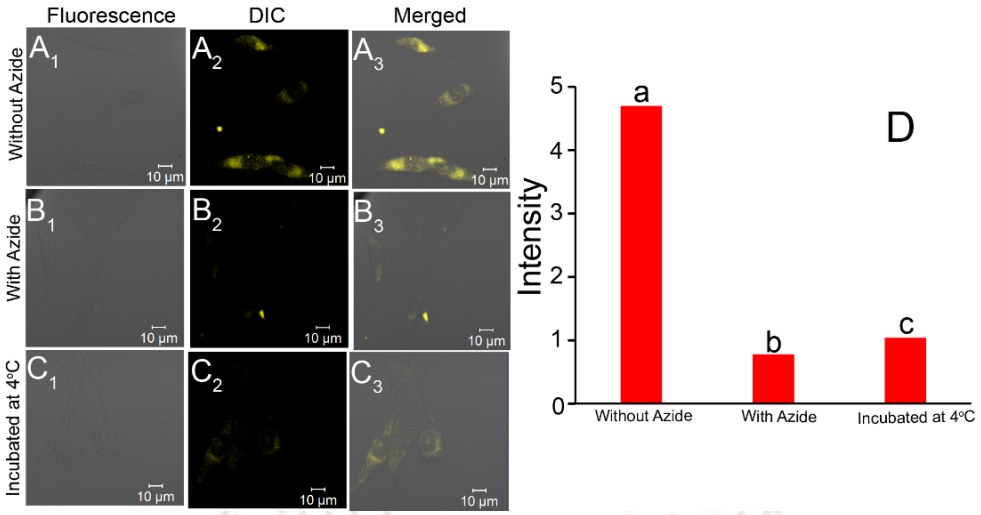

Figure 5.13. CLSM images of HeLa cells treated with HQCald-ZFNs (A) in absence of sodium azide and (B) in presence of 0.1% sodium azide and (C) incubated at 4 °C after adding HQCald-ZFNs in absence of sodium azide (D) Plot of intensities calculated from representative images showed decrease of fluorescence (~ 83%) in case of azide treatment and (~77%) in case of incubation at 4 °C, respectively indicating drastic decrease in HQCald uptake.

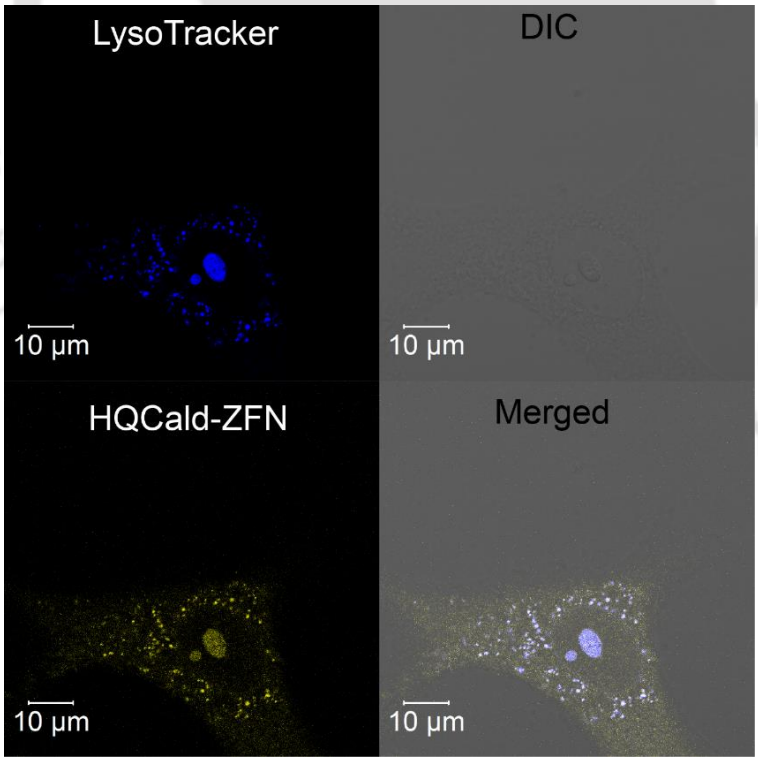

Figure 5.14. CLSM Images showing colocalization of HQCald-ZFNs with LysoTracker-labeled lysosomes of HeLa cells. Pseudo blue color is used to label LysoTracker's emission.[23,24]

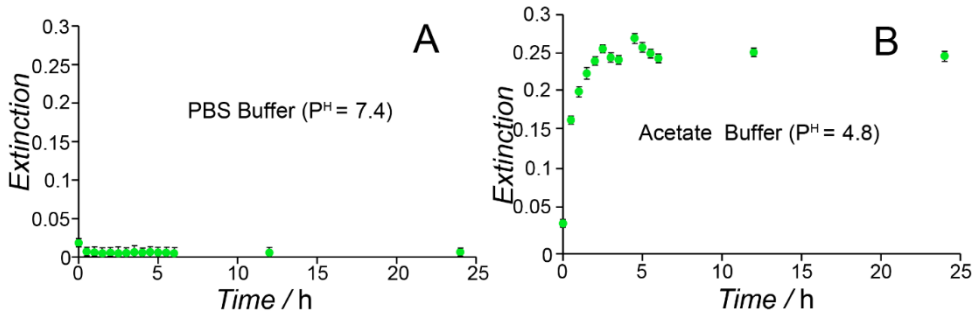

Figure 5.15. Release of HQCald from HQCald-ZFN at (A) PBS buffer (pH =7.4) and (B) at acetate buffer (pH=4.8) measured in terms of increase in UV visible absorbance at 374 nm of supernatant (after centrifugation at 25,000 RCF for 25 min).

5.3. Conclusion

In conclusion, we have successfully developed a new type of magnetofluorescent NPs (HQCald-ZFNs) using $ZnFe_2O_4$ NP as magnetic core and subsequently converting the surface Zn ions to fluorescent complexes using HQCald (an anticancer derivative of HQ) as complexing ligands. HQCald-ZFNs exhibited good quantum yield, high photostability, considerable excited-state lifetime and increase in *ON* state at single particle level making them suitable candidates for both ensemble and single particle level bioimaging. CLSM studies of successfully demonstrated *in vitro* bioimaging capability of HQCald-ZFNs in ensemble and single particle levels. Moreover, superparamagnetic nature of HQCald-ZFNs was utilized to achieve magnetic targeting. Finally, MTT based viability assay in HeLa, HepG2 and A375 cells revealed considerable antiproliferative activity of HQCald-ZFNs against these cancer cells with IC_{50} values of 81.1 µg/mL, 32.6 µg/mL, and 12.9 µg/mL, respectively. Thus, the present HQCald-ZFNs with efficient bioimaging capability, responsiveness toward magnetic targeting and excellent anti-proliferative effect on cancer cells *in vitro* can lead to effective anticancer theranostics.

References:

1. Xu, Y.; Sherwood, J.; Qin, Y.; Holler, R. A.; Bao, Y. A General Approach to the Synthesis and Detailed Characterization of Magnetic Ferrite Nanocubes *Nanoscale* **2015**, *7*, 12641– 12649.
2. Xu, Z. C.; Hou, Y. L.; Sun, S. H. Magnetic Core/Shell Fe3O4/Au and Fe3O4/Au/Ag Nanoparticles with Tunable Plasmonic Properties *J. Am. Chem. Soc.* **2007**, *129,* 8698– 8699.
3. Jiang, B.; Han, C.; Li, B.; He, Y.; Lin, Z. In-Situ Crafting of ZnFe2O4 Nanoparticles Impregnated within Continuous Carbon Network as Advanced Anode Materials *ACS Nano* **2016**, *10*, 2728– 2735.
4. Rivero, M.; Campo, A. del; Mayoral, A.; Mazario, E.; Marcos, J. S.; Bonilla, A. M. Synthesis and structural characterization of Zn_xFe_{3-xO4} ferrite nanoparticles obtained by an electrochemical method *RSC Adv.* **2016**, *6*, 40067-40076.
5. Bhandari, S.; Roy, S.; Chattopadhyay, A. Enhanced Photoluminescence and Thermal Stability of Zinc Quinolate Following Complexation on the Surface of Quantum Dot *RSC Adv.* **2014**, *4*, 24217–24221.
6. Bhandari, S.; Khandelia, R.; Pan, U. N.; Chattopadhyay, A. Surface Complexation-Based Biocompatible Magnetofluorescent Nanoprobe for Targeted Cellular Imaging *ACS Appl. Mater. Interfaces* **2015**, *7*, 17552–17557.
7. Bhandari, S.; Roy, S.; Pramanik, S.; Chattopadhyay, A. Surface Complexation Reaction for Phase Transfer of Hydrophobic Quantum Dot from Nonpolar to Polar Medium *Langmuir* **2014**, *30*, 10760– 10765.
8. Pan, H. C; Liang, F.; Mao, C.; Zhu, J.; Chen, H. Highly Luminescent Zinc(II)-Bis(8-hydroxyquinoline) Complex Nanorods: Sonochemical Synthesis, Characterizations, and Protein Sensing *J. Phys. Chem. B* **2007**, *111*,5767– 5772.
9. 9. Chan, S. H.; Chui, C. H.; Chan, S. W.; Kok, S. H. L.; Chan, D.; Tsoi, M. Y. T.; Leung, P. H. M.; Lam, A. K. Y.; Chan, A. S.; Lam, K. H.; Tang, J. C. Synthesis of 8-Hydroxyquinoline Derivatives as Novel Antitumor Agents *ACS Med. Chem. Lett.* **2013**, *4,* 170-174.
10. Song, H.; Zhu, L.; Li, Y.; Lou, Z.; Xiao, M.; Ye, Z. Preparation of $ZnFe_2O_4$ Nanostructures and Highly Efficient Visible-Light-Driven Hydrogen Generation with the Assistance of Nanoheterostructures *J. Mater. Chem. A* **2015**, *3*, 8353– 8360.
11. Manikandan, A.; Vijaya, J. J.; Sundararajan, M.; Meganathan, C.; Kennedy, L. J.; Bououdina, M. Optical and Magnetic Properties of Mg-Doped ZnFe2O4 Nanoparticles Prepared By Rapid Microwave Combustion Method Superlattices *Microstruct.* **2013**, *64*, 118– 131.

12. Pavani, S. R. P., Thompson, M. A., Biteen, J. S., Lord, S. J., Liu, N., Twieg, R. J., Piestun, R. and Moerner, W. E. Three-dimensional, single-molecule fluorescence imaging beyond the diffraction limit by using a double-helix point spread function *Proc. Nat. Acad. Sci. U.S.A.* **2009,** *106*, 2995–2999.
13. Lane, L. A.; Smith, A. M.; Lian, T.; Nie, S. Compact and Blinking-Suppressed Quantum Dots for Single-Particle Tracking in Live *Cells J. Phys. Chem. B* **2014**, *118,* 14140– 14147.
14. Shen, H.; Tauzin, L. J.; Baiyasi, R.; Wang, W.; Moringo, N.; Shuang, B.; Landes, C. F. Single Particle Tracking: From Theory to Biophysical Applications *Chem. Rev.* **2017,** *117*, 7331– 7376.
15. Gonda, K.; Miyashita, M.; Higuchi, H.; Tada, H.; Watanabe, T.M.; Watanabe, M.; Ishida, T.; Ohuchi, N.Predictive diagnosis of the risk of breast cancer recurrence after surgery by single-particle quantum dot imaging *Sci. Rep*. **2015**, *5*, 14322-14336.
16. Miyashita, M.; Gonda, K.; Tada, H.; Watanabe, M.; Kitamura,N.; Kamei, T.; Sasano, H.; Ishida, T.; Ohuchi, N.; Quantitative diagnosis of HER2 protein expressing breast cancer by single-particle quantum dot imaging *Cancer medicine*, **2016***, 5*, 2813-2824.
17. Bhandari, S.; Khandelia, R.; Pan, U. N.; Chattopadhyay, A. Surface Complexation-Based Biocompatible Magnetofluorescent Nanoprobe for Targeted Cellular Imaging *ACS Appl. Mater. Interfaces* **2015,** *7,* 17552–17557.
18. Bárcena, C.; Sra, A. K.; Chaubey, G. S.; Khemtong, C.; Liu, J. P.; Gao, J. Zinc Ferrite Nanoparticles as MRI Contrast Agents *Chem. Commun.* **2008**, *19*, 2224– 2226.
19. Lam,K.-H.; Lee, K. K.-H.; Gambari, R.; S. Kok, H.-L.; Kok, T.-W.; Chan, A. S.-C.; Bian, Z.-X.; Wong, W.-Y.; Wong, R. S.-M.; Lau, F.-Y. Anti-tumour and pharmacokinetics study of 2-Formyl-8-hydroxy-quinolinium chloride as Galipea longiflora alkaloid analogue *Phytomedicine,* **2014**, *21*, 877-882.
20. Dutta, A.; Dutta, D.; Sanpui, P. Chattopadhyay, A. Biomimetically crystallized protease resistant zinc phosphate decorated with gold atomic clusters for bioimaging *Chem. Commun.* **2017**, *53*, 1277-1280.
21. Oh, N.; Park, J. H. Endocytosis and Exocytosis of Nanoparticles in Mammalian Cells *Int. J. Nanomed.* **2014**, 9 51– 63.
22. Soroka, K.; Vithanage, R. S.; Phillips, D. A.; Walker, B.; Dasgupta, P.K. Fluorescence Properties of Metal Complexes of 8-Hydroxyquinoline-5-sulfonic Acid and Chromatographic Applications *Anal. Chem.,* **1987**, *59*, 629-636.
23. Belizaire, R.; Unanue, E. R. Targeting Proteins to Distinct Subcellular Compartments Reveals Unique Requirements for MHC Class I and II Presentation *Proc. Natl. Acad. Sci. U.S.A.* **2009,** *106*, 17463–17468.

24. Hu, Y.-B.; Dammer, E. B.; Ren, R.-J; Wang, G. The endosomal-lysosomal system: from acidification and cargo sorting to neurodegeneration *Transl. Neurodegener*., **2015**, 4, 18-28.

CHAPTER 6

Summary and Future Prospects

In summary, the present thesis reports the fabrication of four different multifunctional theranostics nanomaterials (MFTNPs) for potential cancer theranostics. This has been achieved by: (i) by assembling gold nanorods, iron oxide nanoparticles, and gold nanoclusters within BSA nanoparticles and subsequently loading doxorubicin in it, (ii) preparing lysozyme mediated nanoscale aggregates of gold coated ironoxide core-shell nanoparticles followed by coating them with luminescent BSA stabilized gold nanoclusters and loading chemotherapeutic drug doxorubicin in it, (iii) by developing green emitting complexes on the surface of zinc ferrite nanoparticles with HQ and subsequently loading artemisinin on it, and (iv) fabricating yellow emitting complexes on the surface of zinc ferrite nanoparticles with derivative of HQ 8-hydroxy-2-quinolinecarboxaldehyde. All the MFTNPs developed here has been demonstrated for fluorescent bioimaging, *in vitro* magnetic targeting and anticancer efficacy. Moreover, some of them have also been demonstrated for photothermal therapy, combination therapy, two-photon or single particle based bioimaging and magnetic resonance imaging. Taken together, all the MFTNPs showed significant cancer theranostics effect in *in vitro* model. However, future studies should be carried out in animal models in order to employ them clinical treatments. Additionally, the unification strategies used here to fabricate MFTNPs namely use of protein matrix and surface complexation are versatile in nature and hence should be further explored for the development of newer MFTNPs with novel theranostics potential.

The design and the development of different MFTNPs in the present thesis was carried out through systematic modification of one from the other with the objective to mainly reduce the complexity of the system, to make it more robust and to ultimately achieve all the functionalities in a single nanostructure. In the second chapter, all the different components AuNRs, IONPs and Au nanoclusters

were separately incorporated into BSA nanoparticle to achieve plasmonic and magneto fluorescent properties. In the third chapter, the complexity was reduced by using a single nanomaterial (IO@Au NPs) for both plasmonic and magnetic functionalities instead of using two separate materials. And the robustness of the system was increased by coating the IONPs with Au to protect the IONPs in acidic environment of stomach. In the fourth chapter surface complexation reaction was carried out on the magnetic zinc ferrite nanoparticle's surface to achieve a single nanoparticle with magneto-fluorescent characteristic. After that the drug artemisinin was loaded into it to achieve the anticancer effect. In chapter five, the complexity was further reduced and the robustness was increased by simply replacing the surface complexing ligand HQ with an anticancer active ligand 8-hydroxy-2-quinolinecarboxaldehyde, which eliminate the requirement of an additional drug.

In the second and third chapters, Dox was used as the chemotherapeutic drug. Basically, the loading and release of Dox in these two nanocarriers are mainly based on the hydrophobic, hydrophilic, hydrogen boding and Van der Waals interaction with the protein BSA and lysozyme with Dox. These interactions of Dox and proteins are basically reversible in nature, permitting encapsulated molecules to be released. We observed ~92% encapsulation of Dox in the Chapter-2 (in case of MFNCs) when 147.5 L^{-1} MFNCs was incubated with 3.28 μg mL^{-1} of Dox. In the third chapter (in case of PML-MFNCs), when 3.28 μg mL^{-1} of Dox was incubated with 162.3 μg mL^{-1} PML-MF nanocarrier 82% encapsulation was observed. From these data it is clear that the encapsulation of Dox/mg of carrier was slightly higher in MFNCs compared to PML-MF nanocarrier. This could be because of the differences in composition of the proteins and contribution of the protein to the overall mass of the nanocarriers. In the fourth chapter, the amount of artemisinin present in 1 mg of drug loaded HQ-ZFNPs@BSA was calculated to be 0.23 μg with encapsulation efficiency 79%. This result could not be compared with the encapsulation efficiency of the Chapter-1 or Chapter-2 as the drug is different thus, the interaction of the drug with BSA would also be different. In the fourth chapter, the drug 8-hydroxy-2-quinolinecarboxaldehyde itself acts as the

complexing agent for the surface Zn^{2+} ions present on zinc ferrite nanoparticles thus the encapsulation efficacy was not possible to be calculated.

Among many proteins, BSA was chosen for designing the experiments reported in the thesis because albumin proteins are present in blood plasma and thus immunological responses against it would be very limited and moreover due to structural similarities, BSA could easily be replaced with HSA for the preparation of similar nanocarriers for *in vivo* applications. In addition, some types of tumors (for examples prostate, lung and breast) possess over-expressed albumin receptors, hence naturally facilitating preferential accumulation of albumin based nanocarriers onto the tumor. Furthermore, the only clinically approved nanocarrier, abraxane, is also based on albumin protein and pharmacokinetics of this has been extensively studied, thus, pharmacokinetics study of albumin-based carriers is well established. Lysozyme also helps in limiting immunological responses and easily forms aggregates in presence of nanoparticles. Due to the above reasons, BSA and lysozyme have been chosen for the developments of all the nanocarriers.

Although, the present thesis did not involve direct *in vivo* experiments, yet all the nanocarriers were designed keeping in mind future *in vivo* applicability. Towards the goal, the primary focus was to use inorganic nanoparticles containing only non-toxic metals. Hence inorganic nanoparticles made of iron, zinc and gold were used in this study as none of these elements demonstrate toxicity. Secondly, all the nanocarriers designed in the present thesis contain albumin protein on their surface. As discussed earlier, presence of albumin on the surface of the nanocarriers could restrict the immunological responses and may also achieve targeting capability for certain type of cancer. In addition, for any nanocarrier to acts as a drug delivery vehicle, it is important to have high stability in blood during circulation in the body. In this regard we have tested the stability of the nanocarriers in human blood serum. We found all the nanocarriers in the present thesis work have high stability in human blood serum for at least 24 h. Another important factor for *in vivo* application is the size of the nanocarriers to achieve passive targeting. In chapter-2 the reported average size of the nanocarrier is

120.5 ± 27.6 nm and the average hydrodynamic diameter (δH) of water-dispersed MFNCs was estimated to be 203.1 nm; this size rage is within the limit to achieve passive targeting. In chapter-4 and chapter-5, the size of the nanocarrier reported is around 10 nm; this sized nanocarriers could also be helpful for passive targeting as the size range for the nanocarrier for passive targeting is considered to be 10 nm-200 nm. The PML-MF nanocarrier (Chapter-3) is relatively larger in size (average hydrodynamic diameter 711 nm). This higher sized nanocarriers ideally would not be able to achieve passive targeting; however, the smaller sized PML-MF nanocarriers could be developed along the lines of the synthetic protocol stated in this chapter with a modification of using reduced quantity of lysozyme with respect to the IO@Au NPs.

In vivo studies and modification of the nanocarrier based on the findings of those *in vivo* responses would be one the most important continuity of the present thesis towards future commercial realization of these MFTNPs. Moreover, integration of the active targeting following surface modification of the nanocarrier, loading of multiple drugs together and achieving magnetic hyperthermia along with plasmonic photothermal therapy are some important aspect which could be explored in future.

Appendix

A2: Chapter 2

***Characterization of Au NRs,* Fe_3O_4 NPs, *Au nanoclusters and MFNCs*:** Digital images of aqueous dispersions of Au NRs, Fe_3O_4 NPs, Au nanoclusters and MFNCs were taken using a Nikon Coolpix L810 camera; while Spectroline UV-lamp of 365 nm was used to visualize their photoluminescence. The UV-visible extinction and photoluminescence spectra of samples were recorded in a Hitachi U-2900 UV-vis spectrophotometer and FluoroMax-4 spectrofluorimeter (HORIBA JobinYvon), respectively. Powder X-ray diffraction patterns were recorded in Brucker D8 Advance X-ray diffractometer (for Au NRs) and Rigaku TTRAX III X-ray diffractometer (for Fe_3O_4 NPs). Vibrating sample magnetometer (VSM 7410 series) was used for measuring magnetic properties of the samples. For transmission electron microscopy (TEM), aqueous dispersions of appropriate samples were deposited on carbon-coated copper TEM grids and air dried. TEM, high resolution TEM (HRTEM) images and selected area electron diffraction (SAED) patterns of the samples were obtained in JEOL JEM 2100 operating at an accelerating voltage of 200 kV. Gatan Digital Micrograph software was used to obtain inverse fast Fourier transform (IFFT) images. Elemental concentration of iron in the MFNCs, following acid digestion, was measured using Varian AA240FS atomic absorption spectrometer. Christ Alpha 1-4 LD lyophilizer was used to obtain lyophilized powder form aqueous dispersions of BSA-stabilized Au nanocluster and MFNCs. Dynamic light scattering (DLS) based particle size analysis and zeta potential of the samples were done using Zetasizer Nano ZS90, Model No. ZEN3690, Malvern. For field emission scanning electron microscopy (FESEM), aqueous dispersion of MFNCs was deposited on an aluminium foil-wrapped glass slide and then air-dried. Finally, gold coating was done in a SC7620 "Mini" Polaron Sputter Coater (Quorum Technologies, Newhaven, England) and the sample was analyzed with SIGMA, Carl Zeiss field emission scanning electron microscope.

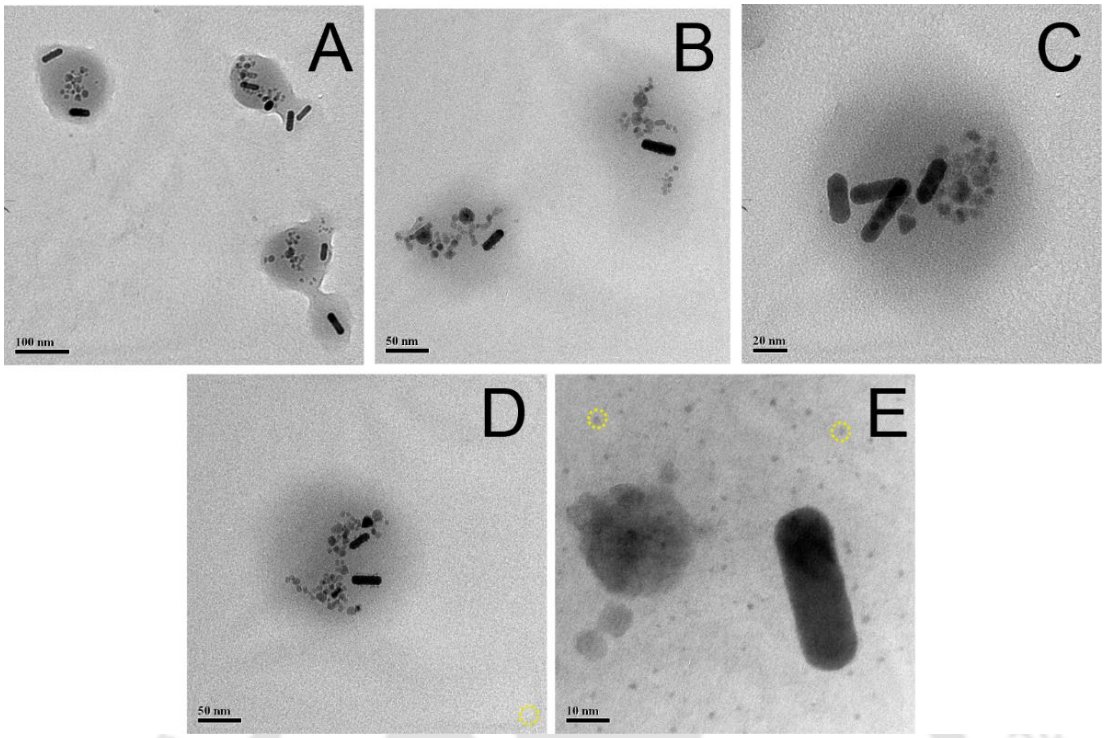

Figure A.2.1. (A-D) Additional TEM images of MFNCs (scale bar: 100 nm in A, 50 nm in B, 20 nm in C and 50 nm in D). (E) TEM image of a MFNC at higher magnification demonstrating the presence of individual AuNR, IONPs and Au nanoclusters (a few marked with yellow circles) (scale bar: 10 nm).

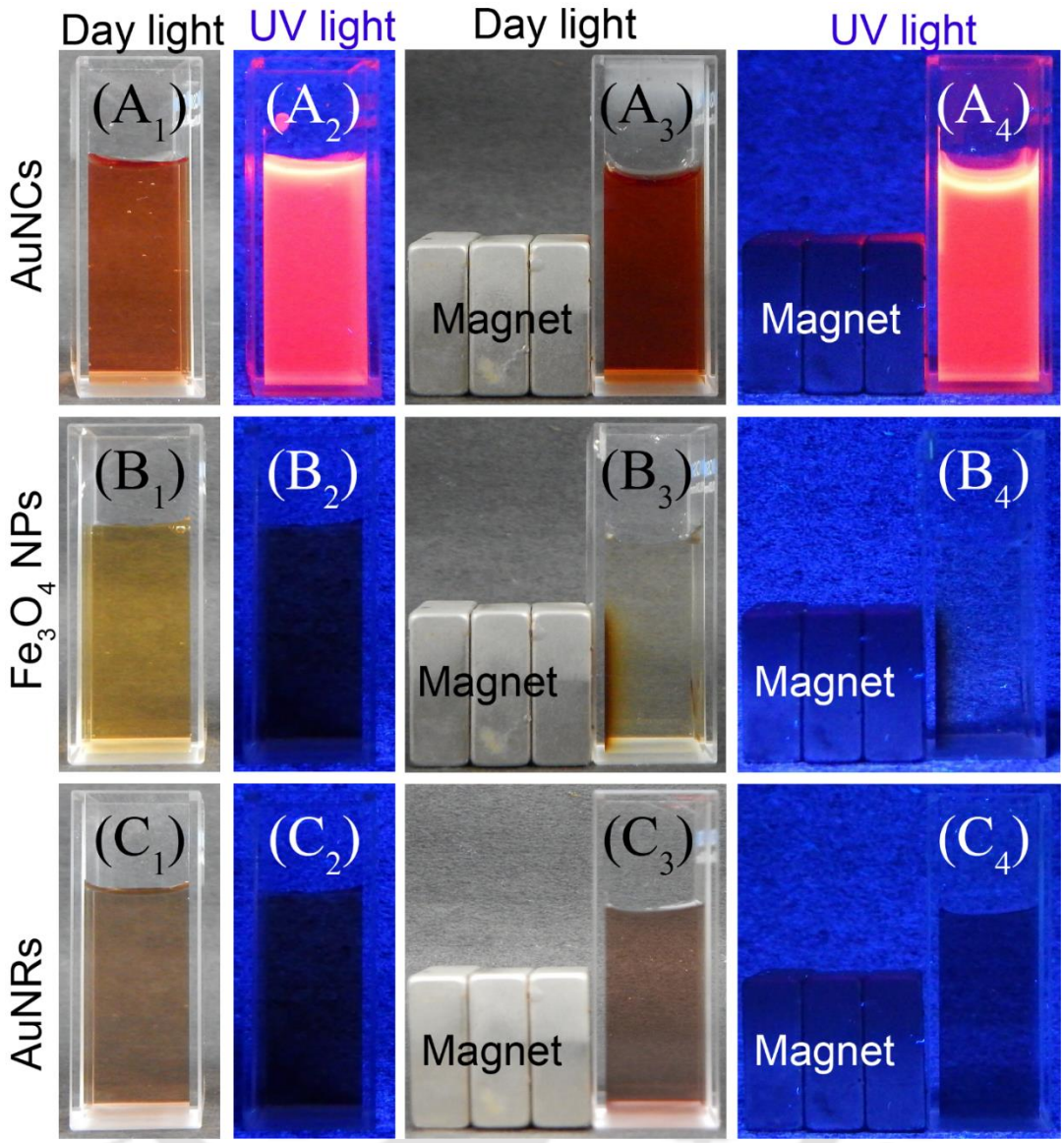

Figure A.2.2. Digital images of aqueous dispersion of (A) BSA-stabilized Au nanoclusters, (B) IONPs and (C) AuNRs. Subscripts 1 and 2 denote dispersion under daylight and UV light (365 nm), respectively. Subscripts 3 and 4 denote dispersion in presence of external magnet under daylight and UV light (365 nm), respectively.

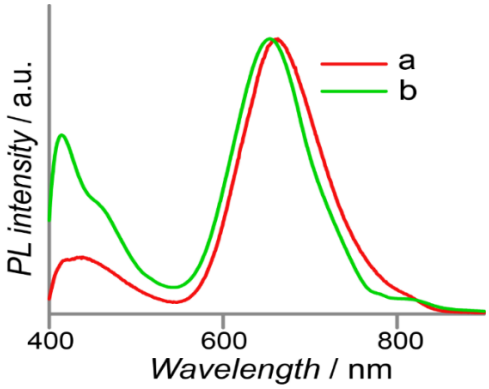

Figure A.2.3. Normalized emission spectra of (a) BSA-stabilized Au nanoclusters and (b) MFNCs at the excitation wavelength of 365 nm showing a blue-shift of the emission maximum from 663 nm (Au nanoclusters) to 650 nm (MFNCs). Additional peak around ~430 nm is due to emission of the BSA.

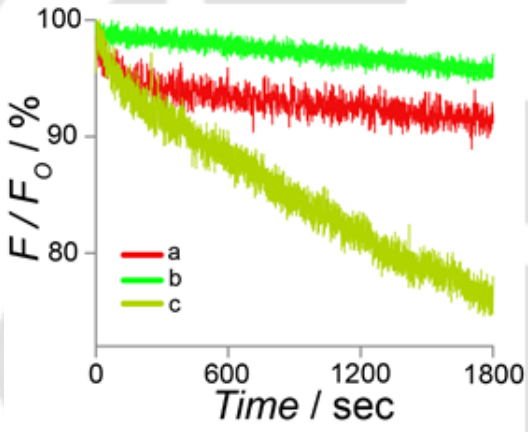

Figure A.2.4. Photostability of (a) BSA-stabilized Au nanoclusters (λ_{em} = 663 nm), (b) MFNCs (λ_{em} = 650 nm) and (c) FITC (λ_{em} = 525 nm) studied at λ_{ex} of 365 nm.

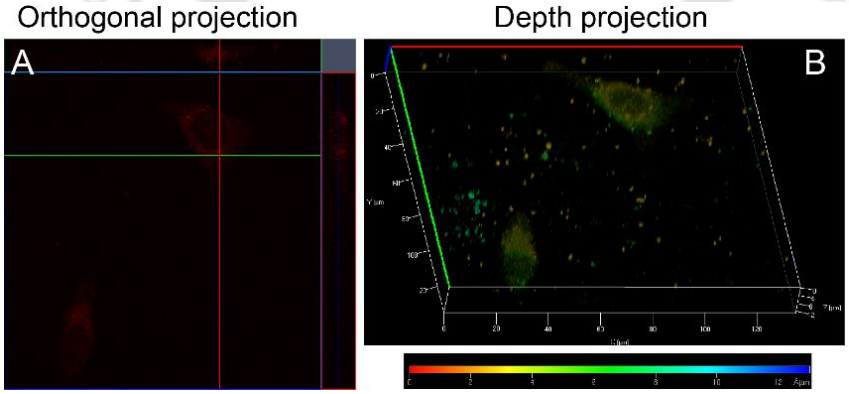

Figure A.2.5. A typical CLSM image of MFNCs treated HeLa cells with corresponding (A) orthogonal and (B) depth projection showing the internalization of MFNCs by the cells.

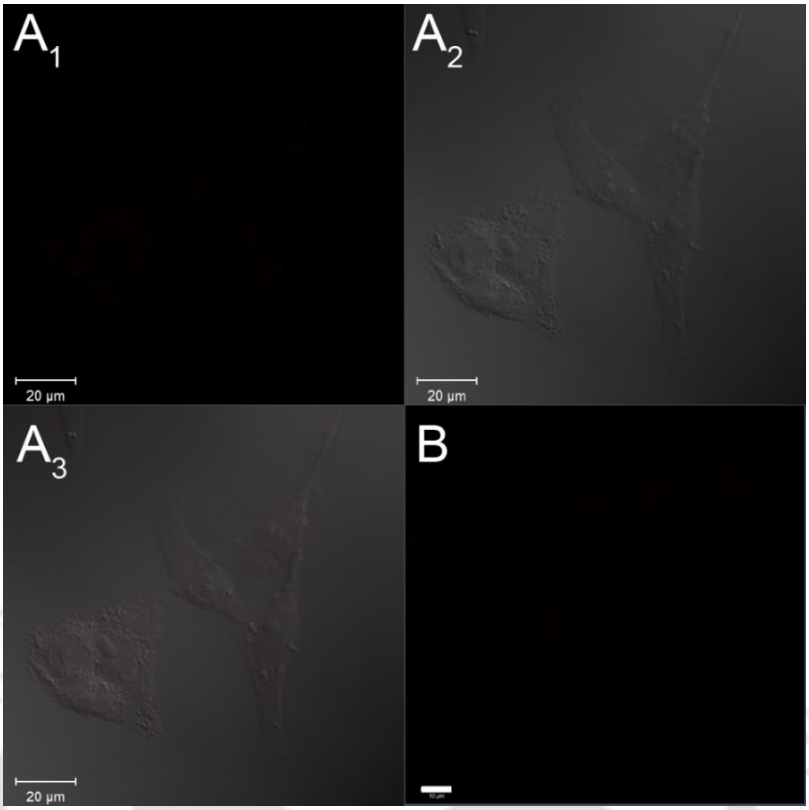

Figure A.2.6. CLSM images of untreated HeLa cells under (A) one photon (488 nm laser excitation; 1, 2 and 3 denote fluorescence, DIC and merged image, respectively; scale bar: 20 μm) and (B) 730 nm multi-photon laser excitation (scale bar: 10 μm).

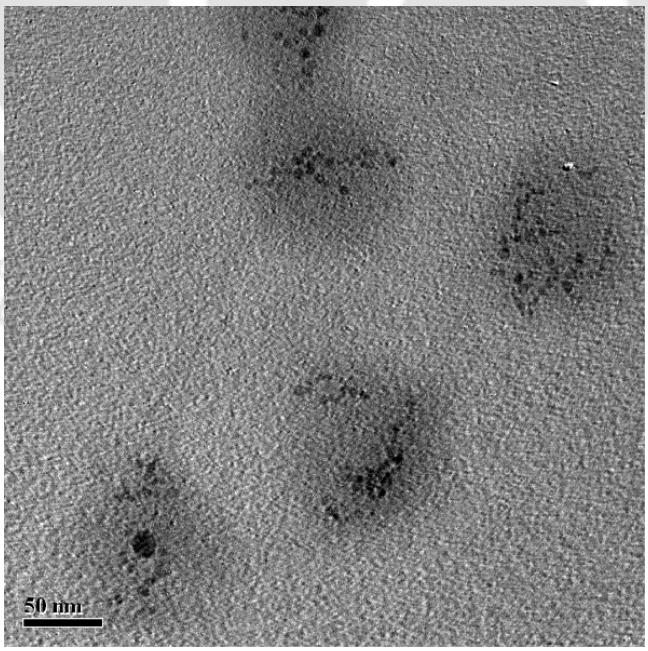

Figure A.2.7. TEM image of control MFNCs without AuNRs used in PPTT experiment *in vitro* (scale bar: 50 nm).

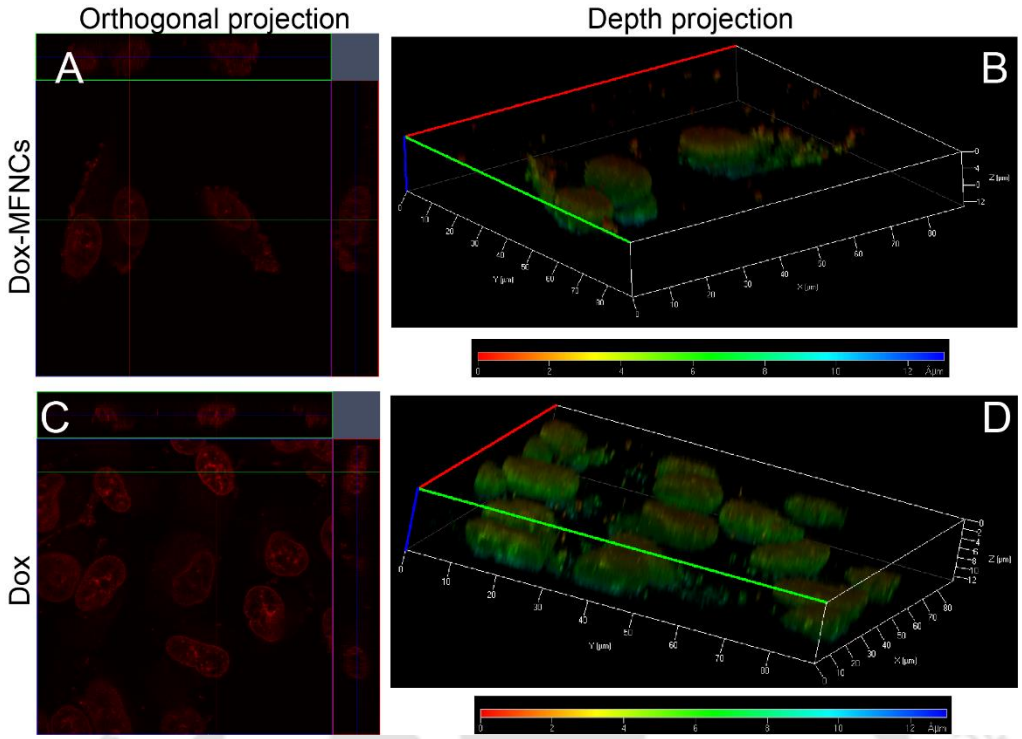

Figure A.2.8. A typical CLSM image of Dox-MFNCs treated HeLa cells with corresponding (A) orthogonal and (B) depth projection showing the internalization of Dox-MFNCs by the cells. CLSM image of Dox-treated HeLa cells with corresponding (C) orthogonal and (D) depth projection showing the internalization of the drug.

A3: Chapter 3

Instruments used for characterization: All the photoluminescence spectra were recorded in HORIBA JobinYvon FluoroMax-4 spectrofluorimeter. All the extinction spectra were recorded in Hitachi U-2900 UV-vis spectrophotometer. All the X-ray Powder diffraction (XRD) studies of the nanomaterials were carried out in Rigaku TTRAX III X-ray diffractometer. Superparamagnetic nature and corresponding magnetic saturation of the IONPs, IO@Au NPs and PML-MF nanocarriers were tested using 7410 series vibrating sample magnetometer. Transmission electron microscopic images, high resolution transmission electron microscopic images (HRTEM), selected area electron diffraction (SAED) patterns and elemental mapping of all the samples were recorded using JEOL JEM 2100 or JEOL JEM 2100F transmission electron microscope. Gatan Digital Micrograph software was used to find out the IFFT patterns and corresponding lattice spacing of the HRTEM images. Carl Zeiss confocal laser scanning microscope LSM 880 was used to obtain all the cell images and corresponding Z-stack images.

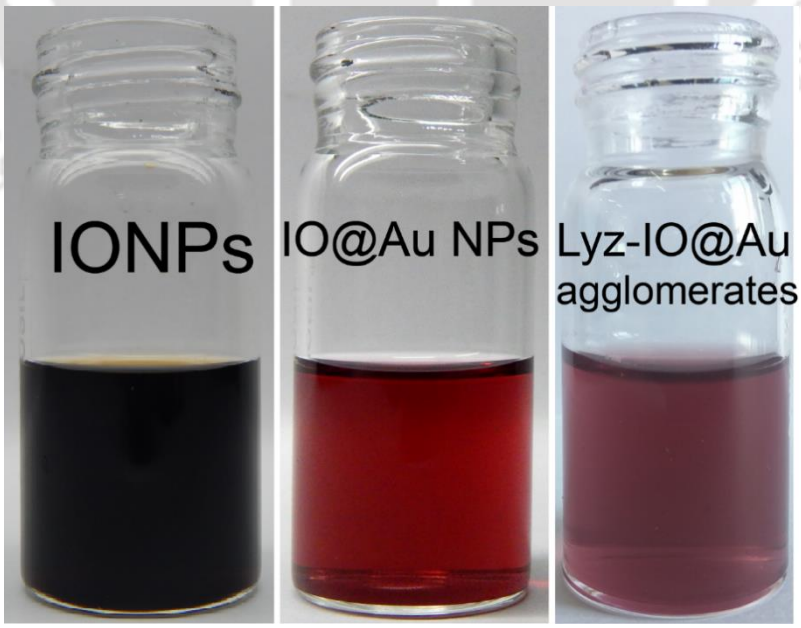

Figure A.3.1. Digital images of aqueous dispersion IONPs, IO@Au NPs and IO@AuNPs-Lyz agglomerates showing color change from black to red to purple-blue.

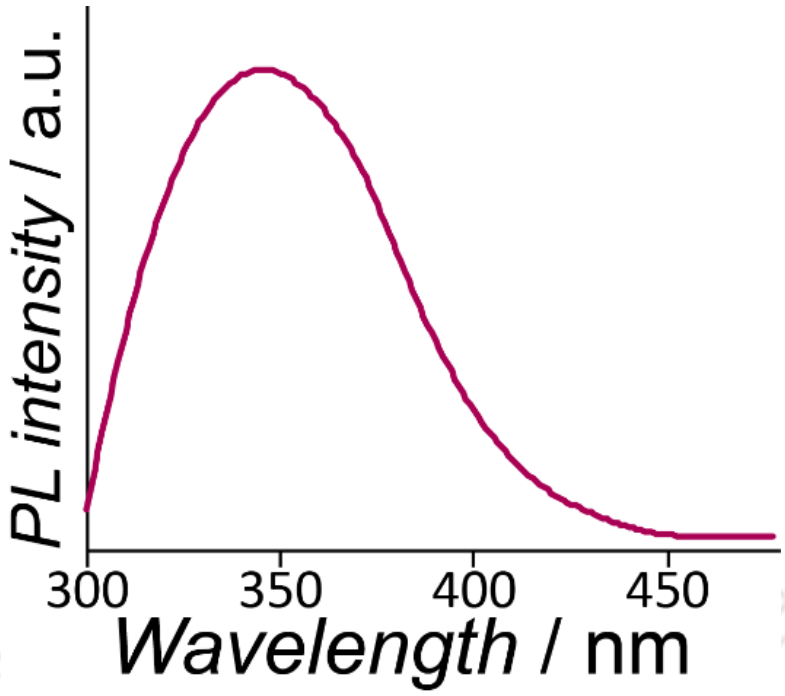

Figure A.3.2. Emission spectrum of the aqueous solution of BSA at an excitation of 278 nm.

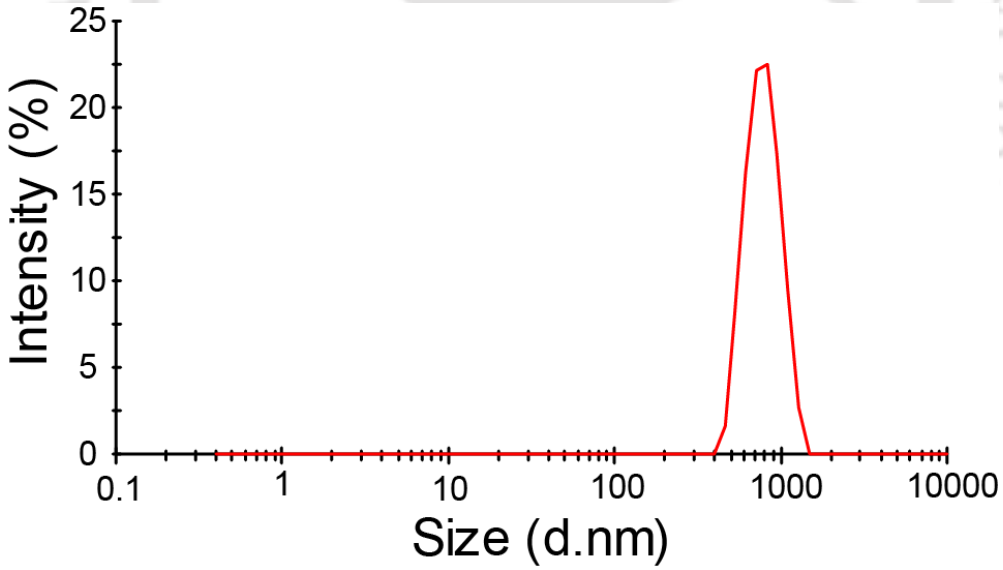

Figure A.3.3. Distribution of hydrodynamic diameters of PML-MF nanocarriers (dispersed in aqueous medium) as measured by DLS.

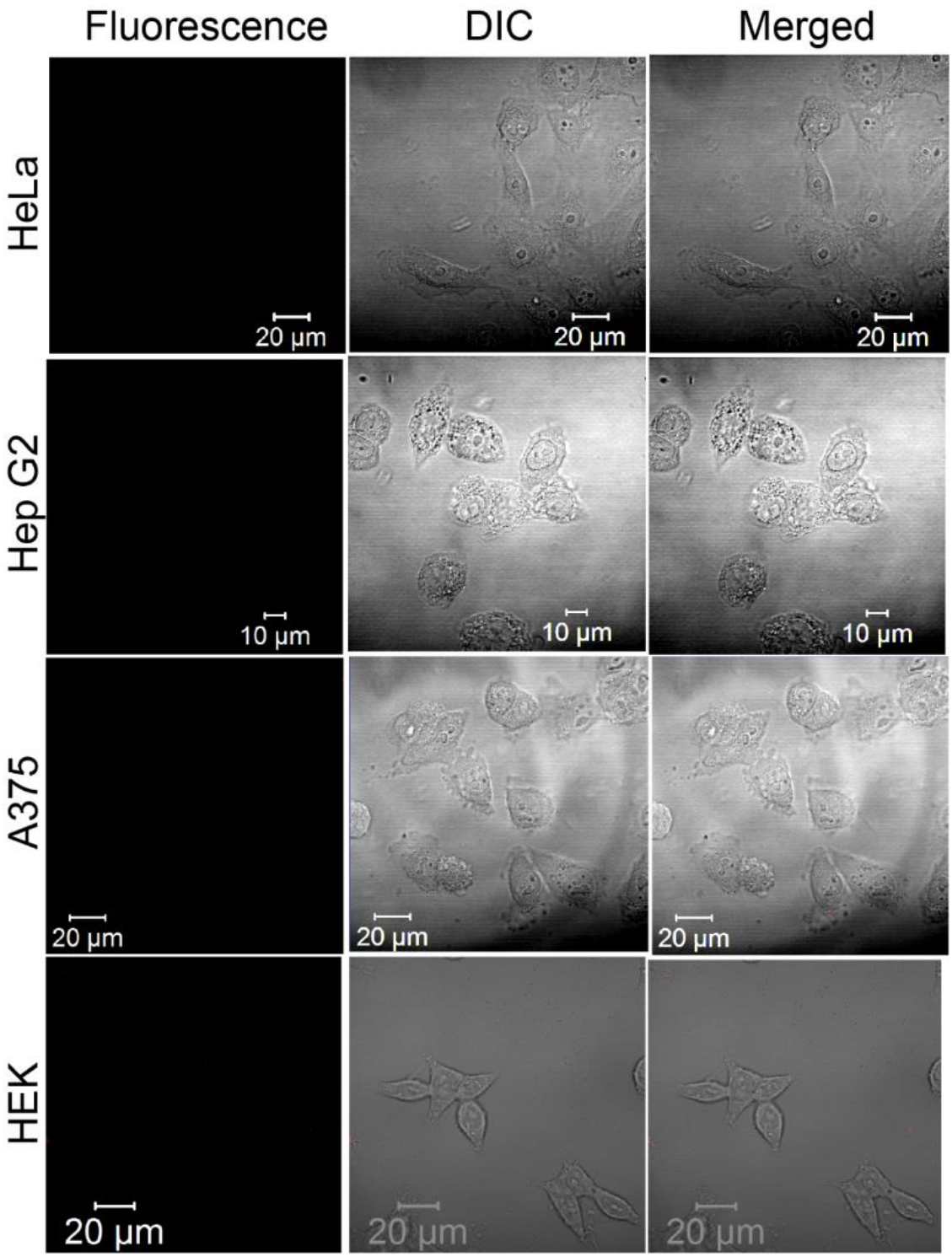

Figure A.3.4. Control CLSM image of HeLa, HepG2, A375 and HEK cells at 488 nm excitation.

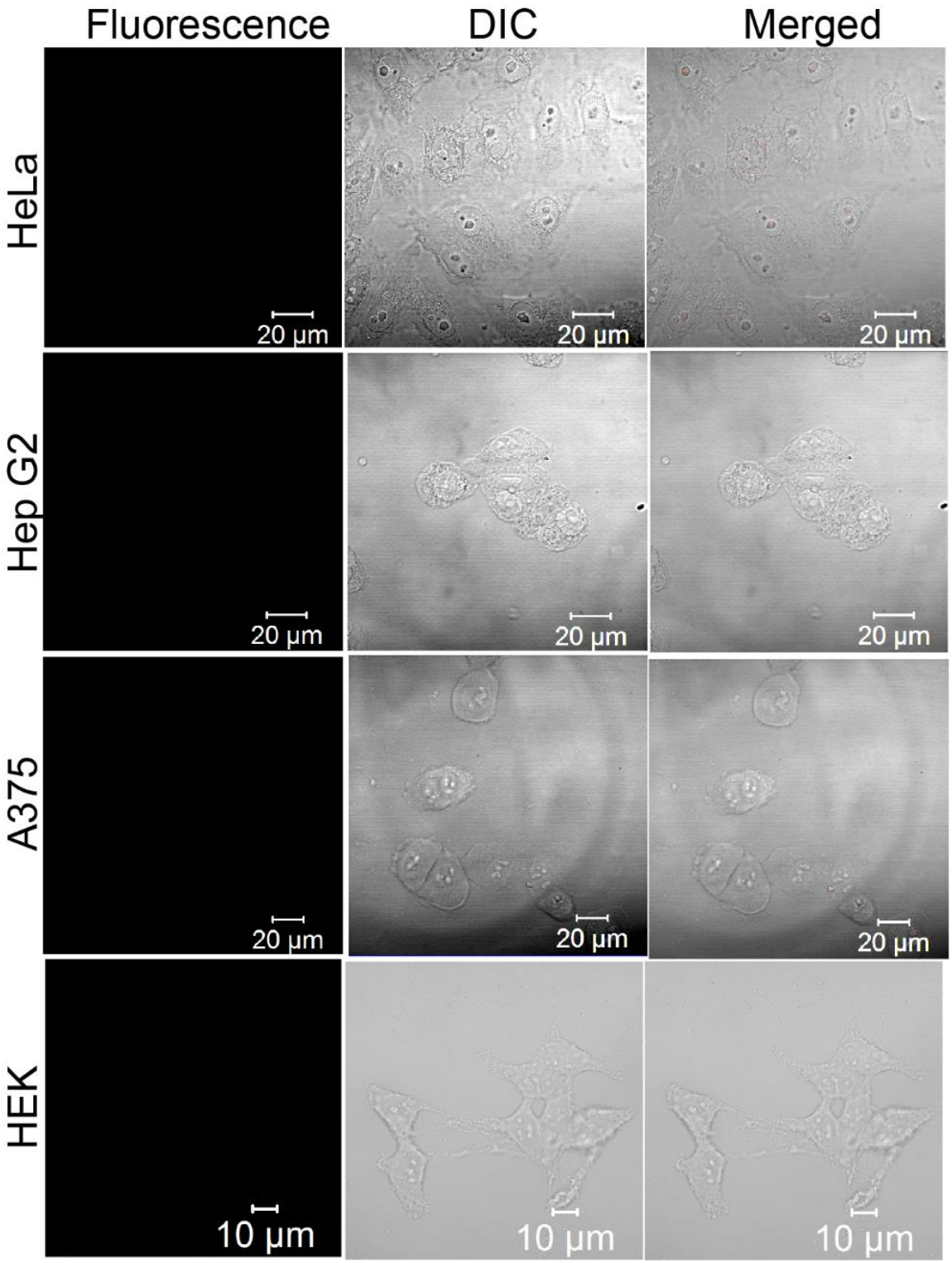

Figure A.3.5. Control CLSM image of HeLa, HepG2, A375 and HEK cells at 355 nm excitation.

A4: Chapter 4

Instruments used for characterization: Transmission electron microscopic images, high resolution transmission electron microscopic images (HR-TEM) and selected area electron diffraction (SAED) patterns and energy-dispersive X-ray spectrum (EDX) were obtained using JEOL JEM 2100F TEM at 200 KV. Nanoparticle dispersions of appropriate concentration were drop-cast on a carbon-coated copper grids, then dried and visualized under TEM. HR-TEM and SAED images were further analyzed using Gatan Digital Micrograph software to find out lattice fringes. Hitachi U-2900 UV-vis spectrophotometer was used for recording uv-vis absorbance spectra. PL emission and excitation were recorded using HORIBA FluoroMax-4 instrument. Powder XRD pattern of $ZnFe_2O_4$ NPs and other samples were recorded using Rigaku TTRAX III X-ray diffractometer. Magnetic measurements to obtain hysteresis loop and saturation magnetization were performed using 7410 series vibrating sample magnetometer. Carl Zeiss confocal LSM 880 was used to obtain fluorescence image of cells. Nikon Coolpix L810 camera was used to acquire digital photographs.

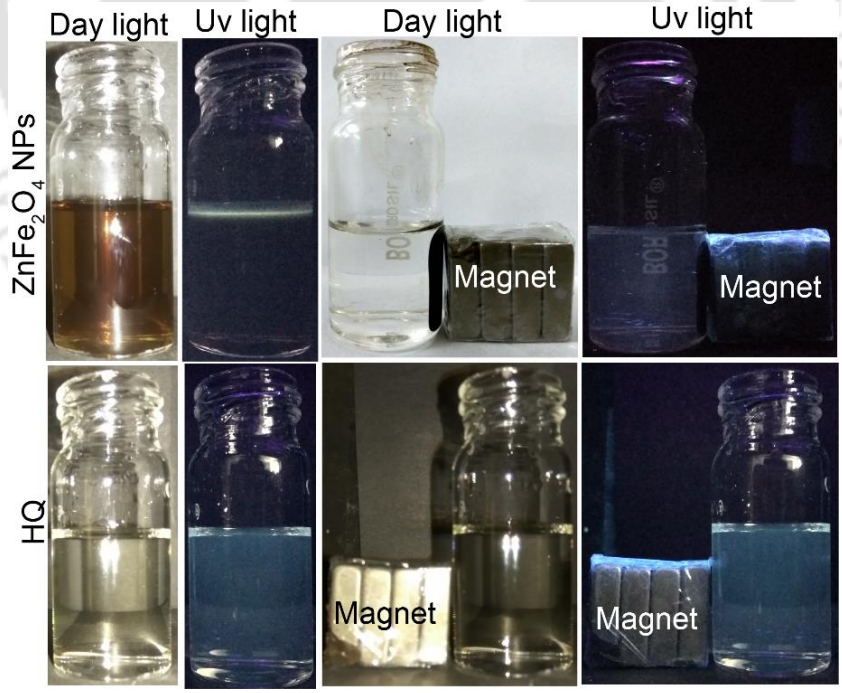

Figure A.4.1. Digital images of $ZnFe_2O_4$ NPs and HQ under day light or UV light and in presence or absence of magnet.

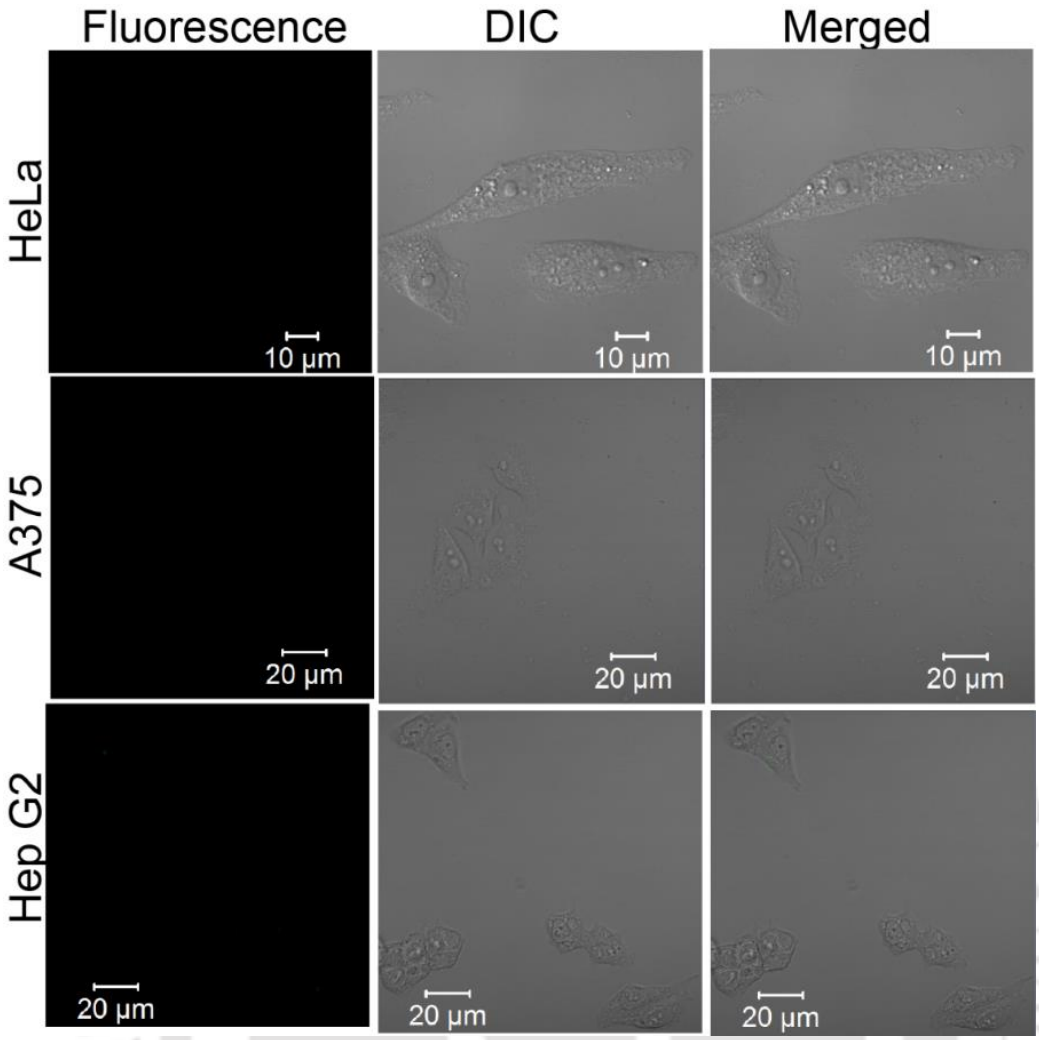

Figure A.4.2. CLSM images of control cells taken in similar sets of conditions as treated one.

A5: Chapter 5

Instruments used for characterization: All the digital Photograph have been taken using Nikon Coolpix L810 camera either in daylight or under Spectroline UV-lamp (365nm) (UV light source). Fluorescence emission and excitation spectra were recorded using HORIBA JobinYvon FluoroMax-4 spectrofluorimeter. UV-vis absorbance spectra were recorded using Hitachi U-2900 UV-vis spectrophotometer. Powder XRD were recorded using Rigaku TTRAX III X-ray diffractometer. Magnetic measurement and hysteresis loop of $ZnFe_2O_4$ NPs and HQCald-ZFNs were obtained from 7410 series vibrating sample magnetometer. TEM images, High resolution TEM (HR-TEM) and Selected Area Electron Diffraction (SAED) patterns and Energy-dispersive X-ray spectrum (EDX) were recorded using JEOL JEM 2100F and JEOL JEM 2100 Transmission Electron Microscope at an operating voltage 200 KV. TEM Samples were prepared by drop casting of dispersion on carbon-coated copper grids. Processing of HR-TEM images to find out IFFT patterns and lattice spacing were carried out using the Gatan Digital Micrograph software. Carl Zeiss laser scanning microscope LSM 880 were used for fluorescence cell imaging.

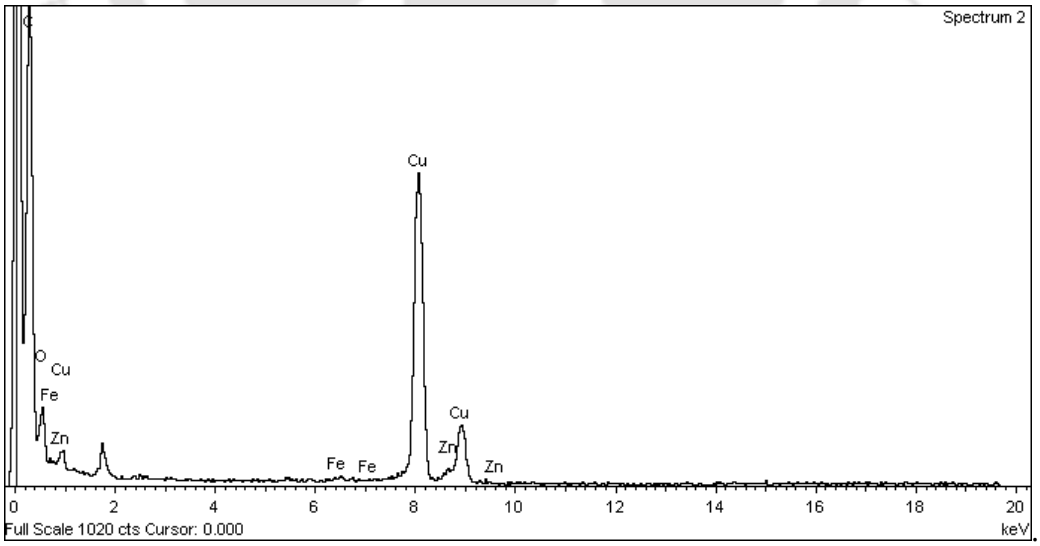

Figure A.5.1. EDX spectrum of HQCald-ZFNs showing presence of both Zn and Fe.

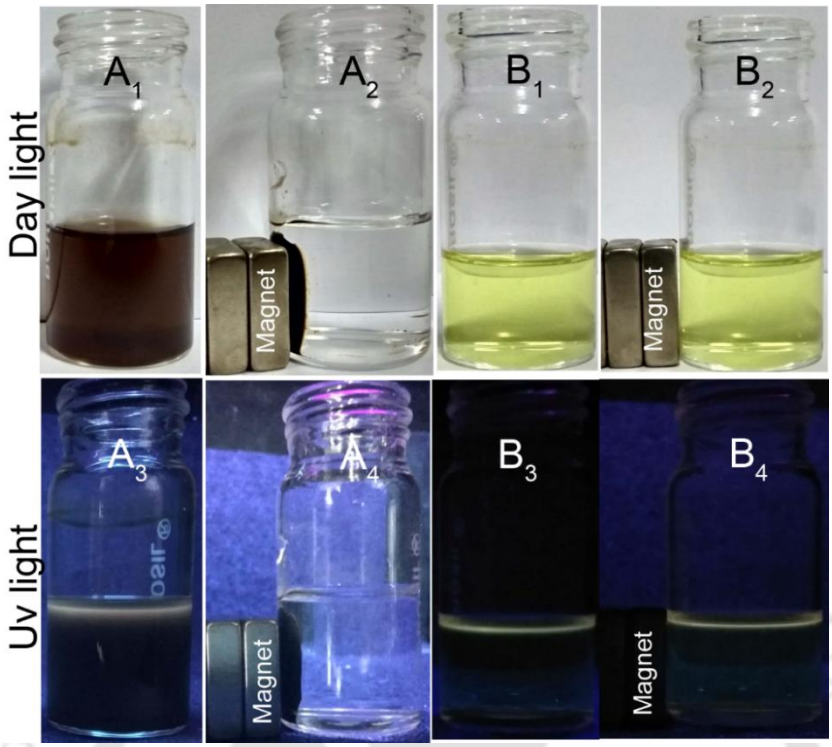

Figure A.5.2. Digital photography of (A) $ZnFe_2O_4$ NPs dispersed in hexane and (B) ethanolic solution of HQCald. Subscript 1,2,3,4 designate in day light, in day light and in presence of magnet, under Uv light (365 nm) and under UV light (365 nm) in presence of magnet respectively.

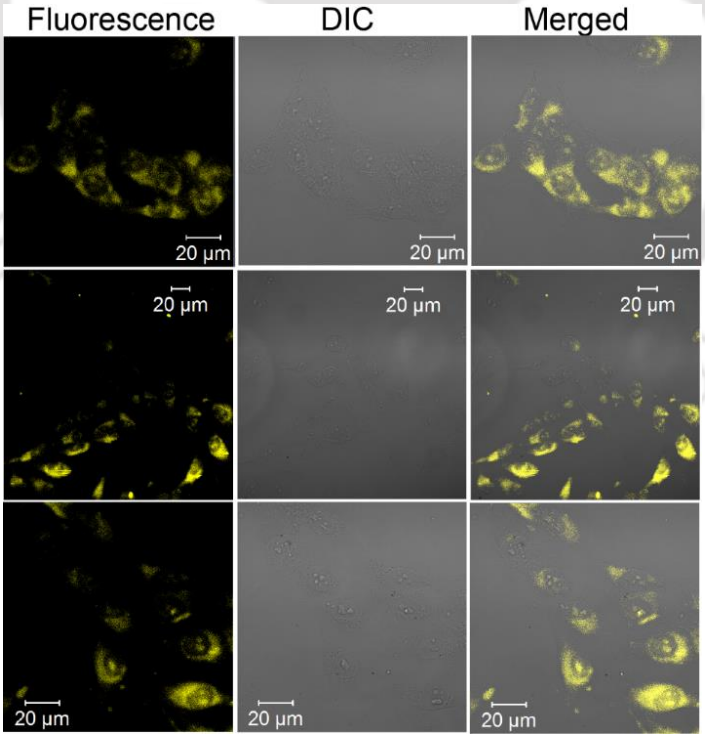

Figure A.5.3. Additional CLSM images of HeLa cells treated with HQCald-ZFNs for 2 h and irradiated with 355 nm laser

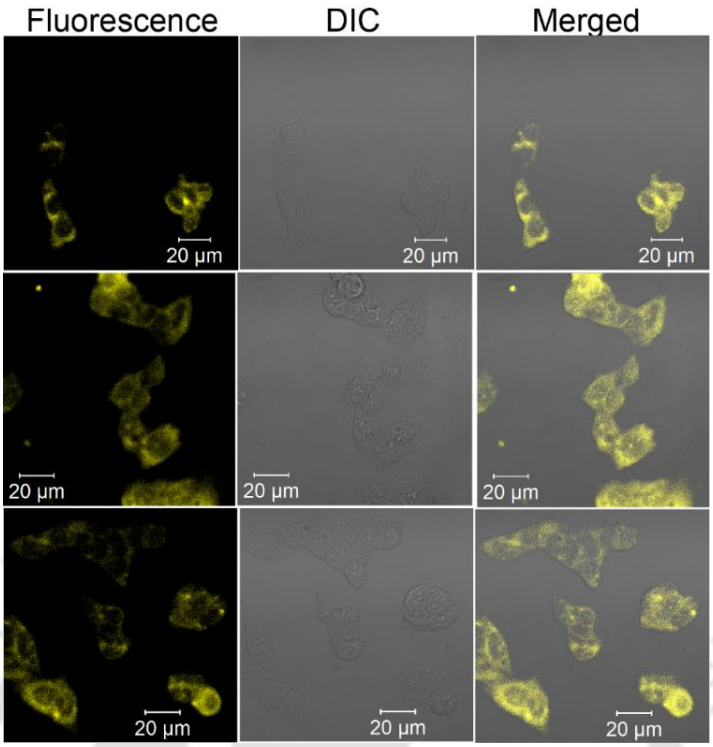

Figure A.5.4. Additional CLSM images of Hep G2 cells treated with HQCald-ZFNs for 2 h and irradiated with 355 nm laser.

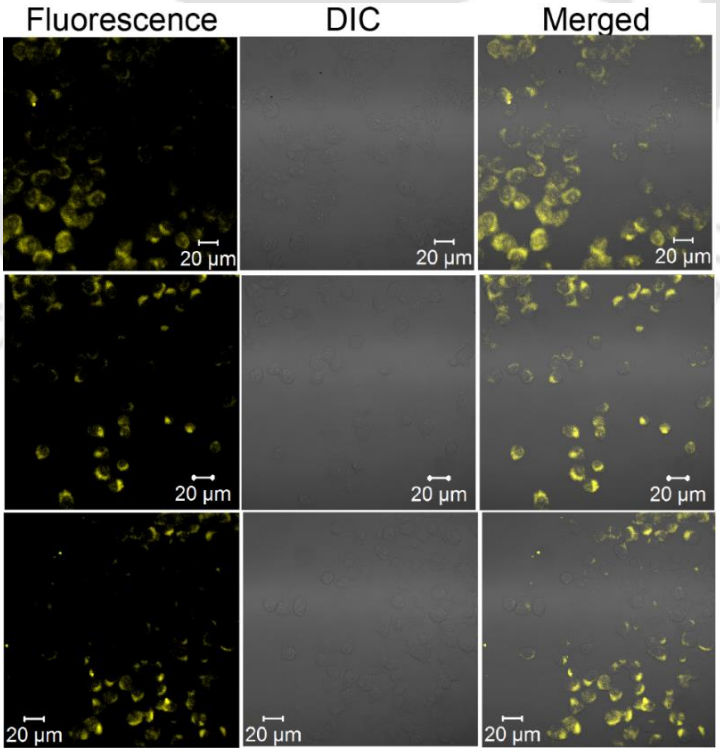

Figure A.5.5. Additional CLSM images of A375 cells treated with HQCald-ZFNs for 2 h and irradiated with 355 nm laser.

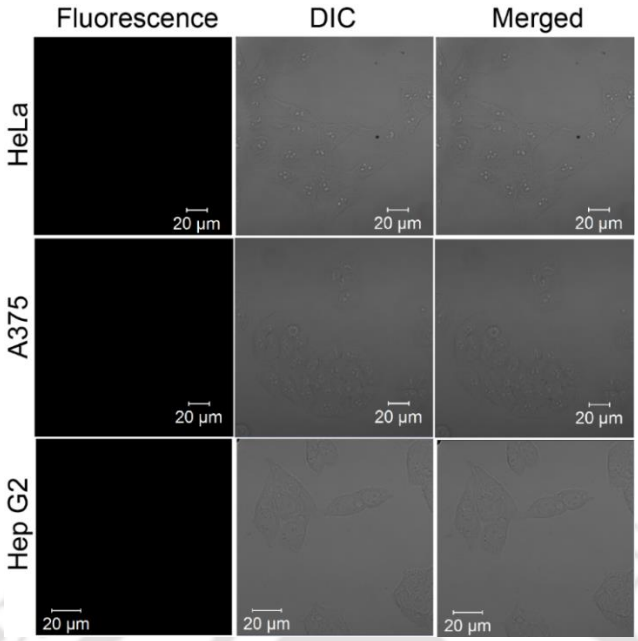

Figure A.5.6. CLSM images of non-treated control cells irradiated with 355 nm laser.

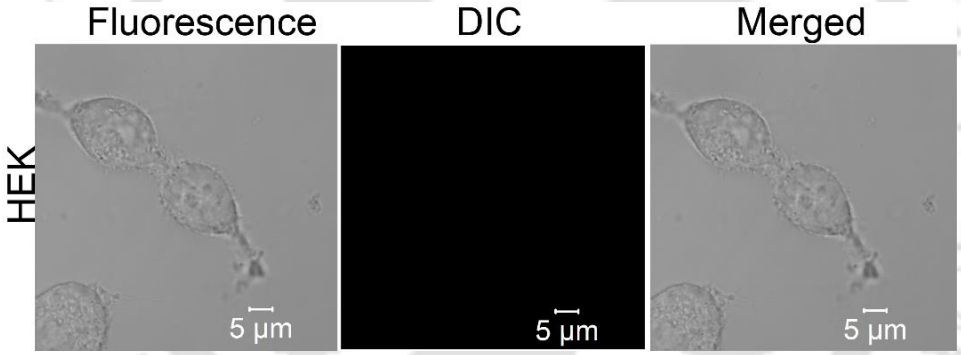

Figure A.5.7. CLSM images control of HEK cells.

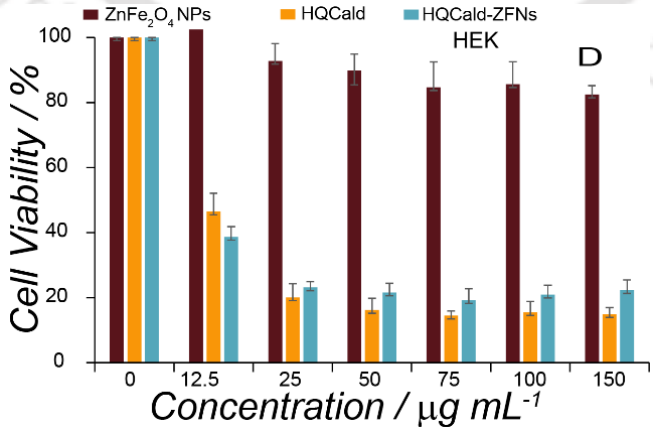

Figure A.5.8. Cell viability of HEK cells treated with different concentrations of $ZnFe_2O_4$ NPs, HQCald and HQCald-ZFNs for 48 h.

List of Publications

1. **Pan, U. N.**; Khandelia, R.; Sanpui, P.; Das, S.; Paul, A.; Chattopadhyay, A. Protein-Based Multifunctional Nanocarriers for Imaging, Photothermal Therapy, and Anticancer Drug Delivery *ACS Appl. Mater. Interfaces.* **2017**, *9*, 19495– 19501. DOI: 10.1021/acsami.6b06099
2. **Pan, U. N.;** Sanpui, P.; Paul, A.; Chattopadhyay, A. Synergistic Anticancer Potential of Artemisinin When Loaded with 8-Hydroxyquinoline-Surface Complexed-Zinc Ferrite Magnetofluorescent Nanoparticles and Albumin Composite. *ACS Appl. Bio Mater.* ***2018,*** *1,* 1229–1235. DOI: 10.1021/acsabm.8b00358
3. **Pan, U. N.;** Sanpui, P.; Paul, A.; Chattopadhyay, A. Surface-Complexed Zinc Ferrite Magnetofluorescent Nanoparticles for Killing Cancer Cells and Single-Particle-Level Cellular Imaging *ACS Appl. Nano Mater.* **2018**. *1*, 2496– 2502. DOI: 10.1021/acsanm.8b00545
4. **Pan, U. N.;** Sanpui, P.; Paul, A.; Chattopadhyay, A. Protein-Nanoparticle Agglomerates as Plasmonic-Magneto-Luminescent Multifunctional Nanocarrier for Imaging and Combination Therapy *ACS Appl. Bio Mater.* **2019**, *28,* 3144-3152. DOI:10.1021/acsabm.9b00210
5. Khandelia, R.; Bhandari, S.; **Pan, U. N.;** Ghosh, S. S.; Chattopadhyay, A. Gold Nanocluster Embedded Albumin Nanoparticles for Two-Photon Imaging of Cancer Cells Accompanying Drug Delivery *Small* **2015,** *11,* 4075– 4081. DOI: 10.1002/smll.201500216
6. Bhandari, S.; Khandelia, R.; **Pan, U. N.;** Chattopadhyay, A. Surface Complexation-Based Biocompatible Magnetofluorescent Nanoprobe for Targeted Cellular Imaging *ACS Appl. Mater. Interfaces* **2015,** *7*, 17552–17557. DOI: 10.1021/acsami.5b04022
7. Pramanik, S.; Bhandari, S.; Roy, S.; **Pan, U. N.;** Chattopadhyay, A. A White Light-Emitting Quantum Dot Complex for Single Particle Level Interaction with Dopamine Leading to Changes in Color and Blinking Profile *Small* **2018**,*14*, 1800323. DOI: 10.1002/smll.201800323

8. Basu, S.; Bhandari, S.; **Pan, U. N.;** Paul, A.; Chattopadhyay, A. Crystalline Nanoscale Assembly of Gold Clusters for Reversible Storage and Sensing of CO_2 via Modulation of Photoluminescence Intermittency *J. Mater. Chem. C* **2018**, *6*, 8205-8211. DOI:10.1039/C8TC02225A
9. Ahmad, K.; Pal, A.; **Pan, U. N.;** Chattopadhyay, A.; Paul, A. Synthesis of Single-Particle Level White-Light Emitting Carbon Dots via a One-Step Microwave Method *J. Mater. Chem. C*, **2018,** *6,* 6691-6697. DOI: 10.1039/c8tc01276h
10. Gayen, C.; Basu, S.; **Pan, U. N.;** Paul, A. Few Particle-Level Chromaticity Index-Based Discrimination of Biothiols Using Chemically Interactive Dual-Emitting Nanoprobe *ACS Omega* **2018**, *3*, 17220−17226. DOI: 10.1021/acsomega.8b02373

Conferences Attended

1. Presented a poster in DAE-BRNS 6th Interdisciplinary Symposium on Materials Chemistry, **ISMC-2016** held at Bhabha Atomic Research Centre, (BARC) Mumbai, India.
2. Presented an oral In **ChemConvene-2017** held at Indian Institute of Technology Guwahati, India.
3. Presented a poster in 5th International Conference on Advanced Nanomaterials and Nanotechnology, **ICANN- 2017** held at Indian Institute of Technology Guwahati, India.

Ph. D. Thesis Evaluation Report

Name of the Candidate : **UDAY NARAYAN PAN**

Roll No. : **126122042**

Department : **Chemistry**

Title of the thesis : **Multifunctionalization of Nanoscale Particles for Cancer Theranostics**

Comments and Suggestions on the Thesis

Indian Examiner

Recommendation: *Based on his work I recommend that Ph.D degree be awarded to Mr. Uday Narayan Pan*

Detailed report

Please find the below comments of the thesis entitled "Multifunctionalization of Nanoscale Particles for Cancer Theranostics" by Mr. Uday Narayan Pan presents development of plasmonic and magneto luminescent nanomaterials for bioimaging, magnetic targeting and plasmonic photothermal therapy. ***The thesis is well written supported by systematically generated results published in reputed journals in the field.*** There are few queries that may be addressed by Mr. Uday Narayan Pan while defending his thesis.

Chapter 2

Comment 1. Magnetic saturation of MFNCs is very low (4.66 emu/g) but the T_2 relaxation is pretty high (448 per mM second) Can this be explained?

Author's response: Iron oxide nanoparticles showed magnetic saturation 28.88 emu/g. Decrease in magnetization from 28.88 emu/g of IONPs to 4.66 emu/g of MFNCs is due to the integration of diamagnetic materials like AuNRs,

BSA and Au nanoclusters, which contribute to the weight only. On the other hand, according to standard convention [*Nat. Commun. 2014, 5, 5093., Chem. Soc. Rev., 2012, 41, 2575–2589*], r_2 relaxivity of the MFNCs was calculated with respect to iron concentration present in MFNCs. Chen et al in their study (Nat. Commun. 2014, 5, 5093.), also observed magnetic saturation to decrease from 63.7 emu/g (Fe_3O_4 NPs) to 15.2 emu/g (silica-CS-SPs) while r2 relaxivity increased from 55.7 mM^{-1} S^{-1} to 402.7 mM^{-1} S^{-1}.

There are some other factors also which influence the r2 relaxivity. Aggregation of magnetic nanoparticles is a major factor known for enhancing r2 relaxivity dramatically [*Nat. Commun. 2014, 5, 5093; Chem. Soc. Rev., 2012, 41, 2575–2589*]. Aggregation of magnetic nanoparticles embedded in a silica nanoparticle can even increase its r2 relaxivity close to its theoretical limits [*Adv. Mater. 2011, 23, 4793–4797*]. Similarly, in our case, the magnetic nanoparticles are embedded in BSA matrix resulting in their close proximity within MFNCs. This could lead to high r2 relaxivity of MFNCs. Moreover, the IONPs used for building the MFNCs were synthesized by thermal decomposition and thereby having better crystallinity compared to IONPs synthesized by co-precipitation method. This also may contribute to higher r2 relaxivity [*J. Phys. Chem. B, 2009, 113,7033–7039, Chem. Soc. Rev., 2012, 41, 2575–2589*] observed for the MFNCs.

Comment 2. In fig 2.13, two photon imaging has only decreased background fluorescence. Is that what intended by using the technique?, as single photon images show fairly good information about particle uptake. In fact, two photon images show Dox predominantly in nucleus, whereas single photon images show some localization in cytoplasm. This requires some introspection.

Authors' response: The photoluminescence of MFNCs having emission at 650 nm, as depicted in the **Scheme 2.1**. and later on experimentally demonstrated in **Figure 2.6**, can be used for imaging the MFNCs inside cancer cells *in vitro* by one-photon (l_{ex} = 488 nm) or two-photon excitation (l_{ex} = 730 nm). Thus, 650 nm emission of the MFNCs will be suitable for *in vitro* imaging of the nanocarriers. Additionally, since the two photon emission (650 nm) and excitation (730 nm) of the MFNCs both lies within the biological window (650-900 nm) suitable for *in*

vivo imaging, the 650 nm emission of the MFNCs could possibly be exploited for *in vivo* imaging with two photon excitation. I believe that the MFNCs having emission maximum at 650 nm and significant emission at higher wavelengths (with ~50% emission intensity around 710 nm) would be useful for effective *in vivo* imaging. Au nanoclusters with similar emission (~650 nm) have been successfully used for *in vivo* imaging (*RSC Adv*., **2015**, 5, 63821–63826, *Nanoscale* **2013**, 5, 1624–1628). For example, Zhang et al. (*RSC Adv*., **2015**, 5, 63821–63826) successfully obtained *in vivo* fluorescent images with the 520 nm excitation and 710 nm emission wavelengths following intra-tumoral injection of Au nanoclusters having emission maximum at 640 nm.

Moreover, as mentioned above, in case of the two-photon imaging the multiphoton laser (730nm) is used which has much better penetration capacity compared to single photon light and due to higher wavelength, it is also less susceptible towards scattering by other cellular components. This could become effective in elimination of the background fluorescence even in case of *in vitro* cell imaging. Dox, on the other hand, always show predominant localization in the nucleus due to its nature of interaction with DNA. In our opinion elimination of background fluorescence following use of multiphoton laser is possibly the reason we did not observed much fluorescence emission intensity in cytoplasm in case of two photon images.

In this regard, the purpose of 650 nm emission as an effective *in vitro* imaging tool and its future potential for *in vivo* imaging have already been discussed in the Thesis (*Page 35*) as below:

"….The results demonstrated that our MFNCs could be probed intracellularly with either conventional one-photon or two-photon imaging. Most importantly, successful two-photon imaging of MFNCs within cancer cells – with excitation and emission falling within the biological window (650-900 nm) – is expected to expand their applicability for effective *in vivo* imaging…."

Chapter 3.

Comment 1. NIR window starts at 650nm and there could be marginal interference from biological molecules. Can the absorption of PML-MF tubed to >650nm? If so how?

Authors' response: In the present multifunctional nanocarrier, as mentioned in the chapter-2, lysozyme helps in agglomeration of the IO@Au NPs. This lysozyme mediated agglomeration of the IO@Au NPs helps in three different ways – (i) the agglomerates have much bigger nanoscale structures compared to IO@Au NPs which have been subsequently coated with BSA-AuNCs to prepare the present PML-MF nanocarriers, (ii) it significantly increases the plasmonic absorbance at the NIR biological spectral window, which helps in improving the plasmonic photothermal ability of the PML-MF nanocarriers, and (iii) like most proteins, lysozymes also possess hydrophobic as well as hydrophilic sites, thus facilitating the loading of chemotherapeutic drug within the PML-MF. Now, if the amount of the lysozymes is increased with respect to the amount of the IO@Au NPs the extent of the agglomeration would increase and the plasmonic absorbance will be more red shifted. Thus, by simply increasing the ratio of lysozymes to IO@Au NPs the absorbance could be shifted to much higher wavelength. Although, increase in the amount of lysozymes with respect to IO@Au NPs would also increase the size of the agglomerates and thus, will increase the overall size of the PML-MF nanocarriers. Very large size PML-MF nanocarriers will negatively impact the passive targeting ability of the nanocarrier following enhanced permeability and retention effect. Thus, a middle ground is chosen in designing PML-MF nanocarrier, where the ratio of lysozyme to IO@Au NPs were adjusted in such a way that the plasmonic photothermal ability is achieved without much affecting the passive targeting ability of it. Moreover, if we start with large size IO@Au NPs it will be easy to achieve absorbance in much higher wavelength in NRI region without much increasing the overall size of the carrier. However, large size IO@Au NPs would be difficult to remove by renal clearance, hence, that approach is avoided.

Comment 2. Quantum yield of AuNCs after encapsulation in PML-MF calculated?

Authors' response: The relative fluorescence quantum yields are calculated with respect to a reference dye. The following formula is used to calculate the quantum yield.

$$Q_s = Q_R \times \frac{I_s}{I_R} \times \frac{A_R}{A_S} \times \frac{\eta_S^2}{\eta_R^2}$$

Where, QS is the quantum yield (Φ) of sample, QR is the quantum yield (Φ) of the reference dye, IS is the area under emission spectrum of sample, IR is the area under emission spectrum of reference dye, AR is the absorbance of the reference dye, AS is the absorbance of the sample, η represents refractive index of the solvent suffix S and R represent sample and reference.

In the present case as it is evident from the **Figure 1** (Thesis figure number **Figure 2.6 A)** the IO@Au NPs has strong absorbance in the same region where of the Au nanocluster absorb light (At 505 nm). Thus, in PML-MF nanocarrier it is not possible to find out the exact contribution in absorbance of Au nanoclusters at 505 nm. Thus, calculation of quantum yield of Au nanocluster from the absorbance data of PML-MF nanocarrier would give highly erroneous result hence, it is avoided in the present study.

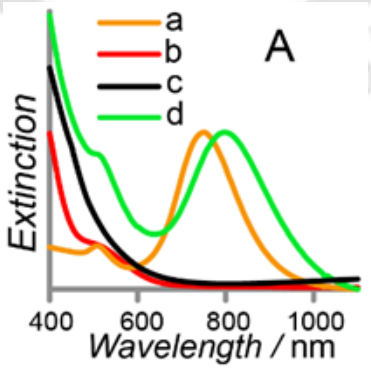

Figure 1. (A) Normalized extinction spectra of (a) Au NRs, (b) Au nanoclusters, (c) IONPs and (d) MFNCs.

Comment 3. Optical interaction between Au nanoclusters and Au nanoparticles is discussed well in literature. Keeping that in mind, will there be any photothermal response if we excite the Au nanocluster in blue region so that its emission at 650 nm excites plasmons of IO@Au?

Authors' response: Photothermal response – if any- would be low for Au nanoclusters as the absorbed light is emitted with high efficiency. Moreover, blue light would not be suitable for *in vivo* photothermal applications even if it indirectly excite the plasmon of IO@Au NPs.

Comment 4. Fig 3.15 and Fig 3.16 shows predominant localization of Dox in nucleus. Dox release within 2h seems like burst release. Should this be concern for drug delivery system?

Authors' response: Doxorubicin is known to have strong interaction with DNA with significant enhancement of fluorescence quantum yield (*Mol. Pharmaceutics2010761959-1973.).* Due to this, it is found that doxorubicin treated cells always shows a significant localization of the fluorescence emission from the nucleus of the cell compared to the cytoplasm of the cells *(Small 11 (33), 4075-4081 ; Small 9 (20), 3493-3493)*.

The loading and release of doxorubicin (Dox) in PML-MF nanocarriers is mainly based on the hydrophobic, hydrophilic, hydrogen boding and Van der Waals interaction with the BSA (J. Mater. Chem. B, 2013, 1,3906; Molecules 2016, 21, 1706; Biochem Biophys Rep. 2016 Sep; 7: 201–205). These interactions of Dox and BSA are basically reversible in nature, permitting encapsulated molecules to be released (Journal of Drug Delivery Volume 2011, Article ID 370308, 15 pages). Diffusion-driven drug release could be the best possible release mechanism for the release of Dox from PML-MF nanocarrier (Journal of Drug Delivery Volume 2011, Article ID 370308, 15 pages). This kind of interactions mostly shows burst release of the drug. We agree with the examiner's concern that the release of the drug in controlled fashion is always desirable for any drug delivery vehicle. We did not achieve that in the present study. Although, the present nanocarrier could be modified to achieve controlled or pH-triggered delivery of the drug.

Moreover, we have observed only 30% release of the Dox over 24h of time in pH buffer 7.4, so, rest of the drug could be photothermally triggered once the carrier goes inside the cells.

Chapter 5

The claim high magnetic saturation for the value 12.7 emu/g, is it appropriate?

Authors' response: IONPs were synthesized following thermal decomposition of iron oleate complexes. In this method highly crystalline IONPs form and show very high saturation magnetization *(Nature Materials volume 3, pages891–895 2004).* In the present case, IONPs showed saturation magnetization 20.9 emu g^{-1}, which was further reduced to 12.7 emu g^{-1} following contribution of diamagnetic BSA and complexing ligand.

Based on his work I recommend that Ph.D degree be awarded to Mr. Uday Narayan Pan.

Abroad Examiner

Recommendation: ***The thesis is commended for the award of the Ph.D. degree.***

Detailed report

The thesis describes the synthesis and *in vitro* application of multi-functional nanostructures comprising plasmonic nanoparticles, magnetic nanoparticles loaded with drugs for cancer theranostics. **The ideas of combining different**

functional nanoparticles is innovative and the thesis represents an advance in nanomedicine. Some points that should be discussed include.

Comment 1: The summary and future prospects chapter is brief. It is important to note that all the experiments are *in vitro* and translational hurdles to apply these novel therapeutics in patients need to be discussed. Specifically, the combined multifunctional nanostructures as seen in Fig 2.4 appear large and disorganized. Is there a way to create synthetic route for monodisperse structure? Also, due to the large size, injection into the vascular system and penetration into tumors may be difficult. As such the thesis would benefit from discussion of transport of these structures and potential applicability *in vivo.*

Comment 2: The thesis would benefit by discussion of the synthesis rationale. What were the different approaches tried to combine the different components, and why was one chosen over another? How does the DOX and other drug loading vary with the different synthetic approaches. What is the role of the protein and why were the specific protein chosen?

Authors' response: In responses to the **Comment-1 and Comment-2** the following part (Marked in **blue**) is included in the summery and future prospects of the present thesis.

Chapter-6

Summary and Future Prospects

"In summary, the present thesis reports the fabrication of four different multifunctional theranostics nanomaterials (MFTNPs) for potential cancer theranostics. This has been achieved by: (i) by assembling gold nanorods, iron oxide nanoparticles, and gold nanoclusters within BSA nanoparticles and subsequently loading doxorubicin in it, (ii) preparing lysozyme mediated nanoscale aggregates of gold coated ironoxide core-shell nanoparticles followed

by coating them with luminescent BSA stabilized gold nanoclusters and loading chemotherapeutic drug doxorubicin in it, (iii) by developing green emitting complexes on the surface of zinc ferrite nanoparticles with HQ and subsequently loading artemisinin on it, and (iv) fabricating yellow emitting complexes on the surface of zinc ferrite nanoparticles with derivative of HQ 8-hydroxy-2-quinolinecarboxaldehyde. All the MFTNPs developed here has been demonstrated for fluorescent bioimaging, *in vitro* magnetic targeting and anticancer efficacy. Moreover, some of them have also been demonstrated for photothermal therapy, combination therapy, two-photon or single particle based bioimaging and magnetic resonance imaging. Taken together, all the MFTNPs showed significant cancer theranostics effect in *in vitro* model. However, future studies should be carried out in animal models in order to employ them clinical treatments. Additionally, the unification strategies used here to fabricate MFTNPs namely use of protein matrix and surface complexation are versatile in nature and hence should be further explored for the development of newer MFTNPs with novel theranostics potential.

The design and the development of different MFTNPs in the present thesis was carried out through systematic modification of one from the other with the objective to mainly reduce the complexity of the system, to make it more robust and to ultimately achieve all the functionalities in a single nanostructure. In the second chapter, all the different components AuNRs, IONPs and Au nanoclusters were separately incorporated into BSA nanoparticle to achieve plasmonic and magneto fluorescent properties. In the third chapter, the complexity was reduced by using a single nanomaterial (IO@Au NPs) for both plasmonic and magnetic functionalities instead of using two separate materials. And the robustness of the system was increased by coating the IONPs with Au to protect the IONPs in acidic environment of stomach. In the fourth chapter surface complexation reaction was carried out on the magnetic zinc ferrite nanoparticle's surface to achieve a single nanoparticle with magneto-fluorescent characteristic. After that the drug artemisinin was loaded into it to achieve the anticancer effect. In chapter five, the complexity was further reduced and the robustness was increased by simply replacing the surface complexing ligand HQ with an anticancer active ligand 8-

hydroxy-2-quinolinecarboxaldehyde, which eliminate the requirement of an additional drug.

In the second and third chapters, Dox was used as the chemotherapeutic drug. Basically, the loading and release of Dox in these two nanocarriers are mainly based on the hydrophobic, hydrophilic, hydrogen boding and Van der Waals interaction with the protein BSA and lysozyme with Dox. These interactions of Dox and proteins are basically reversible in nature, permitting encapsulated molecules to be released. We observed ~92% encapsulation of Dox in the Chapter-2 (in case of MFNCs) when 147.5 L^{-1} MFNCs was incubated with 3.28 μg mL^{-1} of Dox. In the third chapter (in case of PML-MFNCs), when 3.28 μg mL^{-1} of Dox was incubated with 162.3 μg mL^{-1} PML-MF nanocarrier 82% encapsulation was observed. From these data it is clear that the encapsulation of Dox/mg of carrier was slightly higher in MFNCs compared to PML-MF nanocarrier. This could be because of the differences in composition of the proteins and contribution of the protein to the overall mass of the nanocarriers. In the fourth chapter, the amount of artemisinin present in 1 mg of drug loaded HQ-ZFNPs@BSA was calculated to be 0.23 μg with encapsulation efficiency 79%. This result could not be compared with the encapsulation efficiency of the Chapter-1 or Chapter-2 as the drug is different thus, the interaction of the drug with BSA would also be different. In the fourth chapter, the drug 8-hydroxy-2-quinolinecarboxaldehyde itself acts as the complexing agent for the surface Zn^{2+} ions present on zinc ferrite nanoparticles thus the encapsulation efficacy was not possible to be calculated.

Among many proteins, BSA was chosen for designing the experiments reported in the thesis because albumin proteins are present in blood plasma and thus immunological responses against it would be very limited and moreover due to structural similarities, BSA could easily be replaced with HSA for the preparation of similar nanocarriers for *in vivo* applications. In addition, some types of tumors (for examples prostate, lung and breast) possess over-expressed albumin receptors, hence naturally facilitating preferential accumulation of albumin based nanocarriers onto the tumor. Furthermore, the only clinically approved nanocarrier, abraxane, is also based on albumin protein and pharmacokinetics of this has been extensively studied, thus, pharmacokinetics

study of albumin-based carriers is well established. Lysozyme also helps in limiting immunological responses and easily forms aggregates in presence of nanoparticles. Due to the above reasons, BSA and lysozyme have been chosen for the developments of all the nanocarriers.

Although, the present thesis did not involve direct *in vivo* experiments, yet all the nanocarriers were designed keeping in mind future *in vivo* applicability. Towards the goal, the primary focus was to use inorganic nanoparticles containing only non-toxic metals. Hence inorganic nanoparticles made of iron, zinc and gold were used in this study as none of these elements demonstrate toxicity. Secondly, all the nanocarriers designed in the present thesis contain albumin protein on their surface. As discussed earlier, presence of albumin on the surface of the nanocarriers could restrict the immunological responses and may also achieve targeting capability for certain type of cancer. In addition, for any nanocarrier to acts as a drug delivery vehicle, it is important to have high stability in blood during circulation in the body. In this regard we have tested the stability of the nanocarriers in human blood serum. We found all the nanocarriers in the present thesis work have high stability in human blood serum for at least 24 h. Another important factor for *in vivo* application is the size of the nanocarriers to achieve passive targeting. In chapter-2 the reported average size of the nanocarrier is 120.5 ± 27.6 nm and the average hydrodynamic diameter (δH) of water-dispersed MFNCs was estimated to be 203.1 nm; this size rage is within the limit to achieve passive targeting. In chapter-4 and chapter-5, the size of the nanocarrier reported is around 10 nm; this sized nanocarriers could also be helpful for passive targeting as the size range for the nanocarrier for passive targeting is considered to be 10 nm-200 nm. The PML-MF nanocarrier (Chapter-3) is relatively larger in size (average hydrodynamic diameter 711 nm). This higher sized nanocarriers ideally would not be able to achieve passive targeting; however, the smaller sized PML-MF nanocarriers could be developed along the lines of the synthetic protocol stated in this chapter with a modification of using reduced quantity of lysozyme with respect to the IO@Au NPs.

In vivo studies and modification of the nanocarrier based on the findings of those *in vivo* responses would be one the most important continuity of the present

thesis towards future commercial realization of these MFTNPs. Moreover, integration of the active targeting following surface modification of the nanocarrier, loading of multiple drugs together and achieving magnetic hyperthermia along with plasmonic photothermal therapy are some important aspect which could be explored in future."

Comment-3. The overall formatting of the thesis is excellent. However, there are minor grammar issues.

Authors' response: Grammar mistakes has been corrected in the introduction section of the thesis.

The following part (marked in **blue/~~red~~**) is modified in the thesis……..

Page 2:

"**…..** Nanomaterials composed of noble metals like gold, silver and palladium interact with external electromagnetic radiations.[6-7] Under the exposure of a particular wavelength of light surface electrons of these nanomaterials (depending upon their size, shape and constituent metals) form plasmons (coherent oscillation of surface electrons), that cause strong extinction of light (absorption and scattering)……."

Page 4:

"**……**Properties like small~~er~~ and uniform size, high biocompatibility and easy surface functionalization also enhanced their demand for clinical cancer theranostics……."

Page 5:

"……..If the frequency of the alternating magnetic field is sufficiently high, a very small quantity of superparamagnetic nanoparticles may increase the local temperature of the disease sites and resulting in killing of the cancerous cells and thus making them desirable for reducing of collateral damage……"

Page 14:

"……..Nanoparticle surfaces facilitate partial unfolding of the Lyz - which enmesh ~~other~~ more protein molecules and nanoparticles resulting to the agglomeration of the AuNPs…."

Page15:

"……..Thus, the strategy of the formation of inorganic complexes, with anticancer activities, on the surface of magnetic metal oxide nanoparticles, could be used as an alternative method for the development of multifunctional theranostic nanomaterials……"

Overall, **this is a very exciting body of work with peer-reviewed publications in high quality journals.** The combinations of different modalities could definitely advance cancer nanomedicine. **The thesis is well written** but could benefit from a discussion of rational behind different approaches and barriers/challenges for translation *in vivo* in terms of size transport, stability, tumor targeting by EPR or other effects and efficacy, all of which are affected by combining the modalities.

Permissions

TH-2122_126122042

TH-2122_126122042

ELSEVIER LICENSE
TERMS AND CONDITIONS

Dec 24, 2018

This Agreement between IIT GUWAHATI -- UDAY PAN ("You") and Elsevier ("Elsevier") consists of your license details and the terms and conditions provided by Elsevier and Copyright Clearance Center.

License Number	4495460909137
License date	Dec 24, 2018
Licensed Content Publisher	Elsevier
Licensed Content Publication	Trends in Food Science & Technology
Licensed Content Title	Nanocarriers based delivery of nutraceuticals for cancer prevention and treatment: A review of recent research developments
Licensed Content Author	Divya Arora,Sundeep Jaglan
Licensed Content Date	Aug 1, 2016
Licensed Content Volume	54
Licensed Content Issue	n/a
Licensed Content Pages	13
Start Page	114
End Page	126
Type of Use	reuse in a thesis/dissertation
Intended publisher of new work	other
Portion	figures/tables/illustrations
Number of figures/tables/illustrations	1
Format	both print and electronic
Are you the author of this Elsevier article?	No
Will you be translating?	No
Original figure numbers	Fig. 5
Title of your thesis/dissertation	Multifunctionalization of Nanoscale Particles for Cancer Theranostics
Publisher of new work	Indian Institute of Technology Guwahati
Expected completion date	Jan 2019
Estimated size (number of pages)	1
Requestor Location	IIT GUWAHATI BRAHMAPUTRA HOSTEL IIT GUWAHATI KAMRUP GUWAHATI, ASSAM 781039 India Attn: IIT GUWAHATI
Publisher Tax ID	GB 494 6272 12

Total 0.00 USD

Terms and Conditions

INTRODUCTION

1. The publisher for this copyrighted material is Elsevier. By clicking "accept" in connection with completing this licensing transaction, you agree that the following terms and conditions apply to this transaction (along with the Billing and Payment terms and conditions established by Copyright Clearance Center, Inc. ("CCC"), at the time that you opened your Rightslink account and that are available at any time at http://myaccount.copyright.com).

GENERAL TERMS

2. Elsevier hereby grants you permission to reproduce the aforementioned material subject to the terms and conditions indicated.
3. Acknowledgement: If any part of the material to be used (for example, figures) has appeared in our publication with credit or acknowledgement to another source, permission must also be sought from that source. If such permission is not obtained then that material may not be included in your publication/copies. Suitable acknowledgement to the source must be made, either as a footnote or in a reference list at the end of your publication, as follows:
"Reprinted from Publication title, Vol /edition number, Author(s), Title of article / title of chapter, Pages No., Copyright (Year), with permission from Elsevier [OR APPLICABLE SOCIETY COPYRIGHT OWNER]." Also Lancet special credit - "Reprinted from The Lancet, Vol. number, Author(s), Title of article, Pages No., Copyright (Year), with permission from Elsevier."
4. Reproduction of this material is confined to the purpose and/or media for which permission is hereby given.
5. Altering/Modifying Material: Not Permitted. However figures and illustrations may be altered/adapted minimally to serve your work. Any other abbreviations, additions, deletions and/or any other alterations shall be made only with prior written authorization of Elsevier Ltd. (Please contact Elsevier at permissions@elsevier.com). No modifications can be made to any Lancet figures/tables and they must be reproduced in full.
6. If the permission fee for the requested use of our material is waived in this instance, please be advised that your future requests for Elsevier materials may attract a fee.
7. Reservation of Rights: Publisher reserves all rights not specifically granted in the combination of (i) the license details provided by you and accepted in the course of this licensing transaction, (ii) these terms and conditions and (iii) CCC's Billing and Payment terms and conditions.
8. License Contingent Upon Payment: While you may exercise the rights licensed immediately upon issuance of the license at the end of the licensing process for the transaction, provided that you have disclosed complete and accurate details of your proposed use, no license is finally effective unless and until full payment is received from you (either by publisher or by CCC) as provided in CCC's Billing and Payment terms and conditions. If full payment is not received on a timely basis, then any license preliminarily granted shall be deemed automatically revoked and shall be void as if never granted. Further, in the event that you breach any of these terms and conditions or any of CCC's Billing and Payment terms and conditions, the license is automatically revoked and shall be void as if never granted. Use of materials as described in a revoked license, as well as any use of the materials beyond the scope of an unrevoked license, may constitute copyright infringement and publisher reserves the right to take any and all action to protect its copyright in the materials.
9. Warranties: Publisher makes no representations or warranties with respect to the licensed material.
10. Indemnity: You hereby indemnify and agree to hold harmless publisher and CCC, and their respective officers, directors, employees and agents, from and against any and all
TH-2122_126122042

claims arising out of your use of the licensed material other than as specifically authorized pursuant to this license.
11. No Transfer of License: This license is personal to you and may not be sublicensed, assigned, or transferred by you to any other person without publisher's written permission.
12. No Amendment Except in Writing: This license may not be amended except in a writing signed by both parties (or, in the case of publisher, by CCC on publisher's behalf).
13. Objection to Contrary Terms: Publisher hereby objects to any terms contained in any purchase order, acknowledgment, check endorsement or other writing prepared by you, which terms are inconsistent with these terms and conditions or CCC's Billing and Payment terms and conditions. These terms and conditions, together with CCC's Billing and Payment terms and conditions (which are incorporated herein), comprise the entire agreement between you and publisher (and CCC) concerning this licensing transaction. In the event of any conflict between your obligations established by these terms and conditions and those established by CCC's Billing and Payment terms and conditions, these terms and conditions shall control.
14. Revocation: Elsevier or Copyright Clearance Center may deny the permissions described in this License at their sole discretion, for any reason or no reason, with a full refund payable to you. Notice of such denial will be made using the contact information provided by you. Failure to receive such notice will not alter or invalidate the denial. In no event will Elsevier or Copyright Clearance Center be responsible or liable for any costs, expenses or damage incurred by you as a result of a denial of your permission request, other than a refund of the amount(s) paid by you to Elsevier and/or Copyright Clearance Center for denied permissions.

LIMITED LICENSE

The following terms and conditions apply only to specific license types:
15. **Translation**: This permission is granted for non-exclusive world **English** rights only unless your license was granted for translation rights. If you licensed translation rights you may only translate this content into the languages you requested. A professional translator must perform all translations and reproduce the content word for word preserving the integrity of the article.
16. **Posting licensed content on any Website**: The following terms and conditions apply as follows: Licensing material from an Elsevier journal: All content posted to the web site must maintain the copyright information line on the bottom of each image; A hyper-text must be included to the Homepage of the journal from which you are licensing at http://www.sciencedirect.com/science/journal/xxxxx or the Elsevier homepage for books at http://www.elsevier.com; Central Storage: This license does not include permission for a scanned version of the material to be stored in a central repository such as that provided by Heron/XanEdu.
Licensing material from an Elsevier book: A hyper-text link must be included to the Elsevier homepage at http://www.elsevier.com . All content posted to the web site must maintain the copyright information line on the bottom of each image.

Posting licensed content on Electronic reserve: In addition to the above the following clauses are applicable: The web site must be password-protected and made available only to bona fide students registered on a relevant course. This permission is granted for 1 year only. You may obtain a new license for future website posting.
17. **For journal authors:** the following clauses are applicable in addition to the above:
Preprints:
A preprint is an author's own write-up of research results and analysis, it has not been peer-reviewed, nor has it had any other value added to it by a publisher (such as formatting, copyright, technical enhancement etc.).
Authors can share their preprints anywhere at any time. Preprints should not be added to or enhanced in any way in order to appear more like, or to substitute for, the final versions of
TH-2122_126122042

articles however authors can update their preprints on arXiv or RePEc with their Accepted Author Manuscript (see below).
If accepted for publication, we encourage authors to link from the preprint to their formal publication via its DOI. Millions of researchers have access to the formal publications on ScienceDirect, and so links will help users to find, access, cite and use the best available version. Please note that Cell Press, The Lancet and some society-owned have different preprint policies. Information on these policies is available on the journal homepage.
Accepted Author Manuscripts: An accepted author manuscript is the manuscript of an article that has been accepted for publication and which typically includes author-incorporated changes suggested during submission, peer review and editor-author communications.
Authors can share their accepted author manuscript:

- immediately
  - via their non-commercial person homepage or blog
  - by updating a preprint in arXiv or RePEc with the accepted manuscript
  - via their research institute or institutional repository for internal institutional uses or as part of an invitation-only research collaboration work-group
  - directly by providing copies to their students or to research collaborators for their personal use
  - for private scholarly sharing as part of an invitation-only work group on commercial sites with which Elsevier has an agreement
- After the embargo period
  - via non-commercial hosting platforms such as their institutional repository
  - via commercial sites with which Elsevier has an agreement

In all cases accepted manuscripts should:

- link to the formal publication via its DOI
- bear a CC-BY-NC-ND license - this is easy to do
- if aggregated with other manuscripts, for example in a repository or other site, be shared in alignment with our hosting policy not be added to or enhanced in any way to appear more like, or to substitute for, the published journal article.

Published journal article (JPA): A published journal article (PJA) is the definitive final record of published research that appears or will appear in the journal and embodies all value-adding publishing activities including peer review co-ordination, copy-editing, formatting, (if relevant) pagination and online enrichment.
Policies for sharing publishing journal articles differ for subscription and gold open access articles:
Subscription Articles: If you are an author, please share a link to your article rather than the full-text. Millions of researchers have access to the formal publications on ScienceDirect, and so links will help your users to find, access, cite, and use the best available version.
Theses and dissertations which contain embedded PJAs as part of the formal submission can be posted publicly by the awarding institution with DOI links back to the formal publications on ScienceDirect.
If you are affiliated with a library that subscribes to ScienceDirect you have additional private sharing rights for others' research accessed under that agreement. This includes use for classroom teaching and internal training at the institution (including use in course packs and courseware programs), and inclusion of the article for grant funding purposes.
Gold Open Access Articles: May be shared according to the author-selected end-user license and should contain a CrossMark logo, the end user license, and a DOI link to the formal publication on ScienceDirect.
Please refer to Elsevier's posting policy for further information.

TH-2122_126122042

18. **For book authors** the following clauses are applicable in addition to the above: Authors are permitted to place a brief summary of their work online only. You are not allowed to download and post the published electronic version of your chapter, nor may you scan the printed edition to create an electronic version. **Posting to a repository:** Authors are permitted to post a summary of their chapter only in their institution's repository.
19. **Thesis/Dissertation**: If your license is for use in a thesis/dissertation your thesis may be submitted to your institution in either print or electronic form. Should your thesis be published commercially, please reapply for permission. These requirements include permission for the Library and Archives of Canada to supply single copies, on demand, of the complete thesis and include permission for Proquest/UMI to supply single copies, on demand, of the complete thesis. Should your thesis be published commercially, please reapply for permission. Theses and dissertations which contain embedded PJAs as part of the formal submission can be posted publicly by the awarding institution with DOI links back to the formal publications on ScienceDirect.

Elsevier Open Access Terms and Conditions
You can publish open access with Elsevier in hundreds of open access journals or in nearly 2000 established subscription journals that support open access publishing. Permitted third party re-use of these open access articles is defined by the author's choice of Creative Commons user license. See our open access license policy for more information.
Terms & Conditions applicable to all Open Access articles published with Elsevier:
Any reuse of the article must not represent the author as endorsing the adaptation of the article nor should the article be modified in such a way as to damage the author's honour or reputation. If any changes have been made, such changes must be clearly indicated.
The author(s) must be appropriately credited and we ask that you include the end user license and a DOI link to the formal publication on ScienceDirect.
If any part of the material to be used (for example, figures) has appeared in our publication with credit or acknowledgement to another source it is the responsibility of the user to ensure their reuse complies with the terms and conditions determined by the rights holder.
Additional Terms & Conditions applicable to each Creative Commons user license:
CC BY: The CC-BY license allows users to copy, to create extracts, abstracts and new works from the Article, to alter and revise the Article and to make commercial use of the Article (including reuse and/or resale of the Article by commercial entities), provided the user gives appropriate credit (with a link to the formal publication through the relevant DOI), provides a link to the license, indicates if changes were made and the licensor is not represented as endorsing the use made of the work. The full details of the license are available at http://creativecommons.org/licenses/by/4.0.
CC BY NC SA: The CC BY-NC-SA license allows users to copy, to create extracts, abstracts and new works from the Article, to alter and revise the Article, provided this is not done for commercial purposes, and that the user gives appropriate credit (with a link to the formal publication through the relevant DOI), provides a link to the license, indicates if changes were made and the licensor is not represented as endorsing the use made of the work. Further, any new works must be made available on the same conditions. The full details of the license are available at http://creativecommons.org/licenses/by-nc-sa/4.0.
CC BY NC ND: The CC BY-NC-ND license allows users to copy and distribute the Article, provided this is not done for commercial purposes and further does not permit distribution of the Article if it is changed or edited in any way, and provided the user gives appropriate credit (with a link to the formal publication through the relevant DOI), provides a link to the license, and that the licensor is not represented as endorsing the use made of the work. The full details of the license are available at http://creativecommons.org/licenses/by-nc-nd/4.0.
Any commercial reuse of Open Access articles published with a CC BY NC SA or CC BY NC ND license requires permission from Elsevier and will be subject to a fee.
Commercial reuse includes:
TH-2122_126122042

- Associating advertising with the full text of the Article
- Charging fees for document delivery or access
- Article aggregation
- Systematic distribution via e-mail lists or share buttons

Posting or linking by commercial companies for use by customers of those companies.

20. **Other Conditions**:

v1.9

Questions? customercare@copyright.com or +1-855-239-3415 (toll free in the US) or +1-978-646-2777.

TH-2122_126122042

JOHN WILEY AND SONS LICENSE TERMS AND CONDITIONS

Dec 24, 2018

This Agreement between IIT GUWAHATI -- UDAY PAN ("You") and John Wiley and Sons ("John Wiley and Sons") consists of your license details and the terms and conditions provided by John Wiley and Sons and Copyright Clearance Center.

License Number	4495460566996
License date	Dec 24, 2018
Licensed Content Publisher	John Wiley and Sons
Licensed Content Publication	Small
Licensed Content Title	Gold Nanoparticle–Protein Agglomerates as Versatile Nanocarriers for Drug Delivery
Licensed Content Author	Rumi Khandelia, Amit Jaiswal, Siddhartha Sankar Ghosh, et al
Licensed Content Date	Feb 27, 2013
Licensed Content Volume	9
Licensed Content Issue	20
Licensed Content Pages	12
Type of use	Dissertation/Thesis
Requestor type	University/Academic
Format	Print and electronic
Portion	Figure/table
Number of figures/tables	1
Original Wiley figure/table number(s)	Scheme 1
Will you be translating?	No
Title of your thesis / dissertation	Multifunctionalization of Nanoscale Particles for Cancer Theranostics
Expected completion date	Jan 2019
Expected size (number of pages)	1
Requestor Location	IIT GUWAHATI BRAHMAPUTRA HOSTEL IIT GUWAHATI KAMRUP GUWAHATI, ASSAM 781039 India Attn: IIT GUWAHATI
Publisher Tax ID	EU826007151
Total	0.00 USD
Terms and Conditions	

TERMS AND CONDITIONS

This copyrighted material is owned by or exclusively licensed to John Wiley & Sons, Inc. or one of its group companies (each a"Wiley Company") or handled on behalf of a society with which a Wiley Company has exclusive publishing rights in relation to a particular work

(collectively "WILEY"). By clicking "accept" in connection with completing this licensing transaction, you agree that the following terms and conditions apply to this transaction (along with the billing and payment terms and conditions established by the Copyright Clearance Center Inc., ("CCC's Billing and Payment terms and conditions"), at the time that you opened your RightsLink account (these are available at any time at http://myaccount.copyright.com).

Terms and Conditions

- The materials you have requested permission to reproduce or reuse (the "Wiley Materials") are protected by copyright.

- You are hereby granted a personal, non-exclusive, non-sub licensable (on a stand-alone basis), non-transferable, worldwide, limited license to reproduce the Wiley Materials for the purpose specified in the licensing process. This license, **and any CONTENT (PDF or image file) purchased as part of your order,** is for a one-time use only and limited to any maximum distribution number specified in the license. The first instance of republication or reuse granted by this license must be completed within two years of the date of the grant of this license (although copies prepared before the end date may be distributed thereafter). The Wiley Materials shall not be used in any other manner or for any other purpose, beyond what is granted in the license. Permission is granted subject to an appropriate acknowledgement given to the author, title of the material/book/journal and the publisher. You shall also duplicate the copyright notice that appears in the Wiley publication in your use of the Wiley Material. Permission is also granted on the understanding that nowhere in the text is a previously published source acknowledged for all or part of this Wiley Material. Any third party content is expressly excluded from this permission.

- With respect to the Wiley Materials, all rights are reserved. Except as expressly granted by the terms of the license, no part of the Wiley Materials may be copied, modified, adapted (except for minor reformatting required by the new Publication), translated, reproduced, transferred or distributed, in any form or by any means, and no derivative works may be made based on the Wiley Materials without the prior permission of the respective copyright owner.**For STM Signatory Publishers clearing permission under the terms of the STM Permissions Guidelines only, the terms of the license are extended to include subsequent editions and for editions in other languages, provided such editions are for the work as a whole in situ and does not involve the separate exploitation of the permitted figures or extracts,** You may not alter, remove or suppress in any manner any copyright, trademark or other notices displayed by the Wiley Materials. You may not license, rent, sell, loan, lease, pledge, offer as security, transfer or assign the Wiley Materials on a stand-alone basis, or any of the rights granted to you hereunder to any other person.

- The Wiley Materials and all of the intellectual property rights therein shall at all times remain the exclusive property of John Wiley & Sons Inc, the Wiley Companies, or their respective licensors, and your interest therein is only that of having possession of and the right to reproduce the Wiley Materials pursuant to Section 2 herein during the continuance of this Agreement. You agree that you own no right, title or interest in or to the Wiley Materials or any of the intellectual property rights therein. You shall have no rights hereunder other than the license as provided for above in Section 2. No right, license or interest to any trademark, trade name, service mark or other branding ("Marks") of WILEY or its licensors is granted hereunder, and you agree that you shall not assert any such right, license or interest with respect thereto

TH-2122_126122042

- NEITHER WILEY NOR ITS LICENSORS MAKES ANY WARRANTY OR REPRESENTATION OF ANY KIND TO YOU OR ANY THIRD PARTY, EXPRESS, IMPLIED OR STATUTORY, WITH RESPECT TO THE MATERIALS OR THE ACCURACY OF ANY INFORMATION CONTAINED IN THE MATERIALS, INCLUDING, WITHOUT LIMITATION, ANY IMPLIED WARRANTY OF MERCHANTABILITY, ACCURACY, SATISFACTORY QUALITY, FITNESS FOR A PARTICULAR PURPOSE, USABILITY, INTEGRATION OR NON-INFRINGEMENT AND ALL SUCH WARRANTIES ARE HEREBY EXCLUDED BY WILEY AND ITS LICENSORS AND WAIVED BY YOU.

- WILEY shall have the right to terminate this Agreement immediately upon breach of this Agreement by you.

- You shall indemnify, defend and hold harmless WILEY, its Licensors and their respective directors, officers, agents and employees, from and against any actual or threatened claims, demands, causes of action or proceedings arising from any breach of this Agreement by you.

- IN NO EVENT SHALL WILEY OR ITS LICENSORS BE LIABLE TO YOU OR ANY OTHER PARTY OR ANY OTHER PERSON OR ENTITY FOR ANY SPECIAL, CONSEQUENTIAL, INCIDENTAL, INDIRECT, EXEMPLARY OR PUNITIVE DAMAGES, HOWEVER CAUSED, ARISING OUT OF OR IN CONNECTION WITH THE DOWNLOADING, PROVISIONING, VIEWING OR USE OF THE MATERIALS REGARDLESS OF THE FORM OF ACTION, WHETHER FOR BREACH OF CONTRACT, BREACH OF WARRANTY, TORT, NEGLIGENCE, INFRINGEMENT OR OTHERWISE (INCLUDING, WITHOUT LIMITATION, DAMAGES BASED ON LOSS OF PROFITS, DATA, FILES, USE, BUSINESS OPPORTUNITY OR CLAIMS OF THIRD PARTIES), AND WHETHER OR NOT THE PARTY HAS BEEN ADVISED OF THE POSSIBILITY OF SUCH DAMAGES. THIS LIMITATION SHALL APPLY NOTWITHSTANDING ANY FAILURE OF ESSENTIAL PURPOSE OF ANY LIMITED REMEDY PROVIDED HEREIN.

- Should any provision of this Agreement be held by a court of competent jurisdiction to be illegal, invalid, or unenforceable, that provision shall be deemed amended to achieve as nearly as possible the same economic effect as the original provision, and the legality, validity and enforceability of the remaining provisions of this Agreement shall not be affected or impaired thereby.

- The failure of either party to enforce any term or condition of this Agreement shall not constitute a waiver of either party's right to enforce each and every term and condition of this Agreement. No breach under this agreement shall be deemed waived or excused by either party unless such waiver or consent is in writing signed by the party granting such waiver or consent. The waiver by or consent of a party to a breach of any provision of this Agreement shall not operate or be construed as a waiver of or consent to any other or subsequent breach by such other party.

- This Agreement may not be assigned (including by operation of law or otherwise) by you without WILEY's prior written consent.

- Any fee required for this permission shall be non-refundable after thirty (30) days from receipt by the CCC.

TH-2122_126122042

- These terms and conditions together with CCC's Billing and Payment terms and conditions (which are incorporated herein) form the entire agreement between you and WILEY concerning this licensing transaction and (in the absence of fraud) supersedes all prior agreements and representations of the parties, oral or written. This Agreement may not be amended except in writing signed by both parties. This Agreement shall be binding upon and inure to the benefit of the parties' successors, legal representatives, and authorized assigns.

- In the event of any conflict between your obligations established by these terms and conditions and those established by CCC's Billing and Payment terms and conditions, these terms and conditions shall prevail.

- WILEY expressly reserves all rights not specifically granted in the combination of (i) the license details provided by you and accepted in the course of this licensing transaction, (ii) these terms and conditions and (iii) CCC's Billing and Payment terms and conditions.

- This Agreement will be void if the Type of Use, Format, Circulation, or Requestor Type was misrepresented during the licensing process.

- This Agreement shall be governed by and construed in accordance with the laws of the State of New York, USA, without regards to such state's conflict of law rules. Any legal action, suit or proceeding arising out of or relating to these Terms and Conditions or the breach thereof shall be instituted in a court of competent jurisdiction in New York County in the State of New York in the United States of America and each party hereby consents and submits to the personal jurisdiction of such court, waives any objection to venue in such court and consents to service of process by registered or certified mail, return receipt requested, at the last known address of such party.

WILEY OPEN ACCESS TERMS AND CONDITIONS

Wiley Publishes Open Access Articles in fully Open Access Journals and in Subscription journals offering Online Open. Although most of the fully Open Access journals publish open access articles under the terms of the Creative Commons Attribution (CC BY) License only, the subscription journals and a few of the Open Access Journals offer a choice of Creative Commons Licenses. The license type is clearly identified on the article.

The Creative Commons Attribution License

The Creative Commons Attribution License (CC-BY) allows users to copy, distribute and transmit an article, adapt the article and make commercial use of the article. The CC-BY license permits commercial and non-

Creative Commons Attribution Non-Commercial License

The Creative Commons Attribution Non-Commercial (CC-BY-NC)License permits use, distribution and reproduction in any medium, provided the original work is properly cited and is not used for commercial purposes.(see below)

Creative Commons Attribution-Non-Commercial-NoDerivs License

The Creative Commons Attribution Non-Commercial-NoDerivs License (CC-BY-NC-ND) permits use, distribution and reproduction in any medium, provided the original work is properly cited, is not used for commercial purposes and no modifications or adaptations are made. (see below)

Use by commercial "for-profit" organizations

Use of Wiley Open Access articles for commercial, promotional, or marketing purposes requires further explicit permission from Wiley and will be subject to a fee.

TH-2122_126122042

Further details can be found on Wiley Online Library
http://olabout.wiley.com/WileyCDA/Section/id-410895.html

Other Terms and Conditions:

v1.10 Last updated September 2015

Questions? customercare@copyright.com or +1-855-239-3415 (toll free in the US) or +1-978-646-2777.

TH-2122_126122042

Title: Synergistic Anticancer Potential of Artemisinin When Loaded with 8-Hydroxyquinoline-Surface Complexed-Zinc Ferrite Magnetofluorescent Nanoparticles and Albumin Composite

Author: Uday Narayan Pan, Pallab Sanpui, Anumita Paul, et al

Publication: ACS Applied Bio Materials

Publisher: American Chemical Society

Date: Nov 1, 2018

PERMISSION/LICENSE IS GRANTED FOR YOUR ORDER AT NO CHARGE

This type of permission/license, instead of the standard Terms & Conditions, is sent to you because no fee is being charged for your order. Please note the following:

- Permission is granted for your request in both print and electronic formats, and translations.
- If figures and/or tables were requested, they may be adapted or used in part.
- Please print this page for your records and send a copy of it to your publisher/graduate school.
- Appropriate credit for the requested material should be given as follows: "Reprinted (adapted) with permission from (COMPLETE REFERENCE CITATION). Copyright (YEAR) American Chemical Society." Insert appropriate information in place of the capitalized words.
- One-time permission is granted only for the use specified in your request. No additional uses are granted (such as derivative works or other editions). For any other uses, please submit a new request.

TH-2122_126122042

TH-2122_126122042

TH-2122_126122042

Royal Society of Chemistry LICENSE TERMS AND CONDITIONS

Dec 24, 2018

This is a License Agreement between IIT GUWAHATI -- UDAY PAN ("You") and Royal Society of Chemistry ("Royal Society of Chemistry") provided by Copyright Clearance Center ("CCC"). The license consists of your order details, the terms and conditions provided by Royal Society of Chemistry, and the payment terms and conditions.

All payments must be made in full to CCC. For payment instructions, please see information listed at the bottom of this form.

License Number	4495450105316
License date	Dec 24, 2018
Licensed content publisher	Royal Society of Chemistry
Licensed content title	RSC advances
Licensed content date	Jan 1, 2011
Type of Use	Thesis/Dissertation
Requestor type	Academic institution
Format	Print, Electronic
Portion	chart/graph/table/figure
Number of charts/graphs/tables/figures	1
The requesting person/organization is:	Uday Narayan Pan
Title or numeric reference of the portion(s)	Fig. 3
Title of the article or chapter the portion is from	Enhanced photoluminescence and thermal stability of zinc quinolate following complexation on the surface of quantum dots
Editor of portion(s)	N/A
Author of portion(s)	N/A
Volume of serial or monograph.	N/A
Page range of the portion	24219
Publication date of portion	23rd May 2014
Rights for	Main product
Duration of use	Life of current edition
Creation of copies for the disabled	no
With minor editing privileges	no
For distribution to	Worldwide
In the following language(s)	Original language of publication
With incidental promotional use	no
The lifetime unit quantity of new product	Up to 499
Title	Multifunctionalization of Nanoscale Particles for Cancer Theranostics
Institution name	Indian Institute of Technology Guwahati

Expected presentation date	Jan 2019
Billing Type	Invoice
Billing Address	IIT GUWAHATI BRAHMAPUTRA HOSTEL IIT GUWAHATI KAMRUP GUWAHATI, India 781039 Attn: IIT GUWAHATI
Total (may include CCC user fee)	0.00 USD

Terms and Conditions

TERMS AND CONDITIONS
The following terms are individual to this publisher:

None

Other Terms and Conditions:
STANDARD TERMS AND CONDITIONS

1. Description of Service; Defined Terms. This Republication License enables the User to obtain licenses for republication of one or more copyrighted works as described in detail on the relevant Order Confirmation (the "Work(s)"). Copyright Clearance Center, Inc. ("CCC") grants licenses through the Service on behalf of the rightsholder identified on the Order Confirmation (the "Rightsholder"). "Republication", as used herein, generally means the inclusion of a Work, in whole or in part, in a new work or works, also as described on the Order Confirmation. "User", as used herein, means the person or entity making such republication.
2. The terms set forth in the relevant Order Confirmation, and any terms set by the Rightsholder with respect to a particular Work, govern the terms of use of Works in connection with the Service. By using the Service, the person transacting for a republication license on behalf of the User represents and warrants that he/she/it (a) has been duly authorized by the User to accept, and hereby does accept, all such terms and conditions on behalf of User, and (b) shall inform User of all such terms and conditions. In the event such person is a "freelancer" or other third party independent of User and CCC, such party shall be deemed jointly a "User" for purposes of these terms and conditions. In any event, User shall be deemed to have accepted and agreed to all such terms and conditions if User republishes the Work in any fashion.
3. Scope of License; Limitations and Obligations.
3.1 All Works and all rights therein, including copyright rights, remain the sole and exclusive property of the Rightsholder. The license created by the exchange of an Order Confirmation (and/or any invoice) and payment by User of the full amount set forth on that document includes only those rights expressly set forth in the Order Confirmation and in these terms and conditions, and conveys no other rights in the Work(s) to User. All rights not expressly granted are hereby reserved.
3.2 General Payment Terms: You may pay by credit card or through an account with us payable at the end of the month. If you and we agree that you may establish a standing account with CCC, then the following terms apply: Remit Payment to: Copyright Clearance Center, 29118 Network Place, Chicago, IL 60673-1291. Payments Due: Invoices are payable upon their delivery to you (or upon our notice to you that they are available to you for downloading). After 30 days, outstanding amounts will be subject to a service charge of 1-1/2% per month or, if less, the maximum rate allowed by applicable law. Unless otherwise specifically set forth in the Order Confirmation or in a separate written agreement signed by CCC, invoices are due and payable on "net 30" terms. While User may exercise the rights licensed immediately upon issuance of the Order Confirmation, the license is automatically revoked and is null and void, as if it had never been issued, if complete payment for the license is not received on a timely basis either from User directly or through a payment agent, such as a credit card company.
3.3 Unless otherwise provided in the Order Confirmation, any grant of rights to User (i) is "one-time" (including the editions and product family specified in the license), (ii) is non-exclusive and non-transferable and (iii) is subject to any and all limitations and restrictions

(such as, but not limited to, limitations on duration of use or circulation) included in the Order Confirmation or invoice and/or in these terms and conditions. Upon completion of the licensed use, User shall either secure a new permission for further use of the Work(s) or immediately cease any new use of the Work(s) and shall render inaccessible (such as by deleting or by removing or severing links or other locators) any further copies of the Work (except for copies printed on paper in accordance with this license and still in User's stock at the end of such period).

3.4 In the event that the material for which a republication license is sought includes third party materials (such as photographs, illustrations, graphs, inserts and similar materials) which are identified in such material as having been used by permission, User is responsible for identifying, and seeking separate licenses (under this Service or otherwise) for, any of such third party materials; without a separate license, such third party materials may not be used.

3.5 Use of proper copyright notice for a Work is required as a condition of any license granted under the Service. Unless otherwise provided in the Order Confirmation, a proper copyright notice will read substantially as follows: “Republished with permission of [Rightsholder’s name], from [Work's title, author, volume, edition number and year of copyright]; permission conveyed through Copyright Clearance Center, Inc. ” Such notice must be provided in a reasonably legible font size and must be placed either immediately adjacent to the Work as used (for example, as part of a by-line or footnote but not as a separate electronic link) or in the place where substantially all other credits or notices for the new work containing the republished Work are located. Failure to include the required notice results in loss to the Rightsholder and CCC, and the User shall be liable to pay liquidated damages for each such failure equal to twice the use fee specified in the Order Confirmation, in addition to the use fee itself and any other fees and charges specified.

3.6 User may only make alterations to the Work if and as expressly set forth in the Order Confirmation. No Work may be used in any way that is defamatory, violates the rights of third parties (including such third parties' rights of copyright, privacy, publicity, or other tangible or intangible property), or is otherwise illegal, sexually explicit or obscene. In addition, User may not conjoin a Work with any other material that may result in damage to the reputation of the Rightsholder. User agrees to inform CCC if it becomes aware of any infringement of any rights in a Work and to cooperate with any reasonable request of CCC or the Rightsholder in connection therewith.

4. Indemnity. User hereby indemnifies and agrees to defend the Rightsholder and CCC, and their respective employees and directors, against all claims, liability, damages, costs and expenses, including legal fees and expenses, arising out of any use of a Work beyond the scope of the rights granted herein, or any use of a Work which has been altered in any unauthorized way by User, including claims of defamation or infringement of rights of copyright, publicity, privacy or other tangible or intangible property.

5. Limitation of Liability. UNDER NO CIRCUMSTANCES WILL CCC OR THE RIGHTSHOLDER BE LIABLE FOR ANY DIRECT, INDIRECT, CONSEQUENTIAL OR INCIDENTAL DAMAGES (INCLUDING WITHOUT LIMITATION DAMAGES FOR LOSS OF BUSINESS PROFITS OR INFORMATION, OR FOR BUSINESS INTERRUPTION) ARISING OUT OF THE USE OR INABILITY TO USE A WORK, EVEN IF ONE OF THEM HAS BEEN ADVISED OF THE POSSIBILITY OF SUCH DAMAGES. In any event, the total liability of the Rightsholder and CCC (including their respective employees and directors) shall not exceed the total amount actually paid by User for this license. User assumes full liability for the actions and omissions of its principals, employees, agents, affiliates, successors and assigns.

6. Limited Warranties. THE WORK(S) AND RIGHT(S) ARE PROVIDED “AS IS”. CCC HAS THE RIGHT TO GRANT TO USER THE RIGHTS GRANTED IN THE ORDER CONFIRMATION DOCUMENT. CCC AND THE RIGHTSHOLDER DISCLAIM ALL OTHER WARRANTIES RELATING TO THE WORK(S) AND RIGHT(S), EITHER EXPRESS OR IMPLIED, INCLUDING WITHOUT LIMITATION IMPLIED WARRANTIES OF MERCHANTABILITY OR FITNESS FOR A PARTICULAR PURPOSE. ADDITIONAL RIGHTS MAY BE REQUIRED TO USE ILLUSTRATIONS, GRAPHS, PHOTOGRAPHS, ABSTRACTS, INSERTS OR OTHER PORTIONS OF THE WORK (AS OPPOSED TO THE ENTIRE WORK) IN A MANNER CONTEMPLATED

BY USER; USER UNDERSTANDS AND AGREES THAT NEITHER CCC NOR THE RIGHTSHOLDER MAY HAVE SUCH ADDITIONAL RIGHTS TO GRANT.

7. Effect of Breach. Any failure by User to pay any amount when due, or any use by User of a Work beyond the scope of the license set forth in the Order Confirmation and/or these terms and conditions, shall be a material breach of the license created by the Order Confirmation and these terms and conditions. Any breach not cured within 30 days of written notice thereof shall result in immediate termination of such license without further notice. Any unauthorized (but licensable) use of a Work that is terminated immediately upon notice thereof may be liquidated by payment of the Rightsholder's ordinary license price therefor; any unauthorized (and unlicensable) use that is not terminated immediately for any reason (including, for example, because materials containing the Work cannot reasonably be recalled) will be subject to all remedies available at law or in equity, but in no event to a payment of less than three times the Rightsholder's ordinary license price for the most closely analogous licensable use plus Rightsholder's and/or CCC's costs and expenses incurred in collecting such payment.

8. **Miscellaneous.**

8.1 User acknowledges that CCC may, from time to time, make changes or additions to the Service or to these terms and conditions, and CCC reserves the right to send notice to the User by electronic mail or otherwise for the purposes of notifying User of such changes or additions; provided that any such changes or additions shall not apply to permissions already secured and paid for.

8.2 Use of User-related information collected through the Service is governed by CCC's privacy policy, available online here: http://www.copyright.com/content/cc3/en/tools/footer/privacypolicy.html.

8.3 The licensing transaction described in the Order Confirmation is personal to User. Therefore, User may not assign or transfer to any other person (whether a natural person or an organization of any kind) the license created by the Order Confirmation and these terms and conditions or any rights granted hereunder; provided, however, that User may assign such license in its entirety on written notice to CCC in the event of a transfer of all or substantially all of User's rights in the new material which includes the Work(s) licensed under this Service.

8.4 No amendment or waiver of any terms is binding unless set forth in writing and signed by the parties. The Rightsholder and CCC hereby object to any terms contained in any writing prepared by the User or its principals, employees, agents or affiliates and purporting to govern or otherwise relate to the licensing transaction described in the Order Confirmation, which terms are in any way inconsistent with any terms set forth in the Order Confirmation and/or in these terms and conditions or CCC's standard operating procedures, whether such writing is prepared prior to, simultaneously with or subsequent to the Order Confirmation, and whether such writing appears on a copy of the Order Confirmation or in a separate instrument.

8.5 The licensing transaction described in the Order Confirmation document shall be governed by and construed under the law of the State of New York, USA, without regard to the principles thereof of conflicts of law. Any case, controversy, suit, action, or proceeding arising out of, in connection with, or related to such licensing transaction shall be brought, at CCC's sole discretion, in any federal or state court located in the County of New York, State of New York, USA, or in any federal or state court whose geographical jurisdiction covers the location of the Rightsholder set forth in the Order Confirmation. The parties expressly submit to the personal jurisdiction and venue of each such federal or state court.If you have any comments or questions about the Service or Copyright Clearance Center, please contact us at 978-750-8400 or send an e-mail to info@copyright.com.

v 1.1

Questions? customercare@copyright.com or +1-855-239-3415 (toll free in the US) or +1-978-646-2777.

TH-2122_126122042

JOHN WILEY AND SONS LICENSE TERMS AND CONDITIONS

Dec 24, 2018

This Agreement between IIT GUWAHATI -- UDAY PAN ("You") and John Wiley and Sons ("John Wiley and Sons") consists of your license details and the terms and conditions provided by John Wiley and Sons and Copyright Clearance Center.

License Number	4495430658218
License date	Dec 24, 2018
Licensed Content Publisher	John Wiley and Sons
Licensed Content Publication	Small
Licensed Content Title	Gold Nanocluster Embedded Albumin Nanoparticles for Two-Photon Imaging of Cancer Cells Accompanying Drug Delivery
Licensed Content Author	Rumi Khandelia, Satyapriya Bhandari, Uday Narayan Pan, et al
Licensed Content Date	May 4, 2015
Licensed Content Volume	11
Licensed Content Issue	33
Licensed Content Pages	7
Type of use	Dissertation/Thesis
Requestor type	Author of this Wiley article
Format	Print and electronic
Portion	Full article
Will you be translating?	No
Title of your thesis / dissertation	Multifunctionalization of Nanoscale Particles for Cancer Theranostics
Expected completion date	Jan 2019
Expected size (number of pages)	1
Requestor Location	IIT GUWAHATI BRAHMAPUTRA HOSTEL IIT GUWAHATI KAMRUP GUWAHATI, ASSAM 781039 India Attn: IIT GUWAHATI
Publisher Tax ID	EU826007151
Total	0.00 USD
Terms and Conditions	

TERMS AND CONDITIONS

This copyrighted material is owned by or exclusively licensed to John Wiley & Sons, Inc. or one of its group companies (each a"Wiley Company") or handled on behalf of a society with which a Wiley Company has exclusive publishing rights in relation to a particular work (collectively "WILEY"). By clicking "accept" in connection with completing this licensing transaction, you agree that the following terms and conditions apply to this transaction (along with the billing and payment terms and conditions established by the Copyright Clearance Center Inc., ("CCC's Billing and Payment terms and conditions"), at the time that you opened your RightsLink account (these are available at any time at http://myaccount.copyright.com).

Terms and Conditions

- The materials you have requested permission to reproduce or reuse (the "Wiley Materials") are protected by copyright.

- You are hereby granted a personal, non-exclusive, non-sub licensable (on a stand-alone basis), non-transferable, worldwide, limited license to reproduce the Wiley Materials for the purpose specified in the licensing process. This license, **and any CONTENT (PDF or image file) purchased as part of your order,** is for a one-time use only and limited to any maximum distribution number specified in the license. The first instance of republication or reuse granted by this license must be completed within two years of the date of the grant of this license (although copies prepared before the end date may be distributed thereafter). The Wiley Materials shall not be used in any other manner or for any other purpose, beyond what is granted in the license. Permission is granted subject to an appropriate acknowledgement given to the author, title of the material/book/journal and the publisher. You shall also duplicate the copyright notice that appears in the Wiley publication in your use of the Wiley Material. Permission is also granted on the understanding that nowhere in the text is a previously published source acknowledged for all or part of this Wiley Material. Any third party content is expressly excluded from this permission.

- With respect to the Wiley Materials, all rights are reserved. Except as expressly granted by the terms of the license, no part of the Wiley Materials may be copied, modified, adapted (except for minor reformatting required by the new Publication), translated, reproduced, transferred or distributed, in any form or by any means, and no derivative works may be made based on the Wiley Materials without the prior permission of the respective copyright owner.**For STM Signatory Publishers clearing permission under the terms of the STM Permissions Guidelines only, the terms of the license are extended to include subsequent editions and for editions in other languages, provided such editions are for the work as a whole in situ and does not involve the separate exploitation of the permitted figures or extracts,** You may not alter, remove or suppress in any manner any copyright, trademark or other notices displayed by the Wiley Materials. You may not license, rent, sell, loan, lease, pledge, offer as security, transfer or assign the Wiley Materials on a stand-alone basis, or any of the rights granted to you hereunder to any other person.

- The Wiley Materials and all of the intellectual property rights therein shall at all times remain the exclusive property of John Wiley & Sons Inc, the Wiley Companies, or their respective licensors, and your interest therein is only that of having possession of and the right to reproduce the Wiley Materials pursuant to Section 2 herein during the continuance of this Agreement. You agree that you own no right, title or interest in or to the Wiley Materials or any of the intellectual property rights therein. You shall have no rights hereunder other than the license as provided for above in Section 2. No right, license or interest to any trademark, trade name, service mark or other branding ("Marks") of WILEY or its licensors is granted hereunder, and you agree that you shall not assert any such right, license or interest with respect thereto

- NEITHER WILEY NOR ITS LICENSORS MAKES ANY WARRANTY OR REPRESENTATION OF ANY KIND TO YOU OR ANY THIRD PARTY, EXPRESS, IMPLIED OR STATUTORY, WITH RESPECT TO THE MATERIALS OR THE ACCURACY OF ANY INFORMATION CONTAINED IN THE MATERIALS, INCLUDING, WITHOUT LIMITATION, ANY IMPLIED WARRANTY OF MERCHANTABILITY, ACCURACY, SATISFACTORY QUALITY, FITNESS FOR A PARTICULAR PURPOSE, USABILITY, INTEGRATION OR NON-INFRINGEMENT AND ALL SUCH WARRANTIES ARE HEREBY EXCLUDED BY WILEY AND ITS LICENSORS AND WAIVED

BY YOU.

- WILEY shall have the right to terminate this Agreement immediately upon breach of this Agreement by you.

- You shall indemnify, defend and hold harmless WILEY, its Licensors and their respective directors, officers, agents and employees, from and against any actual or threatened claims, demands, causes of action or proceedings arising from any breach of this Agreement by you.

- IN NO EVENT SHALL WILEY OR ITS LICENSORS BE LIABLE TO YOU OR ANY OTHER PARTY OR ANY OTHER PERSON OR ENTITY FOR ANY SPECIAL, CONSEQUENTIAL, INCIDENTAL, INDIRECT, EXEMPLARY OR PUNITIVE DAMAGES, HOWEVER CAUSED, ARISING OUT OF OR IN CONNECTION WITH THE DOWNLOADING, PROVISIONING, VIEWING OR USE OF THE MATERIALS REGARDLESS OF THE FORM OF ACTION, WHETHER FOR BREACH OF CONTRACT, BREACH OF WARRANTY, TORT, NEGLIGENCE, INFRINGEMENT OR OTHERWISE (INCLUDING, WITHOUT LIMITATION, DAMAGES BASED ON LOSS OF PROFITS, DATA, FILES, USE, BUSINESS OPPORTUNITY OR CLAIMS OF THIRD PARTIES), AND WHETHER OR NOT THE PARTY HAS BEEN ADVISED OF THE POSSIBILITY OF SUCH DAMAGES. THIS LIMITATION SHALL APPLY NOTWITHSTANDING ANY FAILURE OF ESSENTIAL PURPOSE OF ANY LIMITED REMEDY PROVIDED HEREIN.

- Should any provision of this Agreement be held by a court of competent jurisdiction to be illegal, invalid, or unenforceable, that provision shall be deemed amended to achieve as nearly as possible the same economic effect as the original provision, and the legality, validity and enforceability of the remaining provisions of this Agreement shall not be affected or impaired thereby.

- The failure of either party to enforce any term or condition of this Agreement shall not constitute a waiver of either party's right to enforce each and every term and condition of this Agreement. No breach under this agreement shall be deemed waived or excused by either party unless such waiver or consent is in writing signed by the party granting such waiver or consent. The waiver by or consent of a party to a breach of any provision of this Agreement shall not operate or be construed as a waiver of or consent to any other or subsequent breach by such other party.

- This Agreement may not be assigned (including by operation of law or otherwise) by you without WILEY's prior written consent.

- Any fee required for this permission shall be non-refundable after thirty (30) days from receipt by the CCC.

- These terms and conditions together with CCC's Billing and Payment terms and conditions (which are incorporated herein) form the entire agreement between you and WILEY concerning this licensing transaction and (in the absence of fraud) supersedes all prior agreements and representations of the parties, oral or written. This Agreement may not be amended except in writing signed by both parties. This Agreement shall be binding upon and inure to the benefit of the parties' successors, legal representatives, and authorized assigns.

- In the event of any conflict between your obligations established by these terms and conditions and those established by CCC's Billing and Payment terms and conditions, these terms and conditions shall prevail.

TH-2122_126122042

- WILEY expressly reserves all rights not specifically granted in the combination of (i) the license details provided by you and accepted in the course of this licensing transaction, (ii) these terms and conditions and (iii) CCC's Billing and Payment terms and conditions.

- This Agreement will be void if the Type of Use, Format, Circulation, or Requestor Type was misrepresented during the licensing process.

- This Agreement shall be governed by and construed in accordance with the laws of the State of New York, USA, without regards to such state's conflict of law rules. Any legal action, suit or proceeding arising out of or relating to these Terms and Conditions or the breach thereof shall be instituted in a court of competent jurisdiction in New York County in the State of New York in the United States of America and each party hereby consents and submits to the personal jurisdiction of such court, waives any objection to venue in such court and consents to service of process by registered or certified mail, return receipt requested, at the last known address of such party.

WILEY OPEN ACCESS TERMS AND CONDITIONS

Wiley Publishes Open Access Articles in fully Open Access Journals and in Subscription journals offering Online Open. Although most of the fully Open Access journals publish open access articles under the terms of the Creative Commons Attribution (CC BY) License only, the subscription journals and a few of the Open Access Journals offer a choice of Creative Commons Licenses. The license type is clearly identified on the article.

The Creative Commons Attribution License

The Creative Commons Attribution License (CC-BY) allows users to copy, distribute and transmit an article, adapt the article and make commercial use of the article. The CC-BY license permits commercial and non-

Creative Commons Attribution Non-Commercial License

The Creative Commons Attribution Non-Commercial (CC-BY-NC)License permits use, distribution and reproduction in any medium, provided the original work is properly cited and is not used for commercial purposes.(see below)

Creative Commons Attribution-Non-Commercial-NoDerivs License

The Creative Commons Attribution Non-Commercial-NoDerivs License (CC-BY-NC-ND) permits use, distribution and reproduction in any medium, provided the original work is properly cited, is not used for commercial purposes and no modifications or adaptations are made. (see below)

Use by commercial "for-profit" organizations

Use of Wiley Open Access articles for commercial, promotional, or marketing purposes requires further explicit permission from Wiley and will be subject to a fee.

Further details can be found on Wiley Online Library

http://olabout.wiley.com/WileyCDA/Section/id-410895.html

Other Terms and Conditions:

v1.10 Last updated September 2015

Questions? customercare@copyright.com or +1-855-239-3415 (toll free in the US) or +1-978-646-2777.

TH-2122_126122042